

Modeling extreme events in ocean acidity and compound extreme events using a comprehensive Earth system model

Inauguraldissertation

der Philosophisch–naturwissenschaftlichen Fakultät
der Universität Bern

vorgelegt von

Friedrich Anton Burger

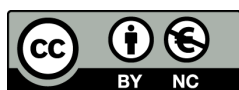
aus Freiburg im Breisgau, Deutschland

Leiter der Arbeit:

Prof. Dr. Thomas Frölicher

Abteilung für Klima– und Umweltphysik

Physikalisches Institut der Universität Bern



This work is licensed under a Creative Commons Attribution-NonCommercial 4.0 International

License: <https://creativecommons.org/licenses/by-nc/4.0/>

Modeling extreme events in ocean acidity and compound extreme events using a comprehensive Earth system model

Inauguraldissertation

der Philosophisch–naturwissenschaftlichen Fakultät
der Universität Bern

vorgelegt von

Friedrich Anton Burger

aus Freiburg im Breisgau, Deutschland

Leiter der Arbeit:

Prof. Dr. Thomas Frölicher

Abteilung für Klima– und Umweltphysik
Physikalisches Institut der Universität Bern

Von der Philosophisch–naturwissenschaftlichen Fakultät angenommen.

Bern, 30.11.2021

Der Dekan

Prof. Dr. Zoltan Balogh

Für meine Eltern,
Bärbel und Uli

Thesis overview and summary

Anthropogenic CO₂ emissions not only cause global warming, but also ocean acidification, i.e., a shift towards higher [H⁺] and lower pH with the accumulation of anthropogenic carbon in seawater. Ocean acidification is a potential threat for many marine species, in particular for calcifying marine invertebrates like mollusks or echinoderms, which are important components of the marine food web. Seasonal variations in [H⁺] and oceanic carbonate system variables, such as the aragonite saturation state (Ω_A) or the partial pressure of CO₂ ($p\text{CO}_2$), have been identified as important modes of variability along with the long-term changes under ocean acidification. These variations are also known to change in amplitude under ocean acidification and may hence become more important in the future. In contrast to these annually occurring variations, relatively little is known about the occurrence of rare and extreme departures from normal conditions in [H⁺] and carbonate system variables. Such extreme events may add substantially to the stress experienced by organisms from the long-term changes under ocean acidification. The global ocean is not only getting more acidic, but it is also getting warmer due to the ocean heat uptake under global warming. These co-occurring changes are of particular concern, since interactions between the environmental stressors potentially aggravate the stress for marine organisms. In consequence, also co-occurring extremes (so-called compound extreme events) in temperature and [H⁺] may pose a higher risk to vulnerable species than extremes in temperature or [H⁺] alone.

In this thesis, a global overview on the occurrence and characteristics of extreme events in [H⁺] and aragonite saturation state (Ω_A) is given. We quantify changes in these extreme events under climate change based on large ensemble simulations of the fully-coupled Earth system model GFDL ESM2M. The drivers of the extremes are assessed and the causes of changes in their characteristics are analyzed. Furthermore, we quantify the frequency of compound extreme events in [H⁺] and temperature and how their frequency may change under ocean warming and acidification.

The introduction (Chapter 1) provides an overview of the global carbon cycle and its perturbation under anthropogenic CO₂ emissions. The properties of oceanic carbonate chemistry and acid-base state are presented, and their biogeochemical control processes discussed. Ocean acidification, the shift towards more acidic conditions due to the oceanic uptake of anthropogenic carbon, and its biological implications are also discussed. Finally, extreme events in ocean acidity are introduced and their role as a potential additional stressor for marine organisms is discussed.

Chapter 2 introduces the GFDL ESM2M Earth system model and describes how the large ensemble simulations that are analyzed in this thesis were conducted. It describes how extreme events are defined in this thesis and compares different approaches for defining these events. Furthermore, the metrics that are used to characterize the extreme events are defined.

Chapter 3, which is published in *Biogeosciences*, analyzes the changes in high-[H⁺] and low- Ω_A extremes under climate change. To do so, we define the extremes relative to fixed preindustrial baselines and relative to shifting-mean baselines. Relative to fixed preindustrial

baselines, the mean changes in $[\text{H}^+]$ and Ω_{A} due to ocean acidification cause both variables to transition to a near-permanent extreme state in the 21st century, at the surface and also at 200 m depth. Relative to shifting-mean baselines, increases in $[\text{H}^+]$ variability cause $[\text{H}^+]$ extremes to become more frequent, intense, long-lasting, and spatially extended. The increases in $[\text{H}^+]$ variability are primarily caused by increases in mean inorganic carbon concentrations (C_{T}) that make $[\text{H}^+]$ more sensitive to variations in its drivers. In contrast, extremes in Ω_{A} are shown to become less frequent when defined relative to shifting-mean baselines, reflecting that Ω_{A} becomes less variable as it declines with ocean acidification.

The frequency of compound extreme events in temperature and $[\text{H}^+]$ in the surface ocean is assessed in Chapter 4. Based on observation-derived data, we show that these compound events occur frequently in the subtropical oceans, while they are much rarer in the equatorial Pacific and the mid-to-high latitudes. This spatial pattern emerges from the regionally varying importance of temperature and carbon for variations in $[\text{H}^+]$. The compound events occur frequently where $[\text{H}^+]$ variations are primarily driven by temperature, and they are relatively rare where $[\text{H}^+]$ variations are mainly driven by C_{T} . Based on large ensemble simulations that were conducted with the GFDL-ESM2M model, we show that ocean acidification and ocean warming cause large increases in the frequency of these compound events under fixed baselines. Smaller increases are projected relative to shifting-mean baselines, which primarily arise due to the increases in $[\text{H}^+]$ variability that are discussed in Chapter 3. Finally, we isolate the effect of changes in the statistical dependence between temperature and $[\text{H}^+]$ on compound event occurrence, finding that an overall reduction in dependence dampens the increases in event frequency, in particular when defined relative to shifting-mean baselines.

The drivers of surface $[\text{H}^+]$ extreme events within the GFDL ESM2M model are investigated in Chapter 5. In the subtropics, we find that the buildup of $[\text{H}^+]$ extreme events is mainly caused by positive anomalies in air-sea heat fluxes, which increase temperature and thus $[\text{H}^+]$. These temperature increases are dampened by reductions in convective mixing from the nonlocal KPP parameterization, which normally offsets the air-sea heat loss in the subtropics. In the mid-to-high latitudes, we find positive anomalies in the vertical mixing and diffusion of temperature to be the main driver of the buildup of $[\text{H}^+]$ extremes, either due to reduced heat loss to the subsurface or due to increased upward heat transport from the subsurface. In the equatorial Pacific, event buildup is mainly driven by advection of C_{T} . The decay of $[\text{H}^+]$ extreme events is predominantly caused by reductions in C_{T} due to outgassing of carbon to the atmosphere. Furthermore, increased heat losses to the atmosphere in the subtropics and enhanced biological production in the tropics contribute substantially to $[\text{H}^+]$ extreme event decay.

The main results of Chapters 3-5 are summarized and discussed in Chapter 6. Caveats of the analyses are listed and an outlook on potential future projects is given.

Contents

Thesis overview and summary	5
1 Introduction	9
1.1 The global carbon cycle and its role in the climate system	9
1.2 The ocean's carbonate chemistry and biogeochemistry	12
1.3 Ocean acidification	18
1.4 Extreme events in ocean acidity	21
2 Methods	27
2.1 GFDL ESM2M Earth system model	27
2.2 Simulation design	30
2.3 Extreme event definition and metrics	33
3 Increase in ocean acidity variability and extremes	47
4 Compound marine heatwaves and ocean acidity extremes	79
4.1 Introduction	80
4.2 Results	81
4.3 Discussion and conclusions	87
4.4 Methods	90
5 Drivers of ocean acidity extreme events	113
5.1 Introduction	114
5.2 Methods	115
5.3 Results	119
5.4 Discussion and conclusions	126
5.5 Appendix of Chapter 5	130
6 Discussion and outlook	139
6.1 Summary and discussion of the main results	139
6.2 Caveats and limitations	146
6.3 Outlook	149

Appendix: Modeling activities with the GFDL ESM2M model at CSCS	155
Acknowledgements	165
Publications	167
Erklärung gemäss Art. 18 PromR Phil.-nat. 2019	169

Chapter 1

Introduction

In this thesis, extreme events in ocean acidity (quantified by $[H^+]$ or pH) and related oceanic carbonate system variables are analyzed. In addition, compound extreme events in ocean acidity and temperature are investigated. The changes in these extremes under anthropogenic climate change and co-occurring ocean acidification are discussed. Chapter 1 provides the basic knowledge that is necessary for the remainder of this thesis.

Sect. 1.1 introduces the global carbon cycle and its role in the climate system. The chemical properties of inorganic carbon in the ocean and the biogeochemical processes that drive variations in inorganic carbon are discussed in detail in Sect. 1.2, as these are of fundamental importance for the oceanic acid-base state. Ocean acidification, the shift towards more acidic ocean conditions due to the oceanic uptake of anthropogenic CO_2 emissions, and its biological implications are discussed in Sect. 1.3. Finally, extreme events in ocean acidity and related carbonate chemistry variables are introduced and the current state of the research on these events is resumed in Sect. 1.4.

1.1 The global carbon cycle and its role in the climate system

Carbon is exchanged in large quantities between the ocean, atmosphere, and land (Fig. 1.1). By far the most carbon (38 000 GtC (gigatons or billion tons of carbon); Ciais et al., 2013) is stored in inorganic molecules in the ocean, mainly in bicarbonate and carbonate ions (Sect. 1.2.1). Substantial, although much smaller amounts of carbon are also stored as dissolved organic carbon in the ocean (700 GtC; Ciais et al., 2013). Carbon in the ocean is predominantly located in the intermediate and deep ocean (about 97 % of total oceanic carbon; Siegenthaler & Sarmiento, 1993). Compared to the large reservoir size, the exchange of oceanic carbon with the atmosphere by air-sea gas exchange is relatively small, making the ocean a long-term storage that adjusts to changes in atmospheric carbon only on timescales of centuries and millennia (Joos et al., 2013).

In the atmosphere, carbon is mainly stored as carbon dioxide (CO_2), while other forms such as methane (CH_4) or carbon monoxide (CO) account for less than one percent of atmospheric carbon (Ciais et al., 2013). At preindustrial times (around year 1750), about 589 GtC were stored in the atmosphere (Ciais et al., 2013). The atmospheric carbon reservoir is thus much smaller than the oceanic carbon reservoir (1.5 % of the oceanic reservoir at preindustrial times). Gross fluxes between atmosphere and land (soils and vegetation) are similarly large than those between atmosphere and ocean (120 GtC per year and 90 GtC, respectively (Fig. 1.1); Ciais et al., 2013). Atmosphere-land exchange fluxes are caused by photosynthetic uptake of CO_2 in plants and by release of carbon from autotrophic respiration in plants and heterotrophic respiration in soils. A smaller amount of carbon is also exchanged between land and ocean through river

runoff. On timescales of several millennia to hundreds of thousands of years, carbon variations due to other processes like sedimentation on the ocean floor and rock weathering also become important (Jeltsch-Thömmes & Joos, 2020).

The global carbon cycle

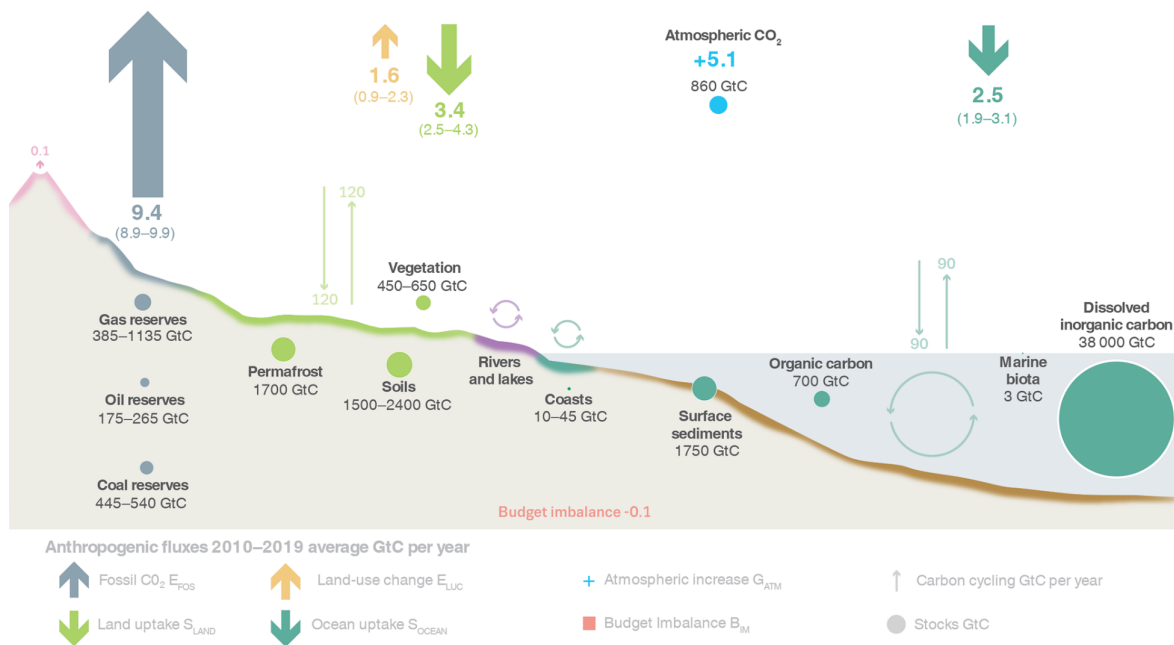


Figure 1.1: A scheme of the reservoirs of carbon in the global carbon cycle (circles; numbers in GtC, gigatons of carbon) and the fluxes between these reservoirs (arrows; in GtC per year). Thin arrows indicate gross fluxes between the reservoirs and thick arrows indicate net changes in the reservoirs due to anthropogenic perturbation. The figure is taken from Friedlingstein et al. (2020). The atmospheric carbon reservoir is given for present-day conditions and thus differs from that reported in the text for preindustrial times.

The natural carbon cycle has been substantially perturbed since the industrialization. Since 1850, the atmospheric concentration of CO₂ has risen by about 45 % (Friedlingstein et al., 2020) from around 285 parts per million volume (volumetric mixing ratio, ppmv) to 412 ppmv in year 2020 (Friedlingstein et al., 2020). This increase in atmospheric CO₂ is caused by CO₂ emissions from fossil fuel combustion (68 % of total emissions) and land use change, which is mainly due to deforestation (32 % of total emissions; Friedlingstein et al., 2020). At present-day, emissions from land use changes are less important compared to fossil fuel emissions. For example for the year 2019, the contribution from land use change emissions to total emissions was only 16 % (Friedlingstein et al., 2020).

This increase in atmospheric CO₂ has also caused an imbalance in the naturally occurring exchange fluxes between the carbon reservoirs (thin arrows in Fig. 1.1), resulting in net carbon fluxes from the atmosphere into the ocean (around 2.5 PgC per year in the last decade; Friedlingstein et al., 2020) and land (3.4 PgC per year; thick arrows in Fig. 1.1). About 41 % of the anthropogenic carbon emissions since 1850 have stayed in the atmosphere. Around 32 % of the carbon emissions have been taken up by the land vegetation and soils, and around 25 % have been dissolved in the oceans (Friedlingstein et al., 2020). During the 21st century, atmospheric CO₂ concentrations are expected to further increase¹. Under the ‘middle of the road’ shared socio-economic pathway SSP2-4.5, atmospheric CO₂ increases to 603 ppmv by 2100 (Meinshausen et al., 2020). However, atmospheric CO₂ may also be much higher at that time, such as 867 ppmv

¹Only under the low-end greenhouse gas emission scenario SSP1-1.9, the atmospheric CO₂ concentration is lower in year 2100 than it is today (Meinshausen et al., 2020).

under the medium-to-high emission scenario SSP3-7.0 (Meinshausen et al., 2020). Land and ocean are also projected to take up more carbon under scenarios with higher emissions, although the fraction of carbon that remains in the atmosphere is projected to be higher under scenarios with higher emissions (Masson-Delmotte et al., 2021). The concentration of the greenhouse gas CO_2 is of immediate importance for global warming.

The greenhouse effect is based on a partial absorption of the thermal radiation that is emitted by the Earth's surface by gases in the atmosphere. A part of the absorbed radiation is emitted back to the surface, resulting in higher surface temperatures. Most of the natural greenhouse effect is caused by water vapor. Yet, the greenhouse effect from increasing concentrations in CO_2 is the main driver of anthropogenic climate change (Masson-Delmotte et al., 2021).

The increase in atmospheric CO_2 concentration ($[\text{CO}_2]$) causes a radiative imbalance between incoming shortwave (mainly visible and ultraviolet) solar radiation and the outgoing longwave (mainly infrared) radiation. This radiative imbalance, referred to as *radiative forcing*, causes an increase in atmospheric temperatures until a new equilibrium between incoming and outgoing radiation is reached. The radiative forcing of CO_2 was approximated by Myhre et al. (1998) as

$$RF(\text{CO}_2) \simeq 5.35 \text{ W m}^{-2} \ln \frac{[\text{CO}_2]}{[\text{CO}_2]_0}, \quad (1.1)$$

growing logarithmically with the ratio between atmospheric CO_2 concentration and a preindustrial reference concentration $[\text{CO}_2]_0$. The logarithmic growth reflects that less additional longwave radiation is absorbed by a CO_2 molecule if $[\text{CO}_2]$ is already high. The radiative forcing from a doubling of $[\text{CO}_2]$ is 3.7 W m^{-2} .

Treating the Earth as a black body that emits longwave radiation at an effective radiation temperature T , the difference between incoming and outgoing radiation per unit area (h) is zero in equilibrium,

$$0 = h = \frac{S_0}{4} (1 - \alpha) - \sigma T^4, \quad (1.2)$$

with the planetary albedo α that specifies the proportion of reflected incoming shortwave radiation, for example due to polar ice caps, the solar constant $S_0 = 1367 \text{ W m}^{-2}$, and the Stefan Boltzmann constant $\sigma = 5.67 \cdot 10^{-8} \text{ W m}^{-2} \text{ K}^{-4}$. Adding the radiative forcing to the energy balance, T must increase to some extent (the temperature change is denoted by ΔT) to compensate the radiative forcing by increased outgoing longwave radiation. Under the new equilibrium, it is

$$0 = \Delta h + RF \simeq \underbrace{\frac{\partial h}{\partial T}}_{\lambda} \Delta T + RF, \quad (1.3)$$

with the climate feedback parameter $\lambda = \frac{\partial h}{\partial T}$. Assuming a constant albedo $\alpha = 0.3$ and using Eq. (1.2), it is $\lambda = 3.8 \text{ W m}^{-2} \text{ K}^{-1}$ and the increase in temperature (Eq. 1.3) is here thus 1°C . However, positive feedback factors in λ , such as from a decrease in albedo α with temperature or the water vapor feedback, have been neglected here. The current best estimate for the equilibrium temperature change due to a doubling in atmospheric $[\text{CO}_2]$ is 3°C with a likely range of 2.5°C to 4°C (Masson-Delmotte et al., 2021).

1.2 The ocean's carbonate chemistry and biogeochemistry

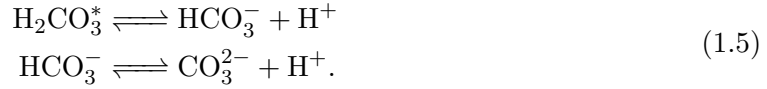
1.2.1 Oceanic carbonate chemistry

When seawater is in equilibrium with the atmosphere that contains CO_2 , there will be an equilibrium between CO_2 in the gas phase and aqueous CO_2 in the solution. Aqueous CO_2 reacts with H_2O to form carbonic acid H_2CO_3 . Since the two species are hard to separate experimentally, they are usually combined, here denoted by H_2CO_3^* (Sarmiento & Gruber, 2006). The concentration of aqueous CO_2 and H_2CO_3 ($[\text{H}_2\text{CO}_3^*]$, concentrations in mole per kg solution are denoted by square brackets) at a given partial pressure of CO_2 in the atmosphere, $p\text{CO}_2$, is given by

$$[\text{H}_2\text{CO}_3^*] = K_0 \cdot p\text{CO}_2, \quad (1.4)$$

with K_0 the solubility of CO_2 that follows *Henry's law* (Henry & Banks, 1803). The solubility of CO_2 (Eq. 1.4) decreases with temperature (Fig. 1.2a) and to a lesser extent also with salinity (Fig. 1.2b).

Carbonic acid, a weak acid, dissociates to some extent into its conjugate bases, bicarbonate ions HCO_3^- and carbonate ions CO_3^{2-} , thereby increasing the hydrogen ion concentration² $[\text{H}^+]$ and hence the acidity of seawater. These reactions are given by



The dissociation constants for these reactions, which result from the law of mass action, are

$$\begin{aligned} K_1 &= \frac{[\text{HCO}_3^-][\text{H}^+]}{[\text{H}_2\text{CO}_3^*]} \\ K_2 &= \frac{[\text{CO}_3^{2-}][\text{H}^+]}{[\text{HCO}_3^-]}. \end{aligned} \quad (1.6)$$

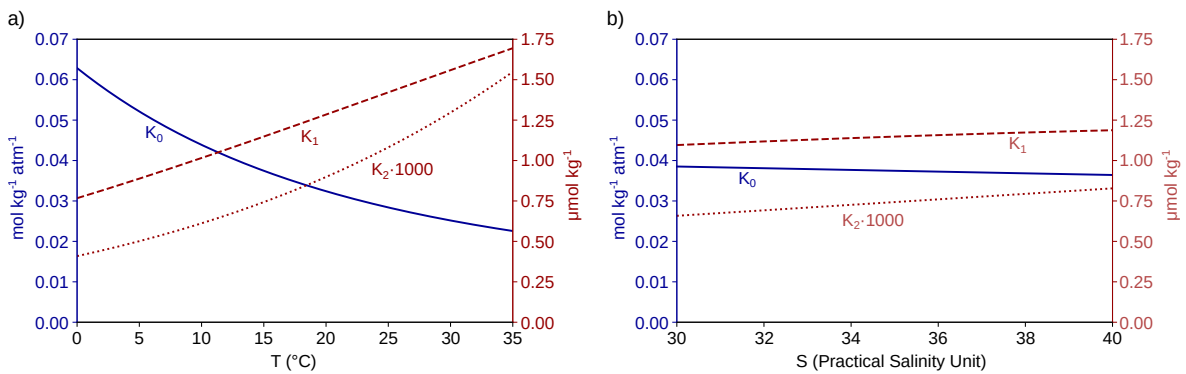


Figure 1.2: a) The temperature dependence of CO_2 solubility (following Weiss (1974); left axis in blue) and the dissociation constants of carbonic acid (following Lueker et al. (2000); right axis in red) at salinity $S=35$ PSU. K_2 is smaller than K_1 by a factor 1000. b) The salinity dependence of CO_2 solubility (left axis in blue) and the dissociation constants of carbonic acid (right axis in red) at $T=15$ °C.

The dissociation constants of carbonic acid (Eq. 1.6) increase with temperature and to a lesser extent with salinity (Fig. 1.2). The reason for the salinity dependence is that we here use concentrations instead of ion activities to describe the chemical equilibria. The difference

²The hydrogen ion H^+ is equivalent to a free proton. In this thesis, the term *hydrogen ion* is used.

between concentration and activity increases with the amount of ions in the solution, resulting in a salinity dependence of the dissociation constants (Zeebe & Wolf-Gladrow, 2001). The dissociation constants also depend on pressure (Millero, 1979, 1995). However, the effect of pressure variations is relatively small in the surface ocean (Zeebe & Wolf-Gladrow, 2001).

Dissolved inorganic carbon, C_T , the total concentration of carbonic species, is given by

$$C_T = [H_2CO_3^*] + [HCO_3^-] + [CO_3^{2-}]. \quad (1.7)$$

At fixed temperature and salinity, the contributions of the carbonic species $H_2CO_3^*$, HCO_3^- , and CO_3^{2-} to C_T depend on $[H^+]$, or equivalently pH, which is defined as $pH = -\log[H^+]$. The relative contributions of $H_2CO_3^*$, HCO_3^- , and CO_3^{2-} to C_T over the pH range observed in the open surface ocean are shown in Fig. 1.3. The relative contribution of carbonate ions (CO_3^{2-}) to C_T decreases strongly with decreasing pH (increasing $[H^+]$), while the relative contributions of $H_2CO_3^*$ and HCO_3^- increase with decreasing pH.

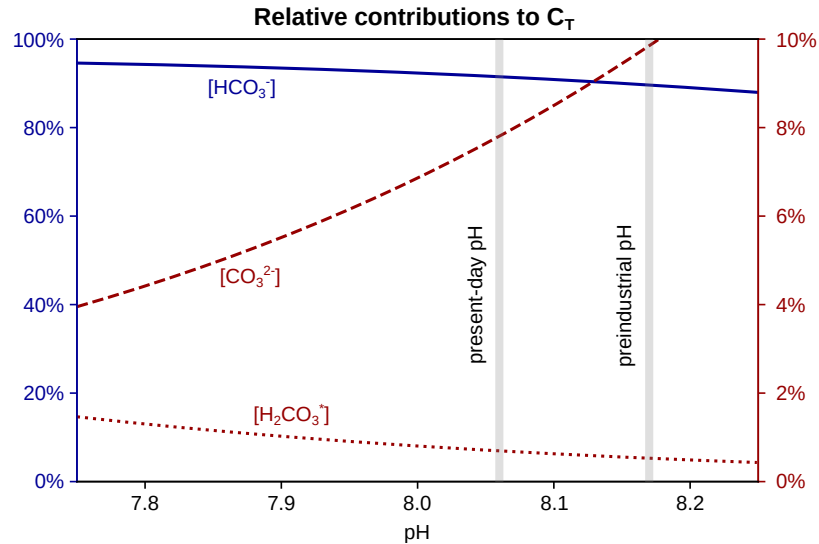


Figure 1.3: The relative contributions of carbonic acid and aqueous CO_2 ($[H_2CO_3^*]$), bicarbonate ions ($[HCO_3^-]$), and carbonate ions ($[CO_3^{2-}]$) to dissolved inorganic carbon (C_T) as a function of seawater pH for fixed temperature $T=15^\circ C$ and salinity $S=35$. The result was calculated from Eq. 1.6 using the dissociation constants K_1 and K_2 from Lueker et al. (2000). $[HCO_3^-]$ (blue) is displayed relative to the left axis and $[H_2CO_3^*]$ and $[CO_3^{2-}]$ (red) use the right axis. Furthermore, the present-day global average surface ocean pH (around 8.06; Jiang et al., 2019; Rhein et al., 2013) as well as preindustrial surface ocean pH (around 8.17; Rhein et al., 2013) are indicated.

The hydrogen ion concentration $[H^+]$ increases with temperature and salinity due to the temperature and salinity dependence of the dissociation constants (Fig. 1.2). It also depends on the amount of dissolved inorganic carbon (C_T). However, the effect on $[H^+]$ from a change in C_T depends on which of the three carbonate species changes. An increase in $[H_2CO_3^*]$, for example, leads to an increase in $[H^+]$ due to the dissociation of $H_2CO_3^*$ (Eq. 1.5). In contrast, an increase in $[CO_3^{2-}]$ results in the reverse reaction where H^+ is bound by CO_3^{2-} . Thus, $[H^+]$ also depends on the concentration of bases such as CO_3^{2-} that may bind H^+ ions and thereby reduce $[H^+]$. The excess of bases over acids, which may release H^+ in a solution, is quantified by total alkalinity A_T (Dickson & Goyet, 1994). Within the carbonate system, alkalinity results from CO_3^{2-} that may bind two H^+ ions and HCO_3^- that may bind one H^+ ion. Hence, carbonate alkalinity is

$$A_{carb} = [HCO_3^-] + 2[CO_3^{2-}]. \quad (1.8)$$

Carbonate alkalinity A_{carb} is responsible for about 95 % of A_T (Sarmiento & Gruber, 2006). Other contributions are due to the self-dissociation of water, the dissociation of boric, silicic, phosphoric, and hydrofluoric acids, as well as due to ammonia and hydrosulfide ions (Dickson & Goyet, 1994)

$$A_T = [\text{HCO}_3^-] + 2[\text{CO}_3^{2-}] + [\text{B}(\text{OH})_4^-] + [\text{OH}^-] + [\text{HPO}_4^{2-}] + 2[\text{PO}_4^{3-}] \\ + [\text{SiO}(\text{OH})_3^-] + [\text{NH}_3] + [\text{HS}^-] - [\text{H}^+] - [\text{HF}] - [\text{H}_3\text{PO}_4]. \quad (1.9)$$

Total alkalinity and dissolved inorganic carbon themselves are conservative quantities that are independent of changes in salinity or temperature. They are thus well suited to characterize the state of the carbonate system along with temperature and salinity. An increase in C_T under constant A_T , such as when CO_2 dissolves in seawater (Eq. 1.4), results in an increase in $[\text{H}^+]$. However, $[\text{H}^+]$ can also be reduced when C_T changes co-occur with A_T changes, for example when calcium carbonate minerals dissolve and release CO_3^{2-} , increasing A_T twice as much as C_T .

A simple analytical approximation of $[\text{H}^+]$ can be given when approximating A_T by A_{carb} and when assuming $[\text{H}_2\text{CO}_3^*]$, which globally contributes less than 1 % to surface ocean C_T under present-day conditions (Fig. 1.3), to be zero (Sarmiento & Gruber, 2006). Based on Eqs. 1.6-1.8, one obtains

$$[\text{H}^+] \simeq K_2(T, S) \cdot \frac{2 C_T / A_T - 1}{1 - C_T / A_T}. \quad (1.10)$$

Under this approximation, $[\text{H}^+]$ is proportional to K_2 , which is increasing more than linearly with temperature (Fig. 1.2a). Furthermore, it is a function of the ratio between C_T and A_T . It increases when a relative change in C_T is larger than a co-occurring relative change in A_T and else decreases. This approximation is not suited for cases in which the contribution of $[\text{H}_2\text{CO}_3^*]$ to C_T is not negligible (assumed to be zero in Eq. (1.10)). In that case, C_T approaches A_{carb} . The balance between A_T and C_T is then also more sensitive to the other contributors to A_T that were omitted in Eq. (1.10).

$[\text{H}^+]$ and pH are defined with respect to different scales. In this thesis, $[\text{H}^+]$ and pH are defined with respect to the *total scale* (Dickson, 1984), where $[\text{H}^+]$ consists of free hydrogen ions (that bond to water molecules to form H_3O^+ and H_9O_4^+ (Dickson, 1984)) and hydrogen sulfate ions.

The cycling of calcium carbonate in the ocean is an important contributor to variations in oceanic carbonate chemistry and plays a major role for calcifying organisms that build shell structures from calcium carbonate. Calcium carbonate minerals such as aragonite or calcite in the ocean are formed from calcium ions (Ca^{2+}) and carbonate ions (CO_3^{2-}). In the reversed process, when CaCO_3 minerals dissolve in seawater, calcium and carbonate ions are released. The calcium carbonate saturation state Ω quantifies whether mineral formation or mineral dissolution is favored. It is defined as the product of $[\text{Ca}^{2+}]$ and $[\text{CO}_3^{2-}]$ divided by the solubility product $K_{\text{sp}} = [\text{Ca}^{2+}]_{\text{sat}} \cdot [\text{CO}_3^{2-}]_{\text{sat}}$, i.e. the product of the two concentrations in equilibrium with mineral CaCO_3 :

$$\Omega = \frac{[\text{Ca}^{2+}] \cdot [\text{CO}_3^{2-}]}{[\text{Ca}^{2+}]_{\text{sat}} \cdot [\text{CO}_3^{2-}]_{\text{sat}}}. \quad (1.11)$$

CaCO_3 mineral formation is favored when $\Omega > 1$ (*supersaturated waters*) and CaCO_3 mineral dissolution is favored when $\Omega < 1$ (*undersaturated waters*). $[\text{Ca}^{2+}]$ is abundant in the open ocean and spatial changes in $[\text{Ca}^{2+}]$ are on the order of one or two percent (Broecker & Peng, 1982). As a result, Ω can be approximated by the carbonate ion concentration relative to the saturation

concentration $[\text{CO}_3^{2-}]_{\text{sat}}$ (when mineral formation and dissolution are in equilibrium). The saturation concentration $[\text{CO}_3^{2-}]_{\text{sat}}$ decreases with temperature and it increases with pressure (mainly determined by depth) and salinity. The solubility of CaCO_3 minerals and hence the saturation concentration for CO_3^{2-} depends on the mineral type, most often aragonite or calcite. In this thesis, the saturation state for the less-stable aragonite minerals is analyzed,

$$\Omega_A \simeq \frac{[\text{CO}_3^{2-}]}{[\text{CO}_3^{2-}]_{\text{sat,A}}}. \quad (1.12)$$

In the surface ocean, Ω_A mostly depends on the carbonate ion concentration $[\text{CO}_3^{2-}]$. Again assuming $[\text{H}_2\text{CO}_3^*]$ to be negligible (such as under a preindustrial climate in the surface ocean) and assuming A_T to equal A_{carb} (Eq. 1.8), one obtains

$$[\text{CO}_3^{2-}] \simeq A_T - C_T. \quad (1.13)$$

1.2.2 Ocean biogeochemistry

In the previous section, dissolved inorganic carbon (C_T), total alkalinity (A_T), temperature (T), and to a lesser extent salinity (S) have been shown to drive variations in carbonate chemistry variables and ocean acidity. This section discusses the regional differences and vertical gradients in these driving variables and how these cause regional differences and vertical gradients in carbonate chemistry variables like $[\text{H}^+]$ and Ω_A .

Dissolved inorganic carbon is generally increased in high latitude regions relative to the low latitudes (Fig. 1.4a). The main reason is that the solubility of CO_2 in seawater increases with decreasing temperature (Fig. 1.2a) and is thus highest in the high latitudes where surface ocean temperatures are close to or below 0°C (Fig. 1.4c). For example, a low-latitude water parcel with a temperature of 25°C , alkalinity of $2325 \mu\text{mol kg}^{-1}$, and salinity of 35 PSU in equilibrium with the atmosphere with $360 \mu\text{atm}$ CO_2 partial pressure has a dissolved inorganic carbon concentration of around $2000 \mu\text{mol kg}^{-1}$. Dissolved inorganic carbon concentration is increased by more than $150 \mu\text{mol kg}^{-1}$ when the same water parcel is moved to a high-latitude region with 5°C water temperature³. Observed gradients between low and high latitude regions are often smaller because seawater and the atmosphere are usually not in equilibrium. Equilibration time is long for CO_2 compared to other gases, because the inorganic carbonate system acts as a buffer for changes in $[\text{CO}_2]$: most of the CO_2 that enters the ocean dissociates into bicarbonate and carbonate ions, prolonging the time until $[\text{CO}_2]$ reaches an equilibrium concentration (Orr, 2011). Equilibrium C_T also varies with alkalinity (Fig. 1.2b). A decrease in A_T by $50 \mu\text{mol kg}^{-1}$ in the aforementioned high-latitude water parcel results in a decrease in equilibrium C_T by more than $40 \mu\text{mol kg}^{-1}$. Salinity and alkalinity (which closely resembles the pattern of surface salinity (Figs. 1.4b vs. 1.4d)) tend to be lower in high latitude regions compared to subtropical regions, because precipitation is dominant in high latitudes while evaporation is stronger in subtropical regions.

A clear latitudinal gradient is also apparent in the ratio of C_T to A_T and likewise in the difference between A_T and C_T (Figs. 1.4g, h). $[\text{H}^+]$ and Ω_A are sensitive to the proportions of C_T and A_T , for example to the ratio of C_T to A_T (approximated $[\text{H}^+]$; Eq. 1.10) or to the difference between A_T and C_T (approximated $[\text{CO}_3^{2-}]$; Eq. 1.13). The aragonite saturation state Ω_A (Eq. 1.12) in the surface ocean is mostly determined by C_T and A_T . It is decreased in

³calculated with the *mocsy 2.0* carbonate chemistry package (Orr & Epitalon, 2015). Total silicate concentration was set to $7.35 \mu\text{mol kg}^{-1}$ and total phosphate concentration was chosen as $0.63 \mu\text{mol kg}^{-1}$.

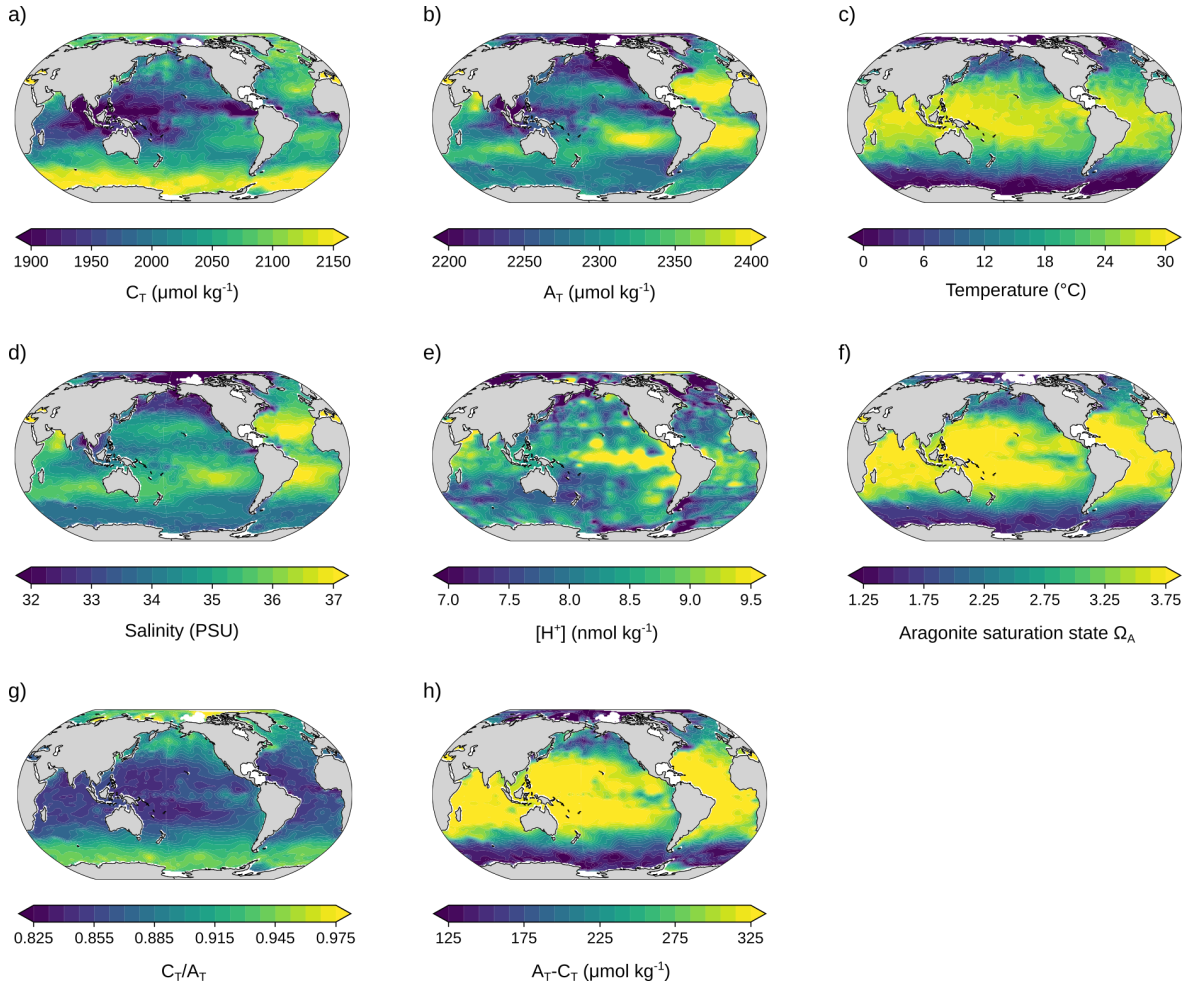


Figure 1.4: Spatial maps for surface a) dissolved inorganic carbon C_T , b) total alkalinity A_T , c) temperature, d) salinity, e) hydrogen ion concentration $[H^+]$, f) aragonite saturation state Ω_A , g) the ratio of C_T to A_T , and h) the difference between A_T and C_T . The spatial maps show surface data from the Global Ocean Data Analysis Project, Version 2 (*GLODAPv2*; Key et al., 2015).

regions where the difference between A_T and C_T is small like in the high latitudes (compare Figs. 1.4f and h). $[H^+]$, in contrast, is also sensitive to differences in temperature. The latitudinal gradients in C_T to A_T ratio and in temperature (Figs. 1.4c, g) oppose each other. As a result, smaller latitudinal differences are observed for $[H^+]$ (Figs. 1.4e).

The driving variables not only vary between regions but also within the water column. Large vertical gradients in C_T , A_T , T , S are observed. Temperature decreases with depth (Fig. 1.5c), because seawater density is in most ocean regions controlled by temperature. Warmer and lighter water floats on top of colder and heavier water.

Dissolved inorganic carbon (C_T) and to a lesser extent total alkalinity (A_T) increase with depth because of three mechanisms, the *soft tissue pump*, the *carbonate pump*, and the *gas exchange pump*, which only acts on C_T (Sarmiento & Gruber, 2006). When organic 'soft-tissue' matter is formed through photosynthesis in the photic zone of the ocean, carbon dioxide and organic nutrients such as nitrate and ammonium are consumed (Sarmiento & Gruber, 2006). As a result, C_T is reduced in the surface ocean. Furthermore, alkalinity is increased under nitrate-based production and decreased under ammonium-based production (Brewer & Goldman, 1976). When dead organic material sinks in the water column, it is remineralized. Therefore,

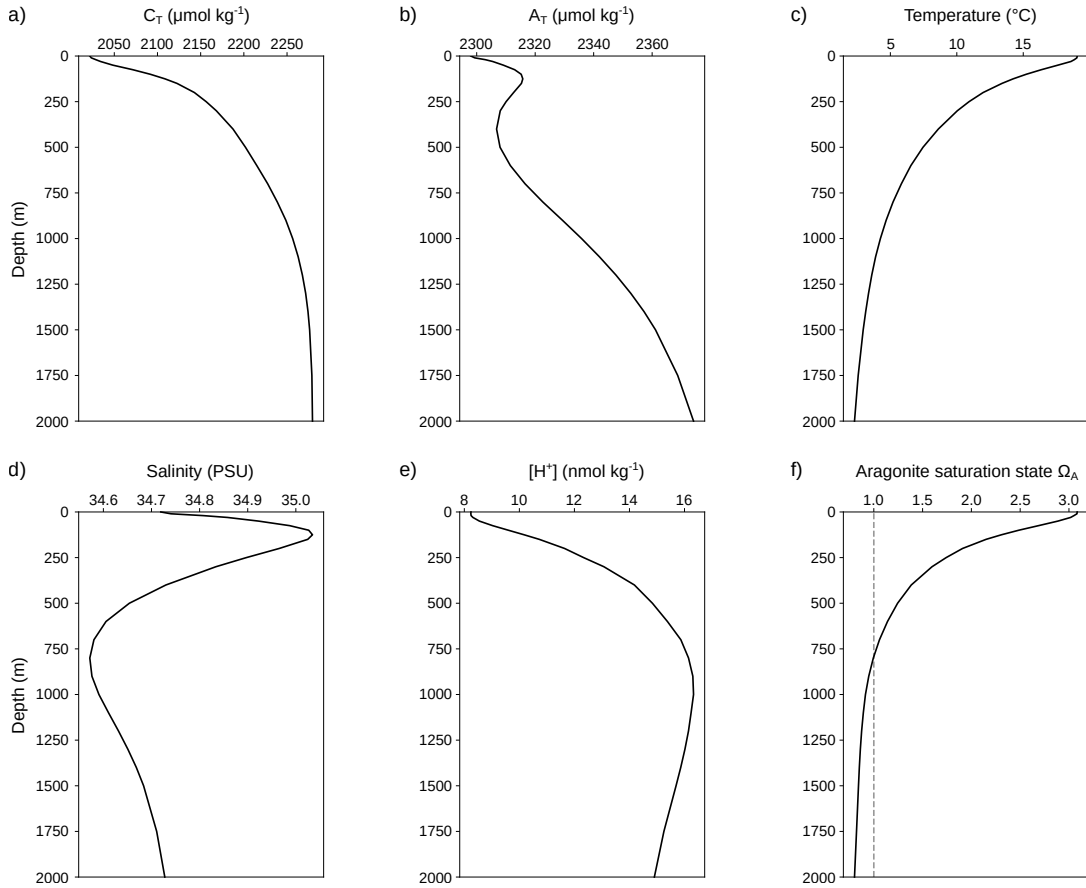


Figure 1.5: Globally averaged depth profiles for a) dissolved inorganic carbon (C_T), b) total alkalinity (A_T), c) temperature, d) salinity, e) hydrogen ion concentration ($[H^+]$), and f) aragonite saturation state (Ω_A). The vertical profiles show data from the Global Ocean Data Analysis Project, Version 2 (*GLODAPv2*; Key et al., 2015).

C_T and A_T undergo the opposite changes as during organic matter production, resulting in increasing C_T at subsurface (Fig. 1.5a). Remineralization of organic matter occurs mainly in the main thermocline above 1000 m depth (Sarmiento & Gruber, 2006).

Due to biogenic calcification, i.e., the biological formation of $CaCO_3$ minerals, A_T and C_T are decreased in the ratio 2:1. When organic material that is ballasted with biogenic $CaCO_3$ sinks below the calcium carbonate saturation horizon (gray dashed line in Fig. 1.5f), dissolution of biogenic $CaCO_3$ results in an increase in A_T and C_T in the ratio 2:1, i.e. driving larger increases in A_T than in C_T (compare Figs. 1.5a, b). These increases in A_T due to the *carbonate pump* occur mainly below 1000 m depth where waters are undersaturated with respect to calcium carbonate (Fig. 1.5f).

The *gas exchange pump* influences C_T but not A_T . It arises because deep and bottom water formation occurs in high-latitude oceans. In these cold waters, the solubility of CO_2 is larger than in low-latitude regions (Fig. 1.2a), resulting in larger C_T concentrations (Fig. 1.4d) that are transported to the subsurface by deep and bottom water formation.

Freshwater fluxes, such as due to evaporation and precipitation, cause changes in salinity as well as in A_T and C_T . A comparison of Figs. 1.5a, b and Fig. 1.5d shows that the vertical profile of A_T is generally more similar to that of salinity compared to the vertical profile of C_T .

Hydrogen ion concentration ($[H^+]$) increases with depth until a depth of about 1000 m

(Fig. 1.5e). There, the ratio between C_T and A_T starts to decrease again with depth, causing also a decrease in $[H^+]$ (see simplified expression in Eq. (1.10)). The aragonite saturation state monotonically decreases with depth despite the larger increases in A_T below 1000 m depth, because the saturation concentration for $[CO_3^{2-}]$ increases with pressure and thus with depth (see Eq. (1.12)).

1.3 Ocean acidification

1.3.1 Changes in oceanic carbonate chemistry with the uptake of anthropogenic CO_2

In addition to driving global warming, anthropogenic CO_2 also causes ocean acidification, often called *the other CO_2 problem* (Doney et al., 2009). Since 1850, about 165 billion tons of carbon (25 % of anthropogenic carbon emissions since then; Sect. 1.1) have entered the ocean. Despite the large natural inorganic carbon pool, this invasion of anthropogenic carbon has substantially altered the dissolved inorganic carbon concentrations in the ocean. If the perturbation of these 165 GtC were homogeneously distributed over the mass of ocean water (about $1.4 \cdot 10^{21}$ kg; Clark, 1982), dissolved inorganic carbon would increase everywhere by about $10 \mu\text{mol kg}^{-1}$. However, this is not the case. While the surface ocean closely follows the atmospheric perturbation in CO_2 , the transport of anthropogenic carbon to the deep ocean takes long times.

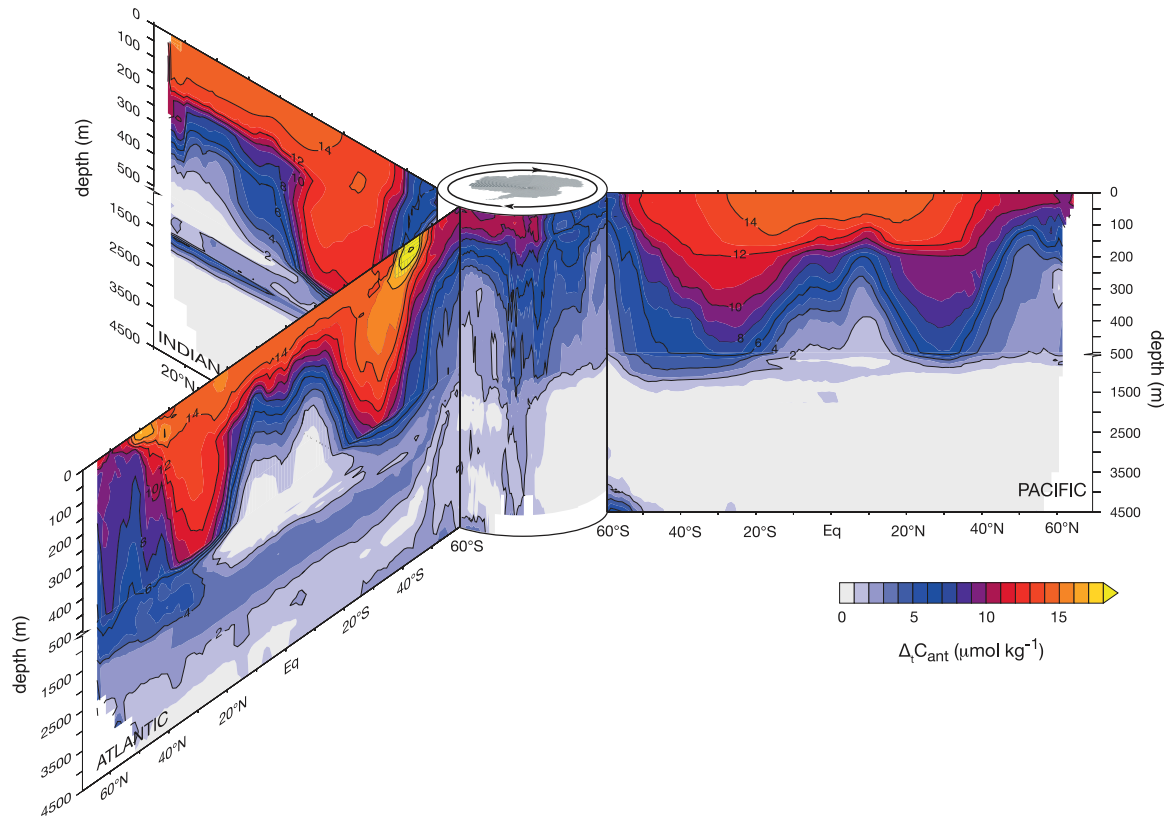


Figure 1.6: Zonal-mean vertical sections for the change in anthropogenic carbon between 1994 and 2007 in the Atlantic, the Pacific, and the Indian Ocean. The figure is taken from Gruber et al. (2019).

In the previous section, it has been discussed that water formation from surface waters in high latitude regions is an important mechanism for sustaining the natural vertical gradient in C_T . Water formation is also important for transporting anthropogenic carbon to the interior

ocean. The age of water masses, i.e., the time span since a water mass was formed at the surface⁴, varies between decades and centuries for mode and intermediate waters (Talley et al., 2011; Gruber et al., 2019) and multiple centuries to millennia for deep waters in the North Pacific (Matsumoto, 2007). In consequence, it takes a long time until anthropogenic carbon is transported to the deep ocean, and only comparably little anthropogenic carbon has invaded the deep ocean yet. Based on global estimates from the Global Ocean Data Analysis Project, Version 2 (*GLODAPv2*; Key et al., 2015), anthropogenic carbon has globally increased surface ocean C_T by $56 \mu\text{mol kg}^{-1}$. The increase in C_T due to anthropogenic carbon becomes smaller with depth, being $40 \mu\text{mol kg}^{-1}$ at 200 m, $10 \mu\text{mol kg}^{-1}$ at 1000 m, and $4 \mu\text{mol kg}^{-1}$ at 2000 m depth. Vertical sections of the changes in anthropogenic carbon between 1994 and 2007 in the Atlantic, Pacific, and Indian Ocean are depicted in Fig. 1.6, showing large increases in anthropogenic carbon in subtropical mode waters and also a substantial anthropogenic signal in the comparably young North Atlantic Deep Water.

The uptake of anthropogenic carbon dioxide by the ocean increases dissolved inorganic carbon concentrations in the ocean while not directly altering alkalinity (compare definitions of C_T and A_T ; Eqs. 1.7 and 1.9). As a result, it substantially alters the relative proportions of C_T and A_T (Fig. 1.4) and strongly influences oceanic carbonate chemistry and acidity. Hydrogen ion concentration $[\text{H}^+]$ is increased, because most of the invading anthropogenic CO_2 , which increases C_T , forms carbonic acid and dissociates into bicarbonate ions (HCO_3^-) and H^+ , increasing both $[\text{HCO}_3^-]$ and $[\text{H}^+]$. A large part of the $[\text{H}^+]$ increase is buffered by the reaction of CO_3^{2-} with H^+ to HCO_3^- (Orr, 2011). The H^+ ions that are not neutralized by the reaction with CO_3^{2-} increase $[\text{H}^+]$ and lower pH ($\text{pH} = -\log[\text{H}^+]$). It is estimated that surface ocean pH has globally dropped by about 0.11 units between 1770 and 2000 (Jiang et al., 2019, indicated in Fig. 1.3). The decrease in pH by 0.11 from a preindustrial level of around 8.17 corresponds to a 29 % increase in $[\text{H}^+]$ ⁵. The decrease in $[\text{H}^+]$ is larger in high-latitude waters. For example, the decrease in pH between year 1770 and year 2000 in the Arctic Ocean is estimated to be about 0.16 (Jiang et al., 2019). This is because changes in $[\text{H}^+]$ are more buffered by the reaction with CO_3^{2-} when $[\text{CO}_3^{2-}]$ is high. Carbonate ion concentration is well approximated by the difference between A_T and C_T (Eq. 1.13), which is much lower in high-latitude regions compared to low-latitude regions (Fig. 1.4h). The increase in $[\text{H}^+]$ and the decrease in pH due to an increase in C_T is thus larger in the high latitudes.

The neutralization of H^+ by CO_3^{2-} also decreases $[\text{CO}_3^{2-}]$ and hence reduces Ω_A (Eq. 1.12). Since preindustrial times, surface ocean $[\text{CO}_3^{2-}]$ has decreased globally by more than 10 % (Orr et al., 2005). The decrease in $[\text{CO}_3^{2-}]$ and Ω_A is larger in low latitude regions compared to high latitude regions (Orr et al., 2005), consistent with the stronger buffering of $[\text{H}^+]$ changes by CO_3^{2-} there. However, Ω_A is naturally much lower in high-latitude oceans (Fig. 1.4f). These are thus most prone to transition from supersaturated conditions ($\Omega_A > 1$) to undersaturated conditions ($\Omega_A < 1$) due to the decline in $[\text{CO}_3^{2-}]$ with ocean acidification, impacting calcifying organisms that rely on aragonite shells.

1.3.2 Impacts of ocean acidification on marine organisms

The knowledge on the biological implications of ocean acidification has much expanded in recent years (Doney et al., 2020). Vulnerabilities vary between species, life stages, and in some cases also populations, complicating a general assessment of impacts from ocean acidification on

⁴Ocean age can be determined, for example, from the concentration of radiocarbon (^{14}C), which is mainly produced in the atmosphere and decays with a half-life of around 5700 y.

⁵Ocean acidification characterizes the shift towards more acidic conditions in the ocean, but the ocean remains slightly basic in the foreseeable future, despite the substantial decreases in basicity with ocean acidification.

marine organisms (Doney et al., 2020). However, calcifying invertebrates are overall found to be most vulnerable (Doney et al., 2020).

In general, marine organisms critically depend on a stable pH within their cells and also in extracellular fluids. To ensure a stable acid-base state, organisms regulate their internal pH through a variety of mechanisms (Claiborne et al., 2002), such as through respiratory compensation, where excretion of CO_2 is stimulated through increased respiration, or through ion transport, for example by Na^+/H^+ exchange (Perry & Gilmour, 2006). When the capacity to sustain internal pH under low environmental pH through acid-base regulation is exceeded, organisms suffer from acidosis, impairing physiological processes such as enzyme activity and protein synthesis. It is expected that marine invertebrates are most sensitive to ocean acidification because of their limited capacity for acid-base regulation (Pörtner, 2008), including mollusks like pteropods (Bednaršek et al., 2012), echinoderms (Miles et al., 2007), bryozoa, and cnidaria (Knoll et al., 2007; Pörtner, 2008). These hypometabolic organisms may not be able to afford the energetic costs of acid-base regulation due to insufficient energy budgets (Bednaršek et al., 2018), in particular when food supply is limited. Insufficient energetic supply under ocean acidification may also trigger metabolic suppression, with negative impacts on growth and reproduction (Seibel et al., 2012).

Furthermore, these species are calcifiers that build calcium carbonate shells. Biogenic calcification is limited by the availability of carbonate ions, which is reduced under ocean acidification. In consequence, a reduction in calcification is expected. Furthermore, waters with $\Omega < 1$ are corrosive for calcium carbonate shells, such as those of pteropods (Bednaršek et al., 2012). Consequently, shells that are in contact with the surrounding seawater are damaged by shell dissolution⁶. Organisms have been shown to repair shell structures that are damaged by dissolution (Peck et al., 2018). However, such repair calcification is energetically demanding and may thus not be possible (Lischka & Riebesell, 2017). Decreases in Ω_A have also been shown to threaten coral reefs by dissolution of the underlying reef sediments already at a relatively high value of Ω_A of 2.92 ± 0.16 (Eyre et al., 2018).

Marine fish may be less affected by ocean acidification due to a higher capacity for acid base regulation compared to many invertebrates (Pörtner et al., 2011; Heuer & Grosell, 2014). However, studies suggest potential behavioral (Munday et al., 2014) and olfactory (Nilsson et al., 2012) impairments in fish under ocean acidification, possibly because neurotransmitter functionality is affected by changes in $[\text{Cl}^-]$ and $[\text{HCO}_3^-]$ as a result of acid base regulation (Chivers et al., 2014). Yet, these results are currently debated (Clark et al., 2020; Munday et al., 2020). Other currently investigated impacts on fish concern, for example, otolith growth (a CaCO_3 structure in the ear necessary for balance), mitochondrial metabolism, and aerobic scope (Heuer & Grosell, 2014; Doney et al., 2020).

Ocean acidification can be beneficial to phytoplankton, because the efficiency of photosynthesis depends on the availability of CO_2 in seawater. Consequently, ocean acidification can stimulate phytoplankton growth (Tortell et al., 2008).

The impacts of ocean acidification on organisms generally depend on an organisms life stage, often with increased sensitivity in early life stages such as for larvae and juveniles (Kroeker et al.,

⁶Depending on the calcifying species, shells consist of the calcium carbonate mineral calcite or aragonite, which differ in their solubility. Aragonite shells dissolve already under less acidic conditions compared to calcite shells (Orr et al., 2005). However, the link between species survival and mineral solubility has been questioned (Busch & McElhany, 2017).

2013; Bednaršek et al., 2019). Also, food web interactions between species can cause cascading effects in ecosystems under ocean acidification (Spisla et al., 2021). The impacts of ocean acidification may be reinforced by co-occurring changes in other environmental stressors. For example, ocean warming may impair organismal performance under ocean acidification (Bednaršek et al., 2018), in particular under limited food availability (Lischka & Riebesell, 2017).

1.4 Extreme events in ocean acidity

The study of ocean acidification is a relatively new field of science (Gattuso & Hansson, 2011). Nonetheless, the long-term changes in carbonate chemistry variables like $[\text{H}^+]$ and Ω under climate change are relatively well understood (Orr et al., 2005; Steinacher et al., 2009). Much less is known about the temporal variability in these variables, including the occurrence of extreme departures from normal conditions and potential future changes in such extreme variations.

Seasonal variations in carbonate chemistry variables have been shown to contribute significantly to the occurrence of the detrimental conditions for marine organisms that were discussed in Sect. 1.3.2. For example, surface waters in the Southern Ocean are expected to become undersaturated with respect to aragonite and calcite during wintertime $[\text{CO}_3^{2-}]$ minima already decades before annual mean conditions will become corrosive to these minerals (McNeil & Matear, 2008). Similarly, hypercapnia (when seawater $p\text{CO}_2$ exceeds $1000 \mu\text{atm}$) is projected to occur much earlier in the 21st century during seasonal variations than in the annual mean (McNeil & Sasse, 2016). Seasonal variations in $[\text{H}^+]$, $p\text{CO}_2$, and Ω_A will change significantly with the oceanic uptake of anthropogenic carbon as a result of the nonlinearity of oceanic carbonate chemistry (Sect. 1.2.1). The higher background C_T concentration causes an amplification of seasonal variations in $[\text{H}^+]$ (Kwiatkowski & Orr, 2018; Fassbender et al., 2018) and in $p\text{CO}_2$ (McNeil & Sasse, 2016; Landschützer et al., 2018), while seasonal variations in Ω_A decrease (Kwiatkowski & Orr, 2018).

Also, discrete events during which $[\text{H}^+]$ or $p\text{CO}_2$ is much higher or Ω_A is much lower than usual may add to the stress experienced by marine organisms from ocean acidification. In general, extremes are understood as events during which *a variable is above (or below) a threshold value near the upper (or lower) end of the range of observed values of the variable* (Pörtner et al., 2019). Such events are here referred to as *ocean acidity extreme events* or *OAX events*. It has been shown that already several days of aragonite undersaturation can cause substantial shell dissolution in pteropods (Bednaršek et al., 2014), corroborating the potential importance of ocean acidity extremes for marine ecosystems. However, OAX events have barely been observed in the ocean (Bednaršek et al., 2018), because direct measurements for $[\text{H}^+]$ or other carbonate system variables are not available at the global scale and at high temporal resolution, as it is the case for sea surface temperature based on satellite remote sensing (Reynolds et al., 2007). As a result, very little is currently known about the magnitude, spatial extent, and duration of OAX events in the global ocean. Furthermore, the driving mechanisms of these events have not yet been assessed in most ocean regions.

Their counterparts for ocean temperature, so-called *marine heatwaves* or *MHWs*, have been extensively studied in recent years (Hobday et al., 2016; Frölicher et al., 2018; Laufkötter et al., 2020; Oliver et al., 2021) and are recognized as a major threat for marine ecosystems (Smale et al., 2019; Hughes et al., 2017). Extreme events in multiple ecosystem stressors, like temperature and $[\text{H}^+]$, may also occur at the same time and location. Such compound extreme events are of particular concern because the impacts on organisms may be non-additive and larger than

anticipated (Boyd & Brown, 2015; Gruber et al., 2021).

In this thesis, extremes in ocean acidity are analyzed for the first time at the global scale. In Chapter 2, it is described how extremes are defined in this thesis and the extreme event metrics used to characterize the events are introduced. High- $[\text{H}^+]$ extreme events and low- Ω_{A} extremes and their changes with ocean acidification and global warming are characterized in Chapter 3. Compound extremes in temperature and $[\text{H}^+]$, here referred to as *MHW-OAX events*, and changes in their occurrence with ocean acidification and warming are analyzed in Chapter 4. The driving processes of $[\text{H}^+]$ extreme events are discussed in Chapter 5.

References

- Bednaršek, N., Feely, R. A., Beck, M. W., Glippa, O., Kanerva, M., & Engström-Öst, J., 2018. El Niño-Related Thermal Stress Coupled With Upwelling-Related Ocean Acidification Negatively Impacts Cellular to Population-Level Responses in Pteropods Along the California Current System With Implications for Increased Bioenergetic Costs, *Frontiers in Marine Science*, 5(December), 1–17.
- Bednaršek, N., Tarling, G. A., Bakker, D. C. E., Fielding, S., Jones, E. M., Venables, H. J., Ward, P., Kuzirian, A., Lézé, B., Feely, R. A., & Murphy, E. J., 2012. Extensive dissolution of live pteropods in the southern ocean, *Nature Geoscience*, 5, 881–885.
- Bednaršek, N., Feely, R. A., Reum, J. C. P., Peterson, B., Menkel, J., Alin, S. R., & Hales, B., 2014. *Limacina helicina* shell dissolution as an indicator of declining habitat suitability owing to ocean acidification in the california current ecosystem, *Proceedings of the Royal Society B: Biological Sciences*, 281(1785), 20140123.
- Bednaršek, N., Feely, R. A., Howes, E. L., Hunt, B. P. V., Kessouri, F., León, P., Lischka, S., Maas, A. E., McLaughlin, K., Nezhlin, N. P., Sutula, M., & Weisberg, S. B., 2019. Systematic review and meta-analysis toward synthesis of thresholds of ocean acidification impacts on calcifying pteropods and interactions with warming, *Frontiers in Marine Science*, 6, 227.
- Boyd, P. W. & Brown, C. J., 2015. Modes of interactions between environmental drivers and marine biota, *Frontiers in Marine Science*, 2, 9.
- Brewer, P. G. & Goldman, J. C., 1976. Alkalinity changes generated by phytoplankton growth 1, *Limnology and Oceanography*, 21(1), 108–117.
- Broecker, W. & Peng, T., 1982. *Tracers in the Sea*, Eldigio Press, New York,.
- Busch, D. S. & McElhany, P., 2017. Using mineralogy and higher-level taxonomy as indicators of species sensitivity to pH: A case-study of Puget Sound, *Elementa: Science of the Anthropocene*, 5.
- Chivers, D. P., McCormick, M. I., Nilsson, G. E., Munday, P. L., Watson, S.-A., Meekan, M. G., Mitchell, M. D., Corkill, K. C., & Ferrari, M. C. O., 2014. Impaired learning of predators and lower prey survival under elevated CO₂: a consequence of neurotransmitter interference, *Global Change Biology*, 20(2), 515–522.
- Ciais, P., Sabine, C., Bala, G., Bopp, L., Brovkin, V., Canadell, J., Chhabra, A. and DeFries, R., Galloway, J., Heimann, M., Jones, C. and Le Quéré, C., Myneni, R., Piao, S., & Thornton, P., 2013. Carbon and other biogeochemical cycles, *Climate Change 2013: The Physical Science Basis. Contribution of Working Group I to the Fifth Assessment Report of the Intergovernmental Panel on Climate Change [Stocker, T.F., D. Qin, G.-K. Plattner, M. Tignor, S.K. Allen, J. Boschung, A. Nauels, Y. Xia, V. Bex and P.M. Midgley (eds.)]. Cambridge University Press, Cambridge, United Kingdom and New York, NY, USA.*
- Claiborne, J. B., Edwards, S. L., & Morrison-Shetlar, A. I., 2002. Acid–base regulation in fishes: cellular and molecular mechanisms, *Journal of Experimental Zoology*, 293(3), 302–319.
- Clark, T. D., Raby, G. D., Roche, D. G., Binning, S. A., Speers-Roesch, B., Jutfelt, F., & Sundin, J., 2020. Ocean acidification does not impair the behaviour of coral reef fishes, *Nature*, 577(7790), 370–375.
- Clark, W. C., 1982. Carbon dioxide review 1982, *Science (Washington, D.C.)*; (United States).
- Dickson, A., 1984. pH scales and proton-transfer reactions in saline media such as sea water, *Geochimica et Cosmochimica Acta*, 48(11), 2299–2308.
- Dickson, A. G. & Goyet, C., 1994. Handbook of methods for the analysis of the various parameters of the carbon dioxide system in sea water. version 2, *United States*.
- Doney, S. C., Fabry, V. J., Feely, R. A., & Kleypas, J. A., 2009. Ocean acidification: The other CO₂ problem, *Annual Review of Marine Science*, 1(1), 169–192.
- Doney, S. C., Busch, D. S., Cooley, S. R., & Kroeker, K. J., 2020. The impacts of ocean acidification on marine ecosystems and reliant human communities, *Annual Review of Environment and Resources*, 45(1), 83–112.
- Eyre, B. D., Cyronak, T., Drupp, P., Carlo, E. H. D., Sachs, J. P., & Andersson, A. J., 2018. Coral reefs will transition to net dissolving before end of century, *Science*, 359(6378), 908–911.
- Fassbender, A. J., Rodgers, K. B., Palevsky, H. I., & Sabine, C. L., 2018. Seasonal asymmetry in the evolution of surface ocean pCO₂ and pH thermodynamic drivers and the influence on sea-air CO₂ flux, *Global Biogeochemical Cycles*, 32(10), 1476–1497.

- Friedlingstein, P., O'Sullivan, M., Jones, M. W., Andrew, R. M., Hauck, J., Olsen, A., Peters, G. P., Peters, W., Pongratz, J., Sitch, S., Le Quéré, C., Canadell, J. G., Ciais, P., Jackson, R. B., Alin, S., Aragão, L. E. O. C., Arneeth, A., Arora, V., Bates, N. R., Becker, M., Benoit-Cattin, A., Bittig, H. C., Bopp, L., Bultan, S., Chandra, N., Chevallier, F., Chini, L. P., Evans, W., Florentie, L., Forster, P. M., Gasser, T., Gehlen, M., Gilfillan, D., Gkritzalis, T., Gregor, L., Gruber, N., Harris, I., Hartung, K., Haverd, V., Houghton, R. A., Ilyina, T., Jain, A. K., Joetzjer, E., Kadono, K., Kato, E., Kitidis, V., Korsbakken, J. I., Landschützer, P., Lefèvre, N., Lenton, A., Lienert, S., Liu, Z., Lombardozzi, D., Marland, G., Metzl, N., Munro, D. R., Nabel, J. E. M. S., Nakaoka, S.-I., Niwa, Y., O'Brien, K., Ono, T., Palmer, P. I., Pierrot, D., Poulter, B., Resplandy, L., Robertson, E., Rödenbeck, C., Schwinger, J., Séférian, R., Skjelvan, I., Smith, A. J. P., Sutton, A. J., Tanhua, T., Tans, P. P., Tian, H., Tilbrook, B., van der Werf, G., Vuichard, N., Walker, A. P., Wanninkhof, R., Watson, A. J., Willis, D., Wiltshire, A. J., Yuan, W., Yue, X., & Zaehle, S., 2020. Global carbon budget 2020, *Earth System Science Data*, 12(4), 3269–3340.
- Frölicher, T. L., Fischer, E. M., & Gruber, N., 2018. Marine heatwaves under global warming, *Nature*, 560(7718), 360–364.
- eds Gattuso, J.-P. & Hansson, L., 2011. *Ocean Acidification*, Oxford University Press.
- Gruber, N., Clement, D., Carter, B. R., Feely, R. A., van Heuven, S., Hoppema, M., Ishii, M., Key, R. M., Kozyr, A., Lauvset, S. K., Lo Monaco, C., Mathis, J. T., Murata, A., Olsen, A., Perez, F. F., Sabine, C. L., Tanhua, T., & Wanninkhof, R., 2019. The oceanic sink for anthropogenic CO₂ from 1994 to 2007, *Science*, 363(6432), 1193–1199.
- Gruber, N., Boyd, P. W., Frölicher, T. L., & Vogt, M., 2021. Ocean biogeochemical extremes and compound events, *Nature*, *in review*.
- Henry, W. & Banks, J., 1803. III. experiments on the quantity of gases absorbed by water, at different temperatures, and under different pressures, *Philosophical Transactions of the Royal Society of London*, 93, 29–274.
- Heuer, R. M. & Grosell, M., 2014. Physiological impacts of elevated carbon dioxide and ocean acidification on fish, *American Journal of Physiology-Regulatory, Integrative and Comparative Physiology*, 307(9), R1061–R1084.
- Hobday, A. J., Alexander, L. V., Perkins, S. E., Smale, D. A., Straub, S. C., Oliver, E. C., Benthuisen, J. A., Burrows, M. T., Donat, M. G., Feng, M., Holbrook, N. J., Moore, P. J., Scannell, H. A., Sen Gupta, A., & Wernberg, T., 2016. A hierarchical approach to defining marine heatwaves, *Progress in Oceanography*, 141, 227–238.
- Hughes, T. P., Kerry, J. T., Álvarez-Noriega, M., Álvarez-Romero, J. G., Anderson, K. D., Baird, A. H., Babcock, R. C., Beger, M., Bellwood, D. R., Berkelmans, R., Bridge, T. C., Butler, I. R., Byrne, M., Cantin, N. E., Comeau, S., Connolly, S. R., Cumming, G. S., Dalton, S. J., Diaz-Pulido, G., Eakin, C. M., Figueira, W. F., Gilmour, J. P., Harrison, H. B., Heron, S. F., Hoey, A. S., Hobbs, J.-P. A., Hoogenboom, M. O., Kennedy, E. V., Kuo, C.-y., Lough, J. M., Lowe, R. J., Liu, G., McCulloch, M. T., Malcolm, H. A., McWilliam, M. J., Pandolfi, J. M., Pears, R. J., Pratchett, M. S., Schoepf, V., Simpson, T., Skirving, W. J., Sommer, B., Torda, G., Wachenfeld, D. R., Willis, B. L., & Wilson, S. K., 2017. Global warming and recurrent mass bleaching of corals, *Nature*, 543(7645), 373–377.
- Jeltsch-Thömmes, A. & Joos, F., 2020. Modeling the evolution of pulse-like perturbations in atmospheric carbon and carbon isotopes: the role of weathering–sedimentation imbalances, *Climate of the Past*, 16(2), 423–451.
- Jiang, L.-Q., Carter, B. R., Feely, R. A., Lauvset, S. K., & Olsen, A., 2019. Surface ocean pH and buffer capacity: past, present and future, *Scientific Reports*, 9(1), 18624.
- Joos, F., Roth, R., Fuglestedt, J. S., Peters, G. P., Enting, I. G., von Bloh, W., Brovkin, V., Burke, E. J., Eby, M., Edwards, N. R., Friedrich, T., Frölicher, T. L., Halloran, P. R., Holden, P. B., Jones, C., Kleinen, T., Mackenzie, F. T., Matsumoto, K., Meinshausen, M., Plattner, G.-K., Reisinger, A., Segschneider, J., Shaffer, G., Steinacher, M., Strassmann, K., Tanaka, K., Timmermann, A., & Weaver, A. J., 2013. Carbon dioxide and climate impulse response functions for the computation of greenhouse gas metrics: a multi-model analysis, *Atmospheric Chemistry and Physics*, 13(5), 2793–2825.
- Key, R. M., Olsen, A., van Heuven, S., Lauvset, S. K., Velo, A., Lin, X., Schirnick, C., Kozyr, A., Tanhua, T., Hoppema, M., Jutterström, S., Steinfeldt, R., Jeansson, E., Ishii, M., Perez, F. F., & Suzuki, T., 2015. Global ocean data analysis project, version 2 (GLODAPv2), NDP document, Carbon Dioxide Information Analysis Center, OAK RIDGE NATIONAL LABORATORY Oak Ridge, Tennessee 37831-6335.
- Knoll, A. H., Bambach, R. K., Payne, J. L., Pruss, S., & Fischer, W. W., 2007. Paleophysiology and end-permian mass extinction, *Earth and Planetary Science Letters*, 256(3), 295–313.

- Kroeker, K. J., Kordas, R. L., Crim, R., Hendriks, I. E., Ramajo, L., Singh, G. S., Duarte, C. M., & Gattuso, J.-P., 2013. Impacts of ocean acidification on marine organisms: quantifying sensitivities and interaction with warming, *Global Change Biology*, 19(6), 1884–1896.
- Kwiatkowski, L. & Orr, J. C., 2018. Diverging seasonal extremes for ocean acidification during the twenty-first century, *Nature Climate Change*, 8(2), 141–145.
- Landschützer, P., Gruber, N., Bakker, D. C. E., Stemmler, I., & Six, K. D., 2018. Strengthening seasonal marine CO₂ variations due to increasing atmospheric CO₂, *Nature Climate Change*, 8(2), 146–150.
- Laufkötter, C., Zscheischler, J., & Frölicher, T. L., 2020. High-impact marine heatwaves attributable to human-induced global warming, *Science*, 369(6511), 1621–1625.
- Lischka, S. & Riebesell, U., 2017. Metabolic response of Arctic pteropods to ocean acidification and warming during the polar night/twilight phase in Kongsfjord (Spitsbergen), *Polar Biology*, 40(6), 1211–1227.
- Lueker, T. J., Dickson, A. G., & Keeling, C. D., 2000. Ocean pCO₂ calculated from dissolved inorganic carbon, alkalinity, and equations for K₁ and K₂: validation based on laboratory measurements of CO₂ in gas and seawater at equilibrium, *Marine Chemistry*, 70(1), 105–119.
- Masson-Delmotte, V., Zhai, P., Pirani, A., Connors, S. L., Péan, C., Berger, S., Caud, N., Chen, Y., Goldfarb, L., Gomis, M. I., Huang, M., Leitzell, K., Lonnoy, E., Matthews, J., Maycock, T. K., Waterfield, T., Yelekçi, O., Yu, R., & Zhou, B., 2021. IPCC, 2021: Summary for policymakers, *Climate Change 2021: The Physical Science Basis. Contribution of Working Group I to the Sixth Assessment Report of the Intergovernmental Panel on Climate Change*.
- Matsumoto, K., 2007. Radiocarbon-based circulation age of the world oceans, *Journal of Geophysical Research: Oceans*, 112(C9).
- McNeil, B. I. & Matear, R. J., 2008. Southern ocean acidification: A tipping point at 450-ppm atmospheric CO₂, *Proceedings of the National Academy of Sciences of the United States of America*, 105(48), 18860–18864.
- McNeil, B. I. & Sasse, T. P., 2016. Future ocean hypercapnia driven by anthropogenic amplification of the natural CO₂ cycle, *Nature*, 529, 383–386.
- Meinshausen, M., Nicholls, Z. R. J., Lewis, J., Gidden, M. J., Vogel, E., Freund, M., Beyerle, U., Gessner, C., Nauels, A., Bauer, N., Canadell, J. G., Daniel, J. S., John, A., Krummel, P. B., Luderer, G., Meinshausen, N., Montzka, S. A., Rayner, P. J., Reimann, S., Smith, S. J., van den Berg, M., Velders, G. J. M., Vollmer, M. K., & Wang, R. H. J., 2020. The shared socio-economic pathway (SSP) greenhouse gas concentrations and their extensions to 2500, *Geoscientific Model Development*, 13(8), 3571–3605.
- Miles, H., Widdicombe, S., Spicer, J. I., & Hall-Spencer, J., 2007. Effects of anthropogenic seawater acidification on acid–base balance in the sea urchin *psammechinus miliaris*, *Marine Pollution Bulletin*, 54(1), 89–96.
- Millero, F. J., 1979. The thermodynamics of the carbonate system in seawater, *Geochimica et Cosmochimica Acta*, 43(10), 1651–1661.
- Millero, F. J., 1995. Thermodynamics of the carbon dioxide system in the oceans, *Geochimica et Cosmochimica Acta*, 59(4), 661–677.
- Munday, P. L., Cheal, A. J., Dixon, D. L., Rummer, J. L., & Fabricius, K. E., 2014. Behavioural impairment in reef fishes caused by ocean acidification at CO₂ seeps, *Nature Climate Change*, 4(6), 487–492.
- Munday, P. L., Dixon, D. L., Welch, M. J., Chivers, D. P., Domenici, P., Grosell, M., Heuer, R. M., Jones, G. P., McCormick, M. I., Meekan, M., Nilsson, G. E., Ravasi, T., & Watson, S.-A., 2020. Methods matter in repeating ocean acidification studies, *Nature*, 586(7830), E20–E24.
- Myhre, G., Highwood, E. J., Shine, K. P., & Stordal, F., 1998. New estimates of radiative forcing due to well mixed greenhouse gases, *Geophysical Research Letters*, 25(14), 2715–2718.
- Nilsson, G. E., Dixon, D. L., Domenici, P., McCormick, M. I., Sørensen, C., Watson, S.-A., & Munday, P. L., 2012. Near-future carbon dioxide levels alter fish behaviour by interfering with neurotransmitter function, *Nature Climate Change*, 2(3), 201–204.
- Oliver, E. C., Benthuyssen, J. A., Darmaraki, S., Donat, M. G., Hobday, A. J., Holbrook, N. J., Schlegel, R. W., & Sen Gupta, A., 2021. Marine heatwaves, *Annual Review of Marine Science*, 13(1), 313–342.

- Orr, J., 2011. Recent and future changes in ocean carbonate chemistry, *Ocean Acidification*, pp. 41–66.
- Orr, J. C. & Epitalon, J.-M., 2015. Improved routines to model the ocean carbonate system: mocsy 2.0, *Geoscientific Model Development*, 8(3), 485–499.
- Orr, J. C., Fabry, V. J., Aumont, O., Bopp, L., Doney, S. C., Feely, R. A., Gnanadesikan, A., Gruber, N., Ishida, A., Joos, F., Key, R. M., Lindsay, K., Maier-Reimer, E., Matear, R., Monfray, P., Mouchet, A., Najjar, R. G., Plattner, G.-K., Rodgers, K. B., Sabine, C. L., Sarmiento, J. L., Schlitzer, R., Slater, R. D., Totterdell, I. J., Weirig, M.-F., Yamanaka, Y., & Yool, A., 2005. Anthropogenic ocean acidification over the twenty-first century and its impact on calcifying organisms, *Nature*, 437(7059), 681–686.
- Peck, V. L., Oakes, R. L., Harper, E. M., Manno, C., & Tarling, G. A., 2018. Pteropods counter mechanical damage and dissolution through extensive shell repair, *Nature Communications*, 9(1), 264.
- Perry, S. & Gilmour, K., 2006. Acid–base balance and CO₂ excretion in fish: Unanswered questions and emerging models, *Respiratory Physiology & Neurobiology*, 154(1), 199–215.
- eds Pörtner, H.-O., Roberts, D., Masson-Delmotte, V., Zhai, P., Tignor, M., Poloczanska, E., Mintenbeck, K., Alegría, A., Nicolai, M., Okem, A., Petzold, J., Rama, B., & Weyer, N., 2019. *Annex I: Glossary. In: IPCC Special Report on the Ocean and Cryosphere in a Changing Climate*, In Press.
- Pörtner, H., 2008. Ecosystem effects of ocean acidification in times of ocean warming: a physiologist’s view, *Marine Ecology Progress Series*, 373, 203–217.
- Pörtner, H.-O., Gutowska, M., Ishimatsu, A., Lucassen, M., Melzner, F., & Seibel, B., 2011. Effects of ocean acidification on nektonic organisms, *Ocean Acidification*, pp. 154–175.
- Reynolds, R. W., Smith, T. M., Liu, C., Chelton, D. B., Casey, K. S., & Schlax, M. G., 2007. Daily high-resolution-blended analyses for sea surface temperature, *Journal of Climate*, 20(22), 5473 – 5496.
- Rhein, M., Rintoul, S., Aoki, S., Campos, E., Chambers, D., Feely, R., Gulev, S., Johnson, G., Josey, S., Kostianoy, A., Mauritzen, C., Roemmich, D., Talley, L., & Wang, F., 2013. Observations: Ocean, *Climate Change 2013: The Physical Science Basis. Contribution of Working Group I to the Fifth Assessment Report of the Intergovernmental Panel on Climate Change [Stocker, T.F., D. Qin, G.-K. Plattner, M. Tignor, S.K. Allen, J. Boschung, A. Nauels, Y. Xia, V. Bex and P.M. Midgley (eds.)]. Cambridge University Press, Cambridge, United Kingdom and New York, NY, USA.*
- Sarmiento, J. & Gruber, N., 2006. *Ocean Biogeochemical Dynamics*, Princeton University Press.
- Seibel, B. A., Maas, A. E., & Dierssen, H. M., 2012. Energetic plasticity underlies a variable response to ocean acidification in the pteropod, limacina helicina antarctica, *PLOS ONE*, 7(4), 1–6.
- Siegenthaler, U. & Sarmiento, J. L., 1993. Atmospheric carbon dioxide and the ocean, *Nature*, 365(6442), 119–125.
- Smale, D. A., Wernberg, T., Oliver, E. C. J., Thomsen, M., Harvey, B. P., Straub, S. C., Burrows, M. T., Alexander, L. V., Benthuisen, J. A., Donat, M. G., Feng, M., Hobday, A. J., Holbrook, N. J., Perkins-Kirkpatrick, S. E., Scannell, H. A., Sen Gupta, A., Payne, B. L., & Moore, P. J., 2019. Marine heatwaves threaten global biodiversity and the provision of ecosystem services, *Nature Climate Change*, 9(4), 306–312.
- Spisla, C., Taucher, J., Bach, L. T., Haunost, M., Boxhammer, T., King, A. L., Jenkins, B. D., Wallace, J. R., Ludwig, A., Meyer, J., Stange, P., Minutolo, F., Lohbeck, K. T., Nauendorf, A., Kalter, V., Lischka, S., Sswat, M., Dörner, I., Ismar-Rebitz, S. M. H., Aberle, N., Yong, J. C., Bouquet, J.-M., Lechtenböcker, A. K., Kohnert, P., Krudewig, M., & Riebesell, U., 2021. Extreme levels of ocean acidification restructure the plankton community and biogeochemistry of a temperate coastal ecosystem: A mesocosm study, *Frontiers in Marine Science*, 7, 1240.
- Steinacher, M., Joos, F., Frölicher, T. L., Plattner, G.-K., & Doney, S. C., 2009. Imminent ocean acidification in the arctic projected with the NCAR global coupled carbon cycle-climate model, *Biogeosciences*, 6(4), 515–533.
- Talley, L., Pickard, G., Emery, W., & Swift, J., 2011. *Descriptive Physical Oceanography: An Introduction Sixth Edition*, Academic Press.
- Tortell, P. D., Payne, C. D., Li, Y., Trimborn, S., Rost, B., Smith, W. O., Riesselman, C., Dunbar, R. B., Sedwick, P., & DiTullio, G. R., 2008. CO₂ sensitivity of southern ocean phytoplankton, *Geophysical Research Letters*, 35(4).
- Weiss, R., 1974. Carbon dioxide in water and seawater: the solubility of a non-ideal gas, *Marine Chemistry*, 2(3), 203 – 215.
- Zeebe, R. E. & Wolf-Gladrow, D., 2001. *CO₂ in seawater: Equilibrium, kinetics, isotopes*, Elsevier, Amsterdam.

Chapter 2

Methods

2.1 GFDL ESM2M Earth system model

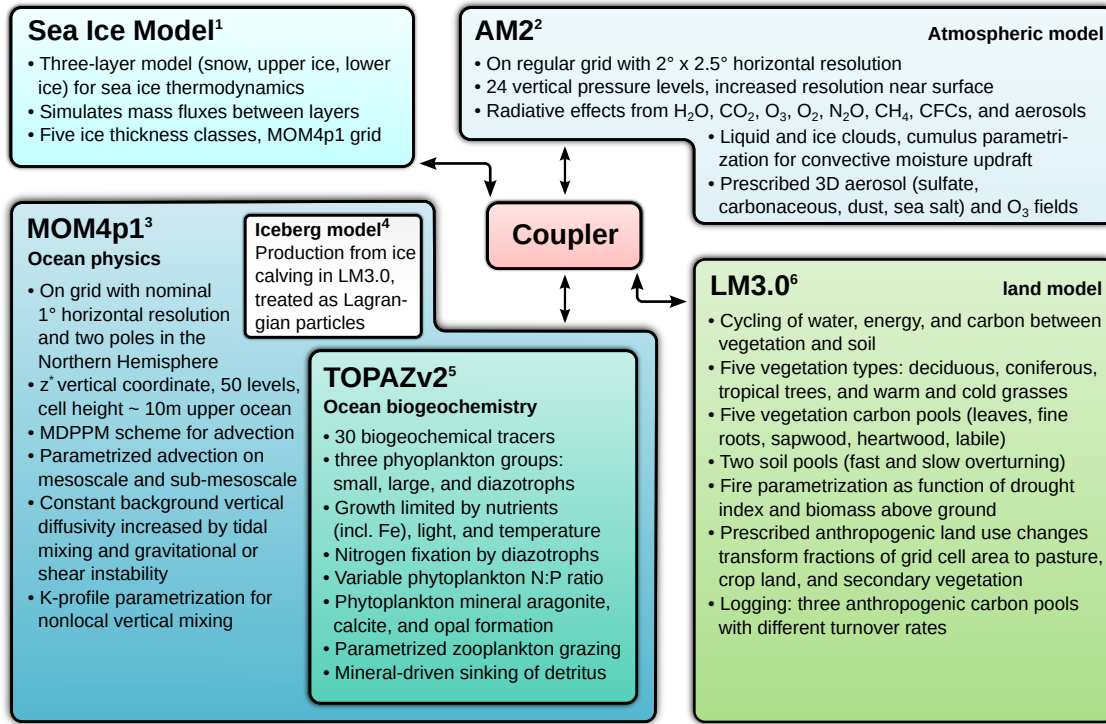
The simulations used in this thesis were run with the fully coupled Earth system model GFDL ESM2M (Dunne et al., 2012), which was released in 2012. The model was developed at the Geophysical Fluid Dynamics Laboratory (GFDL) in Princeton as the successor of the GFDL CM2.1 global circulation model (Delworth et al., 2006). While simulating similar climate characteristics as CM2.1 (Dunne et al., 2012), ESM2M also explicitly simulates the cycling of carbon in the Earth system (Dunne et al., 2013), which makes it one of the first publicly available Earth system models developed at GFDL¹.

The GFDL ESM2M model consists of model components for the ocean, sea ice, atmosphere, and land. The ocean component also includes ocean biogeochemistry. The coupler program handles fluxes between these components. Fluxes are interpolated between the grids of the components so that energy, mass, and tracer mass is conserved while cycling between the components. The ocean component was run with a time step of two hours. Also fluxes between the ocean and sea ice components were exchanged using a two-hour time step. Fluxes between ocean and atmosphere and fluxes from the land to the ocean are handled on the same two-hour time step, because these fluxes are passed through the ice model. Atmosphere, land, and sea ice components used a faster 30-minute time step. A scheme summarizing the model components is shown in Fig. 2.1.

2.1.1 Ocean component

The physical ocean state is simulated by the Modular Ocean Model version 4p1 (MOM4p1; Griffies, 2009) with a nominal horizontal 1° degree resolution. The zonal resolution is increased up to $1/3^\circ$ near the equator. The horizontal grid is a tripolar grid with two poles north of 65° latitude that are located over North America and Eurasia, respectively (Murray, 1996). The vertical grid has 50 levels and a resolution of about 10 m in the upper 230 m of the water column. The resolution decreases below and is about 300 m at 5000 m depth. Unlike for the time-independent horizontal grid, vertical grid cell spacing is allowed to change with time to represent variations in sea surface height. Using a rescaled vertical coordinate, sea surface height variations implicitly adjust the vertical cell spacing throughout the water column (Griffies, 2009; Adcroft & Campin, 2004). MOM4p1 simulates the advection of physical and biogeochemical tracers that results from the resolved velocity field using the MDPPM numerical scheme (Marshall et al., 1997). MOM4p1 includes parametrizations for unresolved eddy-induced advection on the mesoscale (Griffies, 1998) and sub-mesoscale (Fox-Kemper et al., 2008). Furthermore, tracer fluxes from isopycnal (neutral)

¹together with the very similar GFDL ESM2G model that only differs in the physical ocean component.



¹Winton (2000); ²Anderson et al. (2004); ³Griffies (2009); ⁴Martin & Adcroft (2010); ⁵Dunne et al. (2013); ⁶Shevliakova et al. (2009)

Figure 2.1: Characteristics of the model components of the GFDL ESM2M model. Fluxes between these model components are handled by the coupler.

and vertical (approximately diapycnal) diffusion are simulated. Vertical diffusion is represented by a constant background diffusivity, the K-profile parameterization by Large et al. (1994) representing vertical mixing in the ocean boundary layer, as well as tidal mixing (Lee et al., 2006; Simmons et al., 2004). In addition, the nonlocal part of the K-profile parameterization for the ocean boundary layer (Large et al., 1994) implements convective vertical mixing in the boundary layer, which occurs under buoyancy loss of surface waters. More information on the model parametrizations for vertical mixing is given in Chapter 5 and Vogt et al. (in preparation).

2.1.2 Ocean biogeochemical component

The ocean biogeochemistry is simulated by Tracers of Ocean Phytoplankton with Allometric Zooplankton version two (TOPAZv2). It simulates the cycling of 30 biogeochemical tracers such as carbon, nitrogen, phosphorus, silicon, iron, oxygen, alkalinity, and lithogenic material (see supplement of Dunne et al., 2013). The uptake of nutrients such as nitrate, ammonium, phosphate, iron, and silicate is simulated for three phytoplankton groups: small (prokaryotic pico- and nanoplankton), large (further divided into diatoms other eukaryotes), and diazotrophic phytoplankton (nitrogen fixing species). The growth of phytoplankton is limited by temperature (Eppley, 1972), and by the availability of light and the aforementioned nutrients (more details in the Appendix section of Frölicher et al., 2020). The diazotrophic phytoplankton group also fixes N₂ to form organic nitrogen. Stoichiometric phytoplankton phosphorus to nitrogen ratios are allowed to vary with the environmental conditions (Klausmeier et al., 2004). Phytoplankton is lost due to parameterized zooplankton grazing, transforming phytoplankton biomass into detritus and dissolved organic material. Over time, detritus and dissolved organic material are remineralized,

transforming the biogeochemical tracers back to their inorganic forms. Furthermore, the sinking of detritus is simulated, depending on the ballast from biogenic calcium carbonate (calcite and aragonite) or silica (opal). Finally, the formation of sediments from sinking detritus in the bottom grid cell is simulated, also allowing for the cycling of surface sediment calcite. The loss through sediment formation is balanced by an external input from rivers and atmospheric dust. Alkalinity changes as a result of dissolution and formation of CaCO_3 minerals, nitrate- and ammonium-based biological production and remineralization, as well as nitrification and denitrification.

Carbonate chemistry, depending on dissolved inorganic carbon, alkalinity, temperature, salinity, phosphate, silicate, and pressure, and the air-sea CO_2 exchange are based on the OCMIP2 recommendations (Najjar & Orr, 1998). The dissociation constants for carbonic acid and bicarbonate are those from Dickson & Millero (1987), based on Mehrbach et al. (1973). The solubility of carbon dioxide follows Weiss (1974). Air-sea CO_2 exchange is simulated when surface ocean CO_2 concentration differs from a saturation concentration that depends on solubility of carbon dioxide and fugacity of atmospheric CO_2 . Gas transfer velocity is determined by wind speed and Schmidt number (Wanninkhof, 1992).

2.1.3 Other model components

The sea ice component (Winton, 2000) is on the same horizontal grid as the ocean component and similar to that in CM2.1 (Delworth et al., 2006). Ice thermodynamics is simulated based on a three-layer model with two ice layers (lower ice and upper ice) and one snow layer. Mass fluxes between these vertical layers and the resulting layer thickness changes are taken into account. Sea ice concentration is stored for five ice thickness classes.

The atmosphere component is version 2 of the Atmospheric Model (AM2; Anderson et al., 2004) that was already used for CM2.1. It is on a grid with $2 \times 2.5^\circ$ horizontal resolution and 24 vertical pressure levels up to a height of about 40 km. The vertical resolution is increased near the surface and comparably low in the stratosphere, which is only represented by five pressure levels (Anderson et al., 2004). The radiative effects from H_2O , CO_2 , O_3 , O_2 , N_2O , CH_4 , four chlorofluorocarbon (CFC) species, and different aerosol species (sulfate, hydrophylic and hydrophobic carbonaceous, dust, sea salt) are considered. The diurnal cycle of solar insolation is taken into account. Atmospheric physics includes a cumulus parameterization for convective moisture updraft, liquid and ice clouds, vertical diffusion including a K-profile scheme, and gravity wave drag. Atmospheric aerosols from non-volcanic and volcanic origin as well as ozone are prescribed by external monthly-mean three-dimensional input fields. Furthermore, N_2O , CH_4 , and CFC concentrations are prescribed by global annual-mean time series.

The land component, given by the Land Model version 3.0 (LM3.0; Shevliakova et al., 2009), simulates the cycling of water, both in liquid and frozen phase, energy, and carbon. It simulates multi-layer soil dynamics for water and temperature and vegetation dynamics that include five competing vegetation types: deciduous, coniferous, tropical trees, and warm and cold grasses. Five vegetation carbon pools (leaves, fine roots, sapwood, heartwood, labile carbon stores) and two soil carbon pools (with fast and slow exchange rates) are simulated. Vegetation change from fire is implemented as a function of biomass above ground and a drought indicator. Anthropogenic land use changes can be prescribed based on external input fields. These land use changes drive transitions between the fractions of each grid cell that are covered by natural vegetation, pasture, crop land, and secondary vegetation. River runoff and solid ice runoff to represent land ice calving are simulated. For the latter, an iceberg model transports excess snow from the land model as icebergs over the ocean domain. These are treated as Lagrangian particles whose trajectory is determined from the interaction with the atmosphere, ocean, and sea ice components (Martin & Adcroft, 2010).

2.1.4 Model performance

Simulations by the ESM2M model contributed to the fifth phase of the Coupled Model Intercomparison Project (CMIP5; Taylor et al., 2012). ESM2M shows a relatively low bias in simulated present-day global average sea surface temperature (SST) and similar spatial patterns compared to observation-based data (Bopp et al., 2013). Similar to other CMIP5 generation models, biases are larger for the spatial patterns in carbonate system variables, in particular pH (Bopp et al., 2013). Globally, the GFDL-ESM2M model overestimates present-day net primary productivity (NPP). It was found to simulate the largest NPP among CMIP5 Earth system models (Bopp et al., 2013; Laufkötter et al., 2015). However, simulated export production is relatively smaller (Bopp et al., 2013), and the ESM2M model shows comparably small biases in the strength of the biological carbon pumps (Oka, 2020). ESM2M has also been shown to simulate a cumulative oceanic uptake of anthropogenic carbon that is close to observational estimates (Bronse laer et al., 2017) and acidification trends in mode and intermediate waters that are comparable to those in the CMIP5 multi-model mean (Resplandy et al., 2013).

The equilibrium climate sensitivity, the equilibrium atmospheric near-surface temperature increase from a doubling of CO₂ with respect to preindustrial levels, was identified as 3.3 K (Paynter et al., 2018). This value was determined from a 4430 yr simulation with doubled atmospheric CO₂ that followed a ramp up simulation during which CO₂ was increased from the preindustrial concentration. The equilibrium climate sensitivity of the ESM2M model is in agreement with observational estimates. Based on multiple lines of evidence, Sherwood et al. (2020) estimate the Earth’s climate sensitivity to be between 2.6 K and 3.9 K with (66 % confidence interval). Likewise, the sixth assessment report of the IPCC estimates equilibrium climate sensitivity to be between 2.5 K and 4.0 K (likely range; Masson-Delmotte et al., 2021). The ESM2M model simulates a comparably low transient climate response (TCR) to increases in atmospheric CO₂. TCR is defined as the increase in near-surface atmospheric temperature around the time of CO₂ doubling in a 1 % CO₂-increase-per-year simulation relative preindustrial conditions. The TCR of 1.4 K for the ESM2M model is lower than the CMIP5 multi-model mean of 1.8 K and the CMIP6 multi-model mean of 2.0 K (Meehl et al., 2020). Reflecting the relatively low transient climate response, projected increases in sea surface temperature during the 21st century are at the low end of CMIP5 model projections (Bopp et al., 2013). The ESM2M model projects only small changes in NPP (Bopp et al., 2013; Laufkötter et al., 2015).

2.2 Simulation design

For the analyses presented in this thesis, a number of simulations with the ESM2M model were performed at the Swiss National Supercomputing Centre (CSCS). These model simulations simulated either the preindustrial state of the climate system or the climate system response to anthropogenic activities since the beginning of the industrial revolution. A sketch of the simulations is shown in Fig. 2.2, and a complete list of simulations performed with the ESM2M model is given in Appendix 6.

To represent the preindustrial climate, the atmospheric concentrations for CO₂, CH₄, and N₂O were held at the preindustrial volume fractions of 286 parts per million (Fig. 2.2a), 805 parts per billion, and 276 parts per billion, respectively. To allow for short-term variations in atmospheric CO₂ due to interactions with the ocean and land components, atmospheric CO₂ was allowed to vary on sub-annual timescale while it is pushed back to the prescribed preindustrial value by a restoring CO₂ flux. The time scale of this restoring flux was chosen such that a perturbed atmospheric CO₂ concentration returns to the prescribed value within

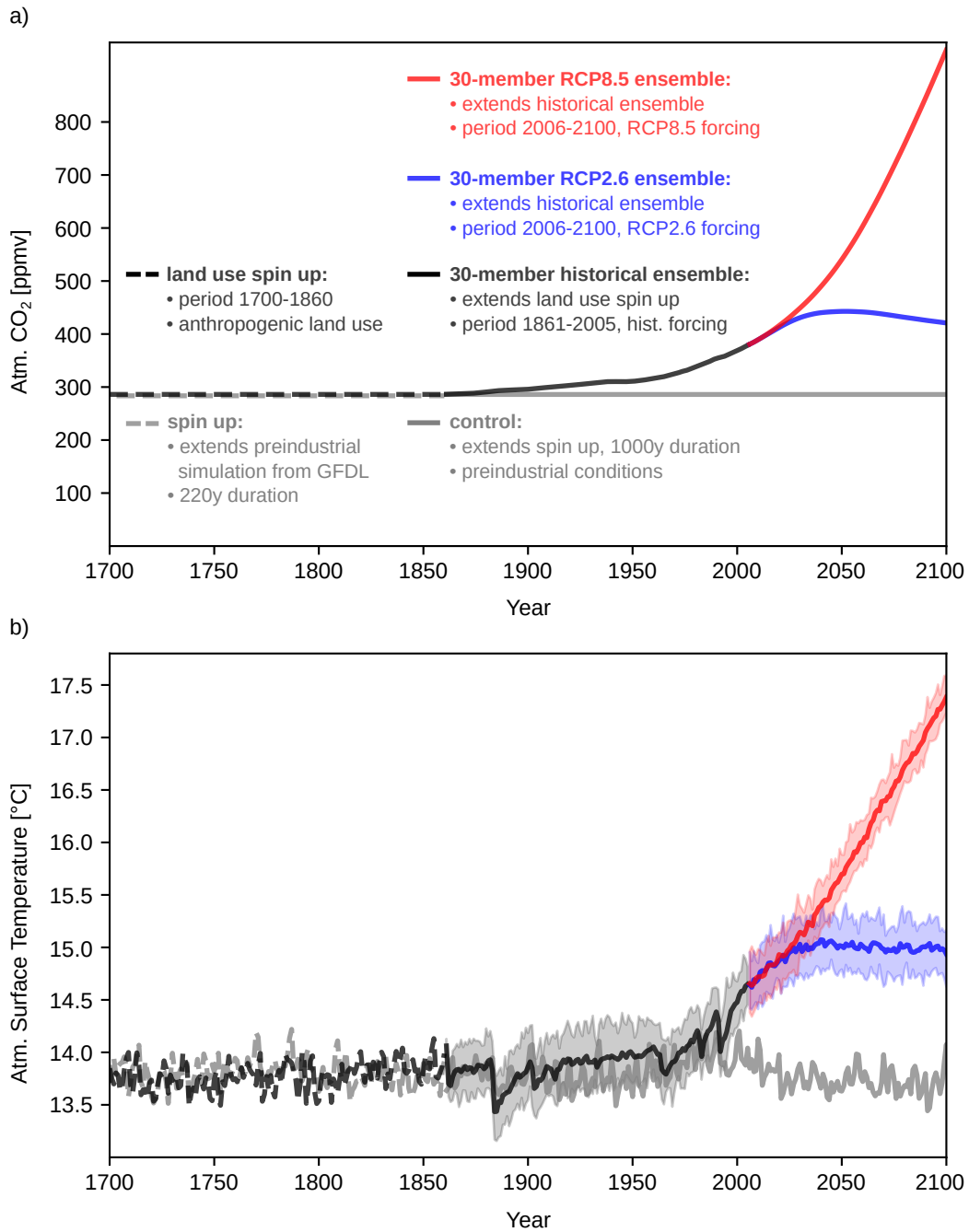


Figure 2.2: (a) Prescribed atmospheric CO₂ and key characteristics for the spin up, land use spin up, and control simulations, as well as the historical, RCP2.6, and RCP8.5 ensemble simulations (Appendix Table A.2). (b) Simulated global average atmospheric surface temperature (temperature at 2 meters above ground) for the same simulations. For the historical, RCP2.6, and RCP8.5 ensemble simulations, ensemble means are shown as thick lines and ensemble ranges are shown as shaded areas.

one year. Furthermore, solar forcing as well as aerosol and ozone concentrations were held at preindustrial levels as represented by the year 1860. No aerosol forcing from volcanic eruptions was included. The vegetation simulated by the land model was allowed to evolve freely, simulating potential vegetation without constraints from anthropogenic land use (Shevliakova et al., 2009). The preindustrial simulations were initialized from a 220 y spin-up simulation that in turn

was initialized from a quasi-equilibrated 1000 y preindustrial control simulation run at GFDL. The simulation at GFDL was started from present-day World Ocean Atlas temperature and salinity fields (Locarnini et al., 2006; Antonov et al., 2006) for the ocean component and from CM2.1 model output (Delworth et al., 2006) for the atmosphere component. The 220 yr spin-up simulation at CSCS was necessary to ensure stability of the model under the new computing infrastructure.

To simulate the climate system response to anthropogenic perturbations during the historical period (here defined as the period 1861-2005), ensemble simulations with historical forcing were performed. Historical forcings included prescribed time-dependent atmospheric CO_2 , CH_4 , N_2O (Meinshausen et al., 2011), ozone (based on Cionni et al. (2011)), and aerosol concentrations (provided by J.-F. Lamarque), as well as time-varying solar forcing (Lean, 2009). Atmospheric aerosol forcing from historical volcanic eruptions was taken into account (Sato et al., 1993; Stenchikov et al., 1998). Furthermore, anthropogenic land use changes were included. The land use changes (Hurtt et al., 2006) prescribe time-dependent transitions rates that transform parts of the grid cell area covered by natural vegetation in LM3.0 to pasture, crop land, and secondary, regrown vegetation (Shevliakova et al., 2009). Secondary vegetation describes land that was cut down at least once. The carbon contained in cut vegetation is partially distributed over three anthropogenic carbon pools, which release carbon back to the atmosphere on different timescales, and partially transformed into soil carbon. Activating land use changes causes a rapid initial decline in total land (vegetation and soil) carbon. This is because all land use changes since year 1500 are applied when land use is activated, resulting in a transition of fully-grown primary vegetation to secondary vegetation over a large area. Consequently, a large amount of vegetation carbon is transferred to the anthropogenic carbon pools and to the atmosphere. This initial shock in total land carbon is followed by a slower increase in land carbon on decadal timescales that is due to a regrowth of secondary vegetation on the area that was cut down when activating land use. Eventually, land carbon decreases again due to the anthropogenic land use changes that transform natural and secondary vegetation to pasture and crop land (Sentman et al., 2011). To exclude the imprint of the initial shock and the recovery phase on land carbon from the historical simulations, we first ran a land use only simulation under preindustrial conditions but with land use changes over the period 1700-1860 following the approach by Sentman et al. (2011) (called 'land use spin up' in Fig. 2.2). After this period, the land carbon cycle and land-atmosphere carbon fluxes are in quasi-equilibrium again.

A 30-member perturbed initial condition ensemble of historical simulations was then initialized from this land use only simulation by slightly perturbing ocean temperature in one grid cell in each ensemble member (Wittenberg et al., 2014; Palter et al., 2018; Frölicher et al., 2020). To do so, different small seawater temperature perturbations on the order of $10^{-5} \text{ }^\circ\text{C}$ ($\pm 1 \cdot 10^{-5} \text{ K}$, $\pm 2 \cdot 10^{-5} \text{ K}$, $\pm 3 \cdot 10^{-5} \text{ K}$, $\pm 4 \cdot 10^{-5} \text{ K}$, $\pm 5 \cdot 10^{-5} \text{ K}$) were added either to a surface grid cell in the Weddell sea (70.5°S 51.5°W , ensemble members 2-10), to a surface grid cell in the North Atlantic (63.5°N 4.5°W , ensemble members 11-20), or to a grid cell at 2000 m depth in the North Pacific (44.5°N 179.5°W , ensemble members 21-30). Such small perturbation in seawater temperature propagate through all simulated variables due to the chaotic nature of the climate system (Lorenz, 1963), eventually resulting in independence of variability between the ensemble members. Ensemble members can be considered as independent after about three years at sea surface, while approximate independence of ensemble members is reached later at subsurface (Frölicher et al., 2020), for example approximately after eight years at 200 m depth (Chapter 3).

The historical 30-member ensemble simulation over the period 1861-2005 was extended by two 30-member ensemble simulations over the 21st century (period 2006-2100) that represent contrasting scenarios for the 21st century (Fig. 2.2). The first follows the high greenhouse gas emission and

no mitigation scenario RCP8.5, a representative concentration pathway (RCP) scenario that leads to 8.5 W/m^2 radiative forcing increase with respect to preindustrial conditions by year 2100 (Riahi et al., 2011). At that time, atmospheric CO_2 concentration is assumed to be around 930 parts per million volume (ppmv). RCP8.5 assumes no climate policy, with sustained fossil-fuel based energy production and large population increases, resulting in high energy demand and greenhouse gas emissions that are on the high end of likely scenarios for the 21st century van Vuuren et al. (2011a). In contrast, the second ensemble simulation follows the low greenhouse gas emission and high mitigation RCP2.6 scenario (van Vuuren et al., 2011b), under which radiative forcing increases only by 2.6 W/m^2 by 2100. Under RCP2.6, atmospheric CO_2 peaks at 440 ppmv in the middle of the 21st century and stabilizes at around 420 ppmv by year 2100. The scenario assumes effective climate policy, a shift towards renewable and nuclear energy production, and an effective use of negative emission technology. Greenhouse gas emissions under RCP2.6 are thus on the low end of likely scenarios van Vuuren et al. (2011a). An overview over the simulations is shown in Fig. 2.2.

The preindustrial simulation as well as the ensemble simulations for the historical period and the RCP8.5 and RCP2.6 scenarios store 3D output on daily-mean resolution for physical ocean variables such as potential temperature, salinity, and potential density and for biogeochemical variables such as alkalinity, dissolved inorganic carbon, hydrogen ion concentration, and aragonite and calcite saturation state (complete list of output on daily-mean resolution in Appendix Table A.1). In addition, 2D output on daily-mean resolution is stored for atmospheric reference temperature and wind stress, as well as several ocean fields such as surface chlorophyll and $p\text{CO}_2$. In addition, a part of the simulations stored daily-mean data for temperature and dissolved inorganic carbon tendency terms and the limitation terms of phytoplankton growth. Daily-mean resolution was chosen to facilitate the analysis of extreme events that last shorter than a month and that arise partially due to variations on sub-monthly timescales (see Sect. 2.3.1) and to analyze the processes behind these short-lived extreme events.

2.3 Extreme event definition and metrics

An extreme event is a discrete event in time (with a start and an end) and space (covering a confined area) during which a variable exceeds predefined thresholds. These extreme event thresholds are generally defined such that extremes occur rarely and represent unusual conditions in the variable of interest. Often, these conditions are expected to pose a risk to vulnerable and exposed natural and human systems.

In Sect. 2.3.1, the definitions for extreme event thresholds used in these thesis are introduced. Furthermore, the choice of reference period and the influence of the temporal resolution of the underlying data is discussed. In Sect. 2.3.2, extreme event metrics to characterize extremes are introduced and linked to the underlying statistical properties of the data.

2.3.1 Definition of extreme event thresholds

Absolute and relative thresholds

Extreme events can be generally defined based on relative and on absolute thresholds. Relative thresholds are based on the distribution of data. As a result, they are specific to the statistical properties of the data at each location. In contrast, absolute thresholds are defined based on criteria that are independent of the observed data distribution. Prominent examples are the calcium carbonate saturation state threshold of one (Morse & Mackenzie, 1990) that separates supersaturated from undersaturated waters and the oxygen concentration threshold of $2 \text{ mg O}_2 \text{ liter}^{-1}$ ($60 \mu\text{mol kg}^{-1}$) (Vaquer-Sunyer & Duarte, 2008) below which waters are considered

as hypoxic. Waters that are undersaturated with respect to calcium carbonate are corrosive to calcium carbonate minerals such as those in shells of marine invertebrates (Bednaršek et al., 2012). Organisms are stressed or may die under hypoxic conditions, in particular higher animals (Stramma et al., 2008). Such absolute thresholds are often informed by known ecological limits. Hence, so-defined extreme events likely have relevant ecological impacts. However, such ecologically informed criteria are often defined independently from the geographical location and only apply for some certain organisms and ecosystems. This hinders the application of absolute thresholds for studies on a global scale, since the statistical properties of variables often drastically change between different regions. As a result, the analyzed variable may be in a permanent extreme state in one region while never being extreme in another region. Furthermore, fixed absolute thresholds often don't take into account that organisms in different ecosystems are likely to a certain extent adapted to local conditions. A way forward is here to determine absolute biologically informed thresholds that vary between ecosystems. For example, Clarke et al. (2021) define an aerobic growth index that contrasts oxygen supply with demand for different species, also taking into account regional differences in water temperature. However, defining biologically informed thresholds that vary between ecosystems requires knowledge of the species and their ecological boundaries in the individual ecosystems. Such data is currently not available for carbonate system variables such as $[H^+]$ or the calcium carbonate saturation state.

The analyses in this thesis rely on relative thresholds calculated as spatially-varying percentile thresholds determined from the local data distributions. While this definition is not directly linked to the ecological impacts, it has the advantage that extremes based on spatially-varying percentile thresholds occur with the same frequency everywhere. This ensures that extremes represent rare deviations from normal conditions in every region. Furthermore, it is expected that the variations in relative thresholds, arising from the variations in data distributions, to some extent mirror variations in the ecological boundaries of the organisms that are adapted to the location conditions at different geographical locations. As a result, relative thresholds may be similar in their ecological significance across regions, despite the regional variations in thresholds.

Defining relative thresholds

Relative extreme event thresholds are widely used in the literature (e.g., Hobday et al., 2016; Frölicher et al., 2018; Oliver et al., 2021). Depending on the research question, different approaches to define relative thresholds are chosen. These approaches mainly differ in how seasonality in the time series data is treated. This is important since seasonality is often the main mode of variability in the data (Chapter 3). For example, for surface $[H^+]$ and within daily-mean output from a preindustrial control simulation (Appendix Table A.1), seasonality is globally responsible for 81 % of the variance in the data. One approach is to calculate *fixed percentile thresholds* based on the full time series at each location (e.g. Frölicher et al., 2018). Extremes then often occur at the time of year when the seasonal cycle takes its maximum. This definition for extreme event thresholds is used in Chapter 3 to study changes in extreme events in $[H^+]$ and Ω_A . Another approach that removes the imprint from the seasonal cycle on the occurrence of extremes is to use *anomaly thresholds*. There, the seasonal cycle is subtracted from the data, and a percentile threshold is then calculated from the obtained seasonal anomalies (e.g. Zscheischler et al., 2014; Le Grix et al., 2021). Extremes can then in principle occur throughout the year. However, in regions where the variability in the data changes strongly between seasons, for example due to seasonal sea ice cover that isolates the ocean from the atmosphere and solar insolation, extremes occur mostly in the more variable seasons. A third approach under which extremes are equally likely throughout the year is to define *seasonally varying thresholds* (e.g. Hobday et al., 2016). There, a threshold is defined for each calendar day individually. As a result, the seasonally varying thresholds vary with the seasonal cycle and with seasonal changes in variability (Fig. 2.3),

and neither the seasonal cycle nor seasonal changes in variability imprint on the occurrence probability of extreme events. Observational time series are often too short to calculate a percentile threshold for each calendar day. This limitation can be bypassed by increasing the amount of data using a window approach where a certain amount of data before and after the calendar day of interest is also taken into account to calculate the threshold (Hobday et al., 2016). Seasonally varying thresholds are used in Chapters 4 and 5. In Chapter 4, where compound events in temperature and $[H^+]$ are assessed, seasonally varying thresholds are chosen so that the frequency of compound events is not a consequence of the dependence between the seasonal cycles of the two variables. Likewise in Chapter 5, where the drivers of $[H^+]$ events are analyzed, seasonally varying thresholds are chosen to separate the drivers of extreme events in $[H^+]$ from the drivers of its seasonal cycle. The differences between fixed thresholds, anomaly thresholds, and seasonally varying thresholds are illustrated in Fig. 2.3. Some studies further impose an additional duration criterion on ocean extreme events, for example defining the extremes to last at least for 5 days (Hobday et al., 2016; Oliver et al., 2018). Such a minimum duration criterion is not used in this thesis. It can result in the exclusion of a significant fraction of extremes. For example, for preindustrial surface $[H^+]$ simulated by the ESM2M model, a minimum duration criterion of 5 d would globally exclude 43 % of extreme events, when these are based on fixed 99th percentile thresholds.

Choice of percentile

To define the extreme events, it is further necessary to choose a percentile for the thresholds. When analyzing extremes in high values, the 90th (e.g. Hobday et al., 2016; Le Grix et al., 2021) and the 99th percentiles (e.g. Frölicher et al., 2018) are often chosen. The percentile should be chosen high enough so that extremes represent exceptional states that are relevant to ecosystems and the dependent human communities. However, the percentiles need to be low enough to ensure robust percentile definition and sufficient data for statistical analyses². In Chapter 3, the 99th percentile is chosen. In Chapter 4, the lower 90th percentile is used to obtain a sufficient amount of compound extremes for analysis in regions where compound events in temperature and $[H^+]$ are rare and to allow for the comparison to short observational time series. Furthermore, the seasonally varying thresholds that are used in Chapter 4 are more robust when based on a lower percentile. Therefore, the 90th percentile was also chosen in Chapter 5. Sensitivity analyses with different percentile choices reveal that the obtained spatial patterns in extreme and compound event characteristics are relatively insensitive to the percentile choice (Chapters 3 and 4): While the percentile threshold choice directly modulates the likelihood of extreme events at each location, it often has a much smaller effect on spatial differences in extreme event metrics. Relative increases in extreme event event likelihood due to anthropogenic perturbations can be much larger for extremes based on higher percentile thresholds (Chapters 3 and 4).

Reference period and baselines

When analyzing extreme events in a transient or changing climate, a reference period needs to be defined in which the percentile thresholds are defined. Depending on the analyzed variable, this choice has a large impact on the frequency of extremes. For example, when defining surface $[H^+]$ extreme events based on fixed 99th percentiles under preindustrial conditions in a model simulation, the number of extreme event days increases sharply from the initial value of 3.65 days per year under historical forcing, crossing 300 days per year already before year 2000

²In this thesis, the percentiles are directly estimated from the data. This is possible because the analyzed model simulations provide enough data for robust estimation of the percentiles. An alternative approach that relies on extreme value theory is to model the exceedances of a relatively low threshold (i.e., the difference between the data and the threshold where the data exceeds the threshold) by a generalized Pareto distribution. Higher percentiles can then be determined analytically from that distribution (Coles, 2001). This approach is particularly useful when the length of a time series is too short to robustly estimate such higher percentiles from the data.

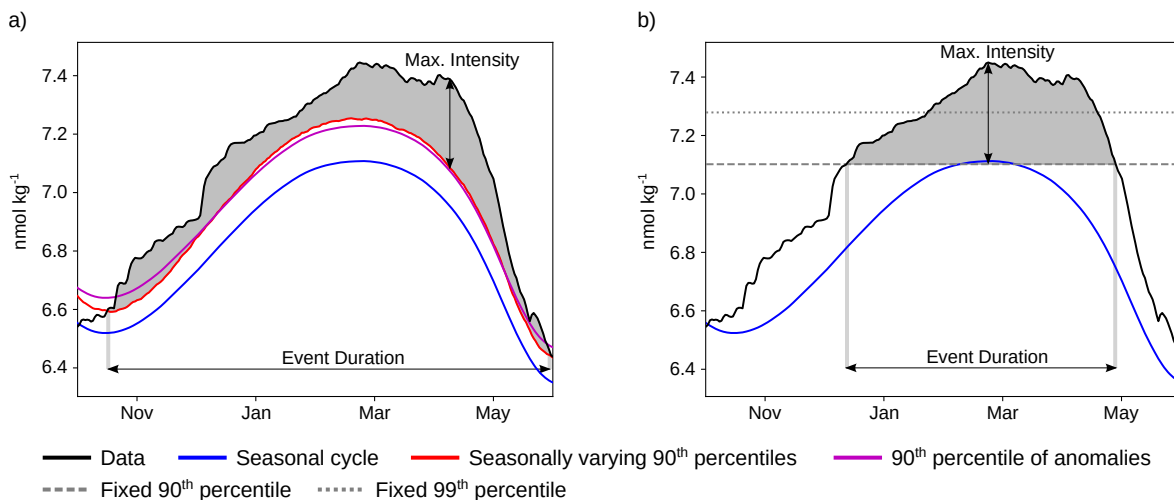


Figure 2.3: A surface $[\text{H}^+]$ extreme event in the subpolar North Pacific simulated by the GFDL ESM2M model in years 564 and 565 of the 1000-yr long preindustrial control simulation. The data was averaged over the subpolar North Pacific region ($45\text{--}60^\circ\text{N}$, $140\text{--}200^\circ\text{W}$) before analysis. The $[\text{H}^+]$ data is shown in black and its climatological seasonal cycle is shown in blue. (a) The extreme event when defined relative to seasonally varying 90th percentiles (red line). Duration (228 d) and maximal intensity (0.30 nmol kg^{-1}) are shown with arrows. For comparison, also the 90th percentile of seasonal anomalies (with the seasonal cycle added) is shown (magenta line). (b) The extreme event when defined relative to the fixed 90th percentile threshold (grey dashed line). Here, duration is 136 d and intensity is 0.35 nmol kg^{-1} . The fixed 99th percentile threshold is shown for comparison (grey dotted line).

(Chapter 3). This is because the trends in $[\text{H}^+]$ from ocean acidification are large compared to internal $[\text{H}^+]$ variability. In the analyses of model data in Chapters 3 to 5, percentile thresholds were defined under preindustrial conditions. To analyze observation-based data, the observational period was used as reference period (Chapter 4).

It is debated whether extreme events should be defined relative to fixed reference periods (*fixed baseline*), or whether extreme events should instead be defined with respect to a *shifting-mean baseline* that accounts for the changes in the mean state of the analyzed variable with climate change. In the context of marine heatwaves, Jacox (2019) argues that ocean temperatures during MHWs are much higher than ‘normal’ temperatures, which themselves will shift as the ocean warms with climate change. In other words, the baseline ocean temperature will shift, and future MHWs should therefore be defined relative to the shifted baseline.’ Oliver et al. (2019) note that whether a fixed or shifting-mean baseline should be used depends on ecological adaption time scales: For organisms with little capability for adaption, a fixed baseline is likely more meaningful, while a shifting-mean baseline may be more meaningful for organisms that are able to adapt to the transient changes in mean state. In Chapters 3 and 4 where changes in extreme events are analyzed, we report changes with respect to both, fixed and shifting, baselines. To determine the shifting-mean baseline that accounts for the transient changes in the mean state, it is necessary to increase the percentile thresholds determined during the reference period according to the transient changes in the variables mean state³. A simple approach is to identify the variables’ mean state in a transient time series by fitting a linear or higher-order polynomial model to the data (Kwiatkowski & Orr, 2018). However, the functional shape of the forced change in mean state of a variable is generally not known. Fitting a too-low order polynomial function poses the risk of falsely identifying parts of the forced mean change as multi-year variations around the assumed forced change. Fitting a too-high order polynomial function, on the other hand, poses the opposite risk of falsely identifying multi-year variability with forced changes in the variable.

³Identically, one can also subtract these changes in the variables mean state from the data prior to identifying extreme events.

An alternative non-parametric approach is possible when a large ensemble of simulations is available. The forced mean change can then be identified with the change in the ensemble mean after removing the seasonal variations that are present in all ensemble members from the ensemble mean. The remaining stochastic variations in the individual ensemble members tend to average out when calculating the ensemble mean and the mean state that undergoes the forced changes is exposed. This approach is taken in Chapters 3 and 4.

Temporal resolution

Results for extreme event analyses depend on the temporal resolution of the data for two reasons. First, higher temporal resolution allows to resolve more variability. Studies that depend on monthly-mean data miss some of the variability that is resolved in daily-mean data. However, the difference is often relatively small for carbonate chemistry-related variables. For example, the variance in surface $[H^+]$ in a preindustrial simulation based on monthly-mean data is globally only 5 % smaller than the variance based on daily-mean data. The difference is relatively small since seasonality, the most important mode of variability, is represented by daily-mean as well as by monthly mean-data. However, the model likely does not fully resolve day-to-day variations in $[H^+]$. As a result, this proportion may be different in reality. The variance of seasonal anomalies is more sensitive to the temporal resolution. Anomaly variance is globally reduced by 13 % when based on monthly-mean data instead of daily-mean data, indicating a larger importance of sub-monthly resolution when analyzing extremes based on anomaly thresholds or seasonally varying thresholds. The second reason is that the minimum duration of an extreme event is given by the temporal resolution of the data. As a result, extremes calculated from monthly-mean data last for at least one month. This is in contrast to the duration of extremes in most surface-ocean variables when calculated from daily-mean data. For example, extremes based on fixed 99th percentiles in a preindustrial simulation by the ESM2M model globally last on average only 11 days.

Using sub-daily resolution that resolves the diurnal cycle further increases the variability in the data (Hofmann et al., 2011), in particular in coastal regions (Torres et al., 2021). While the ESM2M model incorporates the diurnal cycle in insulation and biological activity, the model likely doesn't fully capture diurnal variability. Hence the analyses in this thesis are limited to data with daily-mean temporal resolution.

2.3.2 Extreme event metrics

Definition of extreme event metrics

Extreme event metrics quantify the properties of extreme events. These metrics generally either quantify the frequency of events, the intensity of events, the duration of events, or the area or volume covered by events. Event intensity and duration for a single simulated event in the North Atlantic is shown in Fig. 2.3 for fixed and for seasonally varying percentile thresholds.

The frequency of events is quantified equivalently either by the number of time steps within a period (e.g., days per year) during which a variable is under extreme conditions (Chapters 3 and 4), by the probability that a value at a single time step is extreme, often reported relative to a reference probability as a risk or probability ratio (Frölicher et al., 2018), or by reporting the return period that quantifies the average time span between two time steps with extreme conditions (Laufkötter et al., 2020).

Event intensity quantifies the magnitude by which an event deviates from normal conditions. Mean or maximal intensity is calculated as the mean or maximal difference between the data and

the threshold over the duration of a single event (maximal intensity shown in Fig. 2.3), averaged over all events that occur during a period at a location (Chapter 3, Oliver et al., 2018; Frölicher et al., 2018). Maximal intensity is always larger than mean intensity. For example, maximal intensity of surface $[H^+]$ events, based on fixed 99th percentiles in a preindustrial simulation by the ESM2M model, is globally 73 % larger than mean intensity. In Chapter 3, maximal intensity is used as a measure for event intensity. Alternative approaches calculate intensity from the difference between the data and the climatological seasonal cycle over the course of an event (Hobday et al., 2016) and classify extremes in categories according to how much the variable exceeds the threshold in units of the difference between threshold and seasonal cycle (Hobday et al., 2018).

Event duration quantifies the length in time between the onset of an event, where the variable crosses the threshold, and the end of the event, before the variable falls below the threshold again. In Chapter 3, mean duration is reported, given by the arithmetic average over the durations of all events that occur during a period at a location. The duration of a single event is shown in Fig. 2.3. The duration of events depends on the temporal resolution of the data, with longer event duration observed in data with lower temporal resolution (Sect. 2.3.1). Longer-lasting events are usually also more intense. For example, when imposing a minimum-duration criterion of 5 days for fixed 99th percentile extremes in simulated preindustrial surface $[H^+]$, mean event intensity is globally 41 % larger compared to when no minimum-duration criterion is imposed. In some studies, intensity and duration of events are also combined into one metric, such as the cumulative mean intensity that is the product of mean intensity and duration of an event (Frölicher et al., 2018), or similarly degree heating weeks (Hobday et al., 2016).

The area or volume covered by an extreme event in gridded data is calculated as the sum of the surface areas or volumes of all connected grid cells that form a cluster of cells for which the variable is above the respective event threshold. The result depends on whether grid cells are considered as connected only if they share a face, or whether grid cells that share an edge are also considered as connected. For example, the average volume covered by $[H^+]$ extreme events in the upper 200 m of water column, based on fixed 99th percentiles in a preindustrial simulation by the ESM2M model, is 41 % larger when cells that share edges are also considered as connected. Furthermore, results depend on whether clusters are identified in space for each time step individually (Frölicher et al., 2018), or whether they are tracked also in time (Laufkötter et al., 2020). To calculate the volume covered by $[H^+]$ events in Chapter 3, clusters are identified for each time step individually and grid cells are only considered as connected when they share a face.

Underlying statistical properties

Differences in extreme event metrics arise due to differences in the statistical properties of the underlying time series data. To illustrate this, a stationary time series x can be decomposed into its mean seasonal cycle x_s that repeats each year and the seasonal anomalies x_a describing fluctuations around the seasonal cycle (e.g., Oliver et al., 2021)

$$x(t) = x_s(t) + x_a(t). \quad (2.1)$$

The seasonal anomalies have zero mean since they describe deviations from the mean seasonal cycle. When extremes are defined with respect to anomaly percentile or seasonally varying percentile thresholds, intensity and duration of extremes in x are not influenced by the seasonal component x_s . Instead these are solely determined by the seasonal anomalies x_a . Event intensity quantifies by how much an anomaly percentile or a percentile for a calendar day or month is exceeded during the events. It is driven by the variance in the anomalies σ_a^2 . Assuming

a probability density function f for the seasonal anomalies, the average exceedance of the percentile threshold⁴ is given by the conditional expectation value for x_a given it is larger than the percentile x_p ,

$$\frac{1}{P(x_a \geq x_p)} \int_{x_p}^{\infty} dx (x_a - x_p) f(x_a; \sigma_a^2). \quad (2.2)$$

The larger the anomaly variance σ_a^2 , the larger is the statistical weight $f(x_a)$ of large exceedances $x_a - x_p$ and the larger is event intensity.

Event duration depends on the memory within the seasonal anomalies. The stronger the dependence between subsequent values in the seasonal anomalies, the longer lasts a positive anomaly and the larger is the event duration. This can be conceptualized by representing the time series by an autoregressive model (Shumway & Stoffer, 2011; Oliver et al., 2021). For the autoregressive model with lag one, two subsequent values in the time series are connected according to

$$x_a(t+1) = \phi_1 x_a(t) + \varepsilon(t), \quad (2.3)$$

with the parameter ϕ_1 being the lag-one autocorrelation and satisfying $|\phi_1| < 1$, and $\varepsilon(t)$ independent (white) noise. ϕ_1 represents the memory in the climate system. Time series in climate variables will in most cases exhibit positive autocorrelation, because processes that change the variables often evolve on timescales that are long compared to the temporal resolution of the data. The larger the autocorrelation is, the larger is the contribution from variations on long, for example interannual, time scales compared to shorter, for example sub-seasonal, timescales, and the longer is the duration of extreme events. Lag-one autocorrelation in a climate time series, like event duration, also depends on the temporal resolution of the data, with larger autocorrelation expected in data with higher temporal resolution. For example, the lag-one autocorrelation coefficient estimated for surface $[H^+]$ seasonal anomalies within a preindustrial simulation by the ESM2M model is globally 0.99 for daily-mean and 0.70 for monthly-mean data.

When defining extremes based on fixed percentile thresholds, also the seasonal component influences event intensity and duration: Event intensity increases with seasonal variability. Event duration increases with seasonality where the variations in seasonal anomalies are mainly on sub-seasonal timescales while it decreases where anomaly variations are mainly on interannual timescales. The frequency of extreme events is fixed by the choice of percentile threshold during the reference period where percentiles are defined. However, frequency may change under a changing climate.

Extreme event metrics in a changing climate

The frequency of extreme events and extreme event characteristics in many oceanographic variables undergo changes with climate change. Frequency and event characteristics may change due to trends in the variables' mean state, changes in seasonal amplitude, and due to changes in variability of the anomalies. Mean trends influence event occurrence and characteristics when extremes are referenced to a fixed baseline. In contrast, event occurrence and characteristics are not altered by mean trends when referenced to a shifting-mean baseline (see Sect. 2.3.1). Changes in seasonal amplitude and variability of the anomalies are of particular importance for extremes in carbonate system variables, where such changes are expected due to the nonlinearity of the oceans' carbonate chemistry. The nonlinearity of the ocean carbonate system

⁴Average threshold exceedance is identical to mean intensity when there is no dependence between intensity and duration of events. Often, longer events tend to be more intense. In this case, average threshold exceedance is larger than mean intensity that gives more weight to short events by first averaging over each individual event before averaging over all events.

is, for example, apparent from changes in Revelle Factor or buffer capacity (Revelle & Suess, 1957). The impact of seasonal and nonseasonal variability changes on extremes in carbonate chemistry is a particular focus of Chapter 3. Event duration may also change due to a shift in the relative contributions from low and high frequency variations to the variability in the seasonal anomalies. Finally, also changes in the higher moments of the anomaly distribution and changes in the phasing or shape of the seasonal cycle may impose changes in extreme event metrics.

Compound events in two variables

Compound extreme events are extremes where two or more variables are above their respective thresholds at the same time (Seneviratne et al., 2012; Leonard et al., 2014; Zscheischler et al., 2018). Such compound extremes are a particular concern because the combined impact from multiple stressors on ecological and human systems may exceed that of the individual stressors due to synergistic interactions (Boyd & Brown, 2015). Compound extreme events in sea surface temperature and $[\text{H}^+]$ are analyzed in Chapter 4. While the frequency of univariate extremes in the two variables is fixed by the percentile choice during the reference period, the frequency of compound events varies due to the varying statistical dependence between the two variables. If the two variables tend to co-vary with each other, then extremes in both variables also tend to occur together. In contrast, compound extremes are rare if a positive anomaly in one of the variables is usually accompanied by a negative anomaly in the other one. The occurrence probability of compound events is quantified by the likelihood multiplication factor (LMF; Zscheischler & Seneviratne, 2017). It is the ratio between the observed compound event likelihood and the one that would be observed if the two variables were independent, given by the product of the likelihoods of the univariate extremes $P(x_1 > x_{p_1}) \cdot P(x_2 > x_{p_2})$. One measure for the dependence between two variables is the Pearson correlation coefficient. The LMF for compound events observed in a data set can be estimated based on the sample Pearson correlation coefficient r (Methods section in Chapter 4).

In transient time series, the likelihood of compound events can change because of changes in the likelihood of univariate extremes in the two variables, arising due to trends in the variables and changes in variability. Furthermore, compound event occurrence can also change due to changes in the dependence between the two variables.

References

- Adcroft, A. & Campin, J.-M., 2004. Rescaled height coordinates for accurate representation of free-surface flows in ocean circulation models, *Ocean Modelling*, 7(3), 269–284.
- Anderson, J. L., Balaji, V., Broccoli, A. J., Cooke, W. F., Delworth, T. L., Dixon, K. W., Donner, L. J., Dunne, K. A., Freidenreich, S. M., Garner, S. T., Gudgel, R. G., Gordon, C. T., Held, I. M., Hemler, R. S., Horowitz, L. W., Klein, S. A., Knutson, T. R., Kushner, P. J., Langenhost, A. R., Cheung, L. N., Liang, Z., Malyshev, S. L., Milly, P. C. D., Nath, M. J., Ploshay, J. J., Ramaswamy, V., Schwarzkopf, M. D., Shevliakova, E., Sirutis, J. J., Soden, B. J., Stern, W. F., Thompson, L. A., Wilson, R. J., Wittenberg, A. T., & Wyman, B. L., 2004. The new GFDL global atmosphere and land model AM2-LM2: Evaluation with prescribed SST simulations, *Journal of Climate*, 17(24), 4641–4673.
- Antonov, J. I., Locarnini, R. A., Boyer, T. P., Mishonov, A. V., & Garcia, H. E., 2006. World ocean atlas 2005, volume 2: Salinity, *NOAA Atlas NESDIS 62*, U.S. Government Printing Office, Washington, D.C., p. 182 pp.
- Bednaršek, N., Tarling, G. A., Bakker, D. C. E., Fielding, S., Jones, E. M., Venables, H. J., Ward, P., Kuzirian, A., Lézé, B., Feely, R. A., & Murphy, E. J., 2012. Extensive dissolution of live pteropods in the southern ocean, *Nature Geoscience*, 5, 881–885.
- Bopp, L., Resplandy, L., Orr, J. C., Doney, S. C., Dunne, J. P., Gehlen, M., Halloran, P., Heinze, C., Ilyina, T., Séférian, R., Tjiputra, J., & Vichi, M., 2013. Multiple stressors of ocean ecosystems in the 21st century: projections with CMIP5 models, *Biogeosciences*, 10(10).
- Boyd, P. W. & Brown, C. J., 2015. Modes of interactions between environmental drivers and marine biota, *Frontiers in Marine Science*, 2, 9.
- Bronselaer, B., Winton, M., Russell, J., Sabine, C. L., & Khatiwala, S., 2017. Agreement of CMIP5 simulated and observed ocean anthropogenic CO₂ uptake, *Geophysical Research Letters*, 44(24), 12,298–12,305.
- Cionni, I., Eyring, V., Lamarque, J. F., Randel, W. J., Stevenson, D. S., Wu, F., Bodeker, G. E., Shepherd, T. G., Shindell, D. T., & Waugh, D. W., 2011. Ozone database in support of CMIP5 simulations: results and corresponding radiative forcing, *Atmospheric Chemistry and Physics*, 11(21), 11267–11292.
- Clarke, T. M., Wabnitz, C. C., Striegel, S., Frölicher, T. L., Reygondeau, G., & Cheung, W. W., 2021. Aerobic growth index (AGI): An index to understand the impacts of ocean warming and deoxygenation on global marine fisheries resources, *Progress in Oceanography*, 195, 102588.
- Coles, S., 2001. *An Introduction to Statistical Modeling of Extreme Values*, Springer-Verlag London.
- Delworth, T. L., Broccoli, A. J., Rosati, A., Stouffer, R. J., Balaji, V., Beesley, J. A., Cooke, W. F., Dixon, K. W., Dunne, J., Dunne, K. A., Durachta, J. W., Findell, K. L., Ginoux, P., Gnanadesikan, A., Gordon, C. T., Griffies, S. M., Gudgel, R., Harrison, M. J., Held, I. M., Hemler, R. S., Horowitz, L. W., Klein, S. A., Knutson, T. R., Kushner, P. J., Langenhorst, A. R., Lee, H., Lin, S., Lu, J., Malyshev, S. L., Milly, P. C. D., Ramaswamy, V., Russell, J., Schwarzkopf, M. D., Shevliakova, E., Sirutis, J. J., Spelman, M. J., Stern, W. F., Winton, M., Wittenberg, A. T., Wyman, B., Zeng, F., & Zhang, R., 2006. GFDL’s CM2 Global Coupled Climate Models. Part I: Formulation and Simulation Characteristics, *Journal of Climate*, 19(5), 643–674.
- Dickson, A. & Millero, F., 1987. A comparison of the equilibrium constants for the dissociation of carbonic acid in seawater media, *Deep Sea Research Part A. Oceanographic Research Papers*, 34(10), 1733 – 1743.
- Dunne, J. P., John, J. G., Adcroft, A. J., Griffies, S. M., Hallberg, R. W., Shevliakova, E., Stouffer, R. J., Cooke, W., Dunne, K. A., Harrison, M. J., Krasting, J. P., Malyshev, S. L., Milly, P. C. D., Philipps, P. J., Sentman, L. T., Samuels, B. L., Spelman, M. J., Winton, M., Wittenberg, A. T., & Zadeh, N., 2012. GFDL’s ESM2 global coupled climate–carbon earth system models. Part I: Physical formulation and baseline simulation characteristics, *Journal of Climate*, 25(19), 6646–6665.
- Dunne, J. P., John, J. G., Shevliakova, E., Stouffer, R. J., Krasting, J. P., Malyshev, S. L., Milly, P. C. D., Sentman, L. T., Adcroft, A. J., Cooke, W., Dunne, K. A., Griffies, S. M., Hallberg, R. W., Harrison, M. J., Levy, H., Wittenberg, A. T., Phillips, P. J., & Zadeh, N., 2013. GFDL’s ESM2 global coupled climate–carbon earth system models. Part II: Carbon system formulation and baseline simulation characteristics, *Journal of Climate*, 26(7), 2247–2267.
- Eppey, R. W., 1972. Temperature and phytoplankton growth in the sea, *Fish. Bull.*, 70, 41063–41085.
- Fox-Kemper, B., Ferrari, R., & Hallberg, R., 2008. Parameterization of Mixed Layer Eddies. Part I: Theory and Diagnosis, *Journal of Physical Oceanography*, 38(6), 1145–1165.

- Frölicher, T. L., Fischer, E. M., & Gruber, N., 2018. Marine heatwaves under global warming, *Nature*, 560(7718), 360–364.
- Frölicher, T. L., Ramseyer, L., Raible, C. C., Rodgers, K. B., & Dunne, J., 2020. Potential predictability of marine ecosystem drivers, *Biogeosciences*, 17(7), 2061–2083.
- Griffies, S., 2009. Elements of MOM4p1, GFDL ocean group technical report no.6, NOAA/Geophysical Fluid Dynamics Laboratory, Princeton University Forrestal Campus, 201 Forrestal Road, Princeton, NJ 08540-6649.
- Griffies, S. M., 1998. The Gent–McWilliams Skew Flux, *Journal of Physical Oceanography*, 28(6), 831–841.
- Hobday, A. J., Alexander, L. V., Perkins, S. E., Smale, D. A., Straub, S. C., Oliver, E. C., Benthuisen, J. A., Burrows, M. T., Donat, M. G., Feng, M., Holbrook, N. J., Moore, P. J., Scannell, H. A., Sen Gupta, A., & Wernberg, T., 2016. A hierarchical approach to defining marine heatwaves, *Progress in Oceanography*, 141, 227–238.
- Hobday, A. J., Oliver, E. C., Sen Gupta, A., Benthuisen, J. A., Burrows, M. T., Donat, M. G., Holbrook, N. J., Moore, P. J., Thomsen, M. S., Wernberg, T., & Smale, D. A., 2018. Categorizing and naming marine heatwaves, *Oceanography*, 31(2), 162–173.
- Hofmann, G. E., Smith, J. E., Johnson, K. S., Send, U., Levin, L. A., Micheli, F., Paytan, A., Price, N. N., Peterson, B., Takeshita, Y., Matson, P. G., Crook, E. D., Kroeker, K. J., Gambi, M. C., Rivest, E. B., Frieder, C. A., Yu, P. C., & Martz, T. R., 2011. High-frequency dynamics of ocean pH: A multi-ecosystem comparison, *PloS One*, 6(12), 1–11.
- Hurtt, G. C., Froking, S., Fearon, M. G., Moore, B., Shevliakova, E., Malyshev, S., Pacala, S. W., & Houghton, R. A., 2006. The underpinnings of land-use history: three centuries of global gridded land-use transitions, wood-harvest activity, and resulting secondary lands, *Global Change Biology*, 12(7), 1208–1229.
- Jacox, M. G., 2019. Marine heatwaves in a changing climate, *Nature*, 571, 485 – 487.
- Klausmeier, C. A., Litchman, E., Daufresne, T., & Levin, S. A., 2004. Optimal nitrogen-to-phosphorus stoichiometry of phytoplankton, *Nature*, 429(6988), 171–174.
- Kwiatkowski, L. & Orr, J. C., 2018. Diverging seasonal extremes for ocean acidification during the twenty-first century, *Nature Climate Change*, 8(2), 141–145.
- Large, W. G., McWilliams, J. C., & Doney, S. C., 1994. Oceanic vertical mixing: A review and a model with a nonlocal boundary layer parameterization, *Reviews of Geophysics*, 32(4), 363–403.
- Laufkötter, C., Vogt, M., Gruber, N., Aita-Noguchi, M., Aumont, O., Bopp, L., Buitenhuis, E., Doney, S. C., Dunne, J., Hashioka, T., Hauck, J., Hirata, T., John, J., Le Quééré, C., Lima, I. D., Nakano, H., Seferian, R., Totterdell, I., Vichi, M., & Völker, C., 2015. Drivers and uncertainties of future global marine primary production in marine ecosystem models, *Biogeosciences*, 12(23), 6955–6984.
- Laufkötter, C., Zscheischler, J., & Frölicher, T. L., 2020. High-impact marine heatwaves attributable to human-induced global warming, *Science*, 369(6511), 1621–1625.
- Le Grix, N., Zscheischler, J., Laufkötter, C., Rousseaux, C. S., & Frölicher, T. L., 2021. Compound high-temperature and low-chlorophyll extremes in the ocean over the satellite period, *Biogeosciences*, 18(6), 2119–2137.
- Lean, J. L., 2009. Calculations of solar irradiance: Monthly means from 1882 to 2008, annual means from 1610 to 2008, https://solarisheppa.geomar.de/solarisheppa/sites/default/files/data/Calculations_of_Solar_Irradiance.pdf.
- Lee, H.-C., Rosati, A., & Spelman, M. J., 2006. Barotropic tidal mixing effects in a coupled climate model: Oceanic conditions in the northern atlantic, *Ocean Modelling*, 11(3), 464–477.
- Leonard, M., Westra, S., Phatak, A., Lambert, M., van den Hurk, B., McInnes, K., Risbey, J., Schuster, S., Jakob, D., & Stafford-Smith, M., 2014. A compound event framework for understanding extreme impacts, *WIREs Climate Change*, 5(1), 113–128.
- Locarnini, R. A., Mishonov, A. V., Antonov, J. I., Boyer, T. P., & Garcia, H. E., 2006. World ocean atlas 2005, volume 1: Temperature, *NOAA Atlas NESDIS 61, U.S. Government Printing Office, Washington, D.C.*, p. 182 pp.
- Lorenz, E. N., 1963. Deterministic nonperiodic flow, *Journal of the Atmospheric Sciences*, 20(2), 130 – 141.

- Marshall, J., Hill, C., Perelman, L., & Adcroft, A., 1997. Hydrostatic, quasi-hydrostatic, and nonhydrostatic ocean modeling, *Journal of Geophysical Research: Oceans*, 102(C3), 5733–5752.
- Martin, T. & Adcroft, A., 2010. Parameterizing the fresh-water flux from land ice to ocean with interactive icebergs in a coupled climate model, *Ocean Modelling*, 34(3), 111–124.
- Masson-Delmotte, V., Zhai, P., Pirani, A., Connors, S. L., Péan, C., Berger, S., Caud, N., Chen, Y., Goldfarb, L., Gomis, M. I., Huang, M., Leitzell, K., Lonnoy, E., Matthews, J., Maycock, T. K., Waterfield, T., Yelekçi, O., Yu, R., & Zhou, B., 2021. IPCC, 2021: Summary for policymakers, *Climate Change 2021: The Physical Science Basis. Contribution of Working Group I to the Sixth Assessment Report of the Intergovernmental Panel on Climate Change*.
- Meehl, G. A., Senior, C. A., Eyring, V., Flato, G., Lamarque, J.-F., Stouffer, R. J., Taylor, K. E., & Schlund, M., 2020. Context for interpreting equilibrium climate sensitivity and transient climate response from the CMIP6 Earth system models, *Science Advances*, 6(26).
- Mehrbach, C., Culbertson, C. H., Hawley, J. E., & Pytkowicz, R. M., 1973. Measurement of the apparent dissociation constants of carbonic acid in seawater at atmospheric pressure 1, *Limnology and Oceanography*, 18(6), 897–907.
- Meinshausen, M., Smith, S. J., Calvin, K., Daniel, J. S., Kainuma, M. L. T., Lamarque, J.-F., Matsumoto, K., Montzka, S. A., Raper, S. C. B., Riahi, K., Thomson, A., Velders, G. J. M., & van Vuuren, D. P. P., 2011. The rcp greenhouse gas concentrations and their extensions from 1765 to 2300, *Climatic Change*, 109(1), 213.
- Morse, J. & Mackenzie, F., 1990. *Geochemistry of Sedimentary Carbonates*, Elsevier, Amsterdam.
- Murray, R. J., 1996. Explicit generation of orthogonal grids for ocean models, *Journal of Computational Physics*, 126(2), 251–273.
- Najjar, R. & Orr, J., 1998. Design of OCMIP-2 simulations of chlorofluorocarbons, the solubility pump and common biogeochemistry, internal OCMIP report, LSCE/CEA Saclay, Gif-sur-Yvette, France.
- Oka, A., 2020. Ocean carbon pump decomposition and its application to CMIP5 earth system model simulations, *Progress in Earth and Planetary Science*, 7(1), 25.
- Oliver, E. C., Benthuyzen, J. A., Darmaraki, S., Donat, M. G., Hobday, A. J., Holbrook, N. J., Schlegel, R. W., & Sen Gupta, A., 2021. Marine heatwaves, *Annual Review of Marine Science*, 13(1), 313–342.
- Oliver, E. C. J., Donat, M. G., Burrows, M. T., Moore, P. J., Smale, D. A., Alexander, L. V., Benthuyzen, J. A., Feng, M., Sen Gupta, A., Hobday, A. J., Holbrook, N. J., Perkins-Kirkpatrick, S. E., Scannell, H. A., Straub, S. C., & Wernberg, T., 2018. Longer and more frequent marine heatwaves over the past century, *Nature Communications*, 9(1), 1324.
- Oliver, E. C. J., Burrows, M. T., Donat, M. G., Sen Gupta, A., Alexander, L. V., Perkins-Kirkpatrick, S. E., Benthuyzen, J. A., Hobday, A. J., Holbrook, N. J., Moore, P. J., Thomsen, M. S., Wernberg, T., & Smale, D. A., 2019. Projected marine heatwaves in the 21st century and the potential for ecological impact, *Frontiers in Marine Science*, 6, 734.
- Palter, J. B., Frölicher, T. L., Paynter, D., & John, J. G., 2018. Climate, ocean circulation, and sea level changes under stabilization and overshoot pathways to 1.5 K warming, *Earth System Dynamics*, 9(2), 817–828.
- Paynter, D., Frölicher, T. L., Horowitz, L. W., & Silvers, L. G., 2018. Equilibrium climate sensitivity obtained from multimillennial runs of two gfdl climate models, *Journal of geophysical research. Atmospheres*, 123(4), 1921–1941.
- Resplandy, L., Bopp, L., Orr, J. C., & Dunne, J. P., 2013. Role of mode and intermediate waters in future ocean acidification: Analysis of CMIP5 models, *Geophysical Research Letters*, 40(12), 3091–3095.
- Revelle, R. & Suess, H. E., 1957. Carbon dioxide exchange between atmosphere and ocean and the question of an increase of atmospheric CO₂ during the past decades, *Tellus*, 9(1), 18–27.
- Riahi, K., Rao, S., Krey, V., Cho, C., Chirkov, V., Fischer, G., Kindermann, G., Nakicenovic, N., & Rafaj, P., 2011. RCP8.5 — a scenario of comparatively high greenhouse gas emissions, *Climatic Change*, 109(1), 33.
- Sato, M., Hansen, J. E., McCormick, M. P., & Pollack, J. B., 1993. Stratospheric aerosol optical depths, 1850–1990, *Journal of geophysical research. Atmospheres*, 98(D12), 22987–22994.

- Seneviratne, S., Nicholls, N., Easterling, D., Goodess, C., Kanae, S., Kossin, J., Luo, Y., Marengo, J., McInnes, K., Rahimi, M., Reichstein, M., Sorteberg, A., Vera, C., & Zhang, X., 2012. Changes in climate extremes and their impacts on the natural physical environment, *Managing the Risks of Extreme Events and Disasters to Advance Climate Change Adaptation. A Special Report of Working Groups I and II of the Intergovernmental Panel on Climate Change (IPCC)*.
- Sentman, L. T., Shevliakova, E., Stouffer, R. J., & Malyshev, S., 2011. Time scales of terrestrial carbon response related to land-use application: Implications for initializing an earth system model, *Earth Interactions*, 15(30), 1–16.
- Sherwood, S. C., Webb, M. J., Annan, J. D., Armour, K. C., Forster, P. M., Hargreaves, J. C., Hegerl, G., Klein, S. A., Marvel, K. D., Rohling, E. J., Watanabe, M., Andrews, T., Braconnot, P., Bretherton, C. S., Foster, G. L., Hausfather, Z., von der Heydt, A. S., Knutti, R., Mauritsen, T., Norris, J. R., Proistosescu, C., Rugenstein, M., Schmidt, G. A., Tokarska, K. B., & Zelinka, M. D., 2020. An assessment of earth's climate sensitivity using multiple lines of evidence, *Reviews of Geophysics*, 58(4), e2019RG000678.
- Shevliakova, E., Pacala, S. W., Malyshev, S., Hurtt, G. C., Milly, P. C. D., Caspersen, J. P., Sentman, L. T., Fisk, J. P., Wirth, C., & Crevoisier, C., 2009. Carbon cycling under 300 years of land use change: Importance of the secondary vegetation sink, *Global Biogeochemical Cycles*, 23(2), 1–16.
- Shumway, R. H. & Stoffer, D. S., 2011. *Time Series Analysis and Its Applications*, Springer New York Dordrecht Heidelberg London, 3rd edn.
- Simmons, H. L., Jayne, S. R., Laurent, L. C., & Weaver, A. J., 2004. Tidally driven mixing in a numerical model of the ocean general circulation, *Ocean Modelling*, 6(3), 245–263.
- Stenchikov, G. L., Kirchner, I., Robock, A., Graf, H.-F., Antuña, J. C., Grainger, R. G., Lambert, A., & Thomason, L., 1998. Radiative forcing from the 1991 mount pinatubo volcanic eruption, *Journal of geophysical research. Atmospheres*, 103(D12), 13837–13857.
- Stramma, L., Johnson, G. C., Sprintall, J., & Mohrholz, V., 2008. Expanding oxygen-minimum zones in the tropical oceans, *Science*, 320(5876), 655–658.
- Taylor, K. E., Stouffer, R. J., & Meehl, G. A., 2012. An overview of CMIP5 and the experiment design, *Bulletin of the American Meteorological Society*, 93(4), 485–498.
- Torres, O., Kwiatkowski, L., Sutton, A. J., Dorey, N., & Orr, J. C., 2021. Characterizing mean and extreme diurnal variability of ocean CO₂ system variables across marine environments, *Geophysical Research Letters*, 48(5), e2020GL090228.
- van Vuuren, D. P., Edmonds, J., Kainuma, M., Riahi, K., Thomson, A., Hibbard, K., Hurtt, G. C., Kram, T., Krey, V., Lamarque, J.-F., Masui, T., Meinshausen, M., Nakicenovic, N., Smith, S. J., & Rose, S. K., 2011a. The representative concentration pathways: an overview, *Climatic Change*, 109(1), 5.
- van Vuuren, D. P., Stehfest, E., den Elzen, M. G. J., Kram, T., van Vliet, J., Deetman, S., Isaac, M., Klein Goldewijk, K., Hof, A., Mendoza Beltran, A., Oostenrijk, R., & van Ruijven, B., 2011b. RCP2.6: exploring the possibility to keep global mean temperature increase below 2°C, *Climatic Change*, 109(1), 95.
- Vaquer-Sunyer, R. & Duarte, C. M., 2008. Thresholds of hypoxia for marine biodiversity, *Proceedings of the National Academy of Sciences of the United States of America*, 105(40), 15452–15457.
- Vogt, L., Burger, F. A., & Frölicher, T. L., in preperation. Marine heatwave drivers in an earth system model, *Geophysical Research Letters*.
- Wanninkhof, R., 1992. Relationship between wind speed and gas exchange over the ocean, *Journal of Geophysical Research: Oceans*, 97(C5), 7373–7382.
- Weiss, R., 1974. Carbon dioxide in water and seawater: the solubility of a non-ideal gas, *Marine Chemistry*, 2(3), 203 – 215.
- Winton, M., 2000. A reformulated three-layer sea ice model, *Journal of Atmospheric and Oceanic Technology*, 17(4), 525–531.
- Wittenberg, A. T., Rosati, A., Delworth, T. L., Vecchi, G. A., & Zeng, F., 2014. ENSO modulation: Is it decadal predictability?, *Journal of Climate*, 27(7), 2667–2681.

- Zscheischler, J. & Seneviratne, S. I., 2017. Dependence of drivers affects risks associated with compound events, *Sci. Adv.*, 3(6).
- Zscheischler, J., Reichenstein, M., von Buttlar, J., Mu, M., Randerson, J. T., & Mahecha, M. D., 2014. Carbon cycle extremes during the 21st century in CMIP5 models: Future evolution and attribution to climatic drivers, *Geophysical Research Letters*, 41(24), 8853–8861.
- Zscheischler, J., Westra, S., van den Hurk, B. J. J. M., Seneviratne, S. I., Ward, P. J., Pitman, A., AghaKouchak, A., Bresch, D. N., Leonard, M., Wahl, T., & Zhang, X., 2018. Future climate risk from compound events, *Nature Climate Change*, 8(6), 469–477.

Chapter 3

Increase in ocean acidity variability and extremes under increasing atmospheric CO₂

Friedrich A. Burger, Jasmin G. John, and Thomas L. Frölicher

Published in *Biogeosciences*, Volume 17, 4633–4662, 2020.

Biogeosciences, 17, 4633–4662, 2020
<https://doi.org/10.5194/bg-17-4633-2020>
 © Author(s) 2020. This work is distributed under
 the Creative Commons Attribution 4.0 License.



Increase in ocean acidity variability and extremes under increasing atmospheric CO₂

Friedrich A. Burger^{1,2}, Jasmin G. John³, and Thomas L. Frölicher^{1,2}

¹Climate and Environmental Physics, Physics Institute, University of Bern, Bern, Switzerland

²Oeschger Centre for Climate Change Research, University of Bern, Bern, Switzerland

³NOAA/Geophysical Fluid Dynamics Laboratory, Princeton, NJ, USA

Correspondence: Friedrich A. Burger (friedrich.burger@climate.unibe.ch)

Received: 22 January 2020 – Discussion started: 27 January 2020

Revised: 14 July 2020 – Accepted: 6 August 2020 – Published: 25 September 2020

Abstract. Ocean acidity extreme events are short-term periods of relatively high [H⁺] concentrations. The uptake of anthropogenic CO₂ emissions by the ocean is expected to lead to more frequent and intense ocean acidity extreme events, not only due to changes in the long-term mean but also due to changes in short-term variability. Here, we use daily mean output from a five-member ensemble simulation of a comprehensive Earth system model under low- and high-CO₂-emission scenarios to quantify historical and future changes in ocean acidity extreme events. When defining extremes relative to a fixed preindustrial baseline, the projected increase in mean [H⁺] causes the entire surface ocean to reach a near-permanent acidity extreme state by 2030 under both the low- and high-CO₂-emission scenarios. When defining extremes relative to a shifting baseline (i.e., neglecting the changes in mean [H⁺]), ocean acidity extremes are also projected to increase because of the simulated increase in [H⁺] variability; e.g., the number of days with extremely high surface [H⁺] conditions is projected to increase by a factor of 14 by the end of the 21st century under the high-CO₂-emission scenario relative to preindustrial levels. Furthermore, the duration of individual extreme events is projected to triple, and the maximal intensity and the volume extent in the upper 200 m are projected to quintuple. Similar changes are projected in the thermocline. Under the low-emission scenario, the increases in ocean acidity extreme-event characteristics are substantially reduced. At the surface, the increases in [H⁺] variability are mainly driven by increases in [H⁺] seasonality, whereas changes in thermocline [H⁺] variability are more influenced by interannual variability. Increases in [H⁺] variability arise predominantly from increases in the sensi-

tivity of [H⁺] to variations in its drivers (i.e., carbon, alkalinity, and temperature) due to the increase in oceanic anthropogenic carbon. The projected increase in [H⁺] variability and extremes may enhance the risk of detrimental impacts on marine organisms, especially for those that are adapted to a more stable environment.

1 Introduction

Since the beginning of the industrial revolution, the ocean has absorbed about a quarter of the carbon dioxide (CO₂) released by human activities through burning fossil fuel and altering land use (Friedlingstein et al., 2019). Oceanic uptake of anthropogenic CO₂ slows global warming by reducing atmospheric CO₂ but also leads to major changes in the chemical composition of seawater through acidification (Gattuso and Buddemeier, 2000; Caldeira and Wickett, 2003; Orr et al., 2005; Doney et al., 2009). When CO₂ dissolves in seawater, it forms carbonic acid that dissociates into bicarbonate ([HCO₃[−]]), releasing hydrogen ions ([H⁺]) and thereby reducing pH ($\text{pH} = -\log([\text{H}^+])$). The rise in [H⁺] is partially buffered by the conversion of carbonate ions ([CO₃^{2−}]) to [HCO₃[−]]. The associated decline in [CO₃^{2−}] reduces the calcium carbonate saturation state $\Omega = [\text{Ca}^{2+}][\text{CO}_3^{2-}]/([\text{Ca}^{2+}][\text{CO}_3^{2-}]_{\text{sat}})$, i.e., the product of calcium and carbonate ion concentrations relative to the product at saturation. Undersaturated waters with $\Omega < 1$ are corrosive for calcium carbonate minerals. Each type of calcium carbonate mineral has its individual saturation state Ω due to different solubilities, e.g., Ω_{C} for calcite and Ω_{A} for arag-

onite. Over the last four decades the surface ocean pH has declined by about 0.02 pH units per decade (Bindoff et al., 2020). Continued CO₂ uptake by the ocean will further exacerbate ocean acidification in the near future (Caldeira and Wickett, 2003; Orr et al., 2005; Bindoff et al., 2020; Terhaar et al., 2020), with potentially major consequences for marine life (Doney et al., 2009) and ocean biogeochemical cycling (Gehlen et al., 2012).

Superimposed onto the long-term decadal- to centennial-scale ocean acidification trend are short-term extreme events on daily to monthly timescales during which ocean pH and Ω are much lower than usual (Hofmann et al., 2011; Joint et al., 2011; Hauri et al., 2013). These events can be driven by different processes, such as ocean mixing, biological production and remineralization, mineral dissolution, temperature and air–sea gas exchange variations, or a combination thereof (Lauvset et al., 2020). In eastern boundary upwelling systems, for example, short-term upwelling events and mesoscale processes can lead to low-surface-pH events and to short-term shoaling of the saturation horizon (i.e., the depth between the supersaturated upper ocean and the undersaturated deep ocean; Feely et al., 2008; Leinweber and Gruber, 2013). Ocean pH can also rapidly change as a consequence of microbial activity (Joint et al., 2011). Phytoplankton blooms and accompanying respiration drastically increase the partial pressure of CO₂ ($p\text{CO}_2$) and reduce pH in the thermocline (Sarmiento and Gruber, 2006). Such extreme events may have pH levels that are much lower than the mean pH conditions projected for the near future (Hofmann et al., 2011).

Most of the scientific literature on ocean acidification has focused on gradual changes in the mean state in ocean chemistry (Orr et al., 2005; Bopp et al., 2013; Frölicher et al., 2016; Terhaar et al., 2019b). However, to understand the full consequences of ocean acidification on marine organisms and ecosystem services, it is also necessary to understand how variability and extremes in ocean acidity change under increasing atmospheric CO₂ (Kroeker et al., 2020). The ability of marine organisms and ecosystems to adapt to ocean acidification may depend on whether the species have evolved in a chemically stable or a highly variable environment (Rivest et al., 2017; Cornwall et al., 2020). Furthermore, if the frequency and intensity of short-term extreme events strongly increase, in addition to the long-term acidification, some organisms may have difficulties in adapting, especially if key CO₂ system variables cross some critical thresholds, e.g., from calcium carbonate supersaturation to undersaturation. Key plankton species such as coccolithophores (Riebesell et al., 2000), foraminifera, and pteropods (Bednaršek et al., 2012) were found to be adversely affected by low carbonate ion concentrations. After only several days of being exposed to waters which are undersaturated with respect to aragonite, some species such as pteropods already show reduced calcification, growth, and survival rates (Kroeker et al., 2013; Bednaršek et al., 2014).

Carbonate system variability also plays a role in shaping the diversity and biomass of benthic communities (Hall-Spencer et al., 2008; Kroeker et al., 2011). In laboratory experiments in which deep-water corals are exposed to low-pH waters for a week, some corals exhibit reduced calcification, while recovery may be possible when the low-pH condition persists for several months, stressing the importance of high-frequency variability and short-term acidification events (Form and Riebesell, 2012). There is also growing evidence that the organism response to variability in ocean acidity could change with ocean acidification (Britton et al., 2016). Therefore, understanding the temporal variability of ocean carbonate chemistry and how that will change is important for understanding the impacts of ocean acidification on marine organisms and ecosystems (Hofmann et al., 2011).

Changes in extremes can arise from changes in the mean, variability, or shape of the probability distribution (Coles, 2001). There exists no general accepted definition of an extreme event beyond the common understanding that an extreme is rare (Weyer, 2019). As a result, many different approaches exist to define extreme events (Smith, 2011). If a relative threshold (e.g., quantile) is used to define an extreme event, it is important to distinguish between extreme events that are defined with respect to a fixed reference period or baseline, or if the reference period or baseline moves with time. If the baseline is fixed, the changes in the mean state as well as changes in variability and higher moments of the distribution contribute to changes in extreme events (e.g., Fischer and Knutti, 2015; Frölicher et al., 2018; Oliver et al., 2018). However, if a shifting baseline is used, changes in the mean state do not contribute to changes in extreme events (e.g., Stephenson, 2008; Seneviratne et al., 2012; Zscheischler and Seneviratne, 2017; Cheung and Frölicher, 2020; Vogel et al., 2020). In this case, changes in extremes arise solely due to changes in variability and higher moments of the distribution (Oliver et al., 2019). This latter definition ensures that values are not considered extreme solely because the baseline changes under climate change (Jacox, 2019; Oliver et al., 2019). Whether extreme events should be defined with respect to a fixed baseline or with respect to a shifting baseline depends on the scientific question. For example, the shifting-baseline approach may be more appropriate when the ecosystems under consideration are likely able to adapt to the mean changes but not to changes in variability (Seneviratne et al., 2012; Oliver et al., 2019). Here, we use both approaches, with a special focus on the analysis of ocean acidity extremes with respect to shifting baselines.

Under continued long-term ocean acidification (i.e., changes in the mean), one can expect that extreme events in $[\text{H}^+]$ and Ω , when defined with respect to a fixed reference period or baseline, will become more frequent and intense (Hauri et al., 2013). In addition to the changes in the mean, recent studies suggest that the seasonal cycles in $[\text{H}^+]$ and Ω are also strongly modulated under elevated atmospheric CO₂. Higher background concentrations of dissolved inor-

ganic carbon and warmer temperatures produce stronger departures from mean state values for a given change in pertinent physical or chemical drivers for $[H^+]$ and weaker departures for Ω (Kwiatkowski and Orr, 2018; Fassbender et al., 2018). Other studies have also addressed the changes in the seasonal cycle of pCO_2 (Landschützer et al., 2018; Gallego et al., 2018; McNeil and Sasse, 2016; Rodgers et al., 2008; Hauck and Völker, 2015). Over the 21st century and under a high-greenhouse-gas-emission scenario, Earth system model simulations project that the seasonal amplitude in surface $[H^+]$ will increase by 81 %, whereas the seasonal amplitude for aragonite saturation state (Ω_A) is projected to decrease by 9 % globally on average (Kwiatkowski and Orr, 2018). Recent observation-based estimates as well as theoretical arguments support these projected increases in seasonality for $[H^+]$ and pCO_2 (Landschützer et al., 2018; Fassbender et al., 2018). Thus, when extremes are defined with respect to a shifting baseline (i.e., mean state changes are neglected), the frequency and intensity of extreme $[H^+]$ events will likely increase due to increases in variability.

Unlike for marine heatwaves (Frölicher et al., 2018; Collins et al., 2020) and extreme sea level events (Oppenheimer et al., 2020), little is known about the characteristics and changes of extreme ocean acidity events and, if so, only on seasonal timescales (Kwiatkowski and Orr, 2018). A global view of how extreme events in ocean chemistry will unfold in time and space and a mechanistic understanding of the relevant processes is missing. This knowledge gap is of particular concern as it is expected that extreme events in ocean acidity, defined with respect to both a fixed and a shifting baseline, are likely to become more frequent and intense under increasing atmospheric CO_2 . Given the potential for profound impacts on marine ecosystems, quantifying trends and patterns of extreme events in ocean acidity is a pressing issue.

In this study, we use daily mean output of a five-member ensemble simulation under low- and high- CO_2 -emission scenarios of a comprehensive Earth system model to investigate how the occurrence, intensity, duration, and volume of $[H^+]$ and Ω extreme events change under rising atmospheric CO_2 levels. Extreme events defined with respect to both a fixed preindustrial and a shifting baseline are assessed, but the main focus is on extremes with respect to a shifting baseline and how these are affected by variability changes.

2 Methods

2.1 Model and experimental design

The simulations used in this study were made with the fully coupled carbon–climate Earth system model developed at the NOAA Geophysical Fluid Dynamics Laboratory (GFDL ESM2M) (Dunne et al., 2012, 2013). The GFDL ESM2M model consists of ocean, atmosphere, sea-ice, and

land modules and includes land and ocean biogeochemistry. The ocean component is the Modular Ocean Model version 4p1 (MOM4p1), with a nominal 1° horizontal resolution increasing to $1/3^\circ$ meridionally at the Equator, with a tripolar grid north of $65^\circ N$, and with 50 vertical depth levels. The MOM4p1 model has a free surface, with the surface level centered around about 5 m depth, and the spacing between consecutive levels is about 10 m down to a depth of about 230 m (Griffies, 2009) with increasing spacing below. The dynamical sea-ice model uses the same tripolar grid as MOM4p1 (Winton, 2000). The atmospheric model version 2 (AM2) has a horizontal resolution of $2^\circ \times 2.5^\circ$ with 24 vertical levels (Anderson et al., 2004). The land model version 3 (LM3) simulates the cycling of water, energy, and carbon dynamically and uses the same horizontal grid as AM2 (Shevliakova et al., 2009).

The ocean biogeochemical and ecological component is version two of the Tracers of Ocean Phytoplankton with Allometric Zooplankton (TOPAZv2) module that parameterizes the cycling of carbon, nitrogen, phosphorus, silicon, iron, oxygen, alkalinity, lithogenic material, and surface sediment calcite (see Supplement in Dunne et al., 2013). TOPAZv2 includes three explicit phytoplankton groups – small, large, and diazotrophs – and one implicit zooplankton group. The ocean carbonate chemistry is based on the OCMIP2 parameterizations (Najjar and Orr, 1998). The dissociation constants for carbonic acid and bicarbonate ions are from Dickson and Millero (1987), which are based on Mehrbach et al. (1973), and the carbon dioxide solubility is calculated according to Weiss (1974). Total alkalinity in TOPAZv2 includes contributions from phosphoric and silicic acids and their conjugate bases. TOPAZv2 also simulates diurnal variability in ocean physics as well as in phytoplankton growth. While diurnal variations in open-ocean pH are therefore simulated to some extent, we do not expect the model to fully capture the high diurnal variability in seawater chemistry, especially in coastal regions with large biological activity (Kwiatkowski et al., 2016; Hofmann et al., 2011), due to its relatively coarse resolution and simple biogeochemical model.

We ran a five-member ensemble simulation covering the historical 1861–2005 period, followed by a high (RCP8.5; RCP: Representative Concentration Pathway) and a low-greenhouse-gas-emission scenario (RCP2.6) over the 2006–2100 period with prescribed atmospheric CO_2 concentrations. RCP8.5 is a high-emission scenario without effective climate policies, leading to continued and sustained growth in greenhouse gas emissions (Riahi et al., 2011). In the GFDL ESM2M model, global atmospheric surface temperature in the RCP8.5 ensemble is projected to increase by $3.24^\circ C$ (ensemble minimum of $3.17^\circ C$ to ensemble maximum of $3.28^\circ C$) between the preindustrial period and 2081–2100. The RCP2.6 scenario represents a low-emission, high-mitigation future (van Vuuren et al., 2011) with a simulated warming in the GFDL ESM2M model of 1.21 (1.18 –

1.26) °C. The five ensemble members over the historical period were initialized from a multicentury preindustrial control simulation that was extended with historical land use over the 1700–1860 period (Sentman et al., 2011). The five ensemble members were generated by adding different sea surface temperature (SST) disturbances of the order 10^{-5} °C to a surface grid cell in the Weddell Sea at 70.5° S, 51.5° W on 1 January 1861 (Wittenberg et al., 2014; Palter et al., 2018). Although the ocean biogeochemistry is not perturbed directly, $[\text{H}^+]$ and Ω differences between the ensemble members spread rapidly over the globe. On average, the ensemble members can be regarded as independent climate realizations after about 3 years of simulation for surface waters and after about 8 years at 200 m (Frölicher et al., 2020). Neither the choice of the perturbation location nor the choice of the perturbed variable has a discernible effect on the results presented here (Wittenberg et al., 2014). In addition, an accompanying 500-year preindustrial control simulation was performed.

2.2 Analysis

2.2.1 Extreme-event definition and characterization

We analyze daily mean data of $[\text{H}^+]$ and aragonite saturation state Ω_{A} in the upper 200 m of the water column. $[\text{H}^+]$ is on the total scale and hence the sum of the concentrations of free protons and hydrogen sulfate ions. We define an event as a $[\text{H}^+]$ extreme event when the daily mean $[\text{H}^+]$ exceeds the 99th percentile, i.e., occurring once every 100 d. Similarly, we define a Ω_{A} extreme event when the daily mean Ω_{A} falls below the 1st percentile. The percentiles are calculated for each grid cell from daily mean data of the 500-year preindustrial control simulation. In contrast to absolute thresholds, relative thresholds, such as those used here, take into account regional differences in a variable's mean state, variance, and higher moments. Events that are defined based on relative thresholds have the same probability of occurrence across the globe in the period in which they are defined (e.g., preindustrial period; see also Frölicher et al., 2018).

We assess changes in $[\text{H}^+]$ and Ω_{A} extreme events when they are defined with respect to both a fixed preindustrial baseline and a shifting baseline. Under the fixed baseline approach, the secular trends as well as changes in variability and the higher moments of the distribution impose changes in extreme events. Under the shifting-baseline approach, which is the focus of this study, a value is considered extreme when it is much higher or lower than the baseline that undergoes changes due to secular trends in the variable. Thus, changes in the different extreme-event characteristics are only caused by changes in variability and the higher moments of the distributions. To define the extreme events with respect to the shifting baselines, we subtract the secular trends in $[\text{H}^+]$ and Ω_{A} at each grid cell and in each individual ensemble member prior to the calculation of the different extreme-event charac-

teristics based on the preindustrial percentiles (depicted for one grid cell in Fig. 1). The secular trend is calculated as the five-member ensemble mean, which has been additionally smoothed with a 365 d running mean to keep the seasonal signal in the data (further information in Appendix A). The removal of the secular trend ensures that the mean state in the processed data stays approximately constant while day-to-day to interannual variability can change over the simulation period (Fig. 1).

We calculate four extreme-event metrics: (a) the yearly extreme days (in days; number of days per year above the 99th percentile for $[\text{H}^+]$ and below the 1st percentile for Ω_{A}), (b) the annual mean duration (in days; the average number of days above the 99th percentile for $[\text{H}^+]$ and below the 1st percentile for Ω_{A} of single events within a year), (c) the annual mean maximal intensity (in nmol kg^{-1} or Ω_{A} unit; maximum $[\text{H}^+]$ or Ω_{A} anomalies with respect to the percentile threshold over the duration of a single extreme event and then averaged over all events within a year), and (d) the mean volume covered by individual extreme events in the upper 200 m (in km^3 ; mean volume of 3D clusters of connected grid cells that are above the 99th percentile for $[\text{H}^+]$ or below the 1st percentile for Ω_{A} , calculated using the *measure.label* function from the *scikit-image* library for Python for each day; these daily means are then averaged annually). The yearly extreme days, duration, and maximal intensity are calculated for individual grid cells at the surface and at 200 m. While the truncation of extremes between years alters the results for duration and maximal intensity, it allows for the calculation of annual extreme-event characteristics. We focus our analysis not only on the surface, but also on 200 m to study changes in extreme events within the seasonal thermocline. Most organisms susceptible to ocean acidification are found in the upper 200 m, such as reef-forming corals and calcifying phytoplankton.

2.2.2 Decomposition of $[\text{H}^+]$ variability into different variability components

We use three steps to decompose the total temporal variability in $[\text{H}^+]$ into interannual, seasonal, and subannual variability (Fig. 2). In a first step, we calculate the climatological seasonal cycle from the daily mean data by averaging each calendar day over all years in the time period of interest. Seasonal variability is then identified with the time-series variance of this 365 d long seasonal cycle. The secular trend in the daily mean data has been removed with the five-member ensemble mean before doing the analysis. In a second step, we subtract the seasonal cycle from the data and estimate the spectral density (Chatfield, 1996) of this residual time series using the *periodogram* function from the *scipy.signal* Python library. In a third step, we calculate the variance arising from variations on interannual and subannual timescales from the spectral density to obtain interannual and subannual variability (further information is given in Appendix B). Following

this methodology, subannual variability comprises all variations in daily mean data with periodicities of less than a year that are not part of the seasonal cycle.

2.2.3 Taylor expansion of $[H^+]$ and Ω_A variability changes

To understand the processes behind the simulated changes in the variabilities of $[H^+]$ and Ω_A , we decompose these changes into contributions from changes in temperature (T), salinity (S), total alkalinity (A_T), and total dissolved inorganic carbon (C_T). Assuming linearity, the difference of $[H^+]$ from its mean at time step i can be decomposed into contributions from the drivers by employing a first-order Taylor expansion,

$$\begin{aligned} H^+(i) - \bar{H}^+ &\simeq \left. \frac{\partial H^+}{\partial C_T} \right|_{\bar{C}_T, \bar{A}_T, \bar{T}, \bar{S}} (C_T(i) - \bar{C}_T) \\ &+ \left. \frac{\partial H^+}{\partial A_T} \right|_{\bar{C}_T, \bar{A}_T, \bar{T}, \bar{S}} (A_T(i) - \bar{A}_T) \\ &+ \left. \frac{\partial H^+}{\partial T} \right|_{\bar{C}_T, \bar{A}_T, \bar{T}, \bar{S}} (T(i) - \bar{T}) \\ &+ \left. \frac{\partial H^+}{\partial S} \right|_{\bar{C}_T, \bar{A}_T, \bar{T}, \bar{S}} (S(i) - \bar{S}), \end{aligned} \quad (1)$$

and analogously for Ω_A . The partial derivatives are evaluated at \bar{T} , \bar{S} , \bar{C}_T , and \bar{A}_T , i.e., the temporal mean values of the drivers in the period of interest. While it is important to take into account the climatological total phosphate and total silicate concentrations for calculating the partial derivatives (Orr and Epitalon, 2015), one introduces only small errors by neglecting variations in phosphate and silicate. The partial derivatives in Eq. (1) are evaluated using *mocsy 2.0* (Orr and Epitalon, 2015).

Using the Taylor decomposition (Eq. 1), one can for example express the seasonal variation in $[H^+]$ as a function of the drivers' seasonal variations (Kwiatkowski and Orr, 2018). In this study, however, we analyze the time-series variance of $[H^+]$ and Ω_A that also includes variability on other timescales (see Sect. 2.2.2) and the drivers of its changes. From the Taylor approximation (Eq. 1) and the definition of variance (e.g., Coles, 2001), it follows that the variance of $[H^+]$ can be written as a function of the partial derivatives with respect to the drivers (sensitivities), the standard deviations of the drivers, and their pairwise correlation coefficients:

$$\begin{aligned} \sigma_{H^+}^2 &= \left(\frac{\partial H^+}{\partial C_T} \right)^2 \sigma_{C_T}^2 + \left(\frac{\partial H^+}{\partial A_T} \right)^2 \sigma_{A_T}^2 \\ &+ \left(\frac{\partial H^+}{\partial T} \right)^2 \sigma_T^2 + \left(\frac{\partial H^+}{\partial S} \right)^2 \sigma_S^2 \\ &+ 2 \frac{\partial H^+}{\partial C_T} \frac{\partial H^+}{\partial A_T} \text{cov}(C_T, A_T) \\ &+ 2 \frac{\partial H^+}{\partial C_T} \frac{\partial H^+}{\partial T} \text{cov}(C_T, T) \\ &+ 2 \frac{\partial H^+}{\partial C_T} \frac{\partial H^+}{\partial S} \text{cov}(C_T, S) \\ &+ 2 \frac{\partial H^+}{\partial A_T} \frac{\partial H^+}{\partial T} \text{cov}(A_T, T) \\ &+ 2 \frac{\partial H^+}{\partial A_T} \frac{\partial H^+}{\partial S} \text{cov}(A_T, S) \\ &+ 2 \frac{\partial H^+}{\partial T} \frac{\partial H^+}{\partial S} \text{cov}(T, S), \end{aligned} \quad (2)$$

where the pairwise covariances are functions of the standard deviations and correlation coefficients according to $\text{cov}(x, y) = \sigma_x \sigma_y \rho_{x,y}$, and the partial derivatives are again evaluated at the temporal mean values \bar{T} , \bar{S} , \bar{C}_T , and \bar{A}_T . This methodology has also been used to propagate uncertainties in carbonate system calculations (Dickson and Riley, 1978; Orr et al., 2018) and to identify drivers of potential predictability in carbonate system variables (Frölicher et al., 2020). Based on Eq. (2) and the analogous result for Ω_A , a change in variance of $[H^+]$ and Ω_A can be attributed to changes in the sensitivities that arise from changes in the drivers' mean states, to changes in the drivers' standard deviations, and to changes in the pairwise correlations between the drivers. We do so by calculating the Taylor series of Eq. (2) (further information in Appendix C). We then identify the $[H^+]$ variance change from mean changes in the drivers as the sum of all terms in the expansion that describe the contributions of sensitivity changes to the overall change in variance ($\Delta_s \sigma_{H^+}^2$). Likewise, we identify the contribution from standard deviation changes in the drivers ($\Delta_\sigma \sigma_{H^+}^2$). We further group terms in the expansion that stem from simultaneous changes in the sensitivities and standard deviations ($\Delta_{s\sigma} \sigma_{H^+}^2$) and the remaining terms that arise either from correlation changes alone or mixed contributions from correlation changes and changes in sensitivities and standard deviations ($\Delta_{\rho+} \sigma_{H^+}^2$). Since these four components contain all terms in the Taylor series, they exactly reproduce a change in variance represented by Eq. (2),

$$\Delta \sigma_{H^+}^2 = \Delta_s \sigma_{H^+}^2 + \Delta_\sigma \sigma_{H^+}^2 + \Delta_{s\sigma} \sigma_{H^+}^2 + \Delta_{\rho+} \sigma_{H^+}^2. \quad (3)$$

We also assess the contributions to the four components from C_T alone; from C_T and A_T ; and from C_T , A_T , and T . The equivalent procedure is also used to decompose variance change in Ω_A . Further information on the decomposition is given in Appendix C.

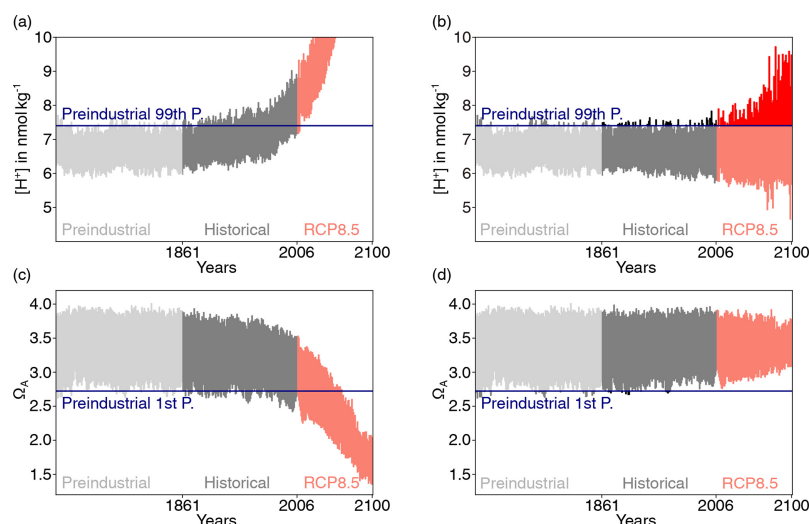


Figure 1. Simulated daily mean surface $[H^+]$ (a) and Ω_A (c) at 40°N and 30°W in the North Atlantic for one ensemble member over the preindustrial period, the 1861–2005 historical period, and the 2006–2100 period under RCP8.5. The same data as in (a) and (c) but with subtracted ensemble-mean changes with respect to the average of the 500-year preindustrial control simulation is shown in panels (b) and (d). For $[H^+]$, the preindustrial 99th percentile threshold (horizontal blue line in panels a and b) is increasingly exceeded even when subtracting the ensemble-mean change, because $[H^+]$ variability increases. In contrast, a reduction in Ω_A variability leads to a reduced undershooting of the preindustrial 1st percentile (d).

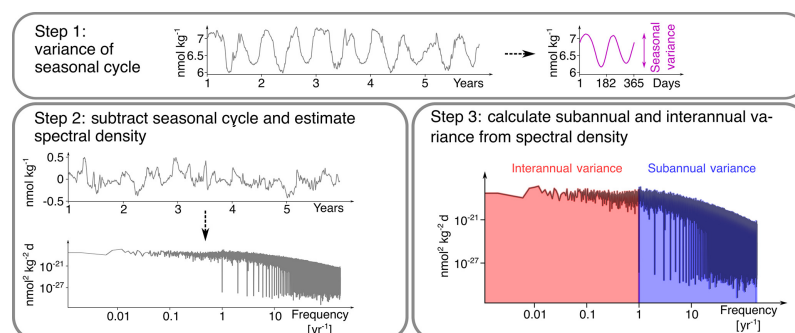


Figure 2. The three-step decomposition of $[H^+]$ variance into interannual, seasonal, and subannual variance, exemplified for a surface grid cell at 40°N and 30°W in the North Atlantic in the preindustrial control simulation. In a first step, the climatological seasonal cycle is determined (over the whole period, only 5 years are depicted here) and its variance is calculated. Note that the seasonal cycle in this grid cell has two minima and maxima. In a second step, the spectral density of the anomalies with respect to the seasonal cycle is calculated. In a third step, interannual and subannual variance is estimated from the spectral density.

2.3 Model evaluation

The focus of our analysis is on changes in variability in $[H^+]$ and Ω_A . As observation-based daily mean data of the inorganic carbon chemistry at the global scale are not available, we limit the evaluation of the Earth system model simulation to the representation of the seasonal cycles of $[H^+]$ and Ω_A , and especially on its changes over the 1982–2015 period. We developed an observation-based dataset for sur-

face monthly $[H^+]$ and Ω_A using monthly surface salinity, temperature, $p\text{CO}_2$, and A_T fields. Salinity and temperature data are taken from the Hadley Centre EN.4.2.1 analysis product (Good et al., 2013). A_T is then calculated using the *LIARv2* total alkalinity regression from salinity and temperature (Carter et al., 2018). For $p\text{CO}_2$, we use the neural-network-interpolated monthly data from Landschützer et al. (2016), which is based on SOCATv4 (Bakker et al., 2016). Although not fully capturing $p\text{CO}_2$ variability in regions

with only few observations (Landschützer et al., 2016), the $p\text{CO}_2$ dataset appears to be generally well suited for analyzing $p\text{CO}_2$ seasonality and changes therein (Landschützer et al., 2018). An exception is the Southern Ocean, where data-based $p\text{CO}_2$ products are uncertain due to sparse data in winter (Gray et al., 2018). $[\text{H}^+]$ and Ω_{A} are then calculated from salinity, temperature, A_{T} , and $p\text{CO}_2$ using the CO2SYS carbonate chemistry package (van Heuven et al., 2011). Uncertainties in the derived seasonal cycles for $[\text{H}^+]$ and Ω_{A} that arise from uncertainties in the observation-based input variables are not quantified in this study.

In most regions, the GFDL ESM2M model captures the observation-based mean seasonal cycle in $[\text{H}^+]$ and Ω_{A} quite well, in particular for Ω_{A} (the mean values of the seasonal amplitudes in Fig. 3). However, potential biases in the mean seasonal amplitudes do not directly have an effect on projected changes in extreme events, as we base the extreme-event definition on relative thresholds.

We then compare the simulated ensemble-mean trends in seasonal amplitude with the observation-based estimates (Fig. 3; Appendix D). Similar to the mean seasonal cycle results, the GFDL ESM2M model captures the observed trends in the seasonal $[\text{H}^+]$ and Ω_{A} amplitudes for different latitudinal bands over the 1982–2015 period relatively well. The ensemble-mean trends in the simulated seasonal $[\text{H}^+]$ amplitudes are positive for all latitude bands (Fig. 3, Table 1), consistent with the observation-based estimates. While the estimates for the simulated trends are significantly larger than zero for all latitude bands, this is not the case for the observation-based trends in the equatorial region (10°S – 10°N) and the northern low latitudes (10 – 40°N) (Table 1). The simulated $[\text{H}^+]$ seasonality trends are significantly smaller (with 90 % confidence level) than estimated from observations in the northern high (40 – 80°N ; orange thick lines in Fig. 3a, b) and southern low latitudes (40 – 10°S ; blue thick lines in Fig. 3a, b), where the trends from the model ensemble are $0.031 \pm 0.012 \text{ nmol kg}^{-1}$ per decade and $0.035 \pm 0.003 \text{ nmol kg}^{-1}$ per decade, compared to the observation-based trends of $0.106 \pm 0.040 \text{ nmol kg}^{-1}$ per decade and $0.055 \pm 0.014 \text{ nmol kg}^{-1}$ per decade, respectively. The simulated ensemble-mean trends for the remaining latitude bands are not significantly different from the observation-based trend estimates.

For the seasonal amplitude of Ω_{A} , we find a significant negative trend in the observation-based data in the northern low latitudes and significant negative trends in the simulations in the northern and southern high latitudes (Table 1). The negative trends in seasonal amplitude in the simulations are significantly different from the observation-based trends in the northern high latitudes (-0.015 ± 0.004 vs. $0.002 \pm 0.009 \text{ } \Omega_{\text{A}}$ units per decade) and in the southern high latitudes (-0.012 ± 0.002 vs. $0.000 \pm 0.005 \text{ } \Omega_{\text{A}}$ units per decade).

In summary, taking into account previous evaluations of the mean states of $[\text{H}^+]$ and Ω_{A} and the underlying drivers in

the GFDL-ESM2M model (Bopp et al., 2013; Kwiatkowski and Orr, 2018), the model performs well against a number of key seasonal performance metrics. However, the model slightly underestimates past increases in seasonal amplitude of $[\text{H}^+]$, especially in the northern and southern high latitudes. In contrast to the observation-based data, the model also projects negative trends in the Ω_{A} seasonal amplitude there. Nevertheless, the observation-based trends in the northern and especially southern high latitudes are uncertain because wintertime data are sparse there. Even though we lack the daily mean observation-based data to undertake a full assessment, it appears that the GFDL ESM2M model is adequate to assess changes in open-ocean variability of $[\text{H}^+]$ and Ω_{A} and to assess changes in extreme events that arise thereof.

3 Results

We first briefly discuss the simulated changes in $[\text{H}^+]$ and Ω_{A} extreme events when these events are defined with respect to a fixed preindustrial baseline period (Sect. 3.1). In Sect. 3.2 and 3.3, these results are contrasted with changes in extremes that are defined with respect to a shifting baseline, i.e., where the secular trends do not alter extreme events. In Sect. 3.4, variability changes are decomposed into sub-annual, seasonal, and interannual variability contributions. The processes leading to variability changes are analyzed in Sect. 3.5.

3.1 Global changes in extremes defined relative to a fixed preindustrial baseline

When using the fixed preindustrial 99th and 1st percentiles to define extreme events in $[\text{H}^+]$ and Ω_{A} , respectively, large increases in the number of days with $[\text{H}^+]$ and Ω_{A} extremes are projected over the 1861–2100 period in both low- and high- CO_2 -emission scenarios (Figs. 4 and A1). Over the historical period, the GFDL ESM2M model projects an increase in yearly extreme days for surface $[\text{H}^+]$ from 3.65 d per year during the preindustrial period to 299 d per year in 1986–2005. By year 2030 and under both CO_2 emission scenarios, the surface ocean is projected to experience a “near-permanent acidity extreme state”; i.e., $[\text{H}^+]$ is above the preindustrial 99th percentile more than 360 d per year. Likewise, the average duration of events saturates near 365 d, and the intensity of events increases strongly, mainly reflecting the large increase in mean $[\text{H}^+]$ (Fig. A1). A similar but slightly delayed evolution in the number, maximal intensity, and duration of $[\text{H}^+]$ extremes is simulated at 200 m (Fig. A1).

Large increases in yearly extreme days are also projected for Ω_{A} when using a fixed preindustrial 1st percentile as a baseline (Fig. 4b). Similar to $[\text{H}^+]$, the entire surface ocean is projected to approach a permanent Ω_{A} extreme state dur-

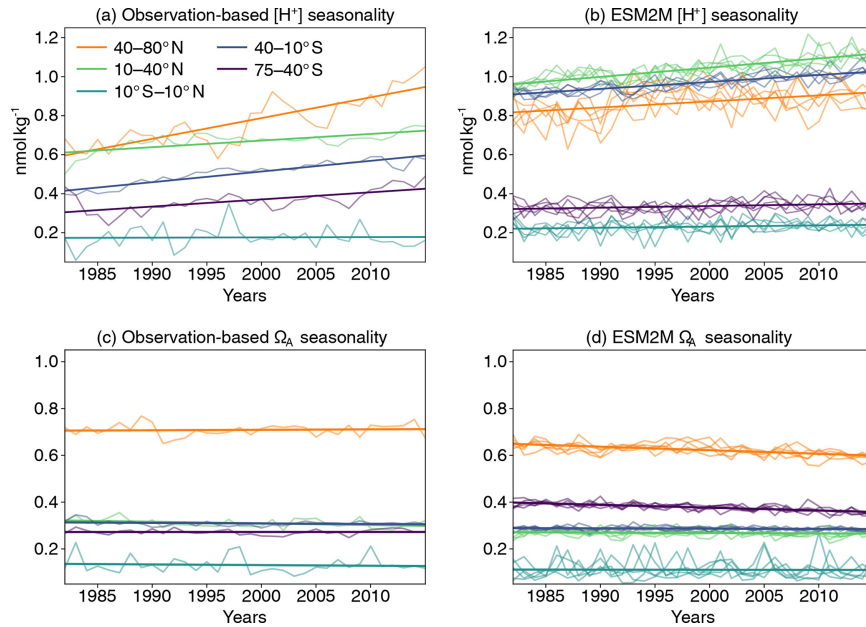


Figure 3. Seasonal amplitude of $[H^+]$ (calculated as yearly maximum minus the yearly minimum after subtracting a cubic spline from the data) over the period 1982–2015 averaged over five different latitude bands for the observation-based estimate (a) and the GFDL ESM2M model historical (1982–2005) and RCP8.5 (2006–2015) ensemble simulations (b), along with the same for data-based Ω_A (c) and simulated Ω_A (d). Linear trends in all panels are overlaid as thick lines. The linear trend of the simulated changes is calculated as the mean of the five individual ensemble trends.

Table 1. Linear trends in seasonal amplitude of $[H^+]$ (in nmol kg^{-1} per decade) and Ω_A (in 10^{-3} per decade) for five latitude bands over the period 1982–2015. Results are shown for the observation-based data (Obs.) and the five-member ensemble mean of the ESM2M model simulations (ESM2M) following the RCP8.5 scenario over 2006–2015. The range (\pm) denotes the 90 % confidence interval.

Latitude	Obs. $[H^+]$	ESM2M $[H^+]$	Obs. Ω_A	ESM2M Ω_A
40–80° N	0.106 ± 0.040	0.031 ± 0.012	1.9 ± 8.7	-15.1 ± 3.8
10–40° N	0.034 ± 0.034	0.047 ± 0.005	-6.7 ± 5.6	-1.8 ± 2.0
10° S–10° N	0.001 ± 0.016	0.006 ± 0.005	-2.8 ± 10.7	-0.5 ± 5.3
40–10° S	0.055 ± 0.014	0.035 ± 0.003	-2.4 ± 5.1	-1.2 ± 1.2
75–40° S	0.037 ± 0.028	0.009 ± 0.004	0.1 ± 4.8	-12.2 ± 1.7

ing the 21st century under the RCP8.5 scenario. A near-permanent extreme state is projected by year 2062. In contrast to $[H^+]$, a permanent Ω_A extreme state of the global ocean is avoided under the RCP2.6 scenario.

3.2 Global changes in extremes defined relative to a shifting baseline

Next, we investigate changes in $[H^+]$ and Ω_A extremes when the extreme events are defined with respect to a shifting (time-moving) baseline; i.e., changes in extremes arise only from changes in variability and higher moments of the distributions. The GFDL ESM2M model projects large increases in the number, intensity, duration, and volume of $[H^+]$ ex-

treme events over the 1861–2100 period (Fig. 5). Over the historical period (from the preindustrial period to 1986–2005), the model projects that the number of surface $[H^+]$ extreme days increases from 3.65 d per year to 10.0 d per year (Fig. 5a, ensemble ranges are given in Table 2). The maximal intensity is projected to increase from 0.08 to 0.12 nmol kg^{-1} (Fig. 5c, Table 2) and the duration from 11 to 15 d (Fig. 5e). Compared to preindustrial conditions, these changes correspond to a 173 % increase in the number of days per year, a 44 % increase in the maximal intensity, and a 45 % increase in the duration of $[H^+]$ extreme events. The volume of individual events is projected to increase by 20 % over the historical period, from a typical volume of $2.7 \times 10^3 \text{ km}^3$, which is

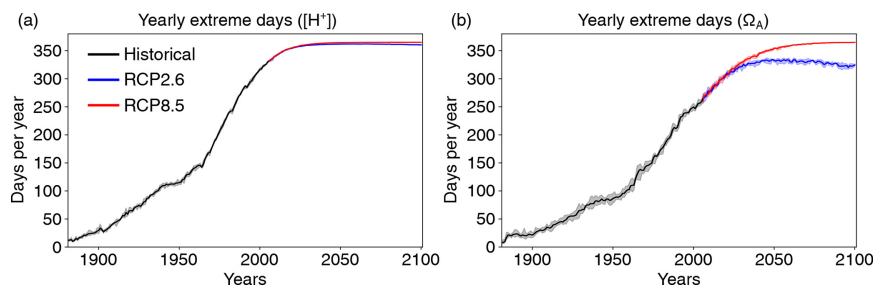


Figure 4. Simulated globally averaged yearly extreme days defined with respect to a fixed baseline for $[H^+]$ using the preindustrial 99th percentile (a) and for Ω_A using the preindustrial 1st percentile (b). Shown are changes at the surface over the 1881–2100 period following historical (black lines) and future scenarios, RCP8.5 (red) and RCP2.6 (blue). The thick lines display the five-member ensemble means, and the shaded areas represent the maximum and minimum ranges of the individual ensemble members.

about 0.004 % of the total ocean volume in the upper 200 m (Fig. 5g), to $3.2 \times 10^3 \text{ km}^3$.

Over the 21st century, extreme events in ocean acidity, defined with respect to a shifting baseline, are projected to further increase in frequency, intensity, duration, and volume (Fig. 5). By 2081–2100 under the RCP8.5 scenario, the number of $[H^+]$ extreme days per year at the surface is projected to increase to 50 d (corresponding to a 1273 % increase relative to the preindustrial period). The maximal intensity is projected to increase to $0.38 \text{ nmol kg}^{-1}$ (371 % increase), the duration to 32 d (199 % increase), and the volume to $13.9 \times 10^3 \text{ km}^3$ (414 % increase).

At 200 m, the $[H^+]$ extreme events in preindustrial conditions are in general more intense ($0.17 \text{ nmol kg}^{-1}$; Fig. 5d) and longer lasting (38 d; Fig. 5f) than at the surface. The stronger extreme events are caused by the overall larger variability at 200 m than at the surface in the preindustrial period. The longer duration is connected to the more pronounced contribution from interannual variability (see Sect. 3.4). However, projected relative changes over the historical period and the 21st century are smaller at 200 m than at the surface and with larger year-to-year variations across the ensembles. Under recent past conditions (1986–2005), the number of extreme days per year at 200 m is 4.3 d per year (corresponding to an 18 % increase since the preindustrial period), the maximal intensity $0.20 \text{ nmol kg}^{-1}$ (18 % increase), and the duration 46 d (21 % increase). By the end of the 21st century under the RCP8.5 scenario, the number of $[H^+]$ extreme days per year is projected to increase to 32 d per year, the maximal intensity to $0.34 \text{ nmol kg}^{-1}$, and the duration to 99 d. Notably, extreme events in $[H^+]$ are projected to become slightly less intense at 200 m than at the surface (0.34 vs. $0.38 \text{ nmol kg}^{-1}$) by the end of the century under RCP8.5, even though they were more intense in preindustrial times at depth. In contrast, surface $[H^+]$ extreme events remain shorter in duration at the end of the century than at 200 m.

Under the RCP2.6 scenario, the magnitude of changes in the different $[H^+]$ extreme-event characteristics by the end of

the century is substantially smaller than in the RCP8.5 scenario. This difference is especially pronounced at the surface (blue lines in Fig. 5). There, the number of extreme days per year, maximal intensity, and duration under the RCP2.6 are projected to be 46 % (44–47), 43 % (43–44), and 75 % (73–77) of that under the RCP8.5 scenario. At depth, the differences between the RCP2.6 and RCP8.5 scenario are less pronounced and only emerge in the second half of the 21st century. As opposed to the surface, the number of $[H^+]$ extreme days per year and the maximal intensity at 200 m as well as the volume of events are projected to increase significantly even after the atmospheric CO_2 concentration stabilizes in RCP2.6 around year 2050. This delayed response in the subsurface is due to the relatively slow surface-to-subsurface transport of carbon. However, this is not the case for the duration, which slightly decreases in the second half of the 21st century at depth (Fig. 5f). This decrease in duration mainly occurs in the subtropics, where events generally last longer (Fig. A3b). It is connected to an increase in the contribution from high-frequency variability to total variability in those regions over that period.

In contrast to $[H^+]$ extreme events, the number of yearly extreme days in Ω_A is projected to decrease over the historical period and during the 21st century under both the RCP8.5 and RCP2.6 scenarios (Fig. 6a–b, Appendix Table A1) when the extreme events are defined with respect to a shifting baseline. The number of surface Ω_A extreme days per year by the end of this century is projected to be 63 % smaller under RCP8.5 and 39 % smaller under RCP2.6 compared to preindustrial conditions (ensemble ranges are given in Table A1). Projected changes at depth are less pronounced than at the surface, again with larger decreases under RCP8.5 than under RCP2.6. Despite this decline in extreme events when defined with respect to a shifting baseline, the long-term decline in the mean state of Ω_A still leads to more frequent occurrence of extreme low Ω_A events when defined with respect to a fixed baseline (see Sect. 3.1).

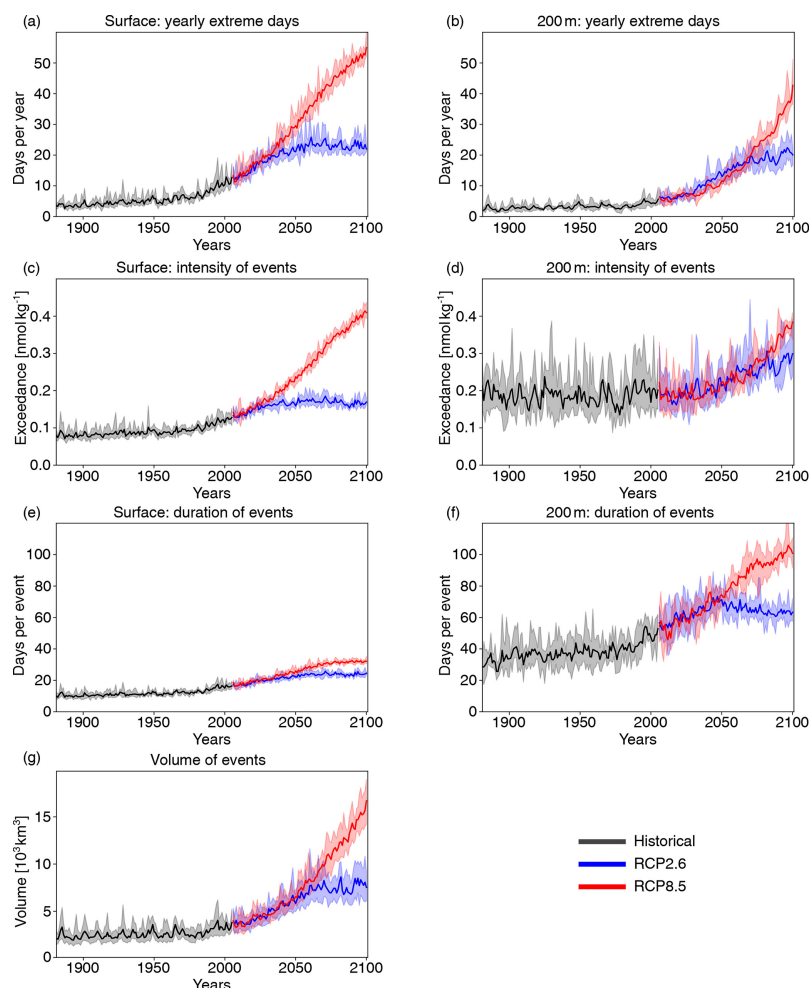


Figure 5. Simulated changes in globally averaged $[H^+]$ extreme-event characteristics over the 1881–2100 period following historical (black lines) and future RCP8.5 (red) and RCP2.6 (blue) scenarios. The extreme events are defined with respect to a shifting baseline. Yearly extreme days, maximal intensity, and duration are shown for the surface (a, c, e) and for 200 m (b, d, f). Volume is shown in (g). The thick lines display the five-member ensemble means, and the shaded areas represent the maximum and minimum ranges of the individual ensemble members.

Table 2. Simulated global ensemble-mean $[H^+]$ extreme-event characteristics, when extremes are defined with respect to a shifting baseline. Values in brackets denote ensemble minima and maxima.

	PI	1986–2005	2081–2100 RCP2.6	2081–2100 RCP8.5
Yearly extreme days surface (days per year)	3.65	10.0 (9.5–10.4)	22.9 (21.9–23.5)	50.1 (50.0–50.3)
200 m (days per year)	3.65	4.3 (3.7–5.1)	19.9 (17.0–22.5)	32.1 (30.9–34.8)
Duration surface (days)	10.6	15.4 (15.0–15.7)	23.8 (23.4–24.1)	31.8 (31.2–32.1)
200 m (days)	38.0	46.0 (42.8–50.0)	62.9 (60.5–66.1)	98.7 (95.1–102.0)
Maximal intensity surface (nmol kg^{-1})	0.08	0.12 (0.11–0.12)	0.17 (0.16–0.17)	0.38 (0.37–0.39)
200 m (nmol kg^{-1})	0.17	0.20 (0.19–0.21)	0.28 (0.25–0.30)	0.34 (0.33–0.34)
Volume ($\times 10^3 \text{ km}^3$)	2.7	3.2 (3.1–3.5)	7.7 (6.9–8.5)	13.9 (13.8–14.1)

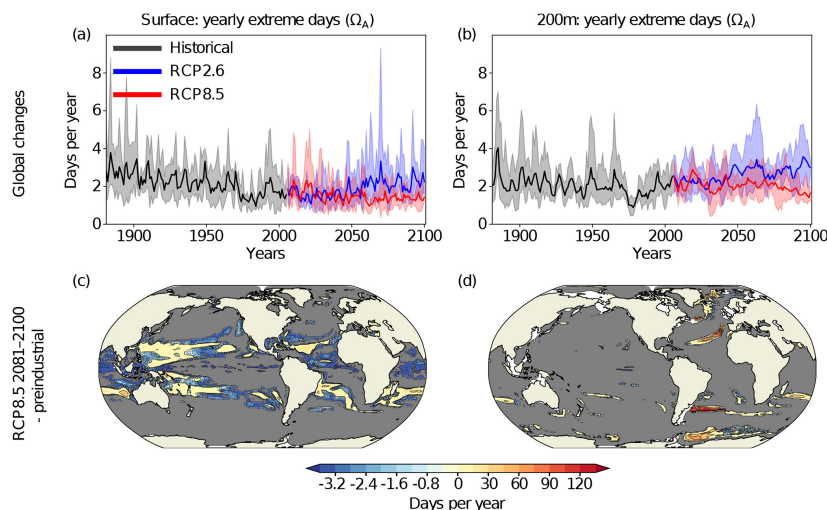


Figure 6. Simulated changes in the yearly number of Ω_A extreme days. The extreme events are defined with respect to a shifting baseline. Panels (a) and (b) show the globally averaged simulated yearly extreme days in Ω_A from 1881 to 2100 following historical (black lines) and future RCP2.6 (blue) and RCP8.5 (red) scenarios at the surface (a) and 200 m (b). The thick lines display the five-member ensemble means, and the shaded areas represent the maximum and minimum range of the individual ensemble members. Panels (c) and (d) show the simulated regional changes in yearly extreme days in Ω_A from the preindustrial period to 2081–2100 under the RCP8.5 scenario at the surface (c) and at 200 m (d). Shown are changes averaged over all five ensemble members. The black lines highlight the pattern structure and gray colors represent regions where no ensemble member simulates extremes during 2081–2100.

3.3 Regional changes in extremes defined relative to a shifting baseline

Surface $[\text{H}^+]$ extremes that are defined with respect to a shifting baseline are projected to become more frequent in 87 % of the surface ocean area by the end of the 21st century under the RCP8.5 scenario. However, the projected changes in these ocean acidity extremes are not uniform over the globe (Fig. 7; Appendix Fig. A3). The largest increases in the number of $[\text{H}^+]$ extreme days per year are projected in the Arctic Ocean (up to +120 d per year), in the subtropical gyres (up to +60 d per year), and in parts of the Southern Ocean and near Antarctica. There are also some regions including the eastern equatorial Pacific and parts of the Southern Ocean where the number of yearly extreme days in surface $[\text{H}^+]$ is projected to decrease. These are in general also the regions where the seasonality in $[\text{H}^+]$ is projected to decrease (see Sect. 3.4 below). The largest absolute changes in intensity of surface $[\text{H}^+]$ extremes (Fig. 7c) are projected for the subtropics, especially in the Northern Hemisphere. For example, events become up to 1 nmol kg^{-1} more intense in the subtropical North Pacific and Atlantic, corresponding roughly to a 10-fold increase in intensity with respect to the preindustrial period. The largest relative increases in intensity are projected for the Arctic Ocean, the North Atlantic, and around Antarctica, where more-than-10-fold increases with respect to the preindustrial period are projected. Re-

gions with large increases in the number of yearly extreme days tend to also show large increases in the duration of extreme events (Fig. 7e). The Arctic Ocean is an exception. Although the number of yearly extreme days increases strongly, the increase in duration is not as pronounced. This discrepancy is because extremes are already long lasting but rare at preindustrial times (Fig. A3). So even though extreme events are projected to occur each year by the end of the century under RCP8.5, the increase in duration is relatively small.

At 200 m, the projected pattern of changes in yearly extreme days generally resembles that at the surface (Fig. 7b). The largest increases in yearly extreme days are projected for parts of the subtropics, the Southern Ocean, and the Arctic Ocean. In contrast to the surface, $[\text{H}^+]$ extremes at 200 m are projected to become less frequent in the equatorial Atlantic, the northern Indian Ocean, the North Pacific, and in large parts of the Southern Ocean. The regions indicating a decline in $[\text{H}^+]$ extremes at depth include also some of the eastern boundary current systems, such as the Humboldt, California, and Benguela Current systems. In most of these regions, extreme events are projected to disappear in the RCP8.5 scenario by the end of this century (gray regions in Fig. 7b). The largest increases in subsurface event intensity are projected in the subtropics (Fig. 7d), whereas the duration of $[\text{H}^+]$ extremes is projected to increase strongly in many regions of the mid-to-high latitudes of both hemispheres (Fig. 7f). The

projected increases in duration at 200 m are much larger than at the surface.

The increase in the number of extreme days per year, the maximal intensity, and the duration is smaller under RCP2.6 compared to RCP8.5 for most of the ocean (Fig. A2). The largest increases in occurrence of extremes under RCP2.6 are simulated for the Arctic Ocean, similar to under RCP8.5, and for parts of the Southern Ocean. The regions in the Southern Ocean where the occurrence of extreme events in $[\text{H}^+]$ is projected to decrease largely overlap with those for RCP8.5, at the surface and at depth. On the other hand, unlike under RCP8.5, a decrease in extreme-event occurrence is only projected for a small fraction of the tropical oceans under RCP2.6.

While the decline in mean Ω_{A} generally leads to lower values in Ω_{A} and thus extreme events are becoming more frequent when defined with respect to a fixed preindustrial baseline (Sect. 3.1), extreme events in Ω_{A} are projected to become less frequent throughout most of the ocean when defined with respect to a shifting baseline (89 % of surface area under RCP8.5 at the end of the 21st century; Fig. 6c). In many regions, extreme events in Ω_{A} are projected to disappear by 2081–2100 under the RCP8.5 scenario (gray regions in Fig. 6c) when defined with respect to a shifting baseline. However, the number of yearly extreme days in Ω_{A} is projected to increase by 10 or more in the subtropical gyres, especially in the western parts of the subtropical gyres. At 200 m, no extreme events are projected for most of the ocean during 2081–2100 under RCP8.5 (Fig. 6d).

3.4 Decomposition of temporal variability in $[\text{H}^+]$

The changes in $[\text{H}^+]$ extreme events defined with respect to a shifting baseline mainly result from changes in $[\text{H}^+]$ variability. These variability changes may arise from changes in interannual variability, seasonal variability, and subannual variability. Thus, we decomposed the total variability into these three components (see Sect. 2.2.2). For the preindustrial period, the model simulates generally larger $[\text{H}^+]$ variance at depth than at the surface (0.42 vs. $0.15 \text{ nmol}^2 \text{ kg}^{-2}$, not shown). Seasonality has the largest contribution at the surface (81 % of total variance). At 200 m, interannual variability has the largest contribution (63 %), and also subannual variability is more important compared to the surface (15 % vs. 8 %).

Over the 1861–2100 period under the historical-RCP8.5 forcing, changes in seasonality clearly dominate the overall change in variability at the surface with 87 % contribution to the overall variance change in the global mean (Fig. 8b, d). Changes in interannual variability (3 % contribution to overall variance change; Fig. 8a, d) and subannual variability (10 %; Fig. 8c, d) play a minor role. The largest increases in variability for all three variability types are projected for the northern high latitudes. Around Antarctica and the southern end of South America, large increases in seasonal variability

are projected (Fig. 8b). In the tropical Pacific and parts of the Southern Ocean, decreases in interannual and seasonal variability are projected (Fig. 8a, b).

In contrast to the surface, changes in interannual and to a lesser extent subannual variability at 200 m are also important for explaining the overall changes in $[\text{H}^+]$ variability (Fig. 8e, g, h). Changes in interannual variability contribute most to overall variance change at the global scale (with 42 % contribution). Seasonal variability changes are almost equally important (37 %), and changes in subannual variability also contribute substantially to changes in total variability (20 %). The patterns of variability changes are very similar across the three temporal components of variability. The largest increases in $[\text{H}^+]$ variability are simulated north and south of the Equator. These regions tend to be already more variable during the preindustrial period (see Fig. A3a). However, the model also projects an increase in variability for regions that are less variable during the preindustrial period, such as northern high latitudes. All three temporal components of variability are projected to decrease in the tropics and parts of the Southern Ocean. The variability decrease in those regions is most pronounced for interannual variability (Fig. 8e).

3.5 Drivers of $[\text{H}^+]$ and Ω_{A} variability changes

In this section, we investigate the changes in the drivers that cause the variability changes in $[\text{H}^+]$ and Ω_{A} . Drivers are carbon (C_{T}), alkalinity (A_{T}), temperature, and salinity. To do so, we attribute changes in $[\text{H}^+]$ and Ω_{A} variability to four factors (see Sect. 2.2.3 for further details): (i) changes in the mean states of the drivers that control the sensitivities ($\Delta_s \sigma_{\text{H}^+}^2$), (ii) changes in the variabilities of the drivers ($\Delta_\sigma \sigma_{\text{H}^+}^2$), (iii) simultaneous changes in the mean states and variabilities of the drivers ($\Delta_{s\sigma} \sigma_{\text{H}^+}^2$; this contribution arises because both mean states and variabilities change and cannot be attributed to either (i) or (ii) alone), and (iv) changes in the correlations between the drivers, also including mixed contributions from correlation changes together with mean state and variability changes ($\Delta_{\rho+} \sigma_{\text{H}^+}^2$). In other words, (iv) describes the change in variability that arises because the correlations between the drivers also change, and not only their mean states and variabilities.

The drivers' mean changes between the preindustrial period and 2081–2100 under RCP8.5 cause a strong increase in surface $[\text{H}^+]$ variability, which is most pronounced in the high latitudes ($\Delta_s \sigma_{\text{H}^+}^2$; red line in Fig. 9a, black dashed line in Fig. 9b). On a global average, these variance changes due to the mean changes in the drivers ($\Delta_s \sigma_{\text{H}^+}^2 = 1.3 \text{ nmol}^2 \text{ kg}^{-2}$) are much larger than the total simulated variance change in $[\text{H}^+]$ ($\Delta \sigma_{\text{H}^+}^2 = 0.5 \text{ nmol}^2 \text{ kg}^{-2}$, dashed gray or solid black line in Fig. 9a). In general, an increase in mean C_{T} , temperature, and salinity would lead to an increase in $\Delta_s \sigma_{\text{H}^+}^2$, whereas an increase in mean A_{T} would lead to a

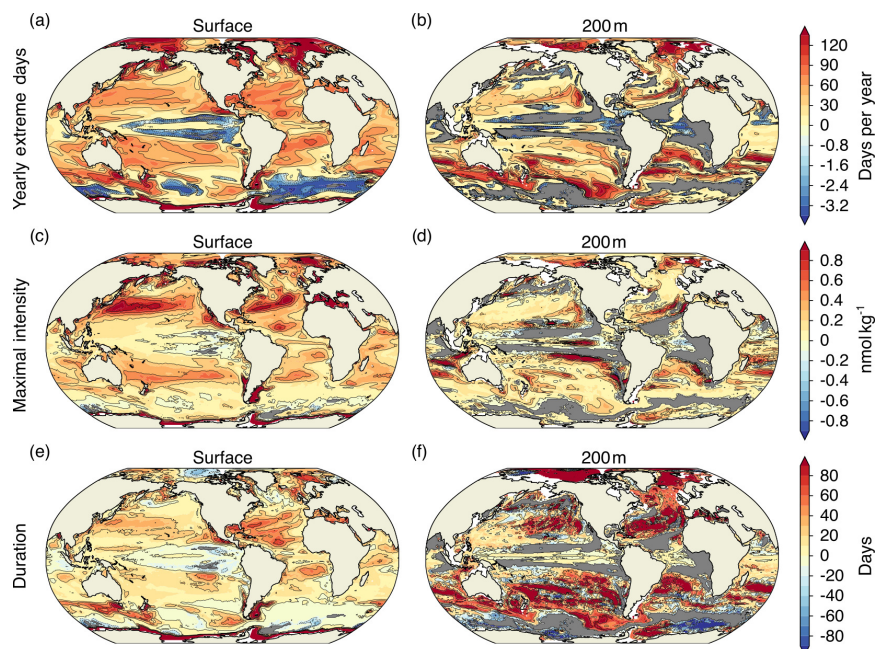


Figure 7. Simulated regional changes in $[H^+]$ extreme-event characteristics from the preindustrial period to the 2081–2100 period under the RCP8.5 scenario at the surface and at depth for the yearly extreme days (a, b), the maximal intensity of events (c, d), and the duration of events (e, f). The extreme events are defined with respect to a shifting baseline. Shown are changes averaged over all five ensemble members. Gray colors represent areas where no extremes occur during 2081–2100, and the black lines highlight pattern structures.

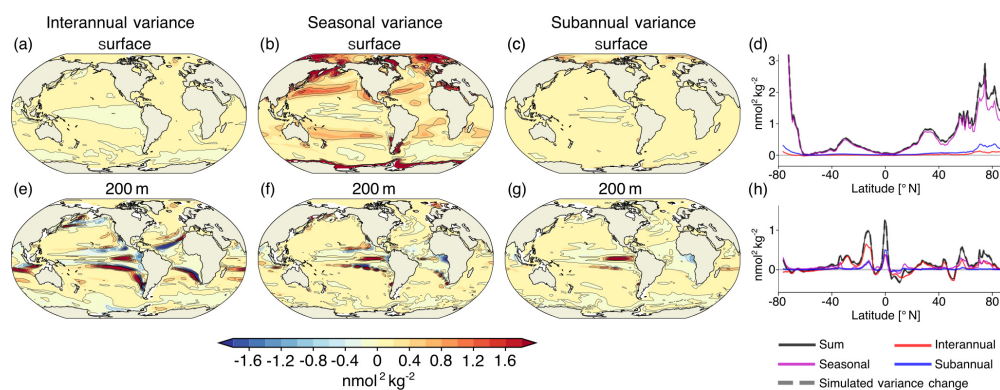


Figure 8. Contribution to projected changes in $[H^+]$ variance from interannual variability (a, e), seasonal variability (b, f), and subannual variability (c, g) between the preindustrial period and the 2081–2100 period under the RCP8.5 forcing at the surface (a–d) and at 200 m (e–h). Shown are the ensemble-mean changes. The black lines highlight the pattern structure. Zonal mean contributions are shown for the surface (d) and for 200 m (h). The sum of the three components (black lines) accurately reproduces the simulated variance change (gray dashed lines).

decrease. The GFDL ESM2M model projects an increase in mean C_T over the entire surface ocean (Fig. A5a) due to the uptake of anthropogenic CO_2 from the atmosphere and therefore an increase in $\Delta_s \sigma_{H^+}^2$ (light blue line in Fig. 9b). In the high latitudes, a relatively small increase in mean C_T leads to

a large increase in $\Delta_s \sigma_{H^+}^2$, because $[H^+]$ is more sensitive to changes in C_T due to the low buffer capacity there. Decreases in mean A_T further contribute to the increase in $\Delta_s \sigma_{H^+}^2$ in the high latitudes (green line in Fig. 9b). In the low-to-mid latitudes and in particular in the Atlantic Ocean, mean surface

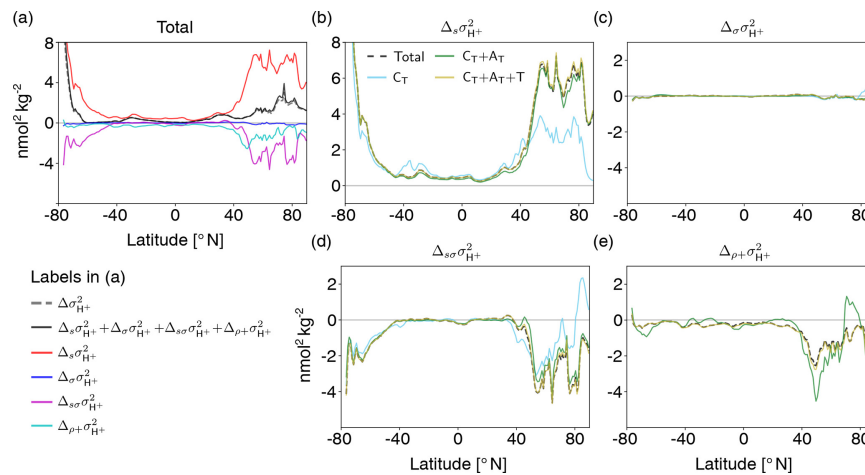


Figure 9. Decomposition of surface $[H^+]$ variability changes into different drivers (C_T , A_T , temperature, and salinity). Shown are changes from the preindustrial period to 2081–2100 following the RCP8.5 scenario. The simulated change in $[H^+]$ variance ($\Delta\sigma_{H^+}^2$) is decomposed into the contribution from changes in the sensitivities that arise from changes in the drivers' mean values ($\Delta_s\sigma_{H^+}^2$), the contribution from changes in the drivers' standard deviations ($\Delta_\sigma\sigma_{H^+}^2$), the contribution from simultaneous changes in the sensitivities and the drivers' standard deviations ($\Delta_{s\sigma}\sigma_{H^+}^2$), and the contribution from correlation changes alone together with simultaneous changes in correlations and sensitivities and standard deviations ($\Delta_{\rho+\sigma}\sigma_{H^+}^2$) (a). The small mismatch between the sum of the components (black line) and simulated variance change (gray dashed line) arises because the decomposition is based on Eq. (2), which is an approximation to simulated $[H^+]$ variance. The contributions to these components from changes in C_T alone (light blue lines); from changes in C_T and A_T (green lines); and from C_T , A_T , and temperature (gold lines) are shown in panels (b)–(e). The dashed black lines in panels (b)–(e) show the total components that contain contributions from all four drivers.

A_T is projected to increase (Fig. A5) and therefore dampens the overall increase in $\Delta_s\sigma_{H^+}^2$ (green line in Fig. 9b). The changes in A_T are largely due to changes in freshwater cycling that also manifest in salinity changes (Fig. A5, Carter et al., 2016). Increases in temperature additionally increase $\Delta_s\sigma_{H^+}^2$, mainly in the northern mid-to-high latitudes (gold line in Fig. 9b), but the overall impact of mean changes in temperature, and especially salinity, is small.

Why is the increase in $\Delta\sigma_{H^+}^2$ (gray dashed or black solid line in Fig. 9a) smaller than the increase from the mean changes (i.e., $\Delta_s\sigma_{H^+}^2$; red line in Fig. 9a)? In the high latitudes, the projected change in the variability of the drivers (Fig. A6) contributes negatively to the $[H^+]$ variability change and counteracts to some degree the increase in $\Delta_s\sigma_{H^+}^2$. These variability changes alone have a small imprint on $\Delta_\sigma\sigma_{H^+}^2$ (blue line in Fig. 9a; black dashed line in Fig. 9c), but the variability changes dampen the increases from the mean changes ($\Delta_{s\sigma}\sigma_{H^+}^2$, magenta line in Fig. 9a, black dashed line in Fig. 9d). The latter contribution is large in the high latitudes, where mean changes alone would lead to a strong increase. In the high latitudes, decreases in C_T variability (Fig. A6a) together with increases in mean C_T (Fig. A5a) can explain much of the negative contribution from $\Delta_{s\sigma}\sigma_{H^+}^2$ (light blue line in Fig. 9d). In the northern high latitudes, mean and variability changes in A_T are also impor-

tant for $\Delta_{s\sigma}\sigma_{H^+}^2$ (green line in Fig. 9d). The additional contribution from changes in the correlations between the drivers ($\Delta_{\rho+\sigma}\sigma_{H^+}^2$; cyan line in Fig. 9a) also tends to contribute negatively to $[H^+]$ variability changes, especially in the North Atlantic, and changes in correlations with temperature play an important role (gold line in Fig. 9e). In summary, the increase in $[H^+]$ variability at the surface is mainly caused by increases in mean C_T attenuated by decreases in C_T variability in the high latitudes. Mean changes in A_T reinforce the increase in $[H^+]$ variability in the northern high latitudes but dampen the increase in the low latitudes.

At 200 m, the projected increase in $\Delta\sigma_{H^+}^2$ (gray dashed or black solid line in Fig. 10a) is also a result of the large increase due to the mean changes in the drivers ($\Delta_s\sigma_{H^+}^2$; red line in Fig. 10a; dashed black line in Fig. 10b) and the decrease due to the interplay between mean changes and decreases in the variability ($\Delta_{s\sigma}\sigma_{H^+}^2$; magenta line in Fig. 10a, black dashed line in Fig. 10d). Similar to the surface, the changes in mean and variability of C_T are the most important drivers of changes (light blue lines in Fig. 10b, d). Increases in mean A_T partially compensate for the increase in $[H^+]$ variability due to the increase in mean C_T (green lines in Fig. 10b, d). Changes in $[H^+]$ variability due to changes in temperature and salinity are small. In contrast to the surface, the individual compensating contributions to

$[\text{H}^+]$ variability change from mean changes and simultaneous mean and variability changes in the drivers, in particular those in C_T , are much larger at 200 m. The global average variance change due to the mean changes in the drivers ($\Delta_s \sigma_{\text{H}^+}^2 = 3.7 \text{ nmol}^2 \text{ kg}^{-2}$) is much larger than the overall simulated variance change ($\Delta \sigma_{\text{H}^+}^2 = 0.1 \text{ nmol}^2 \text{ kg}^{-2}$). The contribution from changes in the correlations between the drivers is overall small (cyan line in Fig. 10a) and stems mainly from changes in the correlation between C_T and A_T (Fig. 10e). Taken together, the increase in $[\text{H}^+]$ variability at 200 m mainly arises from the balance between increases in mean C_T and decreases in C_T variability. Increases in mean A_T dampen these changes.

Unlike for $[\text{H}^+]$, both mean changes ($\Delta_s \sigma_{\Omega}^2$; red lines in Fig. 11) and variability changes in the drivers ($\Delta \sigma_{\Omega}^2$; blue lines in Fig. 11) lead to a decrease in Ω_A variability ($\Delta \sigma_{\Omega}^2$; black dashed lines in Fig. 11). At 200 m, variability changes are even the dominant driver for reductions in Ω_A variability. Simultaneous changes in means and variabilities ($\Delta_s \sigma_{\Omega}^2$; purple lines in Fig. 11) contribute positively and dampen the reduction in Ω_A variability from mean and variability changes alone. Mean and variability changes in C_T are the main drivers for changes in Ω_A variability as indicated by the tight relation between the dashed and solid red, blue, and purple lines in Fig. 11, in particular at 200 m. An exception is the northern high latitudes, where A_T changes also play a substantial role at the surface (not shown). Correlation changes in the drivers ($\Delta_{\rho+\sigma_{\Omega}^2}$; cyan lines in Fig. 11) are of secondary importance and have the largest imprint in the northern mid-to-high latitudes at the surface.

4 Discussion and conclusions

We provide a first quantification of the historical and future changes in extreme events in ocean acidity by analyzing daily mean three-dimensional output from a five-member ensemble simulation of a comprehensive Earth system model. In our analysis, we focus on changes in high- $[\text{H}^+]$ and low- Ω_A extreme events that are defined with respect to a shifting baseline, where changes in extremes arise from changes in daily to interannual variability. Secular trends in the mean state were removed from the model output before analyzing extremes under this approach. We show that such extreme events in $[\text{H}^+]$ are projected to become more frequent, longer lasting, more intense, and spatially more extensive under increasing atmospheric CO_2 concentration, both at the surface and also within the thermocline. Under RCP2.6, the increase in these extreme-event characteristics is substantially smaller than under RCP8.5. The increase in $[\text{H}^+]$ variability is a consequence of increased sensitivity of $[\text{H}^+]$ to variations in its drivers. It is mainly driven by the projected increase in mean C_T and additionally altered by changes in C_T variability and A_T mean and variability as well as changes in the correlations between the drivers. In contrast to $[\text{H}^+]$, variability of

Ω_A is projected to decline in the future. Therefore, extreme events in Ω_A are projected to become less frequent in the future when defined with respect to a shifting baseline. The reason for the decline in variability is that Ω_A , unlike $[\text{H}^+]$, becomes less sensitive to variations in the drivers with the mean increase in C_T . Furthermore, the projected reductions in the drivers' variabilities, mainly in C_T , further reduce Ω_A variability.

The analysis of extreme events defined with respect to fixed preindustrial percentiles reveals that the secular trends in $[\text{H}^+]$ and Ω_A are so large that they lead to year-round or almost-year-round extreme events in the upper 200 m over the entire globe by the end of the 21st century, even under the low-emission scenario RCP2.6. Extreme events are no longer temporally and spatially bounded events that arise due to the chaotic nature of the climate system but describe a permanent new state. Under the fixed baseline approach, the relative contribution of changes in variability or higher moments of the distribution to the changes in the number of extremes is small. For example, the number of yearly extreme days for surface $[\text{H}^+]$ over the 1986–2005 period under the shifting-baseline approach is only 3.8 % of that when defining the extreme events with respect to a fixed preindustrial baseline. This fraction differs regionally, reaching more than 10 % in the North Pacific, the North Atlantic, and the Arctic Ocean. However, we recall here that the changes in the number of $[\text{H}^+]$ extremes when defined with respect to a shifting baseline are large. These changes in variability may need to be taken into account when assessing the impacts of ocean acidity changes on marine organisms, especially when organisms are likely to adapt to the long-term mean changes but not to changes in variability.

We use the 99th percentile of the distribution from a preindustrial simulation for the definition of the extreme $[\text{H}^+]$ events (i.e., a one-in-a-hundred-days event at preindustrial levels), but the results may depend on the choice of this threshold. We tested the sensitivity of our results under the shifting-baseline approach by using also the 99.99th percentile threshold (i.e., a one-day-in-27.4-years event at preindustrial levels). The relative increase in the numbers of extreme $[\text{H}^+]$ days per year is larger for these rare extremes (Fig. 12). For example, nearly every second day with $[\text{H}^+]$ exceeding the 99th percentile (red solid lines in Fig. 12) is also a day with $[\text{H}^+]$ exceeding the 99.99th percentile (red dotted lines in Fig. 12) by the end of the 21st century under RCP8.5, both at the surface and at depth. As a result of this large relative increase in rare extremes, the model projects as many days with $[\text{H}^+]$ exceeding the 99.99th percentile by the end of the century under RCP8.5 (red dotted lines in Fig. 12) as it projects days exceeding the 99th percentile under RCP2.6 (blue solid lines in Fig. 12).

The projected increase in $[\text{H}^+]$ variability and decrease in Ω_A variability also alters the occurrence of extreme events based on absolute thresholds. An often used threshold is $\Omega_A = 1$, below which seawater is corrosive with re-

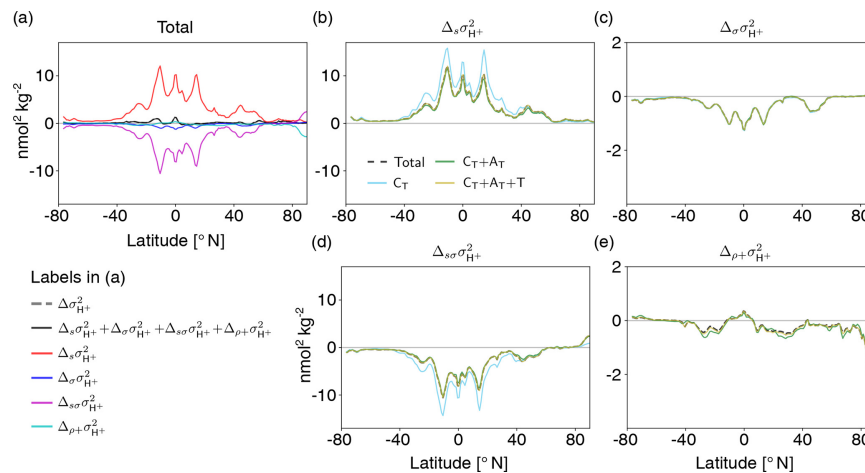


Figure 10. Decomposition of $[H^+]$ variability changes at 200 m into different drivers (C_T , A_T , temperature, and salinity). Shown are changes from the preindustrial period to 2081–2100 following the RCP8.5 scenario. The simulated change in $[H^+]$ variance ($\Delta\sigma_{H^+}^2$) is decomposed into the contribution from changes in the sensitivities that arise from changes in the drivers' mean values ($\Delta_s\sigma_{H^+}^2$), the contribution from changes in the drivers' standard deviations ($\Delta_\sigma\sigma_{H^+}^2$), the contribution from simultaneous changes in the sensitivities and the drivers' standard deviations ($\Delta_{s\sigma}\sigma_{H^+}^2$), and the contribution from correlation changes alone together with simultaneous changes in correlations and sensitivities and standard deviations ($\Delta_{\rho+\sigma}\sigma_{H^+}^2$) (a). The contributions to these components from changes in C_T alone (light blue lines); from changes in C_T and A_T (green lines); and from C_T , A_T , and temperature (gold lines) are shown in panels (b)–(e). The dashed black lines in panels (b)–(e) show the total components that contain contributions from all four drivers.

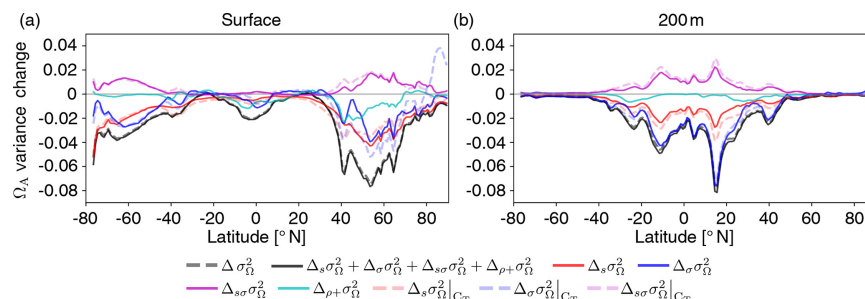


Figure 11. Decomposition of Ω_A variability changes into different drivers. The simulated zonal mean contribution to variance changes in Ω_A (black dashed lines, $\Delta\sigma_{\Omega}^2$) from the preindustrial period to 2081–2100 (RCP8.5) at the surface (a) and at 200 m (b). Shown is the contribution from sensitivity changes (due to mean changes in the drivers) (red lines, $\Delta_s\sigma_{\Omega}^2$), standard deviation changes in the drivers (blue lines, $\Delta_\sigma\sigma_{\Omega}^2$), simultaneous changes in sensitivities and standard deviations (purple lines, $\Delta_{s\sigma}\sigma_{\Omega}^2$), and all contributions that involve changes in the drivers' correlations (cyan lines, $\Delta_{\rho+\sigma}\sigma_{\Omega}^2$). Furthermore, contributions from mean changes, standard deviation changes, and simultaneous mean and standard deviation changes in C_T alone are shown (dashed red, blue, and purple lines, respectively).

spect to the calcium carbonate mineral aragonite (Morse and Mackenzie, 1990). We assess the influence of the general decline in Ω_A variability at the time where a grid cell falls below $\Omega_A = 1$ for the first time. To do so, we compare these times within the historical and RCP8.5 ensemble to those for the hypothetical case where Ω_A variability stays at the preindustrial level but mean Ω_A undergoes the ensemble-mean evolution. We find that the decline in Ω_A variability, which is observed in the historical and RCP8.5 ensemble,

leads to an average delay of the first occurrence of undersaturation by about 11 years at the surface and about 16 years at 200 m. At the surface, these delays of undersaturation occur throughout the high latitudes (Fig. 13a). At depth, the delays are most pronounced in the tropics (Fig. 13b), but delays also occur in the high latitudes. Assuming unchanged seasonality, McNeil and Matear (2008) found that seasonal aragonite undersaturation of surface waters in the Southern Ocean may occur 30 years earlier than annual mean aragonite undersat-

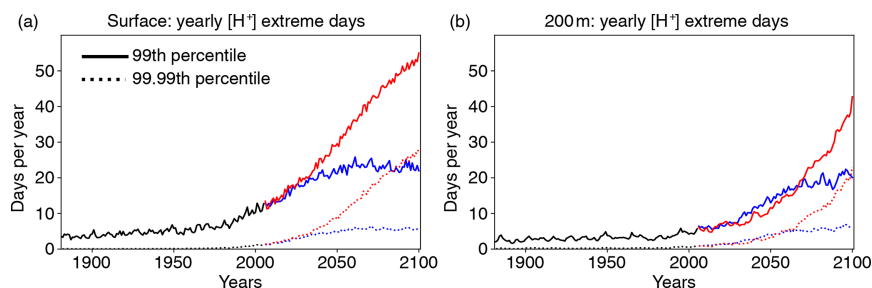


Figure 12. Globally averaged number of yearly extreme days for $[H^+]$ over the historical (black lines), RCP2.6 (blue), and RCP8.5 (red) simulations for the preindustrial 99th (solid lines) and 99.99th percentile (dotted lines) at the surface (a) and 200 m (b). The extreme events are defined with respect to shifting baselines.

uration. However, our simulation shows that the reduction in Ω_A variability delays the onset of undersaturation by about 10 to 15 years in the Southern Ocean relative to a hypothetical simulation where variability does not change. Therefore, changes in variability need to be taken into account when projecting the onset of seasonal undersaturation, especially in the high latitudes and in the thermocline of the tropics.

Previous studies have shown that the seasonal cycle of surface ocean pCO_2 will be strongly amplified under increasing atmospheric CO_2 (Gallego et al., 2018; Landschützer et al., 2018; McNeil and Sasse, 2016) and that a similar amplification is expected for surface $[H^+]$ (Kwiatkowski and Orr, 2018). Here we show that the changes in the seasonal cycle of $[H^+]$ translate into large increases in short-term extreme acidity events at the surface as well as at 200 m, when these events are defined with respect to a shifting baseline. In addition to earlier studies, we also show that changes in subannual variability, which are only partially resolved by monthly mean data, contribute to changes in extreme events in $[H^+]$ under increasing atmospheric CO_2 . Furthermore, we show that the average duration of extreme events at the surface and in recent past conditions (1986–2005) is about 15 d. To resolve such events that last for days to weeks, it is necessary to use daily mean output. Currently, ocean carbonate system variables from models that participate in the sixth phase of the Coupled Model Intercomparison Project are routinely stored with a monthly frequency on the Earth system grid (Jones et al., 2016). We therefore recommend storing and using high-frequency output to study extreme events in the ocean carbonate systems.

Even though we consider our results as robust, a number of potential caveats remain. First, the horizontal resolution of the ocean model in the GFDL ESM2M model is rather coarse and cannot represent critical scales of small-scale circulation structures (e.g., Turi et al., 2018). In addition, the biogeochemical processes included in the GFDL ESM2M model are designed for the open ocean but do not capture the highly variable coastal processes (Hofmann et al., 2011). High-resolution ocean models with improved pro-

cess representations are therefore needed to explore variability in ocean carbonate chemistry, especially in coastal regions and smaller ocean basins, such as the Arctic (Terhaar et al., 2019a, b). Observation-based carbonate system data with daily mean resolution would also be necessary to thoroughly evaluate the models' capability to represent day-to-day variations in carbonate chemistry. Secondly, our results, in particular at the local scale, might depend on the model formulation. As the mean increases in C_T mainly drive the increases in $[H^+]$ variability (see Fig. 9b), we expect that models with larger oceanic uptake of anthropogenic carbon show larger increases in $[H^+]$ variability than models with lower anthropogenic carbon uptake. The GFDL ESM2M model matches observation-based estimates of historical global anthropogenic CO_2 uptake relatively well but still has difficulties in representing the regional patterns in storage (Frölicher et al., 2015). Therefore, the exact regional patterns of C_T changes may differ from model to model. Further studies focusing on the physical processes that lead to the regional C_T changes may help to better constrain the regional patterns in variability changes. In addition, it is currently rather uncertain how $[H^+]$ and Ω_A variability changes as a result of changes in the drivers' variabilities. We have demonstrated that this factor is particularly important for Ω_A and for $[H^+]$ at depth. It is well known that current Earth system models have imperfect or uncertain representations of ocean variability over a range of timescales (Keller et al., 2014; Resplandy et al., 2015; Frölicher et al., 2016). A possible way forward would be to assess variability changes and changes in ocean acidity extreme events within a multimodel ensemble, which would likely provide upper and lower bounds. Finally, it is assumed that physical and biogeochemical changes in the ocean will also increase diurnal variability. In particular in coastal areas, such diurnal variations can have amplitudes that are much larger than the projected changes over the 21st century (Hofmann et al., 2011). However, the GFDL ESM2M model does not fully resolve the diurnal variability. Future studies with Earth system models that resolve diurnal processes are needed to quantify changes in diurnal vari-

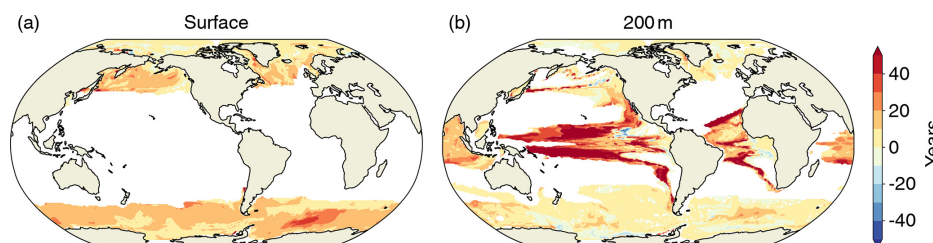


Figure 13. The difference in years between the first occurrence of aragonite undersaturation in the historical and RCP8.5 ensemble and a hypothetical simulation where variability does not change over the 1861–2100 period, but only the mean changes. Positive values (yellow and red) indicate a delayed onset of undersaturation resulting from declines in Ω_A variability.

ability and the impacts of these changes on extreme acidity events.

Our results may also have important consequences for our understanding of the impacts of ocean acidification on marine organisms and ecosystems. The projected increase in the frequency and the duration of ocean acidity extremes implies that marine organisms will have less time to recover from high- $[\text{H}^+]$ events in the future. Organisms that cannot adapt to the large long-term changes in mean $[\text{H}^+]$ will likely be the most impacted. However, even if organisms may be able to adapt to the long-term increase in $[\text{H}^+]$, the large projected increase in $[\text{H}^+]$ extreme events due to changes in variability may push organisms and ecosystems to the limits of their resilience, especially those organisms that are commonly accustomed to a more steady environment. The risks for substantial ecosystem impacts are aggravated by the fact that the frequency and intensity of marine heatwaves are also projected to substantially increase (Frölicher et al., 2018), which also negatively impact marine ecosystems (Wernberg et al., 2016; Smale et al., 2019). The interactions of intensified multiple stressors have the potential to influence marine ecosystems and the ocean's biogeochemical cycles in an unprecedented manner (Gruber, 2011). However, further research is needed to understand the combined impacts of short-term ocean acidity extremes and marine heatwaves on marine ecosystems.

In conclusion, our analysis shows that $[\text{H}^+]$ and Ω_A in the upper 200 m are projected to be almost permanently under extreme conditions by the end of the 21st century when extremes are defined relative to preindustrial baselines. Even when accounting for the changes in the long-term mean, short-term extreme events in $[\text{H}^+]$ are projected to become more frequent, to last longer, to be more intense, and to cover larger volumes of seawater due to increases in $[\text{H}^+]$ variability, potentially adding to the stress on organisms and ecosystems from the long-term increase in ocean acidity.

Appendix A: Identifying and removing the secular trend in the model data

In Sect. 3.2 and 3.3, we analyze the changes in extreme events in $[H^+]$ and Ω_A that arise from day-to-day to interannual variability changes in these variables. We therefore need to remove the secular trends from the data prior to analysis. We estimate the secular trend in a simulation from the five-member ensemble mean, assuming that subannual and interannual to decadal variations in the individual ensemble members are phased randomly and do not imprint on the ensemble mean because they average out. A larger ensemble size would be necessary for this assumption to perfectly hold. However, this potential source of error does not qualitatively alter our results. We remove the seasonal cycle, here defined as the 365 d long mean evolution over the course of a year, from the ensemble mean by smoothing the ensemble mean with a 365 d running mean filter, i.e., by calculating the convolution of the time series with a rectangular window of length 365 and height $1/365$. This filter also removes variability on subannual and interannual timescales and thereby also reduces the error we make due to the small ensemble size that is discussed above. We then subtract the running-mean-filtered ensemble mean from the five ensemble members to remove the secular trend in the individual ensemble members.

Table A1. Simulated global ensemble-mean Ω_A extreme-event characteristics, when extremes are defined with respect to a shifting baseline. Values in brackets denote ensemble minima and maxima.

	PI	1986–2005	2081–2100 RCP2.6	2081–2100 RCP8.5
Yearly extreme days surface (days per year)	3.65	1.8 (1.5–2.2)	2.2 (1.9–2.9)	1.4 (1.1–1.7)
200 m (days per year)	3.65	2.0 (1.5–2.8)	3.0 (2.3–3.7)	1.7 (1.4–2.0)
Duration surface (days)	19.7	17.8 (16.8–18.9)	19.4 (18.1–21.1)	29.3 (27.4–32.6)
200 m (days)	38.6	66.1 (59.7–84.4)	98.7 (89.0–109.0)	111.6 (106.6–122.7)
Maximal intensity surface ($\times 10^{-3}$)	2.9	3.4 (3.3–3.6)	3.2 (3.1–3.5)	1.5 (1.4–1.6)
200 m ($\times 10^{-3}$)	3.3	5.0 (3.9–6.7)	7.9 (6.1–11.1)	6.0 (2.9–9.1)
Volume ($\times 10^3$ km ³)	3.6	3.2 (2.9–3.5)	3.7 (3.0–4.2)	3.4 (3.1–3.7)

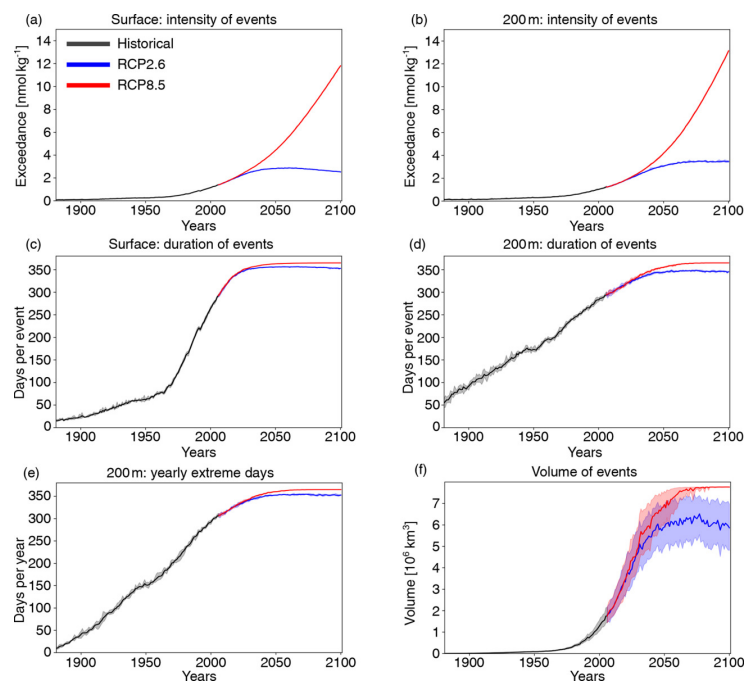


Figure A1. Simulated globally averaged changes in $[H^+]$ extreme events defined with respect to the fixed preindustrial baseline. Shown are changes over the 1861–2100 period following historical (black lines) and future RCP8.5 (red) and RCP2.6 (blue) scenarios for maximal intensity at the surface (a) and at 200 m (b), duration at the surface (c) and at 200 m (d), yearly extreme days at 200 m (e), and volume in the upper 200 m (f). The thick lines display the five-member ensemble means, and the shaded areas represent the maximum and minimum ranges of the individual ensemble members.

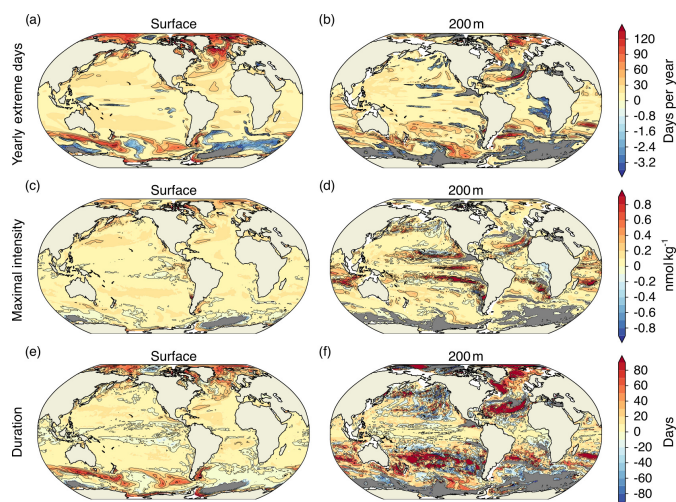


Figure A2. Simulated regional changes in $[H^+]$ extreme-event characteristics between the preindustrial period and 2081–2100 following the RCP2.6 scenario. The extreme events are defined with respect to shifting baselines. Shown are the changes in yearly extreme days (a, b), maximal intensity (c, d), and duration (e, f). Left panels show changes for the surface, whereas right panels show changes for 200 m. Shown are changes averaged over all five ensemble members. The black contours highlight the pattern structures. Gray areas represent areas with no extremes during 2081–2100.

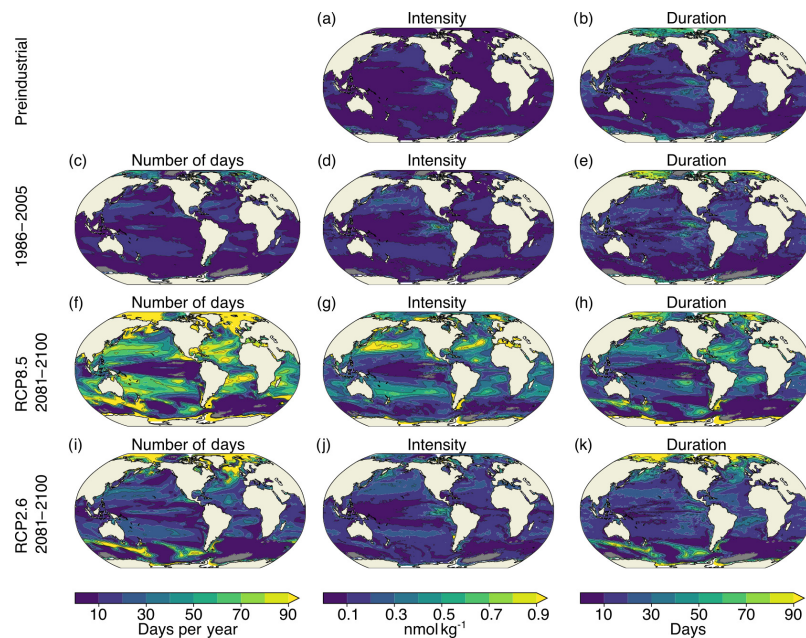


Figure A3. Simulated characteristics of surface $[H^+]$ extreme events for the preindustrial period (a, b), 1986–2005 ensemble mean (c–e), RCP8.5 2081–2100 ensemble mean (f–h), and RCP2.6 2081–2100 ensemble mean (i–k). The extreme events are defined with respect to shifting baselines. Gray colors represent regions where no ensemble member simulates extremes. The black contours highlight the pattern structures.

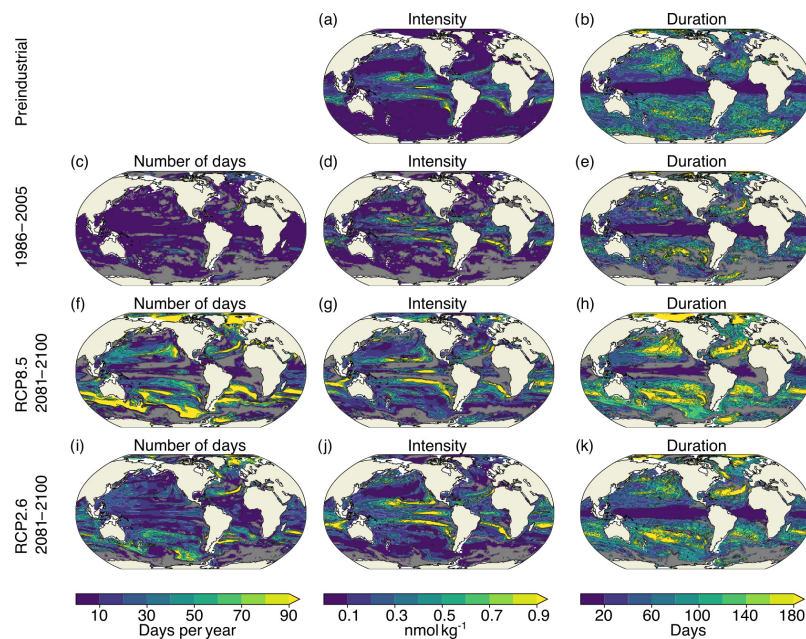


Figure A4. Simulated characteristics of $[H^+]$ extreme events at 200 m for the preindustrial period (a, b), 1986–2005 ensemble mean (c–e), RCP8.5 2081–2100 ensemble mean (f–h), and RCP2.6 2081–2100 ensemble mean (i–k). The extreme events are defined with respect to shifting baselines. Gray colors represent regions where no ensemble member simulates extremes. The black contours highlight the pattern structures.

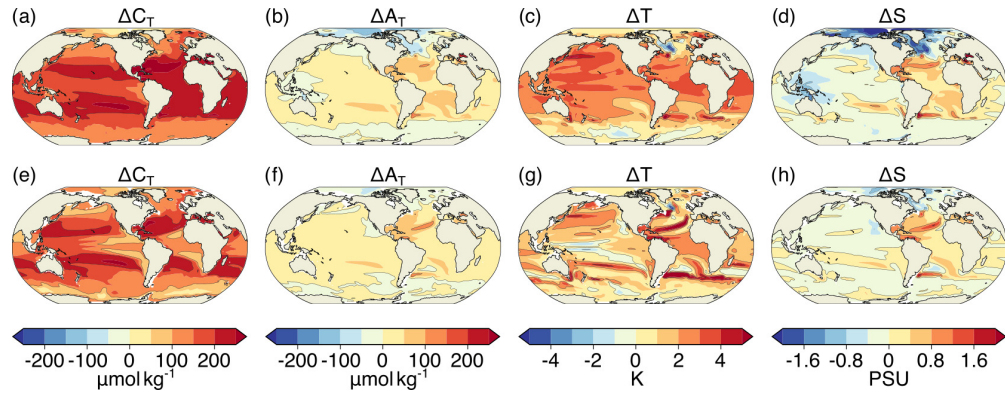


Figure A5. Simulated ensemble-mean changes in mean C_T (a, e), A_T (b, f), T (c, g), and S (d, h) from the preindustrial period to 2081–2100 following the RCP8.5 scenario. Shown are changes for (a–d) the surface and (e–h) at 200 m. The black contours highlight the pattern structures.

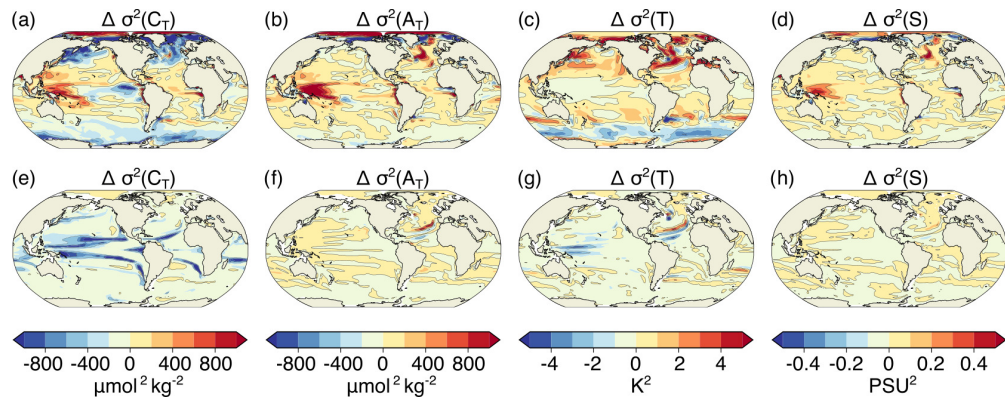


Figure A6. Simulated ensemble-mean changes in the variances of C_T (a, e), A_T (b, f), T (c, g), and S (d, h) from the preindustrial period to 2081–2100 under the RCP8.5 scenario. Shown are changes for (a–d) the surface and (e–h) at 200 m. The black contours highlight the pattern structures.

Appendix B: Identifying interannual and subannual variability

The spectral density describes how the variance in a time series is distributed over different frequencies ν_j . It is proportional to the absolute value squared of the discrete Fourier transformation (DFT) of the time series. Defining the spectral density only for positive frequencies, it is given by

$$f(\nu_j) = 2 \frac{\Delta t^2}{T} \left| \sum_{k=1}^N x_k \cdot \exp(-i2\pi\nu_j \cdot \Delta t k) \right|^2, \quad (\text{B1})$$

with N the number of time steps, x_k the values of the time series at each time step, Δt the time interval between two time steps, $T = N \cdot \Delta t$, and the frequencies $\nu_j = j/T$. The autocovariance is the inverse Fourier transform of the spectral density (Wiener–Khinchine theorem, Chatfield, 1996). In the continuous case, the theorem states

$$\gamma(\tau) = \int_{-\infty}^{\infty} \tilde{f}(\nu) \exp(i2\pi\nu\tau) d\nu, \quad (\text{B2})$$

with the autocovariance function $\gamma(\tau)$ and the spectral density \tilde{f} defined for positive and negative frequencies. Since the two-sided spectral density, \tilde{f} , is a real and even function, one can also use

$$\gamma(\tau) = \int_0^{\infty} f(\nu) \cos(2\pi\nu\tau) d\nu \quad (\text{B3})$$

with the one-sided spectral density $f = 2 \cdot \tilde{f}$ that is used in this text. As a consequence, the variance within the time series, given by the autocovariance at lag zero, is obtained by integrating the spectral density over all positive frequencies, $\sigma^2 = \int_0^{\infty} f(\nu) d\nu$. For a discrete time series, where the maximal resolved frequency is given by $\nu_{\max} = 1/2\Delta t$, the identity reads

$$\sigma^2 = \sum_{j=0}^{N/2} f(\nu_j) \frac{1}{N\Delta t}. \quad (\text{B4})$$

Based on this equation, one can separate the contributions to variance from low-frequency and high-frequency variations. In this study, we determine interannual variability and subannual variability. Interannual variability is calculated by summing over the contributions to variance from all frequencies up to a cycle of once per year, i.e., by evaluating the sum up to i_{cut} for which $\nu_{\text{cut}} = 1/365 \text{ d}^{-1}$. Accordingly, subannual variability is obtained by evaluating the sum from $i_{\text{cut}} + 1$ to $N/2$. Prior to this separation, the seasonal variability is removed from the data by subtracting the 365 d climatology.

Appendix C: Decomposition of $[\text{H}^+]$ variance change

Following Eq. (2) in the main text, the variance in $[\text{H}^+]$ (or Ω_{A}) can be approximated as a function of the four sensitivities

$$s = \left(\frac{\partial H^+}{\partial A_{\text{T}}}, \frac{\partial H^+}{\partial C_{\text{T}}}, \frac{\partial H^+}{\partial S}, \frac{\partial H^+}{\partial T} \right)^{\text{T}} \quad (\text{C1})$$

that in turn depend on the mean values of the drivers, the four standard deviations of the drivers

$$\sigma = (\sigma_{A_{\text{T}}}, \sigma_{C_{\text{T}}}, \sigma_S, \sigma_T)^{\text{T}}, \quad (\text{C2})$$

and the six pairwise correlation coefficients, in matrix notation given by

$$\rho = \begin{pmatrix} 1 & \rho_{AC} & \rho_{AS} & \rho_{AT} \\ \rho_{AC} & 1 & \rho_{CS} & \rho_{CT} \\ \rho_{AS} & \rho_{CS} & 1 & \rho_{ST} \\ \rho_{AT} & \rho_{CT} & \rho_{ST} & 1 \end{pmatrix}. \quad (\text{C3})$$

Based on this notation, we can rewrite Eq. (2) of the main text as

$$\sigma_{\text{H}^+}^2 = \sum_{i=1}^4 \sum_{j=1}^4 s_i s_j \sigma_i \sigma_j \rho_{ij}. \quad (\text{C4})$$

We use Eq. (C4) and decompose the variability change between the preindustrial period and 2081–2100 into the contributions from changes in s , σ , and ρ based on a Taylor expansion. Since $[\text{H}^+]$ variance represented by Eq. (C4) is a polynomial of fifth order in these variables, its Taylor series has five nonvanishing orders. We use the drivers' standard deviations instead of their variances for the decomposition. With the latter, the Taylor expansion would have infinite terms and could not be decomposed exactly as it is done in the following. However, it would asymptotically lead to the same decomposition of $[\text{H}^+]$ variance change into $\Delta_s \sigma_{\text{H}^+}^2$, $\Delta_{\sigma} \sigma_{\text{H}^+}^2$, $\Delta_{s\sigma} \sigma_{\text{H}^+}^2$, and $\Delta_{\rho} \sigma_{\text{H}^+}^2$ that is presented below. Furthermore, it should be noted that the resulting decomposition of $[\text{H}^+]$ variance change only approximates the simulated variance change because it is based on Eq. (C4), which itself is based on a first-order Taylor expansion of $[\text{H}^+]$ with respect to the drivers.

In the following, all terms of the Taylor series are given. We denote the sum of first-order terms that contain changes in the four sensitivities $\Delta s_{1,\dots,4}$ by $\Delta_s^{(1)} \sigma_{\text{H}^+}^2$, the sum of second-order terms that contain changes in the sensitivities and standard deviations by $\Delta_{s\sigma}^{(2)} \sigma_{\text{H}^+}^2$, and so on.

The first order is given by $\Delta^{(1)}\sigma_{\text{H}^+}^2 = \Delta_s^{(1)}\sigma_{\text{H}^+}^2 + \Delta_\sigma^{(1)}\sigma_{\text{H}^+}^2$ with

$$\begin{aligned}\Delta_s^{(1)}\sigma_{\text{H}^+}^2 &= 2 \sum_{k=1}^4 \sum_{j=1}^4 s_j \sigma_k \sigma_j \rho_{kj} \Delta s_k, \\ \Delta_\sigma^{(1)}\sigma_{\text{H}^+}^2 &= 2 \sum_{k=1}^4 \sum_{j=1}^4 s_k s_j \sigma_j \rho_{kj} \Delta \sigma_k, \\ \Delta_\rho^{(1)}\sigma_{\text{H}^+}^2 &= \sum_{k=1}^4 \sum_{l=1}^4 s_k s_l \sigma_k \sigma_l \Delta \rho_{kl}.\end{aligned}\quad (\text{C5})$$

The second order contains

$$\begin{aligned}\Delta_{ss}^{(2)}\sigma_{\text{H}^+}^2 &= \sum_{k=1}^4 \sum_{l=1}^4 \sigma_k \sigma_l \rho_{kl} \Delta s_k \Delta s_l, \\ \Delta_{\sigma\sigma}^{(2)}\sigma_{\text{H}^+}^2 &= \sum_{k=1}^4 \sum_{l=1}^4 s_k s_l \rho_{kl} \Delta \sigma_k \Delta \sigma_l, \\ \Delta_{s\sigma}^{(2)}\sigma_{\text{H}^+}^2 &= 2 \sum_{k=1}^4 \sum_{l=1}^4 (s_l \sigma_l \rho_{kl} \Delta s_k \Delta \sigma_k + s_l \sigma_k \rho_{kl} \Delta s_k \Delta \sigma_l), \\ \Delta_{s\rho}^{(2)}\sigma_{\text{H}^+}^2 &= 2 \sum_{k=1}^4 \sum_{l=1}^4 s_l \sigma_k \sigma_l \Delta s_k \Delta \rho_{kl}, \\ \Delta_{\sigma\rho}^{(2)}\sigma_{\text{H}^+}^2 &= 2 \sum_{k=1}^4 \sum_{l=1}^4 s_k s_l \sigma_l \Delta \sigma_k \Delta \rho_{kl}.\end{aligned}\quad (\text{C6})$$

The third-order terms read

$$\begin{aligned}\Delta_{ss\sigma}^{(3)}\sigma_{\text{H}^+}^2 &= 2 \sum_{k=1}^4 \sum_{l=1}^4 \sigma_l \rho_{kl} \Delta s_k \Delta s_l \Delta \sigma_k, \\ \Delta_{s\sigma\sigma}^{(3)}\sigma_{\text{H}^+}^2 &= 2 \sum_{k=1}^4 \sum_{l=1}^4 s_l \rho_{kl} \Delta s_k \Delta \sigma_k \Delta \sigma_l, \\ \Delta_{ss\rho}^{(3)}\sigma_{\text{H}^+}^2 &= \sum_{k=1}^4 \sum_{l=1}^4 \sigma_k \sigma_l \Delta s_k \Delta s_l \Delta \rho_{kl}, \\ \Delta_{\sigma\sigma\rho}^{(3)}\sigma_{\text{H}^+}^2 &= \sum_{k=1}^4 \sum_{l=1}^4 s_k s_l \Delta \sigma_k \Delta \sigma_l \Delta \rho_{kl}, \\ \Delta_{s\sigma\rho}^{(3)}\sigma_{\text{H}^+}^2 &= 2 \sum_{k=1}^4 \sum_{l=1}^4 (s_l \sigma_k \Delta s_k \Delta \sigma_l \Delta \rho_{kl} + s_l \sigma_l \Delta s_k \Delta \sigma_k \Delta \rho_{kl}).\end{aligned}\quad (\text{C7})$$

The fourth order reads

$$\begin{aligned}\Delta_{ss\sigma\sigma}^{(4)}\sigma_{\text{H}^+}^2 &= \sum_{k=1}^4 \sum_{l=1}^4 \rho_{kl} \Delta s_k \Delta s_l \Delta \sigma_k \Delta \sigma_l, \\ \Delta_{ss\sigma\rho}^{(4)}\sigma_{\text{H}^+}^2 &= 2 \sum_{k=1}^4 \sum_{l=1}^4 \sigma_l \Delta s_k \Delta s_l \Delta \sigma_k \Delta \rho_{kl}, \\ \Delta_{s\sigma\sigma\rho}^{(4)}\sigma_{\text{H}^+}^2 &= 2 \sum_{k=1}^4 \sum_{l=1}^4 s_l \Delta s_k \Delta \sigma_k \Delta \sigma_l \Delta \rho_{kl}.\end{aligned}\quad (\text{C8})$$

And the fifth order is given by

$$\Delta_{ss\sigma\sigma\rho}^{(5)}\sigma_{\text{H}^+}^2 = \sum_{k=1}^4 \sum_{l=1}^4 \Delta s_k \Delta s_l \Delta \sigma_k \Delta \sigma_l \Delta \rho_{kl}.\quad (\text{C9})$$

We identify the variance change from changes in the sensitivities as

$$\Delta_s\sigma_{\text{H}^+}^2 = \Delta_s^{(1)}\sigma_{\text{H}^+}^2 + \Delta_{ss}^{(2)}\sigma_{\text{H}^+}^2,\quad (\text{C10})$$

the change from standard deviation changes as

$$\Delta_\sigma\sigma_{\text{H}^+}^2 = \Delta_\sigma^{(1)}\sigma_{\text{H}^+}^2 + \Delta_{\sigma\sigma}^{(2)}\sigma_{\text{H}^+}^2,\quad (\text{C11})$$

the change from simultaneous changes in sensitivities and standard deviations as

$$\begin{aligned}\Delta_{s\sigma}\sigma_{\text{H}^+}^2 &= \Delta_{s\sigma}^{(2)}\sigma_{\text{H}^+}^2 + \Delta_{ss\sigma}^{(3)}\sigma_{\text{H}^+}^2 \\ &\quad + \Delta_{s\sigma\sigma}^{(3)}\sigma_{\text{H}^+}^2 + \Delta_{ss\sigma\sigma}^{(4)}\sigma_{\text{H}^+}^2,\end{aligned}\quad (\text{C12})$$

and that from correlation changes and mixed contributions that include correlation changes as

$$\begin{aligned}\Delta_{\rho+}\sigma_{\text{H}^+}^2 &= \Delta_{\rho}^{(1)}\sigma_{\text{H}^+}^2 + \Delta_{s\rho}^{(2)}\sigma_{\text{H}^+}^2 + \Delta_{\sigma\rho}^{(2)}\sigma_{\text{H}^+}^2 \\ &\quad + \Delta_{ss\rho}^{(3)}\sigma_{\text{H}^+}^2 + \Delta_{\sigma\sigma\rho}^{(3)}\sigma_{\text{H}^+}^2 + \Delta_{s\sigma\rho}^{(3)}\sigma_{\text{H}^+}^2 \\ &\quad + \Delta_{ss\sigma\rho}^{(4)}\sigma_{\text{H}^+}^2 + \Delta_{s\sigma\sigma\rho}^{(4)}\sigma_{\text{H}^+}^2 + \Delta_{ss\sigma\sigma\rho}^{(5)}\sigma_{\text{H}^+}^2.\end{aligned}\quad (\text{C13})$$

Finally, we calculate the analogs of Eqs. (C10)–(C13) that only take into account changes in C_T ; changes in C_T and A_T ; and changes in C_T , A_T , and T . This is done by calculating $\Delta s_{1,\dots,4}$ only based on mean changes in the considered variables and by setting the standard deviation changes in variables and correlation changes in pairs of variables that are not considered to zero.

Appendix D: Comparison of simulated ensemble-mean trends in seasonal amplitude to observation-based trends

We construct confidence intervals for the observation-based slope estimates following Hartmann et al. (2013). For the simulations, we use the arithmetic average of the five ensemble-member slope estimates, \hat{b}_k , as the estimator,

$$\hat{b} = \frac{1}{5} \sum_{k=1}^5 \hat{b}_k, \quad (\text{D1})$$

with estimated variance

$$\hat{\sigma}_{\hat{b}}^2 = \frac{1}{5^2} \sum_{k=1}^5 \hat{\sigma}_{b_k}^2. \quad (\text{D2})$$

We then construct the confidence interval for \hat{b} as

$$(\hat{b} - q \cdot \hat{\sigma}_{\hat{b}}, \hat{b} + q \cdot \hat{\sigma}_{\hat{b}}), \quad (\text{D3})$$

with q the $(1+p)/2$ quantile (we use $p=0.9$) of the t distribution with $5 \cdot (N-2)$ degrees of freedom. We correct the sample size N (34, the number of years we use for the fits) to a reduced sample size N_r when we find positive lag-one autocorrelation in the residuals of the fits (data – linear regression model). Lag-one autocorrelation is estimated as the average of the five ensemble-member lag-one autocorrelation estimates,

$$\hat{\rho} = \frac{1}{5} \sum_{k=1}^5 \hat{\rho}_k, \quad (\text{D4})$$

and we obtain $N_r = N \cdot (\hat{\rho} - 1)/(\hat{\rho} + 1)$. Positive $\hat{\rho}$ is only found in the northern high latitudes. This is in contrast to the observation-based case, where we find large positive $\hat{\rho}_o$ (up to 0.7) in the residuals of all latitude bands besides the tropical region.

For testing the significance of a difference between the simulation slope estimate \hat{b} and the observation-based estimate \hat{b}_o , we use Welch's test, which assumes different variances for the two estimates (Andrade and Estévez-Pérez, 2014). The variance of the simulation slope estimate is calculated by dividing the ensemble-averaged slope variance by the ensemble size (Eq. D2) and is hence smaller than the observation-based slope variance. If the absolute value of the test statistic

$$\frac{\hat{b} - \hat{b}_o}{\sqrt{\hat{\sigma}_{\hat{b}}^2 + \hat{\sigma}_o^2}} \quad (\text{D5})$$

is larger than the $(1+p)/2$ quantile of the t distribution with (Andrade and Estévez-Pérez, 2014)

$$\frac{(\hat{\sigma}_{\hat{b}}^2 + \hat{\sigma}_{b_o}^2)^2}{\hat{\sigma}_{\hat{b}}^4 / (5 \cdot (N_r - 2)) + \hat{\sigma}_{b_o}^4 / (N_{r,o} - 2)} \quad (\text{D6})$$

degrees of freedom, we consider the observation-based and simulation slope to be different from each other with a confidence level of $p=0.9$.

Data availability. The GFDL ESM2M model data underlying the figures and analyses are available under <https://zenodo.org/record/4032577> (Burger, 2020).

Author contributions. FAB and TLF designed the study. FAB performed the simulations, assisted by TLF and JGJ. FAB performed the analysis and wrote the initial manuscript. All authors contributed to the writing of the paper.

Competing interests. The authors declare that they have no conflict of interest.

Disclaimer. The work reflects only the authors' view; the European Commission and their executive agency are not responsible for any use that may be made of the information the work contains.

Acknowledgements. Friedrich A. Burger and Thomas L. Frölicher thank the CSCS Swiss National Supercomputing Centre for computing resources. The authors thank Elizabeth Drenkard, Fortunat Joos, and Jens Terhaar for discussions and comments; Rick Slater for the help in porting the ESM2M model code to CSCS; and James Orr, Sarah Schlunegger, Jean-Pierre Gattuso, and one anonymous reviewer for their excellent and insightful reviews.

Financial support. This research has been supported by the Swiss National Science Foundation (grant no. PP00P2_170687) and Horizon 2020 (COMFORT, Our common future ocean in the Earth system – quantifying coupled cycles of carbon, oxygen, and nutrients for determining and achieving safe operating spaces with respect to tipping points (grant no. 820989)).

Review statement. This paper was edited by Jean-Pierre Gattuso and reviewed by James Orr, Sarah Schlunegger, and one anonymous referee.

References

- Anderson, J. L., Balaji, V., Broccoli, A. J., Cooke, W. F., Delworth, T. L., Dixon, K. W., Donner, L. J., Dunne, K. A., Freidenreich, S. M., Garner, S. T., Gudgel, R. G., Gordon, C. T., Held, I. M., Hemler, R. S., Horowitz, L. W., Klein, S. A., Knutson, T. R., Kushner, P. J., Langenhost, A. R., Cheung, L. N., Liang, Z., Malyshev, S. L., Milly, P. C. D., Nath, M. J., Ploshay, J. J., Ramaswamy, V., Schwarzkopf, M. D., Shevliakova, E., Sirutis, J. J., Soden, B. J., Stern, W. F., Thompson, L. A., Wilson, R. J., Wittenberg, A. T., and Wyman, B. L.: The New GFDL Global Atmosphere and Land Model AM2–LM2: Evaluation with Prescribed SST Simulations, *J. Clim.*, 17, 4641–4673, <https://doi.org/10.1175/JCLI-3223.1>, 2004.
- Andrade, J. and Estévez-Pérez, M.: Statistical comparison of the slopes of two regression lines: A tutorial, *Anal. Chim. Acta*, 838, 1–12, <https://doi.org/10.1016/j.aca.2014.04.057>, 2014.
- Bakker, D. C. E., Pfeil, B., O'Brien, K. M., Currie, K. I., Jones, S. D., Landa, C. S., Lauvset, S. K., Metzl, N., Munro, D. R., Nakaoka, S.-I., Olsen, A., Pierrot, D., Saito, S., Smith, K., Sweeney, C., Takahashi, T., Wada, C., Wanninkhof, R., Alin, S. R., Becker, M., Bellerby, R. G. J., Borges, A. V., Boutin, J., Bozec, Y., Burger, E., Cai, W.-J., Castle, R. D., Cosca, C. E., DeGrandpre, M. D., Donnelly, M., Eiseid, G., Feely, R. A., Gkritzalis, T., González-Dávila, M., Goyet, C., Guillot, A., Hardman-Mountford, N. J., Hauck, J., Hoppema, M., Humphreys, M. P., Hunt, C. W., Ibáñez, J. S. P., Ichikawa, T., Ishii, M., Juranek, L. W., Kitidis, V., Körtzinger, A., Koffi, U. K., Kozyr, A., Kuwata, A., Lefèvre, N., Lo Monaco, C., Manke, A., Marrec, P., Mathis, J. T., Millero, F. J., Monacchi, N., Monteiro, P. M. S., Murata, A., Newberger, T., Nojiri, Y., Nonaka, I., Omar, A. M., Ono, T., Padín, X. A., Rehder, G., Rutgersson, A., Sabine, C. L., Salisbury, J., Santana-Casiano, J. M., Sasano, D., Schuster, U., Sieger, R., Skjelvan, I., Steinhoff, T., Sullivan, K., Sutherland, S. C., Sutton, A., Tadokoro, K., Telszewski, M., Thomas, H., Tilbrook, B., van Heuven, S., Vandemark, D., Wallace, D. W., and Woosley, R.: Surface Ocean CO₂ Atlas (SOCAT) V4, PANGAEA, <https://doi.org/10.1594/PANGAEA.866856>, 2016.
- Bednaršek, N., Tarling, G. A., Bakker, D. C. E., Fielding, S., Jones, E. M., Venables, H. J., Ward, P., Kuzirian, A., Lézé, B., Feely, R. A., and Murphy, E. J.: Extensive dissolution of live pteropods in the Southern Ocean, *Nat. Geosci.*, 5, 881–885, <https://doi.org/10.1038/ngeo1635>, 2012.
- Bednaršek, N., Feely, R. A., Reum, J. C. P., Peterson, B., Menkel, J., Alin, S. R., and Hales, B.: *Limacina helicina* shell dissolution as an indicator of declining habitat suitability owing to ocean acidification in the California Current Ecosystem, *P. R. Soc. B*, 281, 20140, <https://doi.org/10.1098/rspb.2014.0123>, 2014.
- Bindoff, N. L., Cheung, W. W. L., Kairo, J. G., Arístegui, J., Guinder, V. A., Hallberg, R., Hilmi, N., Jiao, N., Karim, M. S., Levin, L., O'Donoghue, S., Purca Cuicapusa, S. R., Rinkevich, B., Suga, T., Tagliabue, A., and Williamson, P.: Changing Ocean, Marine Ecosystems, and Dependent Communities, in: IPCC Special Report on the Ocean and Cryosphere in a Changing Climate, edited by: Pörtner, H.-O., Roberts, D. C., Masson-Delmotte, V., Zhai, P., Tignor, M., Poloczanska, E., Mintenbeck, K., Alegría, A., Nicolai, M., Okem, A., Petzold, J., Rama, B., and Weyer, N. M., in press, 2020.
- Bopp, L., Resplandy, L., Orr, J. C., Doney, S. C., Dunne, J. P., Gehlen, M., Halloran, P., Heinze, C., Ilyina, T., Séférián, R., Tjiputra, J., and Vichi, M.: Multiple stressors of ocean ecosystems in the 21st century: projections with CMIP5 models, *Biogeosciences*, 10, 6225–6245, <https://doi.org/10.5194/bg-10-6225-2013>, 2013.
- Britton, D., Cornwall, C. E., Revill, A. T., Hurd, C. L., and Johnson, C. R.: Ocean acidification reverses the positive effects of seawater pH fluctuations on growth and photosynthesis of the habitat-forming kelp, *Ecklonia radiata*, *Sci. Rep.*, 6, 26036, <https://doi.org/10.1038/srep26036>, 2016.
- Burger, F. A.: Data used for figures and tables in “Increase in ocean acidity variability and extremes under increasing atmospheric CO₂”, Zenodo, <https://doi.org/10.5281/zenodo.4032577>, 2020.

- Caldeira, K. and Wickett, M. E.: Anthropogenic carbon and ocean pH, *Nature*, 425, 365–365, <https://doi.org/10.1038/425365a>, 2003.
- Carter, B. R., Frölicher, T. L., Dunne, J. P., Rodgers, K. B., Slater, R. D., and Sarmiento, J. L.: When can ocean acidification impacts be detected from decadal alkalinity measurements?, *Global Biogeochem. Cy.*, 30, 595–612, <https://doi.org/10.1002/2015GB005308>, 2016.
- Carter, B. R., Feely, R. A., Williams, N. L., Dickson, A. G., Fong, M. B., and Takeshita, Y.: Updated methods for global locally interpolated estimation of alkalinity, pH, and nitrate, *Limnol. Oceanogr. Method.*, 16, 119–131, <https://doi.org/10.1002/lom3.10232>, 2018.
- Chatfield, C.: The analysis of time series – an introduction, Chapman & Hall/CRC, 5th Edn., 1996.
- Cheung, W. W. L. and Frölicher, T. L.: Marine heatwaves exacerbate climate change impacts for fisheries in the northeast Pacific, *Sci. Rep.*, 10, 6678, <https://doi.org/10.1038/s41598-020-63650-z>, 2020.
- Coles, S.: An Introduction to Statistical Modeling of Extreme Values, Springer-Verlag, London, 2001.
- Collins, M., Sutherland, M., Bouwer, L., Cheong, S.-M., Frölicher, T., Jacot Des Combes, H., Koll Roxy, M., Losada, I., McInnes, K., Ratter, B., Rivera-Arriaga, E., Susanto, R. D., Swingedouw, D., and Tibig, L.: Extremes, Abrupt Changes and Managing Risk, in: IPCC Special Report on the Ocean and Cryosphere in a Changing Climate, edited by: Pörtner, H.-O., Roberts, D. C., Masson-Delmotte, V., Zhai, P., Tignor, M., Poloczanska, E., Mintenbeck, K., Alegría, A., Nicolai, M., Okem, A., Petzold, J., Rama, B., and Weyer, N. M., in press, 2020.
- Cornwall, C. E., Comeau, S., DeCarlo, T. M., Larcombe, E., Moore, B., Giltrow, K., Puerzer, F., D’Alexis, Q., and McCulloch, M. T.: A coralline alga gains tolerance to ocean acidification over multiple generations of exposure, *Nat. Clim. Change*, 10, 143–146, <https://doi.org/10.1038/s41558-019-0681-8>, 2020.
- Dickson, A. and Millero, F.: A comparison of the equilibrium constants for the dissociation of carbonic acid in seawater media, *Deep-Sea Res. Pt. A*, 34, 1733–1743, [https://doi.org/10.1016/0198-0149\(87\)90021-5](https://doi.org/10.1016/0198-0149(87)90021-5), 1987.
- Dickson, A. and Riley, J.: The effect of analytical error on the evaluation of the components of the aquatic carbon-dioxide system, *Mar. Chem.*, 6, 77–85, [https://doi.org/10.1016/0304-4203\(78\)90008-7](https://doi.org/10.1016/0304-4203(78)90008-7), 1978.
- Doney, S. C., Fabry, V. J., Feely, R. A., and Kleydas, J. A.: Ocean Acidification: The Other CO₂ Problem, *Annu. Rev. Mar. Sci.*, 1, 169–192, <https://doi.org/10.1146/annurev.marine.010908.163834>, 2009.
- Dunne, J. P., John, J. G., Adcroft, A. J., Griffies, S. M., Hallberg, R. W., Shevliakova, E., Stouffer, R. J., Cooke, W., Dunne, K. A., Harrison, M. J., Krasting, J. P., Malyshev, S. L., Milly, P. C. D., Philipps, P. J., Sentman, L. T., Samuels, B. L., Spelman, M. J., Winton, M., Wittenberg, A. T., and Zadeh, N.: GFDL’s ESM2 Global Coupled Climate–Carbon Earth System Models, Part I: Physical Formulation and Baseline Simulation Characteristics, *J. Clim.*, 25, 6646–6665, <https://doi.org/10.1175/JCLI-D-11-00560.1>, 2012.
- Dunne, J. P., John, J. G., Shevliakova, E., Stouffer, R. J., Krasting, J. P., Malyshev, S. L., Milly, P. C. D., Sentman, L. T., Adcroft, A. J., Cooke, W., Dunne, K. A., Griffies, S. M., Hallberg, R. W., Harrison, M. J., Levy, H., Wittenberg, A. T., Phillips, P. J., and Zadeh, N.: GFDL’s ESM2 Global Coupled Climate–Carbon Earth System Models, Part II: Carbon System Formulation and Baseline Simulation Characteristics, *J. Clim.*, 26, 2247–2267, <https://doi.org/10.1175/JCLI-D-12-00150.1>, 2013.
- Fassbender, A. J., Rodgers, K. B., Palevsky, H. I., and Sabine, C. L.: Seasonal Asymmetry in the Evolution of Surface Ocean pCO₂ and pH Thermodynamic Drivers and the Influence on Sea–Air CO₂ Flux, *Global Biogeochem. Cy.*, 32, 1476–1497, <https://doi.org/10.1029/2017GB005855>, 2018.
- Feely, R., Chris, S., Hernandez-Ayon, J., Ianson, D., and Hales, B.: Evidence for Upwelling of Corrosive “Acidified” Water onto the Continental Shelf, *Science*, 320, 1490–1492, <https://doi.org/10.1126/science.1155676>, 2008.
- Fischer, E. M. and Knutti, R.: Anthropogenic contribution to global occurrence of heavy-precipitation and high-temperature extremes, *Nat. Clim. Change*, 5, 560–564, <https://doi.org/10.1038/nclimate2617>, 2015.
- Form, A. U. and Riebesell, U.: Acclimation to ocean acidification during long-term CO₂ exposure in the cold-water coral *Lophelia pertusa*, *Glob. Change Biol.*, 18, 843–853, <https://doi.org/10.1111/j.1365-2486.2011.02583.x>, 2012.
- Friedlingstein, P., Jones, M. W., O’Sullivan, M., Andrew, R. M., Hauck, J., Peters, G. P., Peters, W., Pongratz, J., Stith, S., Le Quéré, C., Bakker, D. C. E., Canadell, J. G., Ciais, P., Jackson, R. B., Anthoni, P., Barbero, L., Bastos, A., Bastrikov, V., Becker, M., Bopp, L., Buitenhuis, E., Chandra, N., Chevallier, F., Chini, L. P., Currie, K. I., Feely, R. A., Gehlen, M., Gilfillan, D., Gkritzalis, T., Goll, D. S., Gruber, N., Gutekunst, S., Harris, I., Haverd, V., Houghton, R. A., Hurtt, G., Ilyina, T., Jain, A. K., Joetzer, E., Kaplan, J. O., Kato, E., Klein Goldewijk, K., Korsbakken, J. I., Landschützer, P., Lauvset, S. K., Lefèvre, N., Lenton, A., Lienert, S., Lombardozi, D., Marland, G., McGuire, P. C., Melton, J. R., Metzl, N., Munro, D. R., Nabel, J. E. M. S., Nakaoka, S.-I., Neill, C., Omar, A. M., Ono, T., Peregon, A., Pierrot, D., Poulter, B., Rehder, G., Resplandy, L., Robertson, E., Rödenbeck, C., Séférian, R., Schwinger, J., Smith, N., Tans, P. P., Tian, H., Tilbrook, B., Tubiello, F. N., van der Werf, G. R., Wiltshire, A. J., and Zaehe, S.: Global Carbon Budget 2019, *Earth Syst. Sci. Data*, 11, 1783–1838, <https://doi.org/10.5194/essd-11-1783-2019>, 2019.
- Frölicher, T. L., Sarmiento, J. L., Paynter, D. J., Dunne, J. P., Krasting, J. P., and Winton, M.: Dominance of the Southern Ocean in Anthropogenic Carbon and Heat Uptake in CMIP5 Models, *J. Clim.*, 28, 862–886, <https://doi.org/10.1175/JCLI-D-14-00117.1>, 2015.
- Frölicher, T. L., Rodgers, K. B., Stock, C. A., and Cheung, W. W. L.: Sources of uncertainties in 21st century projections of potential ocean ecosystem stressors, *Global Biogeochem. Cy.*, 30, 1224–1243, <https://doi.org/10.1002/2015GB005338>, 2016.
- Frölicher, T. L., Fischer, E. M., and Gruber, N.: Marine heatwaves under global warming, *Nature*, 560, 360–364, <https://doi.org/10.1038/s41586-018-0383-9>, 2018.
- Frölicher, T. L., Ramseyer, L., Raible, C. C., Rodgers, K. B., and Dunne, J.: Potential predictability of marine ecosystem drivers, *Biogeosciences*, 17, 2061–2083, <https://doi.org/10.5194/bg-17-2061-2020>, 2020.
- Gallego, M. A., Timmermann, A., Friedrich, T., and Zeebe, R. E.: Drivers of future seasonal cycle changes in oceanic pCO₂,

- Biogeosciences, 15, 5315–5327, <https://doi.org/10.5194/bg-15-5315-2018>, 2018.
- Gattuso, J.-P. and Buddemeier, R. W.: Calcification and CO₂, *Nature*, 407, 311–313, <https://doi.org/10.1038/35030280>, 2000.
- Gehlen, M., Gruber, N., Gangstro, R., Bopp, L., and Oschlies, A.: Biogeochemical Consequences of Ocean Acidification and Feedback to the Earth System, chap. 12, in: *Ocean Acidification*, edited by: Gattuso, J.-P. and Hansson, L., Oxford University Press, 230–248, 2012.
- Good, S. A., Martin, M. J., and Rayner, N. A.: EN4: Quality controlled ocean temperature and salinity profiles and monthly objective analyses with uncertainty estimates, *J. Geophys. Res.-Ocean.*, 118, 6704–6716, <https://doi.org/10.1002/2013JC009067>, 2013.
- Gray, A. R., Johnson, K. S., Bushinsky, S. M., Riser, S. C., Russell, J. L., Talley, L. D., Wanninkhof, R., Williams, N. L., and Sarmiento, J. L.: Autonomous Biogeochemical Floats Detect Significant Carbon Dioxide Outgassing in the High-Latitude Southern Ocean, *Geophys. Res. Lett.*, 45, 9049–9057, <https://doi.org/10.1029/2018GL078013>, 2018.
- Griffies, S.: ELEMENTS OF MOM4p1, GFDL ocean group technical report no.6, NOAA/Geophysical Fluid Dynamics Laboratory, Princeton University Forrestal Campus, 201 Forrestal Road, Princeton, NJ 08540-6649, 2009.
- Gruber, N.: Warming up, turning sour, losing breath: ocean biogeochemistry under global change, *Philos. T. R. Soc. A*, 369, 1980–1996, <https://doi.org/10.1098/rsta.2011.0003>, 2011.
- Hall-Spencer, J. M., Rodolfo-Metalpa, R., Martin, S., Ransome, E., Fine, M., Turner, S. M., Rowley, S. J., Tedesco, D., and Buia, M.-C.: Volcanic carbon dioxide vents show ecosystem effects of ocean acidification, *Nature*, 454, 96–99, <https://doi.org/10.1038/nature07051>, 2008.
- Hartmann, D., Klein Tank, A., Rusticucci, M., Alexander, L., Brönnimann, S., Charabi, Y., Dentener, F., Dlugokencky, E., Easterling, D., Kaplan, A., Soden, B., Thorne, P., Wild, M., and Zhai, P.: Observations: Atmosphere and Surface Supplementary Material, *Climate Change 2013: The Physical Science Basis. Contribution of Working Group I to the Fifth Assessment Report of the Intergovernmental Panel on Climate Change*, 2013.
- Hauck, J. and Völker, C.: Rising atmospheric CO₂ leads to large impact of biology on Southern Ocean CO₂ uptake via changes of the Revelle factor, *Geophys. Res. Lett.*, 42, 1459–1464, <https://doi.org/10.1002/2015GL063070>, 2015.
- Hauri, C., Gruber, N., McDonnell, A. M. P., and Vogt, M.: The intensity, duration, and severity of low aragonite saturation state events on the California continental shelf, *Geophys. Res. Lett.*, 40, 3424–3428, <https://doi.org/10.1002/grl.50618>, 2013.
- Hofmann, G. E., Smith, J. E., Johnson, K. S., Send, U., Levin, L. A., Micheli, F., Paytan, A., Price, N. N., Peterson, B., Takeshita, Y., Matson, P. G., Crook, E. D., Kroeker, K. J., Gambi, M. C., Rivest, E. B., Frieder, C. A., Yu, P. C., and Martz, T. R.: High-Frequency Dynamics of Ocean pH: A Multi-Ecosystem Comparison, *PloS One*, 6, 1–11, <https://doi.org/10.1371/journal.pone.0028983>, 2011.
- Jacox, M. G.: Marine heatwaves in a changing climate, *Nature*, 571, 485–487, <https://doi.org/10.1038/d41586-019-02196-1>, 2019.
- Joint, I., Doney, S. C., and Karl, D. M.: Will ocean acidification affect marine microbes?, *ISME J.*, 5, 1–7, <https://doi.org/10.1038/ismej.2010.79>, 2011.
- Jones, C. D., Arora, V., Friedlingstein, P., Bopp, L., Brovkin, V., Dunne, J., Graven, H., Hoffman, F., Ilyina, T., John, J. G., Jung, M., Kawamiya, M., Koven, C., Pongratz, J., Raddatz, T., Randerson, J. T., and Zaehle, S.: C4MIP – The Coupled Climate–Carbon Cycle Model Intercomparison Project: experimental protocol for CMIP6, *Geosci. Model Dev.*, 9, 2853–2880, <https://doi.org/10.5194/gmd-9-2853-2016>, 2016.
- Keller, K. M., Joos, F., and Raible, C. C.: Time of emergence of trends in ocean biogeochemistry, *Biogeosciences*, 11, 3647–3659, <https://doi.org/10.5194/bg-11-3647-2014>, 2014.
- Kroeker, K. J., Micheli, F., Gambi, M. C., and Martz, T. R.: Divergent ecosystem responses within a benthic marine community to ocean acidification, *P. Natl. Acad. Sci. USA*, 108, 14515–14520, <https://doi.org/10.1073/pnas.1107789108>, 2011.
- Kroeker, K. J., Kordas, R. L., Crim, R., Hendriks, I. E., Ramajo, L., Singh, G. S., Duarte, C. M., and Gattuso, J.-P.: Impacts of ocean acidification on marine organisms: quantifying sensitivities and interaction with warming, *Glob. Change Biol.*, 19, 1884–1896, <https://doi.org/10.1111/gcb.12179>, 2013.
- Kroeker, K. J., Bell, L. E., Donham, E. M., Hoshijima, U., Lummis, S., Toy, J. A., and Willis-Norton, E.: Ecological change in dynamic environments: Accounting for temporal environmental variability in studies of ocean change biology, *Glob. Change Biol.*, 26, 54–67, <https://doi.org/10.1111/gcb.14868>, 2020.
- Kwiatkowski, L. and Orr, J. C.: Diverging seasonal extremes for ocean acidification during the twenty-first century, *Nat. Clim. Change*, 8, 141–145, <https://doi.org/10.1038/s41558-017-0054-0>, 2018.
- Kwiatkowski, L., Gaylord, B., Hill, T., Hosfelt, J., Kroeker, K. J., Nebuchina, Y., Ninokawa, A., Russell, A. D., Rivest, E. B., Sesboüé, M., and Caldeira, K.: Nighttime dissolution in a temperate coastal ocean ecosystem increases under acidification, *Sci. Rep.*, 6, 22984, <https://doi.org/10.1038/srep22984>, 2016.
- Landschützer, P., Gruber, N., and Bakker, D. C. E.: Decadal variations and trends of the global ocean carbon sink, *Global Biogeochem. Cy.*, 30, 1396–1417, <https://doi.org/10.1002/2015GB005359>, 2016.
- Landschützer, P., Gruber, N., Bakker, D. C. E., Stemmler, I., and Six, K. D.: Strengthening seasonal marine CO₂ variations due to increasing atmospheric CO₂, *Nat. Clim. Change*, 8, 146–150, <https://doi.org/10.1038/s41558-017-0057-x>, 2018.
- Lauvset, S. K., Carter, B. R., Perez, F. F., Jiang, L.-Q., Feely, R. A., Velo, A., and Olsen, A.: Processes Driving Global Interior Ocean pH Distribution, *Global Biogeochem. Cy.*, 34, e2019GB0006, <https://doi.org/10.1029/2019GB006229>, 2020.
- Leinweber, A. and Gruber, N.: Variability and trends of ocean acidification in the Southern California Current System: A time series from Santa Monica Bay, *J. Geophys. Res.-Ocean.*, 118, 3622–3633, <https://doi.org/10.1002/jgrc.20259>, 2013.
- McNeil, B. I. and Matear, R. J.: Southern Ocean acidification: A tipping point at 450-ppm atmospheric CO₂, *P. Natl. Acad. Sci. USA*, 105, 18860–18864, <https://doi.org/10.1073/pnas.0806318105>, 2008.
- McNeil, B. I. and Sasse, T. P.: Future ocean hypercapnia driven by anthropogenic amplification of the natural CO₂ cycle, *Nature*, 529, 383–386, <https://doi.org/10.1038/nature16156>, 2016.
- Mehrbach, C., Culbertson, C. H., Hawley, J. E., and Pytkowicz, R. M.: MEASUREMENT OF THE APPARENT DISSOCIATION CONSTANTS OF CARBONIC ACID IN SEAWATER

- AT ATMOSPHERIC PRESSURE 1, *Limnol. Oceanogr.*, 18, 897–907, <https://doi.org/10.4319/lo.1973.18.6.0897>, 1973.
- Morse, J. and Mackenzie, F.: *Geochemistry of Sedimentary Carbonates*, Elsevier, Amsterdam, 1990.
- Najjar, R. and Orr, J.: Design of OCMIP-2 simulations of chlorofluorocarbons, the solubility pump and common biogeochemistry, internal ocmip report, LSCE/CEA Saclay, Gif-sur-Yvette, France, 1998.
- Oliver, E. C. J., Donat, M. G., Burrows, M. T., Moore, P. J., Smale, D. A., Alexander, L. V., Benthuyssen, J. A., Feng, M., Sen Gupta, A., Hobday, A. J., Holbrook, N. J., Perkins-Kirkpatrick, S. E., Scannell, H. A., Straub, S. C., and Wernberg, T.: Longer and more frequent marine heatwaves over the past century, *Nat. Commun.*, 9, 1324, <https://doi.org/10.1038/s41467-018-03732-9>, 2018.
- Oliver, E. C. J., Burrows, M. T., Donat, M. G., Sen Gupta, A., Alexander, L. V., Perkins-Kirkpatrick, S. E., Benthuyssen, J. A., Hobday, A. J., Holbrook, N. J., Moore, P. J., Thomsen, M. S., Wernberg, T., and Smale, D. A.: Projected Marine Heatwaves in the 21st Century and the Potential for Ecological Impact, *Front. Mar. Sci.*, 6, 1–12, <https://doi.org/10.3389/fmars.2019.00734>, 2019.
- Oppenheimer, M., Glavovic, B. C., Hinkel, J., van de Wal, R., Magnan, A. K., Abd-Elgawad, A., Cai, R., Cifuentes-Jara, M., DeConto, R. M., Ghosh, T., Hay, J., Isla, F., Marzeion, B., Meyssignac, B., and Sebesvari, Z.: Sea Level Rise and Implications for Low-Lying Islands, Coasts and Communities, in: *IPCC Special Report on the Ocean and Cryosphere in a Changing Climate*, edited by: Pörtner, H.-O., Roberts, D. C., Masson-Delmotte, V., Zhai, P., Tignor, M., Poloczanska, E., Mintenbeck, K., Alegría, A., Nicolai, M., Okem, A., Petzold, J., Rama, B., and Weyer, N. M., in press, 2020.
- Orr, J. C. and Epitalon, J.-M.: Improved routines to model the ocean carbonate system: mocsy 2.0, *Geosci. Model Dev.*, 8, 485–499, <https://doi.org/10.5194/gmd-8-485-2015>, 2015.
- Orr, J. C., Fabry, V. J., Aumont, O., Bopp, L., Doney, S. C., Feely, R. A., Gnanadesikan, A., Gruber, N., Ishida, A., Joos, F., Key, R. M., Lindsay, K., Maier-Reimer, E., Matear, R., Monfray, P., Mouchet, A., Najjar, R. G., Plattner, G.-K., Rodgers, K. B., Sabine, C. L., Sarmiento, J. L., Schlitzer, R., Slater, R. D., Totterdell, I. J., Weirig, M.-F., Yamanaka, Y., and Yool, A.: Anthropogenic ocean acidification over the twenty-first century and its impact on calcifying organisms, *Nature*, 437, 681–686, <https://doi.org/10.1038/nature04095>, 2005.
- Orr, J. C., Epitalon, J.-M., Dickson, A. G., and Gattuso, J.-P.: Routine uncertainty propagation for the marine carbon dioxide system, *Mar. Chem.*, 207, 84–107, <https://doi.org/10.1016/j.marchem.2018.10.006>, 2018.
- Palter, J. B., Frölicher, T. L., Paynter, D., and John, J. G.: Climate, ocean circulation, and sea level changes under stabilization and overshoot pathways to 1.5 K warming, *Earth Syst. Dynam.*, 9, 817–828, <https://doi.org/10.5194/esd-9-817-2018>, 2018.
- Resplandy, L., Séférian, R., and Bopp, L.: Natural variability of CO₂ and O₂ fluxes: What can we learn from centuries-long climate models simulations?, *J. Geophys. Res.-Ocean.*, 120, 384–404, <https://doi.org/10.1002/2014JC010463>, 2015.
- Riahi, K., Rao, S., Krey, V., Cho, C., Chirkov, V., Fischer, G., Kindermann, G., Nakicenovic, N., and Rafaj, P.: RCP8.5 – A scenario of comparatively high greenhouse gas emissions, *Clim. Change*, 109, 33–57, <https://doi.org/10.1007/s10584-011-0149-y>, 2011.
- Riebesell, U., Zondervan, I., Rost, B., Tortell, P. D., Zeebe, R. E., and Morel, F. M. M.: Reduced calcification of marine plankton in response to increased atmospheric CO₂, *Nature*, 407, 364–367, <https://doi.org/10.1038/35030078>, 2000.
- Rivest, E. B., Comeau, S., and Cornwall, C. E.: The Role of Natural Variability in Shaping the Response of Coral Reef Organisms to Climate Change, *Curr. Clim. Change Rep.*, 3, 271–281, <https://doi.org/10.1007/s40641-017-0082-x>, 2017.
- Rodgers, K. B., Sarmiento, J. L., Aumont, O., Crevoisier, C., de Boyer Montégut, C., and Metzl, N.: A wintertime uptake window for anthropogenic CO₂ in the North Pacific, *Global Biogeochem. Cy.*, 22, 1–16, <https://doi.org/10.1029/2006GB002920>, 2008.
- Sarmiento, J. and Gruber, N.: *Ocean Biogeochemical Dynamics*, Princeton University Press, 2006.
- Seneviratne, S., Nicholls, N., Easterling, D., Goodess, C., Kanae, S., Kossin, J., Luo, Y., Marengo, J., McInnes, K., Rahimi, M., Reichstein, M., Sorteberg, A., Vera, C., and Zhang, X.: Changes in climate extremes and their impacts on the natural physical environment, *Managing the Risks of Extreme Events and Disasters to Advance Climate Change Adaptation*, A Special Report of Working Groups I and II of the Intergovernmental Panel on Climate Change (IPCC), 2012.
- Sentman, L. T., Shevliakova, E., Stouffer, R. J., and Malyshev, S.: Time Scales of Terrestrial Carbon Response Related to Land-Use Application: Implications for Initializing an Earth System Model, *Earth Interact.*, 15, 1–16, <https://doi.org/10.1175/2011EI401.1>, 2011.
- Shevliakova, E., Pacala, S. W., Malyshev, S., Hurtt, G. C., Milly, P. C. D., Caspersen, J. P., Sentman, L. T., Fisk, J. P., Wirth, C., and Crevoisier, C.: Carbon cycling under 300 years of land use change: Importance of the secondary vegetation sink, *Global Biogeochem. Cy.*, 23, 1–16, <https://doi.org/10.1029/2007GB003176>, 2009.
- Smale, D. A., Wernberg, T., Oliver, E. C. J., Thomsen, M., Harvey, B. P., Straub, S. C., Burrows, M. T., Alexander, L. V., Benthuyssen, J. A., Donat, M. G., Feng, M., Hobday, A. J., Holbrook, N. J., Perkins-Kirkpatrick, S. E., Scannell, H. A., Sen Gupta, A., Payne, B. L., and Moore, P. J.: Marine heatwaves threaten global biodiversity and the provision of ecosystem services, *Nat. Clim. Change*, 9, 306–312, <https://doi.org/10.1038/s41558-019-0412-1>, 2019.
- Smith, M. D.: An ecological perspective on extreme climatic events: a synthetic definition and framework to guide future research, *J. Ecol.*, 99, 656–663, <https://doi.org/10.1111/j.1365-2745.2011.01798.x>, 2011.
- Stephenson, D.: Definition, diagnosis, and origin of extreme weather and climate events, in: *Climate Extremes and Society*, edited by: Murnane, R. and Diaz, H., Cambridge University Press, 11–23, 2008.
- Terhaar, J., Orr, J. C., Ethé, C., Regnier, P., and Bopp, L.: Simulated Arctic Ocean Response to Doubling of Riverine Carbon and Nutrient Delivery, *Global Biogeochem. Cy.*, 33, 1048–1070, <https://doi.org/10.1029/2019GB006200>, 2019a.
- Terhaar, J., Orr, J. C., Gehlen, M., Ethé, C., and Bopp, L.: Model constraints on the anthropogenic carbon bud-

- get of the Arctic Ocean, *Biogeosciences*, 16, 2343–2367, <https://doi.org/10.5194/bg-16-2343-2019>, 2019b.
- Terhaar, J., Kwiatkowski, L., and Bopp, L.: Emergent constraint on Arctic Ocean acidification in the twenty-first century, *Nature*, 582, 379–383, <https://doi.org/10.1038/s41586-020-2360-3>, 2020.
- Turi, G., Alexander, M., Lovenduski, N. S., Capotondi, A., Scott, J., Stock, C., Dunne, J., John, J., and Jacox, M.: Response of O₂ and pH to ENSO in the California Current System in a high-resolution global climate model, *Ocean Sci.*, 14, 69–86, <https://doi.org/10.5194/os-14-69-2018>, 2018.
- van Heuven, S., Pierrot, D., Rae, J., Lewis, E., and Wallace, D.: MATLAB Program Developed for CO₂ System Calculations, available at: <http://gts.sourceforge.net/> (last access: 13 February 2019), 2011.
- van Vuuren, D. P., Stehfest, E., den Elzen, M. G. J., Kram, T., van Vliet, J., Deetman, S., Isaac, M., Klein Goldewijk, K., Hof, A., Mendoza Beltran, A., Oostenrijk, R., and van Ruijven, B.: RCP2.6: exploring the possibility to keep global mean temperature increase below 2 °C, *Climatic Change*, 109, 95–116, <https://doi.org/10.1007/s10584-011-0152-3>, 2011.
- Vogel, M. M., Zscheischler, J., Fischer, E. M., and Seneviratne, S. I.: Development of Future Heatwaves for Different Hazard Thresholds, *J. Geophys. Res.-Atmos.*, 125, e2019JD032, <https://doi.org/10.1029/2019JD032070>, 2020.
- Weiss, R.: Carbon dioxide in water and seawater: the solubility of a non-ideal gas, *Mar. Chem.*, 2, 203–215, [https://doi.org/10.1016/0304-4203\(74\)90015-2](https://doi.org/10.1016/0304-4203(74)90015-2), 1974.
- Wernberg, T., Bennett, S., Babcock, R. C., de Bettignies, T., Cure, K., Depczynski, M., Dufois, F., Fromont, J., Fulton, C. J., Hovey, R. K., Harvey, E. S., Holmes, T. H., Kendrick, G. A., Radford, B., Santana-Garcon, J., Saunders, B. J., Smale, D. A., Thomsen, M. S., Tuckett, C. A., Tuya, F., Vanderklift, M. A., and Wilson, S.: Climate-driven regime shift of a temperate marine ecosystem, *Science*, 353, 169–172, <https://doi.org/10.1126/science.aad8745>, 2016.
- Weyer, N. M. (Ed.): Annex I: Glossary, in: Special Report on Ocean and Cryosphere in a Changing Climate, edited by: Pörtner, H.-O., Roberts, D., Masson-Delmotte, V., and Zhai, P., 677–701, Intergovernmental Panel on Climate Change, Geneva, 2019.
- Winton, M.: A Reformulated Three-Layer Sea Ice Model, *J. Atmos. Ocean. Technol.*, 17, 525–531, [https://doi.org/10.1175/1520-0426\(2000\)017<0525:ARTLSI>2.0.CO;2](https://doi.org/10.1175/1520-0426(2000)017<0525:ARTLSI>2.0.CO;2), 2000.
- Wittenberg, A. T., Rosati, A., Delworth, T. L., Vecchi, G. A., and Zeng, F.: ENSO Modulation: Is It Decadally Predictable?, *J. Clim.*, 27, 2667–2681, <https://doi.org/10.1175/JCLI-D-13-00577.1>, 2014.
- Zscheischler, J. and Seneviratne, S. I.: Dependence of drivers affects risks associated with compound events, *Sci. Adv.*, 3, 1–10, <https://doi.org/10.1126/sciadv.1700263>, 2017.

Chapter 4

Compound marine heatwaves and ocean acidity extremes

Friedrich A. Burger, Jens Terhaar, and Thomas L. Frölicher

Revised manuscript under review in *Nature Communications*.

Co-occurring marine heatwaves (MHWs) and ocean acidity extreme (OAX) events, i.e., ocean compound MHW-OAX events, can have much larger impacts on marine ecosystems than the individual extreme events. Yet, the location and likelihood of these compound MHW-OAX events, their underlying processes, and their evolution under climate change are currently unknown. Here, we combine observations with a large ensemble simulation of an Earth system model to show that globally 1.8 in 100 months (or one out of five present-day MHWs) are compound MHW-OAX events, almost twice as many as expected for 90th percentile extreme event exceedances if MHWs and OAX events were statistically independent. Compound MHW-OAX events are most likely in the subtropics (2.7 in 100 months; 10° - 40° latitude) and less likely in the equatorial Pacific and the mid-to-high latitudes (0.7 in 100 months; > 40° latitude). The compound event likelihood results from opposing effects of temperature and dissolved inorganic carbon on $[H^+]$. More compound events occur where the positive effect on $[H^+]$ from increased temperatures during MHWs is larger than the negative effect on $[H^+]$ from co-occurring decreases in dissolved inorganic carbon. Under climate change, the likelihood of MHW-OAX events changes due to the mean warming and acidification, due to changes in variability of temperature and $[H^+]$, and due to changes in their interdependence. Among these changes, it is the mean warming and acidification that has the largest effect on MHW-OAX event frequency, increasing it from 12 days per year under preindustrial conditions to 265 days per year at 2°C global warming. Even when mean trends are removed, an increase in $[H^+]$ variability leads to a 60 % increase in the number of compound MHW-OAX days under 2°C global warming. This projected increase in the occurrence of compound MHW-OAX events may cause severe impacts on marine ecosystems.

4.1 Introduction

Anthropogenic climate change has led to an increase in frequency and intensity of ocean extreme events, such as marine heatwaves (Hobday et al., 2016; Oliver et al., 2018; Frölicher et al., 2018; Collins et al., 2019; Holbrook et al., 2019; Laufkötter et al., 2020; Oliver et al., 2021) and ocean acidity extremes (Chapter 3; Burger et al., 2020; Hauri et al., 2013), a trend that is projected to continue over the 21st century (Frölicher et al., 2018; Burger et al., 2020). The predominantly harmful impacts of such individual extreme events on marine ecosystems (Smale et al., 2019; Hughes et al., 2017; Bednaršek et al., 2014) may become more severe when two extreme events occur together (Bednaršek et al., 2018; Lischka & Riebesell, 2012; Engström-Öst et al., 2019). These so-called compound events (Leonard et al., 2014; Zscheischler et al., 2018) have been vastly studied on land (Ridder et al., 2020; Zscheischler et al., 2020), whereas marine compound events, such as compound MHW-OAX events (events of unusually high temperature and hydrogen ion concentration, $[H^+]$), are just starting to receive more attention (Le Grix et al., 2021; Gruber et al., 2021).

The impact of compound MHW-OAX events on marine biota may exceed the impact from individual MHW or OAX events, since co-occurring extremes can interact synergistically (Boyd & Brown, 2015). For example, the combination of high temperature and acidity conditions negatively impacted pteropods across cellular, physiological and population levels in the California Current System in 2016 (Bednaršek et al., 2018; Engström-Öst et al., 2019), and some of the devastating impacts of the Northeast Pacific 2013 to 2015 MHW (Cavole et al., 2016) may have been amplified by the co-occurring extreme OA conditions (Gruber et al., 2021). Such rare observations and modeling studies of MHW-OAX events in the ocean are further corroborated by laboratory experiments showing synergistic negative effects on calcification, reproduction and survival (Harvey et al., 2013), and trends towards lower survival, growth, and development (Kroeker et al., 2013) for many species under compound MHW-OAX conditions compared to single extreme conditions, and by mesocosm experiments showing shifts in community structure (Goldenberg et al., 2017; Nagelkerken et al., 2020).

The likelihood of compound MHW-OAX events is influenced by a complex interplay of direct and indirect effects of high temperatures on $[H^+]$ during MHWs. While hot temperatures directly lead to increases in $[H^+]$ via changes in the carbonate chemistry equilibrium (Zeebe & Wolf-Gladrow, 2001), they can also modulate $[H^+]$ indirectly via changes in dissolved inorganic carbon (C_T) (Gruber et al., 2021). These indirect changes of $[H^+]$ during MHWs include a reduction of the CO_2 solubility in surface waters (Weiss, 1974) and an associated net release of oceanic CO_2 to the atmosphere that reduces C_T and $[H^+]$ (Takahashi et al., 2002), an increase in upper ocean thermal stratification (Holbrook et al., 2019) resulting in suppressed mixing of surface waters with carbon-rich subsurface waters and hence a reduction in surface ocean C_T and $[H^+]$ (Doney et al., 2009), as well as changes in organic matter production that reduce C_T and $[H^+]$ if production increases (Doney et al., 2009). The knowledge on compound MHW-OAX events and their drivers is currently very limited due to a lack of direct observations. However, novel observational-based data products (Landschützer et al., 2016; Burger et al., 2020; Good et al., 2013) and large ensemble simulations of comprehensive Earth System Models (ESMs) (Rodgers et al., 2015; Deser et al., 2020) permit us now to study compound MHW-OAX events globally.

Here, we characterize patterns, identify drivers, and assess future changes of compound MHW-OAX events using (i) global monthly gridded observation-based sea surface temperature (SST) (Good et al., 2013) and surface $[H^+]$ data (Chapter 3; Burger et al., 2020) from 1982 to 2019, (ii) time series data of temperature and $[H^+]$ from fifteen ocean stations with either

approximately monthly or 3-hourly measurement frequency collected between 1983 and 2020, and (iii) output from 30 ensemble members of the Earth System Model GFDL ESM2M (Dunne et al., 2012, 2013) at daily resolution covering the period from 1861 to 2100 (see Methods). The analysis is restricted to the open ocean, since the high variability and locally important processes, such as riverine fluxes, in coastal oceans are neither captured by the gridded observation-based product (Landschützer et al., 2020; Carter et al., 2018) nor by the GFDL ESM2M model (Dunne et al., 2013). Extreme events in SST and $[H^+]$ are defined with respect to seasonally varying 90th percentiles (see Methods). The percentile thresholds are determined from the shortest available time step, i.e., monthly for observations and daily for the model output. In this study, compound MHW and OAX events are defined when both extreme hot temperature and high acidity conditions co-occur in space and time. We refer to them as ‘compound MHW-OAX events’. Compound MHW-OAX events are characterized by their frequency (MHW-OAX months per year or MHW-OAX days per year) and the likelihood multiplication factor (LMF). The LMF quantifies the likelihood of the occurrence of a compound event in each region and is proportional to the number of months or days with compound event conditions in a given time period. Precisely, it is defined as the ratio of the actual compound event frequency $f(MHW-OAX\ event)$ and the theoretical frequency if the two variables, here SST and $[H^+]$, were statistically independent $f(MHW\ event) \times f(OAX\ event)$ (Zscheischler & Seneviratne, 2017):

$$LMF = \frac{f(MHW-OAX\ event)}{f(MHW\ event) \times f(OAX\ event)} \quad (4.1)$$

If MHWs and OAX events were statistically independent, the frequency of compound events in percent of months or days would be given by the product of the univariate frequencies of MHWs and OAX events. Under our definition of single extreme events (90th percentile thresholds), this theoretical frequency is $10\% \cdot 10\% = 1\%$ of all months (0.12 months per year if monthly data is used) or days (3.65 days per year if daily data is used). An LMF higher than 1 indicates that compound events occur more often than by chance and that the frequency exceeds 1% of all days or months. An LMF lower than one indicates a reduced likelihood of compound events. As an example, if two out of 100 months were under MHW-OAX conditions, the LMF would be 2 meaning that the likelihood of a compound event would be twice as large as under independence. However, if only one out of 200 months was under MHW-OAX conditions, the LMF would be 0.5 meaning that the likelihood of a compound event would be only half as large as under independence.

4.2 Results

4.2.1 Present-day pattern of compound MHW-OAX event occurrence

The global gridded observation-based data shows that globally 1.8 in 100 months are compound MHW-OAX events (Fig. 4.1). This is 1.8 time more often (LMF=1.8) than expected if variations in SST and $[H^+]$ anomalies were statistically independent. The LMF is larger than one in 65% of the ocean surface area. Compound MHW-OAX extremes are most frequent in the subtropical regions (2.7 in 100 months or LMF = 2.7 over 40° - 10° latitude) and least frequent in the equatorial Pacific (0.8 in 100 months or LMF = 0.8 over 10°S - 10°N latitude) and the high latitudes (0.7 in 100 months or LMF = 0.7 over 40° - 80° latitude; Fig. 4.1). These regions are separated by the contour of LMF equal to one (thin grey contour line in Fig. 4.1) that follows closely the subpolar fronts in both hemispheres and the ENSO region in the central and eastern tropical Pacific.

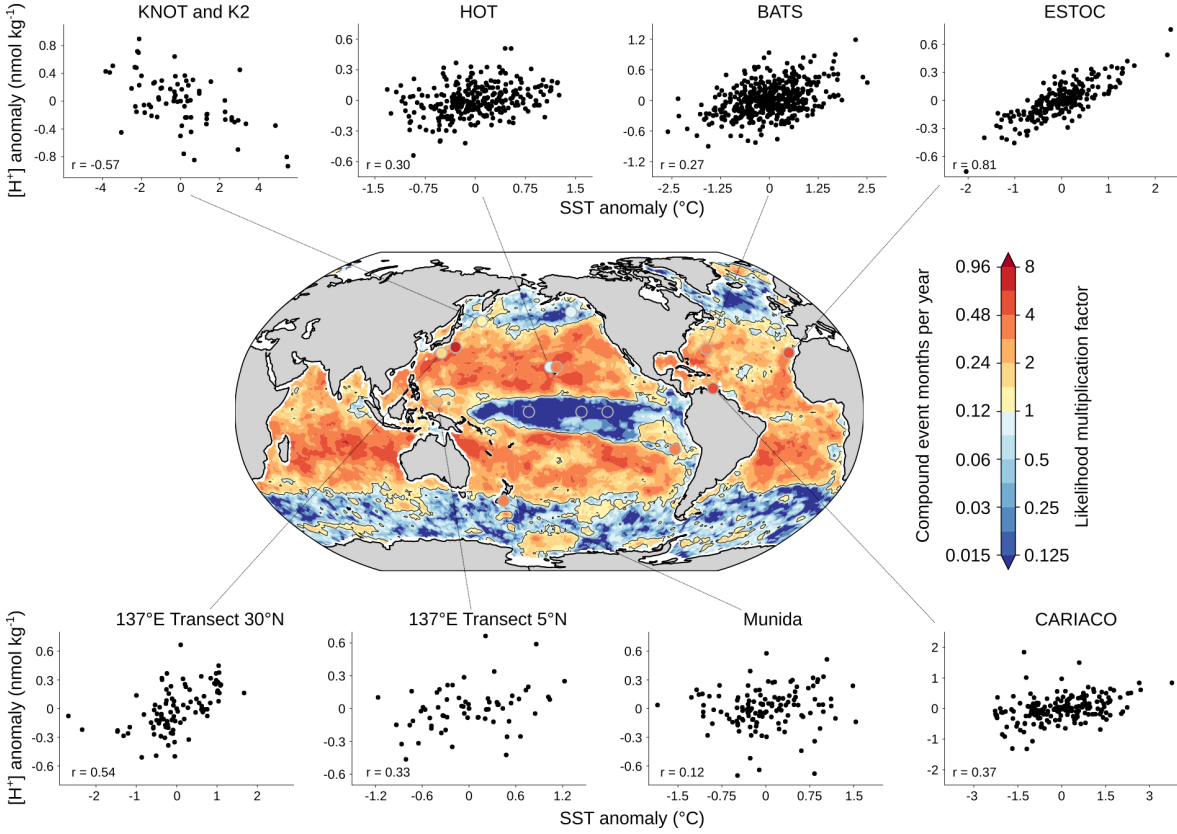


Figure 4.1: The observation-based likelihood multiplication factor of compound MHW-OAX events over the years 1982 to 2019. Map of the likelihood multiplication factor (LMF) based on the global monthly gridded observation-based SST and surface $[H^+]$ data. Warm colors indicate $LMF > 1$ and cold colors indicate $LMF < 1$. These regions are separated by the thin gray contour line. The color bar also indicates the respective number of yearly compound event months. The colored dots indicate the location and the estimated LMFs from 15 observation stations (see Methods). SST and $[H^+]$ anomalies and the correlation coefficient (r) from eight directly measured SST and $[H^+]$ time series are shown around the map. All data was linearly detrended prior to the analysis.

4.2.2 Potential drivers of MHW-OAX events

To better understand the regional differences in the occurrence of MHW-OAX events and possible future changes, we now quantify the underlying drivers and discuss physical and biogeochemical processes. Mathematically, the LMF of MHW-OAX events cannot be decomposed into contributions from its drivers. It is hence approximated by the Pearson correlation coefficient (in the following simply correlation coefficient) of SST and $[H^+]$ anomalies, which can be mathematically decomposed (Ext. Data Fig. 4.5; see Methods). The contributions to the correlation coefficient (Fig. 4.2a) include the direct contribution from variations in SST (Fig. 4.2b), the contribution from variations in salinity-normalized dissolved inorganic carbon (sC_T ; Fig. 4.2c), as well as smaller contributions from variations in salinity-normalized alkalinity (sA_T) and a freshwater cycling term (see Methods, Ext. Data Fig. 4.6). The freshwater term quantifies the direct impact from salinity variations (through changes in precipitation or evaporation, or changes in ocean circulation) and the changes in sC_T and sA_T that are proportional to these salinity variations. Globally, the SST contribution increases the correlation coefficient and LMF everywhere (Fig. 4.2b), and the sC_T contribution reduces the correlation coefficient and LMF everywhere (Fig. 4.2c).

The pattern of the correlation coefficient and LMF depends mainly on the regional balance between the SST and sC_T contributions. The direct contribution from SST to the correlation

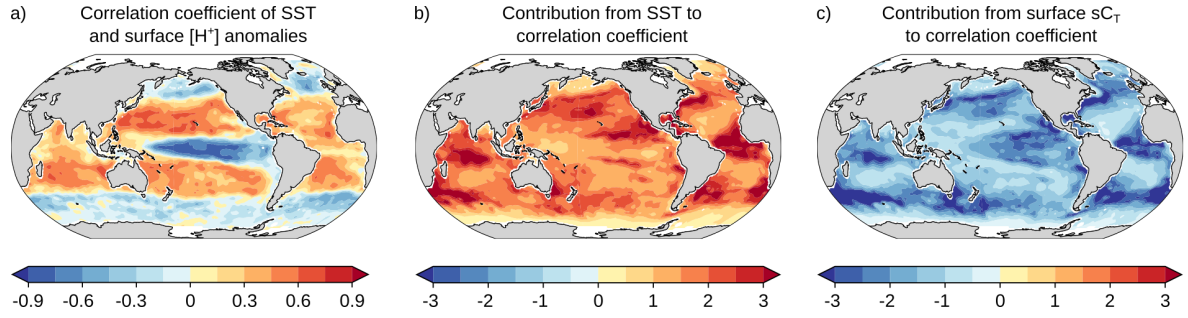


Figure 4.2: The observation-based correlation coefficient of sea surface temperature and $[H^+]$ anomalies and its drivers from 1982 to 2019. (a) Correlation coefficient of sea surface temperature (SST) and surface $[H^+]$ anomalies. The contributions from (b) variations in SST and (c) variations in salinity-normalized C_T to the correlation coefficient (in correlation coefficient units; see Methods). The data was linearly detrended prior to the analysis.

coefficient of SST and $[H^+]$ is everywhere positive because an increase in temperature directly causes a rise in $[H^+]$ (Zeebe & Wolf-Gladrow, 2001, ; Fig. 4.2b). Thus, positive anomalies in SST also cause positive anomalies in $[H^+]$, thereby increasing the likelihood and LMF of compound MHW-OAX events. Conversely, the contribution of sC_T to the correlation coefficient is everywhere negative (Fig. 4.2c) because SST and sC_T anomalies are everywhere negatively correlated (Gruber et al., 2002, ; Ext. Data Fig. 4.7f). Negative anomalies of sC_T during MHWs (high SST) thus reduce $[H^+]$ and reduce the likelihood and LMF of compound MHW-OAX events. The regionally varying magnitude of the positive SST and negative sC_T contributions (Fig. 4.2b, c) is mainly determined by the ratios between the variabilities in SST and sC_T anomalies and the variability in $[H^+]$ anomalies in the respective region (Methods, Ext. Data Fig. 4.7).

To understand the LMF pattern, it is thus essential to understand the processes that cause variability in SST and sC_T . Here we qualitatively describe the contributions of the different processes, but a more quantitative understanding is needed in subsequent studies. Variability in SST and sC_T results from changes in circulation, mixing, and air-sea fluxes (Deser et al., 2010; Sarmiento & Gruber, 2006). Variability in surface sC_T is also caused by changes in biological activity, most importantly net primary production (Sarmiento & Gruber, 2006). Positive anomalies in SST, such as during MHWs, are often connected to negative anomalies in sC_T as these processes often lead to opposite changes in temperature and sC_T . For example, weaker surface winds and enhanced thermal stratification (Holbrook et al., 2019; Oliver et al., 2021) during El Niño conditions in the tropical Pacific (Sen Gupta et al., 2020) drive high sea surface temperatures but at the same time low sC_T due to reductions in mixing and upwelling of colder sC_T -rich waters. Likewise, poleward displacement of warm, low C_T waters in the boundary currents (Feng et al., 2013) lead to opposite changes in temperature and sC_T . The sign of the change in net primary production during positive SST anomalies depends on the regional surface nutrient availability and temperature. In warm, nutrient-poor regions (40°S - 40°N), high temperature anomalies may reduce the nutrient supply from upwelling and mixing, causing a reduction in chlorophyll (Fig. 4.3a) and possibly net primary production, and a coincident increase in sC_T (Sen Gupta et al., 2020; Hayashida et al., 2020; Le Grix et al., 2021). In colder high-latitude regions ($> 40^\circ$ latitude), however, where nutrients are more abundant (Moore et al., 2013), increasing temperatures are associated with higher chlorophyll and primary production (Fig. 4.3a; Hayashida et al., 2020; Le Grix et al., 2021) and reduced sC_T (see contour lines for mean nitrate concentrations in Fig. 4.3a).

The resulting correlation coefficient of SST and $[H^+]$ anomalies and hence the LMF (Fig. 4.2a) depends on the regional balance between these opposing contributions from variations in SST and

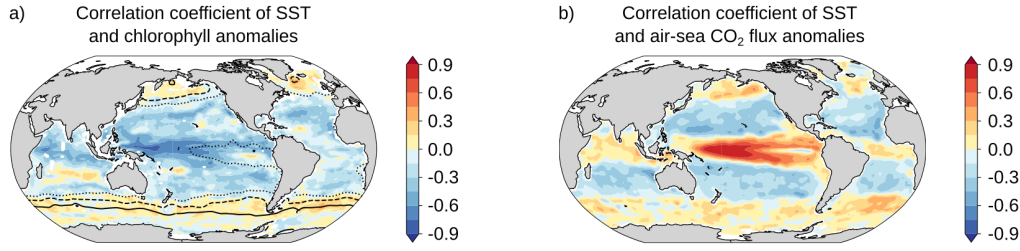


Figure 4.3: The observation-based correlation coefficient of monthly sea surface temperature anomalies and monthly (a) chlorophyll concentration anomalies and (b) air-sea CO_2 flux anomalies (see Methods). The data was linearly detrended prior to the analysis. A negative correlation between SST and chlorophyll anomalies indicates that chlorophyll, and possibly net primary production, is reduced and hence C_T enhanced during MHWs. A negative correlation between SST and air-sea CO_2 flux anomalies indicates that C_T is reduced during MHWs. The contour lines in a) display mean nitrate concentrations from the World Ocean Atlas 2018 (dotted: 3 mol kg^{-1} , dashed: 10 mol kg^{-1} , solid: 20 mol kg^{-1}). Net primary production is here approximated by observation-based chlorophyll concentration (Behrenfeld et al., 2006), although chlorophyll is not always correlated with net primary production, particularly in subtropical regions (Barbier et al., 2018).

in sC_T . In the tropical Pacific, for example, the correlation of SST and $[\text{H}^+]$ anomalies is negative (Fig. 4.2a) corresponding to a low likelihood of MHW-OAX events ($\text{LMF} < 1$) (Fig. 4.1), although the direct effect of temperature (Fig. 4.2b) and the indirect effect of suppressed chlorophyll and biological production (Fig. 4.3a) increase the likelihood of compound MHW-OAX events in this region. Thus, it can be concluded that the reduction in sC_T and hence $[\text{H}^+]$ due to suppressed upwelling and mixing during MHWs in this region must be large enough to overcompensate the positive temperature and biology contributions to $[\text{H}^+]$ and ultimately result in an LMF below 1. In the subtropical gyres, however, the correlation of SST and $[\text{H}^+]$ anomalies is positive, resulting in a high likelihood of MHW-OAX events ($\text{LMF} > 1$) (Fig. 4.2a). There, the combined positive effect from enhanced temperature (Fig. 4.2b) and suppressed chlorophyll (Fig. 4.3a) on $[\text{H}^+]$ must therefore be larger than the negative effect from circulation and mixing. In the high latitudes, the correlation coefficient becomes negative again and compound MHW-OAX events become less likely (Fig. 4.2a). In these colder waters, increases in chlorophyll (Fig. 4.3a) and changes in circulation and mixing reduce sC_T and hence $[\text{H}^+]$ during MHWs more than temperature increases it and cause a lower LMF (Fig. 4.2b).

In addition to circulation, mixing, biological activity, and the direct temperature effect on $[\text{H}^+]$ that determine the sign of the correlation coefficient of SST and $[\text{H}^+]$ anomalies, the magnitude of the correlation and the LMF is further modulated by the changes in air-sea CO_2 flux (Fig. 4.3b). Globally, $[\text{H}^+]$ and $p\text{CO}_2$ anomalies are strongly positively correlated ($r=0.96$). In regions where $[\text{H}^+]$ is increased during high temperatures, $p\text{CO}_2$ is also increased, resulting in outgassing of CO_2 and a reduction in sC_T and $[\text{H}^+]$. In contrast, air-sea CO_2 flux increases $[\text{H}^+]$ in regions where $[\text{H}^+]$ is decreased during high temperatures (Fig. 4.3b). Consequently, air-sea CO_2 flux reduces correlations between SST and $[\text{H}^+]$ where they are positive, and it increases them where they are negative.

4.2.3 Changes in MHW-OAX event occurrence with climate change

Under climate change, the frequency of compound MHW-OAX days is projected to change (Fig. 4.4). Changes in compound MHW-OAX occurrence arise from an increase in the mean state of temperature and $[\text{H}^+]$, from changes in the variability of temperature and $[\text{H}^+]$, as well as changes in the bivariate tail dependence of temperature and $[\text{H}^+]$. To consider different adaption capabilities of organisms and ecosystems, we define changes in compound MHW-OAX frequency with respect to two different baselines (Burger et al., 2020; Oliver et al., 2021; Gruber et al., 2021): relative to a fixed preindustrial baseline and relative to a shifting-mean baseline (see Methods). When defined with respect to a fixed preindustrial baseline, the largest changes in

MHW-OAX frequency by far are expected from long-term ocean warming and acidification trends (Frölicher et al., 2018; Oliver et al., 2019; Burger et al., 2020). This baseline is chosen to show the overall changes in MHW-OAX occurrence and because it is most useful for less resilient and less mobile organisms and ecosystems, such as warm water corals (Hughes et al., 2017; Prada et al., 2017) or other sessile organisms that cannot adapt fast enough to long-term ocean warming and acidification or cannot relocate to favorable ocean habitats (Oliver et al., 2021). Under the shifting-mean baseline, long-term warming and acidification trends are removed. Hence, extremes are defined as deviations from the normal conditions that themselves change over time (Jacox, 2019; Burger et al., 2020). Changes in compound MHW-OAX event occurrence are here mainly caused by changes in temperature and especially $[H^+]$ variability (Oliver et al., 2021; Burger et al., 2020). This definition is chosen to analyze the role of changes in variability and to quantify increased stress for organisms that may accustom to long-term ocean warming and acidification (Muñoz et al., 2015) or can shift their distribution (Pinsky et al., 2013; Cheung et al., 2021), such as fishes or marine mammals. In addition to the two above mentioned definitions, we also define changes in MHW-OAX frequency relative to a fully adapting baseline, which provides additional insights about the drivers of changes in compound MHW-OAX days. Under the fully adapting baseline definition (Vogel et al., 2020), the univariate extreme event likelihood (e.g., the likelihood of marine heatwaves or ocean acidity extreme events) does not change. Instead, changes in compound MHW-OAX frequency only arise from changes in the tail dependence between temperature and $[H^+]$ altering the likelihood that MHWs and OAX events occur together. This definition is chosen to gain additional insights about the drivers of changes, i.e., to identify the impact of dependence changes on changes in MHW-OAX event likelihood.

Relative to a fixed preindustrial baseline (see Methods), the occurrence of MHW-OAX events is simulated to have increased from 12 days per year on average at preindustrial to 167 days per year (165-169, 90 % confidence interval) at 1 °C global warming (14-fold increase) (Fig. 4.4a). Under continued global warming, MHW-OAX occurrence is projected to increase to 265 (263-266; 22-fold increase) days per year for 2 °C warming and to 307 (307-308; 26-fold increase) days per year for 3 °C. The increase in compound MHW-OAX events is mainly determined by the increase in MHWs and therefore long-term ocean warming (Oliver et al., 2019; Frölicher et al., 2018), since $[H^+]$ reaches a near-permanent extreme state (more than 360 days per year) already at a global warming of 0.3 °C (or when atmospheric CO_2 exceeds 340 ppm). A permanent $[H^+]$ extreme state causes, by definition, all MHWs to be also MHW-OAX events (Fig. 4.4a). Compound MHW-OAX event days are projected to increase most in the tropical regions of the Atlantic, the western Pacific, and the Indian Ocean (Fig. 4.4d). There, increasing temperatures exceed the relatively small natural variability earlier than in most other places (Frölicher et al., 2016) and thus lead to relatively larger increases in MHW-OAX events and even near-permanent MHW-OAX events (hatched area in Fig. 4.4d). These permanent MHW-OAX events are projected to occur in 42 (42-43) % of the ocean surface area under 3 °C warming but can be largely avoided under 2 °C warming (10 (9-10) %). In regions, where SST is projected to slightly decrease over the 21st century, such as in the North Atlantic south of Greenland and parts of the Southern Ocean, the frequency of MHWs and hence compound MHW-OAX events decreases (Fig. 4.4d).

When defining extreme events relative to a shifting-mean baseline (see Methods), the occurrence of compound MHW-OAX events is also projected to increase (Fig. 4.4b, e), from 12 compound event days per year at preindustrial to 19 (19-20) days per year at 2 °C warming (1.6-fold increase), and to 23 (22-23) days per year under 3 °C warming (1.9-fold increase; Fig. 4.4b). As opposed to the fixed baseline, the increase in MHW-OAX extreme event occurrence under the shifting-mean baseline definition is mainly caused by a rising number of OAX events (Fig. 4.4b) due to enhanced $[H^+]$ variability in waters with more C_T (Kwiatkowski & Orr, 2018;

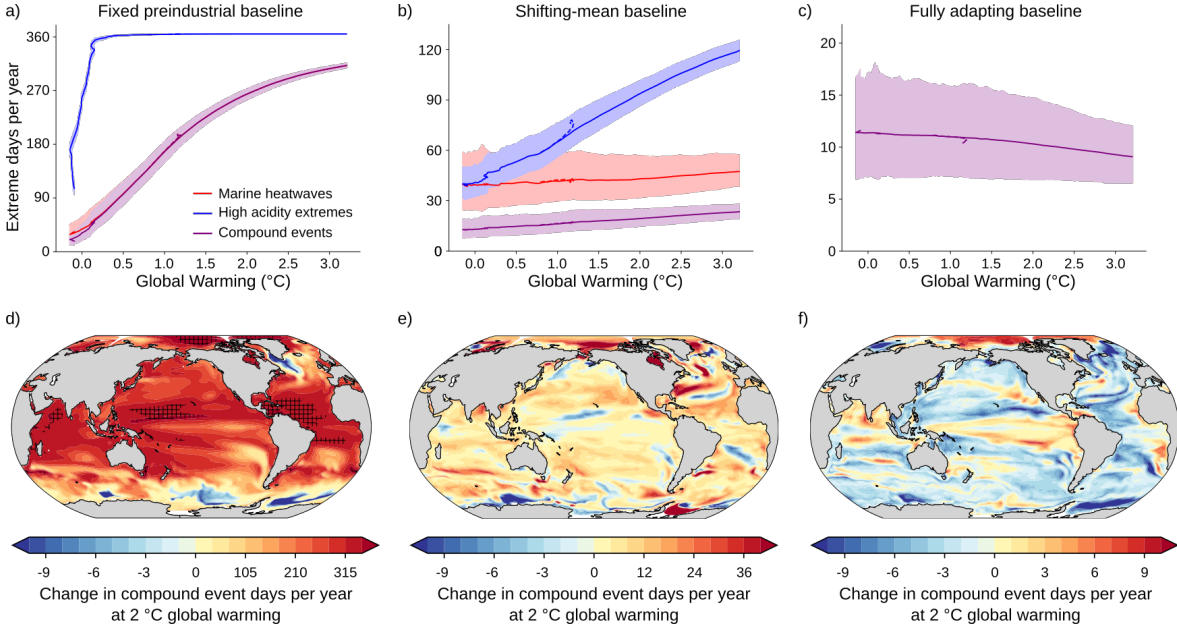


Figure 4.4: Projected changes in compound MHW-OAX events under global warming. (a-c) Global mean number of yearly extreme event days relative to global warming levels for MHWs (red lines), OAX events (blue lines), and compound MHW-OAX events (purple lines) for (a) fixed preindustrial baselines, (b) shifting-mean baselines, and (c) fully adapting baselines. The time series are smoothed with a 21-year running mean filter. Thick lines display the ensemble means and shaded areas depict the 10th and 90th percentile ranges of the 30 ensemble member simulations over the 1861-2100 period following the RCP8.5 scenario during the period 2006-2100. The dashed lines in (a-c) show ensemble mean changes relative to warming levels under the RCP2.6 scenario. Differences between the RCP8.5 and RCP2.6 greenhouse gas scenarios are much smaller than the ensemble spread, indicating that the results are independent of the warming path. (d-f) Regional changes in compound event days relative to the preindustrial period at 2 °C global warming for (d) fixed preindustrial baselines, (e) shifting-mean baselines, and (f) fully adapting baselines. Hatching in (d) indicates areas with year-round compound events (i.e., more than 360 days per year). Only results of the high emissions scenario RCP8.5 scenario are shown in (d-f), because the changes in globally averaged MHW-OAX occurrence are independent of the warming path.

Burger et al., 2020). The strongest increase in compound MHW-OAX is projected for the Arctic Ocean north of 66 °N (Fig. 4.4e), where the reduction of sea ice leads to large increases in temperature (Frölicher et al., 2018) and $[H^+]$ (Kwiatkowski et al., 2020; Burger et al., 2020) variability. Although the increase in compound MHW-OAX under the shifting-mean baseline is highest there, the increase at 2 °C warming is still on average only 7 % of the increase under the fixed baseline. In most other regions, the ratio between increases under the shifting-mean baseline and the fixed baseline is even smaller. An exception is the western boundary current region of the North Atlantic, where relatively large shifting-mean baseline changes exceed 10 % of the fixed baseline changes.

When defining extreme events relative to a fully adapting baseline (see Methods), the occurrence of MHW-OAX is projected to slightly decrease, from 12 days per year at preindustrial to 10 (10-11) days per year under 2 °C global warming and to 9 (9-10) days per year under 3 °C global warming (Fig. 4.4c). The decrease in MHW-OAX event occurrence relative to the fully adapting baseline is equivalent to a reduction in the numerator of the LMF between the two periods and indicates that SST and $[H^+]$ anomalies become less correlated. The reduction in correlation may be attributed to the over-proportional increase in the $[H^+]$ sensitivity with respect to C_T in warmer, high C_T waters (Fassbender et al., 2018). This relative increase in $[H^+]$ sensitivity to C_T is globally 75 % larger than the relative increase in $[H^+]$ sensitivity to temperature at 2 °C global warming in the GFDL ESM2M simulation (Ext. Data Fig. 4.9).

Exceptions to the general decrease in correlation and MHW-OAX events are upwelling regions, such as the eastern equatorial Pacific and the eastern boundary upwelling systems, where a reduction in sC_T variability is simulated, and the Arctic Ocean, where an increase in SST- sC_T correlation is simulated (Fig. 4.4f). Regionally, the changes in MHW-OAX events relative to a fully adapting baseline can be of similar magnitude as those relative to a shifting-mean baseline. For example, in the subtropical North Atlantic (15°N – 30°N , 65°W – 25°W), the occurrence of MHW-OAX increases by 10 days per year relative to a shifting-mean baseline, while it decreases by 5 days relative to a fully adapting baseline under 2°C global warming. This indicates that the reductions in the dependence of SST and $[\text{H}^+]$ that reduce MHW-OAX event occurrence are overcompensated by an increase in $[\text{H}^+]$ and SST variability, resulting in a net increase in MHW-OAX event days relative to a shifting-mean baseline.

4.3 Discussion and conclusions

The robustness of the results presented here depends on the quality of the underlying global gridded observation-based $[\text{H}^+]$ product and fidelity of the GFDL ESM2M model. The global observation-based product was evaluated with in-situ time-series data from 15 ocean stations (panel and dots in Fig. 4.1; Ext. Data Tables 4.1 and 4.2). The differences between the LMFs estimated from the gridded observation-based product and the time series are insignificant at 14 of 15 stations (5 % significance level) when accounting for the large statistical uncertainties (see Methods). Furthermore, the time series estimates show a similar spatial pattern, corroborating our confidence in the gridded observation-based product (Chapter 3; Burger et al., 2020). Locally, the observation-based estimates are uncertain in the Southern Ocean, especially during austral winter, due to a lack of observational $p\text{CO}_2$ data (Landschützer et al., 2016; Gray et al., 2018). Another potential caveat is that we derive $[\text{H}^+]$, among other variables, from SST, which might cause an automatic correlation between both variables and hence gives an inaccurate representation of the LMF. However, multiple lines of evidence suggest that this is not the case. First, the LMF pattern (Fig. 4.1) and the correlation coefficient of SST and surface $[\text{H}^+]$ anomalies based on observations (Fig. 4.2a) looks very similar to the correlation coefficient based on simulated $[\text{H}^+]$ and SST (Ext. Data Fig. 4.10b). Second, the simulated pattern does not change either if A_T is derived from simulated SST and salinity, or if directly simulated A_T is used. Third and most important, the LMFs at ocean stations that provide directly measured $[\text{H}^+]$ are similar to the LMFs calculated from measured SST, salinity, and $p\text{CO}_2$ at these stations. An additional caveat might be that our analysis of gridded observational data is limited to monthly resolution, because most data are not available at higher temporal resolution. However, comparison to high temporal resolution model and buoy-data suggests that the pattern of compound event occurrence is relatively insensitive to the temporal resolution (Ext. Data Table 4.1). We conclude that the used global gridded observation-based $[\text{H}^+]$ product is well suited to analyze compound MHW-OAX events.

The simulations of the GFDL ESM2M model can be considered robust for two reasons. First, the simulated correlation of SST and $[\text{H}^+]$ anomalies at present-day shows good agreement with the spatial pattern of the gridded observational product, despite with a general positive bias in the simulated correlation coefficient in the GFDL model, which is also present in other ESMs from the sixth phase of the Coupled Model Intercomparison Project (CMIP6; Ext. Data Fig. 4.10). This bias suggests that the ESMs generally overestimate the effect of temperature on $[\text{H}^+]$ or underestimate the effect of sC_T variations. Second, the future projections based on fixed and shifting-mean baselines rely mostly on well-understood long-term ocean warming and acidification trends (Bopp et al., 2013; Kwiatkowski et al., 2020), as well as changes in $[\text{H}^+]$ variability with increasing CO_2 (Burger et al., 2020; Kwiatkowski & Orr, 2018), although the

exact numbers of MHW-OAX changes may depend on the model used. Under a fixed baseline, the projected changes in compound MHW-OAX events are mainly driven by secular trends in ocean warming and acidification, which are well simulated by the GFDL ESM2M model over the historical period (Bopp et al., 2013). The fixed-baseline projections are insensitive to the simulated positive bias in the correlation coefficient of SST and $[\text{H}^+]$ anomalies after the onset of near-permanent $[\text{H}^+]$ extreme events at around 0.3°C global warming. Under a shifting-mean baseline, projected changes in MHW-OAX events stem mainly from an increase in $[\text{H}^+]$ variability, which is also considered to be qualitatively robust since it is rooted in the nonlinear response of carbonate chemistry to increasing C_T (Kwiatkowski & Orr, 2018; Burger et al., 2020). However, a slight positive bias in the number of compound event days may be simulated due to the positive bias in correlation of SST and $[\text{H}^+]$. Furthermore, the projected global decline in MHW-OAX events with respect to a fully adapting baseline is likely robust, because it is simulated by all CMIP6 models (Ext. Data Fig. 4.11), and because of the over-proportional increase in C_T sensitivity of $[\text{H}^+]$ compared to the temperature sensitivity under increasing CO_2 that is also expected from carbonate chemistry (Ext. Data Fig. 4.9; Zeebe & Wolf-Gladrow, 2001). However, there is much less agreement between models on the regional scale (Ext. Data Fig. 4.11) as these regional trends can be caused by variability changes in SST or sC_T , by correlation changes between SST and sC_T , or by a combination of these factors. Analysis of these changes in each model is beyond the scope of the paper calling for further analysis.

Here we have analyzed compound marine heatwave and high $[\text{H}^+]$ extreme events, but ocean acidification can also affect marine organisms via increases in $p\text{CO}_2$ or reductions in calcium carbonate saturation states. Due to the high correlation between $[\text{H}^+]$ and $p\text{CO}_2$ anomalies ($r=0.96$ on global average), compound events in $[\text{H}^+]$ and temperature are often also compound events in $p\text{CO}_2$ and temperature as indicated by a very similar LMF pattern for high SST and high $p\text{CO}_2$ compound events (Ext. Data Fig. 4.14). On global average, 78 % of the months with SST- $[\text{H}^+]$ compound events are also identified as months with extremely high $p\text{CO}_2$, potentially causing three-fold stress on ecosystems. Much larger discrepancies are found when analyzing compound low aragonite saturation state and high temperature events. Due to the generally positive correlation of saturation state and temperature, the occurrence of such compound events is very rare ($\text{LMF}=0.03$). This contrasts with the MHW-OAX events analyzed in this study, where high- $[\text{H}^+]$ and high-temperature events overlap relatively often due to the positive temperature dependency of $[\text{H}^+]$ (Xue et al., 2021). Thus, on global average only 2 % of months with high SST- $[\text{H}^+]$ compound events are also months with extremely low aragonite saturation state. That MHW-OAX events are usually not accompanied by extremely low calcium carbonate saturation state may prevent calcifying organisms from additional stress due to impacts on calcification and shell dissolution (Kroeker et al., 2013).

The combination of observations and models allowed to localize MHW-OAX events, estimate their frequency, better understand their drivers, and to project their development in a changing climate. Our results indicate that MHWs and OAX events are not independent and often occur together. This suggests that some of the observed MHWs (Laufkötter et al., 2020) were also compound MHW-OAX events, in particular in the low-to-mid latitudes where we find that one out of four MHWs are also compound MHW-OAX events. The reported impacts of some low-latitude MHWs on marine organisms and ecosystems (Smale et al., 2019) may therefore be also connected to additional stress from high acidity events (Doney et al., 2020). Furthermore, also other co-occurring biogeochemical extreme events such as low oxygen events (Gruber et al., 2021) or low net primary production events (Le Grix et al., 2021) may add to the stress during MHWs. To shed light on different aspects of changes in compound MHW-OAX occurrence, changes were assessed with respect to three different baselines. Compound MHW-OAX days are

projected to become more frequent when considering the trends in SST and $[\text{H}^+]$ as well as increases in their variabilities. When defined with respect to a fixed baseline, the occurrence of MHW-OAX events is projected to strongly increase, with unknown, potentially devastating effects on marine biota. Even if organisms can acclimate and adapt to long-term ocean warming and acidification or can relocate to favorable habitats, they may still be impacted by a 60 % increase in compound MHW-OAX days under 2 °C global warming that emerges mainly from increasing variability in $[\text{H}^+]$. However, we also demonstrate that the decrease in the dependence of temperature and $[\text{H}^+]$ anomalies slightly dampens the increase in the co-occurrence of hot temperature and high acidity extremes, but this effect is small at global scale. The potential threat from rising numbers of MHW-OAX days highlights the urgent need to better understand the organism and ecosystem response to such ocean compound events. Future studies on extreme events should also carefully choose the baseline depending on the impact which they analyze. Choosing the wrong baseline, shifting-mean for unmovable corals, or fixed for fish that can migrate, may lead to an overestimation or underestimation of the impact of changes in extreme events.

4.4 Methods

4.4.1 Definition of extreme and compound events

Marine heatwaves (i.e., hot temperature extremes) and high acidity events (i.e., high $[H^+]$ extremes) were defined as the exceedance of SST and surface $[H^+]$ of their local and seasonally varying 90th percentile. The seasonally varying 90th percentiles were calculated for each calendar month (gridded observational data) or calendar day (GFDL ESM2M model data) separately. Under this definition extreme events have the same occurrence probability throughout the year. For the time series data, there are often too few measurements for a given calendar month over the measurement period (sometimes only 10 or less) to calculate statistically meaningful monthly percentile thresholds (as done for the gridded observation-based data). Therefore, one annual percentile threshold for monthly anomalies was calculated from all monthly anomalies instead of 12 thresholds for each month individually. The difference between calculating the LMF using seasonally varying thresholds compared to annually fixed threshold is generally small. For example, the global average difference between these methods is 0.14 LMF units when using the gridded data-based product. Monthly anomalies were calculated by subtracting from each measurement value the mean of all measurements that were obtained in the same calendar month. The 90th percentile was chosen to have a sufficiently large sample size of observational data for statistical assessments. Sensitivity tests with the GFDL ESM2M model ensemble show that results are qualitatively insensitive to the choice of the percentile (e.g., 90th vs. 95th percentile; not shown). The usage of a percentile threshold allows the quantification of MHWs, OA extremes and MHW-OAXs across locations which differ in variability. Absolute thresholds are often determined from the perspective of local impact, but a globally fixed absolute threshold is only meaningful in some regions, but not in others.

Compound MHW-OAX events are defined as the days or months when both SST and surface $[H^+]$ are above the 90th percentiles at the same time and location. We do not impose a criterion on the minimum duration of compound MHW-OAX events, as it is often applied for MHWs (Hobday et al., 2016). While such a criterion would overall reduce the number of MHW-OAX event days, it would not considerably change the LMF as can be seen from the insensitivity of the LMF to the temporal resolution of the data (Ext. Data Fig. 4.13). The data for the present-day period (gridded observation-based product and time series) were linearly detrended prior to identifying the extreme events.

Temporal changes in MHWs, OAX events, and MHW-OAX events within the large ensemble model simulation were defined with respect to (i) fixed preindustrial baselines (called '*fixed preindustrial baseline*' in Fig. 4.4), (ii) shifting-mean baselines ('*shifting-mean baseline*'), and (iii) fully adapting baselines ('*fully adapting baseline*'). Under a fixed preindustrial baseline, the extreme events were defined with respect to preindustrial seasonally varying 90th percentiles. Under a shifting-mean baseline, these percentile thresholds were shifted according to the ensemble-mean changes with respect to the preindustrial mean state (Chapter 3; Burger et al., 2020). The ensemble mean was smoothed with a 365-day running mean filter to remove its seasonal cycle (Chapter 3; Burger et al., 2020). Under a fully adapting baseline, individual thresholds for SST and $[H^+]$ were calculated for each day of the historical, RCP8.5, and RCP2.6 ensemble simulations. These were determined as the 90th percentiles of the 30-value ensemble distributions for that day as simulated by the respective 30-member ensemble simulation. As a result, the probability for univariate SST and $[H^+]$ extreme events is constant over time. Changes in compound events can thus only arise from changes in the dependence between SST and $[H^+]$.

4.4.2 Analysis methods

a. Extraction of global warming levels

We quantify changes in compound events for different levels of global warming (e.g., in Fig. 4.4d-f for 2 °C global warming). To do so, 20-year periods were identified over which the ensemble-mean change in globally averaged atmospheric near-surface (2m) temperature with respect to preindustrial conditions is closest to a specific global warming level. In the GFDL ESM2M model and under the RCP8.5 scenario, these periods are 2007-2026 (1 °C), 2045-2064 (2 °C), and 2075-2094 (3 °C).

b. Confidence intervals and statistical tests for the LMF estimates

Confidence intervals for the LMF estimates for the time series, gridded data, and GFDL ESM2M ensemble data at the time series locations (Ext. Data Table 4.1) are derived by identifying the counted number of MHW-OAX days/months with the outcome of a binomial experiment (Wilks, 2005), where the binomial ‘success’ probability is given by the conditional probability of observing a MHW-OAX event given a MHW or OAX event. Here, the probability is assumed to be constant over time. Using the *binom* package for *R*, we calculate the Clopper-Pearson confidence interval (Clopper & Pearson, 1934) for the estimated conditional probability, which is directly proportional to the LMF since the probability for MHW and OAX events is a constant, here 0.1. The LMF confidence interval is then obtained by dividing the lower and upper bounds of the Clopper-Pearson confidence interval by 0.1. P-values for the difference between the conditional probabilities estimated for the time series and for the gridded data as well as the GFDL ESM2M model are calculated using the two-sided Fisher’s exact test (Agresti, 2012) (*fisher.test* function for *R*). Fisher’s exact test was chosen due to the often low count of MHW-OAX events in the time series data (Cochran, 1954).

c. Estimation of the LMF from correlation coefficients

The LMF of MHW-OAX events can be approximated by the Pearson correlation coefficient of SST and $[H^+]$ anomalies. When assuming normally distributed monthly anomalies of SST and $[H^+]$, the estimated LMF ($\widehat{\text{LMF}}$) is given by

$$\widehat{\text{LMF}} = \frac{1}{0.1^2} \int_{x_{0.90}}^{\infty} dx_1 \int_{x_{0.90}}^{\infty} dx_2 f(x_1, x_2; r), \quad (4.2)$$

with r denoting the correlation coefficient of SST and $[H^+]$ anomalies. f denotes the bivariate probability density function of two standard normal distributed variables

$$f(x_1, x_2; r) = \frac{1}{2\pi\sqrt{1-r^2}} \exp\left(\frac{-1}{2(1-r^2)}(x_1^2 - 2rx_1x_2 + x_2^2)\right) \quad (4.3)$$

and is the 90th percentile of the standard normal distribution. The integration variables x_1 and x_2 represent SST and $[H^+]$ anomalies, here assumed to be normally distributed. The overall small difference between the counted LMF and the $\widehat{\text{LMF}}$ estimated from the correlation coefficient (global mean deviation of 0.11) for the observation-based gridded data over the period 1982-2019 (Ext. Data Fig. 4.5) suggests that the observed bivariate probability for exceeding the 90th percentile is similar to that assuming normally distributed temperature and $[H^+]$ anomalies and that the correlation coefficient is a good predictor for MHW-OAX compound events.

d. Decomposition of the correlation coefficient into its drivers

The observation-based correlation coefficient of SST and $[\text{H}^+]$ anomalies for a calendar month was decomposed into the contributions from the direct temperature dependence of $[\text{H}^+]$ and contributions from salinity-normalized C_T (sC_T) and A_T (sA_T), as well as the remaining contribution from freshwater variations. For the salinity normalization, C_T and A_T were divided by the ratio of salinity (S , in practical salinity units) to temporal mean salinity. Thus, variations in C_T and A_T stemming from variations in freshwater (precipitation, evaporation, and sea ice melt) have no effect on sC_T and sA_T . As the covariance is linear in its two arguments, covariance of temperature and $[\text{H}^+]$ ($\text{covar}(\text{SST}, [\text{H}^+])$) can be expanded by replacing $[\text{H}^+]$ anomaly (denoted by $[\text{H}^+]$ for simplicity here) with a first order Taylor expansion in the anomalies for SST, sC_T , sA_T , and S :

$$[\text{H}^+] \approx \left. \frac{\partial[\text{H}^+]}{\partial \text{SST}} \right|_{\overline{\text{SST}}, \dots} \cdot \text{SST} + \left. \frac{\partial[\text{H}^+]}{\partial C_T} \right|_{\overline{\text{SST}}, \dots} \cdot C_T + \left. \frac{\partial[\text{H}^+]}{\partial A_T} \right|_{\overline{\text{SST}}, \dots} \cdot A_T + \left. \frac{\partial[\text{H}^+]}{\partial S} \right|_{\overline{\text{SST}}, \dots} \cdot S. \quad (4.4)$$

The partial derivatives $\partial/\partial x$ are evaluated at $\overline{\text{SST}}$, $\overline{C_T}$, $\overline{A_T}$, and \overline{S} , the temporal mean values of the drivers, using *mocsy 2.0* (Orr & Epitalon, 2015). Here, it was assumed that the variations of the partial derivatives over the calendar months can be ignored. Salinity normalization for C_T and A_T is introduced. C_T anomaly is replaced by $sC_T + \frac{\overline{C_T}}{\overline{S}} \cdot S$, with sC_T and S denoting the anomalies in salinity-normalized C_T and salinity, and with $\overline{C_T}$ and \overline{S} denoting their temporal mean values, again assuming that monthly mean values for sC_T and S can be replaced by the temporal mean values. The anomaly in A_T is replaced analogously. Eq. (4.4) is inserted in $\text{covar}(\text{SST}, [\text{H}^+])$. By using bilinearity of covariance and that $\text{covar}(xy) = \sigma_x \sigma_y r_{x,y}$, with σ_x denoting the standard deviation and $r_{x,y}$ denoting the Pearson correlation coefficient, one obtains

$$\begin{aligned} r_{\text{SST}, [\text{H}^+]} = & \frac{\partial[\text{H}^+]}{\partial \text{SST}} \frac{\sigma_{\text{SST}}}{\sigma_{[\text{H}^+]}} + \frac{\partial[\text{H}^+]}{\partial C_T} \frac{\sigma_{sC_T}}{\sigma_{[\text{H}^+]}} r_{\text{SST}, sC_T} + \frac{\partial[\text{H}^+]}{\partial A_T} \frac{\sigma_{sA_T}}{\sigma_{[\text{H}^+]}} r_{\text{SST}, sA_T} \\ & + \left(\frac{\overline{sC_T}}{\overline{S}} \frac{\partial[\text{H}^+]}{\partial C_T} + \frac{\overline{sA_T}}{\overline{S}} \frac{\partial[\text{H}^+]}{\partial A_T} + \frac{\partial[\text{H}^+]}{\partial S} \right) \frac{\sigma_S}{\sigma_{[\text{H}^+]}} r_{\text{SST}, S} + \text{residual}. \end{aligned} \quad (4.5)$$

The terms on the right-hand side of Eq. (4.5) represent the contributions from SST, sC_T , sA_T , and freshwater variations (from left to right). The residual of the decomposition (simulated correlation coefficient minus sum of decomposition terms) for the gridded data product over the period 1982-2019 (Fig. 4.2; Ext. Data Fig. 4.6) is smaller than 0.1 correlation coefficient units for 99 % of the ocean surface (Ext. Data Fig. 4.6c). The freshwater term only has a small imprint on SST- $[\text{H}^+]$ correlation (Ext. Data Fig. 4.6b) since the direct effect from salinity variations on $[\text{H}^+]$ is small and because its effects on C_T and A_T largely compensate each other. Likewise, the contribution from sA_T is comparably small (Ext. Data Fig. 4.6a). The approximation of the correlation coefficient by the contribution of SST and sC_T is precise to 0.1 units in 60 % of the ocean surface and to 0.4 in 92 % of the ocean surface. The sign of the approximated correlation coefficient is correct in 93 % of the ocean surface.

4.4.3 Observation-based data

a. Global sea surface temperature and $[\text{H}^+]$ data

Global monthly SST data on a grid with 1° horizontal spacing from 1982 to 2019 from the version 4.2.1 (EN4.2.1) data set developed by the Met Office Hadley Centre (Good et al., 2013)

were used. EN4 is a gridded product that is based on temperature and salinity profiles, with World Ocean Database (Boyer et al., 2016) being the main source of data. SST is here defined as mean temperature over the uppermost 10 m. The global gridded observation-based $[\text{H}^+]$ (total scale) dataset covering the period from 1982 to 2019 was reconstructed in two steps following the method outlined by Burger et al. (2020) (Chapter 3). In a first step, the SST and surface salinity fields from EN4.2.1 were used to derive total surface alkalinity (A_T) using the *LIARv2* total alkalinity regression algorithm (Carter et al., 2018). In a second step, a monthly $[\text{H}^+]$ field at 1° horizontal grid resolution was derived using the *CO2SYS* carbonate chemistry package (van Heuven et al., 2011) from the monthly, gridded surface salinity, SST, and A_T and from the interpolated global surface $p\text{CO}_2$ product *MPI-SOMFNN* (Landschützer et al., 2016) that covers the period 1982-2019 with monthly-mean temporal resolution and is based on data from the *Surface Ocean CO2 Atlas version 4* (Bakker et al., 2016).

The accuracy of the *LIARv2* algorithm was tested with the GFDL ESM2M model output by comparing directly simulated A_T (A_T^{sim}) with the A_T that was estimated by the *LIARv2* algorithm from simulated SST and surface salinity for one ensemble member over the 1982-2019 period (A_T^{LIAR}). The comparison yields a root-mean-square-error between A_T^{sim} and A_T^{LIAR} of 32 mol kg⁻¹. This difference between the A_T^{sim} and A_T^{LIAR} translates into differences in $[\text{H}^+]$ and hence into differences between the correlation coefficient of SST and $[\text{H}^+]$ anomalies and between the LMF. These differences between the correlation coefficients when using A_T^{sim} and A_T^{LIAR} are below 0.1 units in 99.5 % of the surface ocean and the difference in the LMF is below 0.5 in 96.5 % of the surface ocean area (Ext. Data Fig. 4.12), indicating that our estimated observation-based A_T from SST and sea surface salinity is accurate enough to be used in the calculation of observation-based $[\text{H}^+]$. The same comparison was made for ocean stations where direct A_T measurements are available. The LMF using direct A_T measurements slightly differ from the LMF using estimated A_T (not shown) but remain within the large uncertainty bounds that exist at these stations due to the relatively short observational period, indicating that our LMF results are likely insensitive to the exact choice of estimated A_T .

GFDL ESM2M model output suggests that compound MHW-OAX events are often shorter than one month (Ext. Data Fig. 4.8). Nevertheless, the LMF of present-day compound events can be approximated based on monthly (observational-based) data. Comparison of the LMF obtained from monthly-mean model output to that from daily-mean model output for the period 1982-2019 yields a root-mean-square error of 0.2 (Ext. Data Fig. 4.13). This deviation results mainly from a small bias in the LMF from monthly-mean data compared to daily-mean data (global mean LMF of 2.7 in monthly-mean data vs. 2.9 in daily-mean data; Ext. Data Fig. 4.13c). As such, using monthly data may slightly underestimate the occurrence of MHW-OAX events.

b. Time series of in-situ SST and $[\text{H}^+]$ data

In-situ observations from the KNOT and K2 stations in the north Pacific, the Hawaii Ocean Time-series (HOT), the Bermuda Atlantic Time-series Study (BATS), the European Station for Time series in the Ocean Canary Islands (ESTOC), the 137°E transect at 30°N and at 5°N, the Munida time series, the CARIACO time series, and from seven autonomous open-ocean surface buoys were used in this study (Fig. 4.1; Ext. Data Table 4.2). The KNOT and K2 station data were combined due to their spatial proximity (44°N, 155°E vs 47°N, 160°E) resulting in a total of 15 time series. For the seven autonomous open-ocean surface buoys, monthly means were calculated from the 3-hourly data to match the approximate measurement frequency of the remaining stations. For completeness, the buoy data was also aggregated to daily-means (Ext. Data Table 4.1). Only buoys providing at least 5 years of data were analyzed, being KEO

(Kuroshio Extension Observatory), Papa (Ocean Station Papa), Stratus, TAO125W, TAO140W, TAO170W (NDBC Tropical Atmosphere Ocean 0°N at 125°W, 140°W and 170°W, respectively), and WHOTS (Woods Hole Oceanographic Institution Hawaii Ocean Time-series Station) (Sutton et al., 2019).

$[\text{H}^+]$ was calculated from measured pH at in-situ temperature where available. If pH at in-situ temperature was not available, $[\text{H}^+]$ was calculated from sea surface temperature, salinity, A_T , phosphate, and silicate and, depending on the time series, from either measured C_T or $p\text{CO}_2$ (Ext. Data Table 4.2). If calculated pH was not provided by the data set, *mocsy 2.0* (Orr & Epitalon, 2015) was used to calculate $[\text{H}^+]$ when C_T was measured and *CO2SYS* (van Heuven et al., 2011) was used when $p\text{CO}_2$ was measured. Although *mocsy 2.0* became the standard routine to calculate the marine carbon dioxide system in recent years (Orr et al., 2017), *CO2SYS* was used in the latter case because *mocsy 2.0* does not allow calculation of $[\text{H}^+]$ from $p\text{CO}_2$. However, differences between the *mocsy 2.0* and *CO2SYS* for $[\text{H}^+]$ calculations are small (Orr et al., 2018). Where not available, mean silicate and phosphate concentrations were taken from the closest grid cells of *World Ocean Atlas 2018* (Garcia et al., 2019). For the seven autonomous open-ocean surface buoys, A_T was estimated from measured sea surface temperature and salinity using the *LIARv2* algorithm (Carter et al., 2018).

c. Chlorophyll concentration, nitrate, and air-sea CO_2 flux data

Daily-mean data-assimilated chlorophyll concentration output (Fig. 4.3a) from the NASA Ocean Biogeochemical Model (version NOBM.R2020.1) (Gregg & Rousseaux, 2017) over the period 1998-2018 was used in this study. The model assimilates satellite chlorophyll data from the Sea-viewing Wide Field-of-view Sensor, the Moderate Resolution Imaging Spectroradiometer Aqua and the Visible Infrared Imaging Radiometer Suite and provides daily data within the mixed layer. Monthly mean values were calculated prior to the analysis. Mean nitrate concentration data from the *World Ocean Atlas 2018* (Garcia et al., 2019) was also used in Fig. 4.3a. The observation-based monthly air-sea CO_2 flux data product over the period 1982-2019 shown in Fig. 4.3b is based on the interpolated $p\text{CO}_2$ product (Landschützer et al., 2016; Landschützer et al., 2020) that was used to derive the gridded $[\text{H}^+]$ product.

4.4.4 GFDL ESM2M large ensemble

a. Model setup and simulations

The fully coupled GFDL ESM2M Earth system model (Dunne et al., 2012, 2013), developed at the NOAA Geophysical Fluid Dynamics Laboratory, was used in this study. The physical ocean component of the model, the Modular Ocean Model (version 4p1 (Griffies, 2009)), has a nominal 1° horizontal resolution with increasing resolution near the equator, and 50 vertical levels with vertical resolution decreasing from 10 m at the surface to 300 m at 5000 m depth. This physical ocean model is coupled to the ocean biogeochemistry model TOPAZv2, which simulates 30 tracers and three phytoplankton groups. Zooplankton grazing is implicitly simulated. The ocean carbonate chemistry routines are based on the OCMIP2 protocol (Najjar & Orr, 1998).

A 30-member ensemble simulation from 1861 to 2100 was performed. The large ensemble size allows for a robust assessment of changes in compound events (Fig. 4.4a-c) and is necessary to assess changes in compound events relative to a shifting-mean and fully adapting baseline. The

1861-2005 period was forced with prescribed historical greenhouse gas and aerosol concentrations (Meinshausen et al., 2011). The period from 2006 to 2100 was simulated with greenhouse gas and aerosol concentrations from the low-emissions high mitigation concentration pathway RCP2.6 (van Vuuren et al., 2011) and from the high-emissions no mitigation concentration pathway RCP8.5 (Riahi et al., 2011). However, the main global mean results shown in Figure 4.4 do not depend on the warming path and are hence independent from the emission scenario. As a result, Figure 4.4 mainly shows results for the RCP8.5 scenario. However, global-mean changes for the RCP2.6 scenario are also shown in Fig. 4.4a-c. A 500-year preindustrial control simulation was also performed to calculate the fixed baseline. The initialization procedure of the large ensemble simulation is described in Burger et al. (2020) (Chapter 3). Daily mean ocean temperature and $[\text{H}^+]$ (on the total scale) output from the surface layer of the ocean model (0-10 m) was analyzed.

b. Model evaluation

The capability of the GFDL ESM2M model to simulate the mean state and long-term changes in ocean biogeochemistry and in particular OA extremes as well as MHWs has been extensively evaluated. The model has been shown to capture the mean state in $[\text{H}^+]$ (Bopp et al., 2013) and its mean seasonal cycle (Kwiatkowski & Orr, 2018), as well as changes in $[\text{H}^+]$ seasonality over the last few decades (Chapter 3; Burger et al., 2020). Furthermore, the model reproduces the positive long-term trend in global mean SST (Frölicher et al., 2016) and annual number of MHW days over the satellite period (Frölicher et al., 2018).

In addition, the model’s performance in simulating compound MHW-OAX events was evaluated here. The LMF of MHW-OAX events estimated from model output agrees with the estimates from the time series data in 14 of 15 cases (differences are insignificant under a 5% significance level; Ext. Data Table 4.1). As for the gridded observation-based data product, we find a significant difference for the HOT station. However, the agreement with the WHOTS time series that is measured at the same location indicates that the difference may be due to the temporal resolution of the data: HOT consists of point measurements while the GFDL ESM2M model data and gridded data product provide daily and monthly mean values, as for WHOTS where monthly mean values were calculated from 3-hourly measurements. Moreover, the simulated LMF patterns for MHW-OAX events from monthly model output are similar to the patterns estimated from the gridded observation-based, monthly data product (compare Fig. 4.1 and Ext. Data Fig. 4.13b). However, the GFDL ESM2M model overestimates the occurrence of MHW-OAX events at the global scale (2.7 in the GFDL ESM2M model versus 1.8 in the observation-based product). Locally, the LMF overestimation is especially pronounced in the high latitudes such as the Southern Ocean (40°S-81°S; LMF of 1.9 vs 0.7), the North Pacific (40°N-66°N; 1.9 vs 1.0) and the North Atlantic (40°N-66°N; 1.8 vs 0.8). In the Southern Ocean, however, the observation-based estimates are also uncertain due to a lack of observational data, especially during austral winter for $p\text{CO}_2$ (Landschützer et al., 2016; Gray et al., 2018). Similarly, a bias of too large correlation coefficients of SST and $[\text{H}^+]$ anomalies is evident in all here analyzed CMIP6 model simulations (Ext. Data Fig. 4.10), suggesting that comprehensive ESMs systematically overestimate the effect of temperature on $[\text{H}^+]$ (contributing positively to correlation) compared to the effect of $s\text{C}_\text{T}$ variations (contributing negatively to correlation). Projections based on fixed baselines are insensitive to this positive bias in correlation because MHWs always coincide with OAX events already at 0.3°C global warming when OAX events become near-permanent. However, projections relative to shifting-mean baselines may be slightly positively biased.

When analyzing the correlation coefficient of SST and $[\text{H}^+]$ anomalies, the GFDL ESM2M model performs well compared to most CMIP6 models (Ext. Data Table 4.3), in particular in the subtropics and tropics (red and grey lines in Ext. Data Fig. 4.10k). At the global scale, the GFDL ESM2M model outperforms most of the CMIP6 models (red vs. gray stars in Ext. Data Fig. 4.10l).

Overall, the agreement between the simulated present-day compound MHW-OAX event pattern and the observation-based pattern, in addition to the model's fidelity in simulating recent trends in MHW characteristics (Frölicher et al., 2018) and $[\text{H}^+]$ seasonality (Chapter 3; Burger et al., 2020), gives high confidence in the use of the GFDL ESM2M model for analyzing patterns and trends in compound MHW-OAX events at the global scale.

	LMF				p-value ²	
	Time series (monthly) ¹	Time series (daily mean)	Gridded data (monthly mean)	GFDL ESM2M (daily mean)	Gridded data	GFDL ESM2M
KNOT-K2	1.2 (0.1-4.4)		1.2 (0.5-2.2)	1.4 (1.4-1.4)	1	1
HOT	1.0 (0.3-2.4)		4.6 (3.4-5.8)	4.4 (4.3-4.4)	0.0005*	0.00003*
BATS	3.2 (2.1-4.5)		4.2 (3.0-5.4)	3.9 (3.9-3.9)	0.29	0.19
ESTOC	5.5 (3.5-7.3)		2.8 (1.8-4.0)	3.5 (3.5-3.6)	0.06	0.12
137 °E 30 °N	1.9 (0.3-4.8)		3.4 (2.3-4.6)	3.5 (3.5-3.6)	0.47	0.34
137 °E 5 °N	2.6 (0.5-5.9)		1.6 (0.8-2.7)	2.5 (2.4-2.5)	0.60	1
Munida	3.0 (1.1-5.6)		1.0 (0.4-2.0)	1.3 (1.3-1.4)	0.09	0.10
CARIACO	4.2 (2.3-6.3)		2.0 (1.1-3.1)	2.3 (2.3-2.3)	0.12	0.10
KEO	6.1 (3.1-8.2)	4.5 (3.9-5.0)	3.0 (1.9-4.2)	3.4 (3.3-3.4)	0.06	0.08
Papa	1.0 (0.1-3.9)	0.9 (0.6-1.3)	0.0 (0.0-0.6)	2.4 (2.4-2.5)	0.16	0.46
STRATUS	3.1 (0.9-6.1)	3.5 (3.0-4.0)	1.2 (0.5-2.2)	4.1 (4.1-4.2)	0.14	0.74
TAO125W	0.0 (0.0-2.4)	0.0 (0.0-0.2)	0.0 (0.0-0.6)	0.1 (0.1-0.1)	1	1
TAO140W	0.0 (0.0-2.8)	0.1 (0.0-0.3)	0.0 (0.0-0.6)	0.1 (0.1-0.1)	1	1
TAO170W	0.0 (0.0-3.4)	0.0 (0.0-0.2)	0.0 (0.0-0.6)	0.7 (0.7-0.7)	1	1
WHOTS	3.4 (1.3-6.1)	3.2 (2.7-3.7)	4.6 (3.4-5.8)	4.4 (4.3-4.4)	0.53	0.56

¹For stations KNOT-K2, HOT, BATS, ESTOC, 137 °E 30 °N, 137 °E 5 °N, Munida, and CARIACO, point measurements on roughly monthly resolution were used, for the remaining stations monthly means were calculated from 3-hourly point measurements.

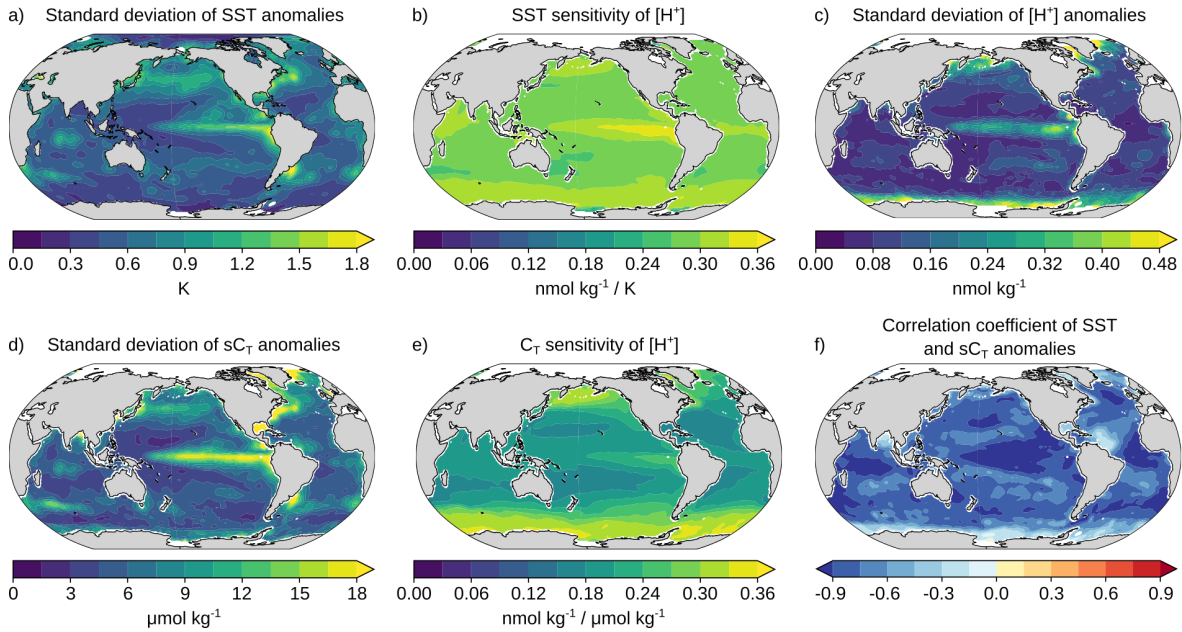
²of difference between monthly time series and monthly-mean gridded data and daily-mean GFDL ESM2M model data.

* Starts indicate significant differences.

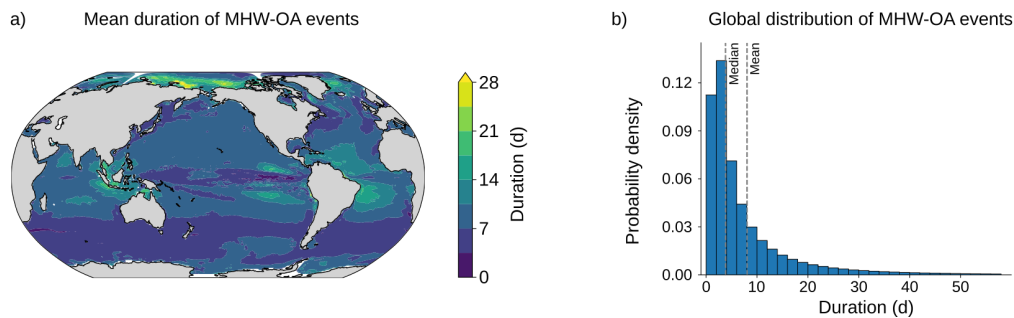
Extended Data Table 4.1: LMF estimates for the time series data, the gridded observation-based data product, and the GFDL ESM2M model ensemble at different locations. For stations KNOT-K2 to CARIACO, results are obtained from roughly monthly point measurements. For stations KEO to WHOTS, the 3-hourly data was first aggregated to from monthly means (column ‘monthly’) or to daily-means (‘daily mean’). Results for the gridded observation-based product and the GFDL ESM2M model ensemble are obtained from monthly-mean data (observation-based product) and daily-mean data (GFDL ESM2M model ensemble) for the period 1982-2019 from averaged time series over the 9 closest grid cells to the time series site. For KNOT-K2, the average of the KNOT and K2 coordinates was used for comparison to the gridded observation-based data and GFDL ESM2M model. Time series (daily mean) shows LMF estimates for the autonomous buoy data when aggregated to daily-mean resolution (see Methods). Uncertainties are given as 90 % confidence intervals and p-values are calculated for differences between the time series estimates and those for the gridded data and GFDL ESM2M model data (see Methods). All data was linearly detrended prior to the analysis.

	Reference	Lat (°N)	Lon (°E)	Period	Number of data points	Measured variables
KNOT	Wakita et al. (2011b)	44.0	155.0	1997-2008	38	SST, S, A _T , C _T , phosphate, silicate
K2	Wakita et al. (2011a)	47.0	160.0	2001-2008	37	SST, S, A _T , C _T , phosphate, silicate
HOT	adapted from Dore et al. (2009)	22.5	-158.0	1988-2018	299	SST, pH, S, A _T , C _T , phosphate, silicate
BATS	Bates & Johnson (2020)	31.4	-64.1	1983-2019	457	SST, S, A _T , C _T
ESTOC	González Dávila: pers. comm.	29.2	-15.5	1995-2020	221	SST, S, A _T , C _T
137°E 30°N	Sasano: pers. comm.	30.0	137.0	2000-2020	94	SST, S, A _T , C _T , phosphate, silicate
137°E 5°N	Sasano: pers. comm.	5.0	137.0	2000-2020	63	SST, S, A _T , C _T , phosphate, silicate
Munida	NZOA-ON data sourced from NIWA	-45.7	171.5	1998-2020	126	SST, S, A _T , pCO ₂
CARIACO	Astor et al. (2013)	10.3	-64.4	1995-2017	188	SST, S, A _T , C _T
KEO	Sutton et al. (2019)	32.3	144.6	2007-2015	18287	SST, S, pCO ₂
Papa	Sutton et al. (2019)	50.1	-144.8	2007-2015	18039	SST, S, pCO ₂
STRATUS	Sutton et al. (2019)	-19.7	-85.6	2006-2015	19200	SST, S, pCO ₂
TAO125W	Sutton et al. (2019)	0.0	-125.0	2004-2017	15546	SST, S, pCO ₂
TAO140W	Sutton et al. (2019)	0.0	-140.0	2004-2015	14279	SST, S, pCO ₂
TAO170W	Sutton et al. (2019)	0.0	-170.0	2005-2012	11686	SST, S, pCO ₂
WHOTS	Sutton et al. (2019)	22.5	-158.0	2004-2015	23216	SST, S, pCO ₂

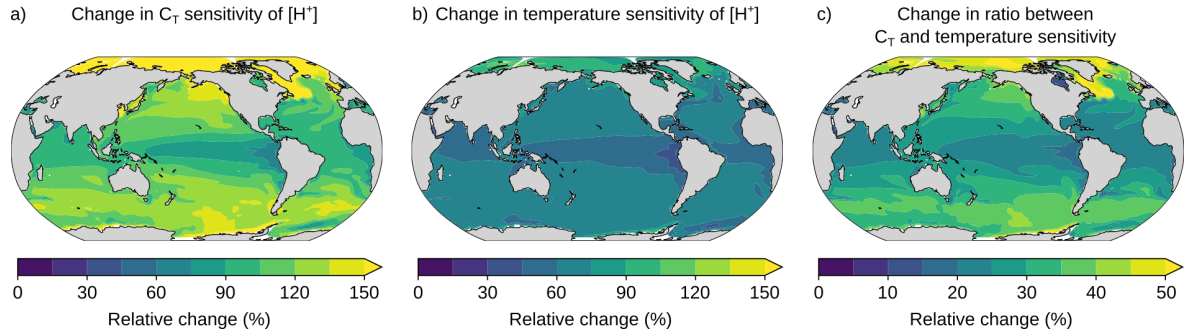
Extended Data Table 4.2: Ocean stations that provide time series data used in this study. The KNOT and K2 station data were combined due to their spatial proximity. SST was measured at every station. [H⁺] was either calculated from measured pH at in-situ temperature (only available for HOT for 204 of 299 measurements), or calculated from measured SST, salinity (S), A_T, phosphate, silicate, and either C_T or pCO₂. For the autonomous buoy data (stations KEO to WHOTS), the raw number of 3-hourly measurements is given. Here, either monthly-mean or daily-mean values are calculated from these.



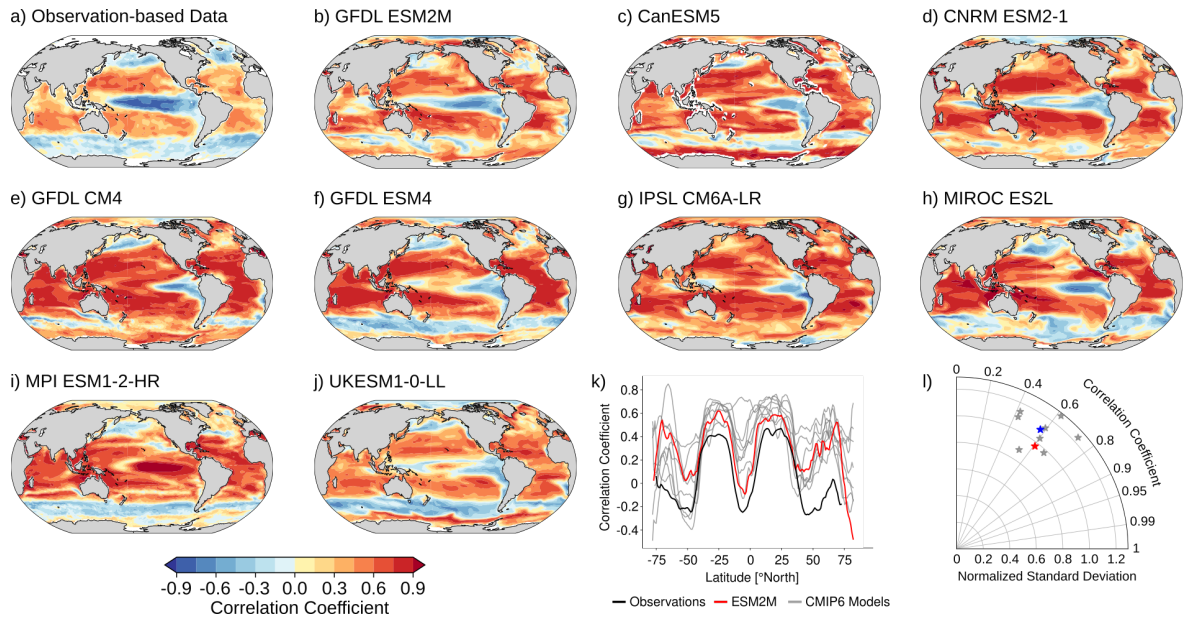
Extended Data Figure 4.7: Individual terms underlying the SST and sC_T contributions to the correlation coefficient of SST and $[H^+]$ anomalies. (a) The standard deviation of SST anomalies, (b) the temperature sensitivity of $[H^+]$, (c) the standard deviation of $[H^+]$ anomalies, (d) the standard deviation of sC_T anomalies, (e) the C_T sensitivity of $[H^+]$, and (f) the correlation coefficient of SST and sC_T anomalies. The data was linearly detrended before analysis. (a-c) form the SST contribution to the correlation coefficient of SST and $[H^+]$ anomalies, and (c-f) form the sC_T contribution (Eq. 4.5).



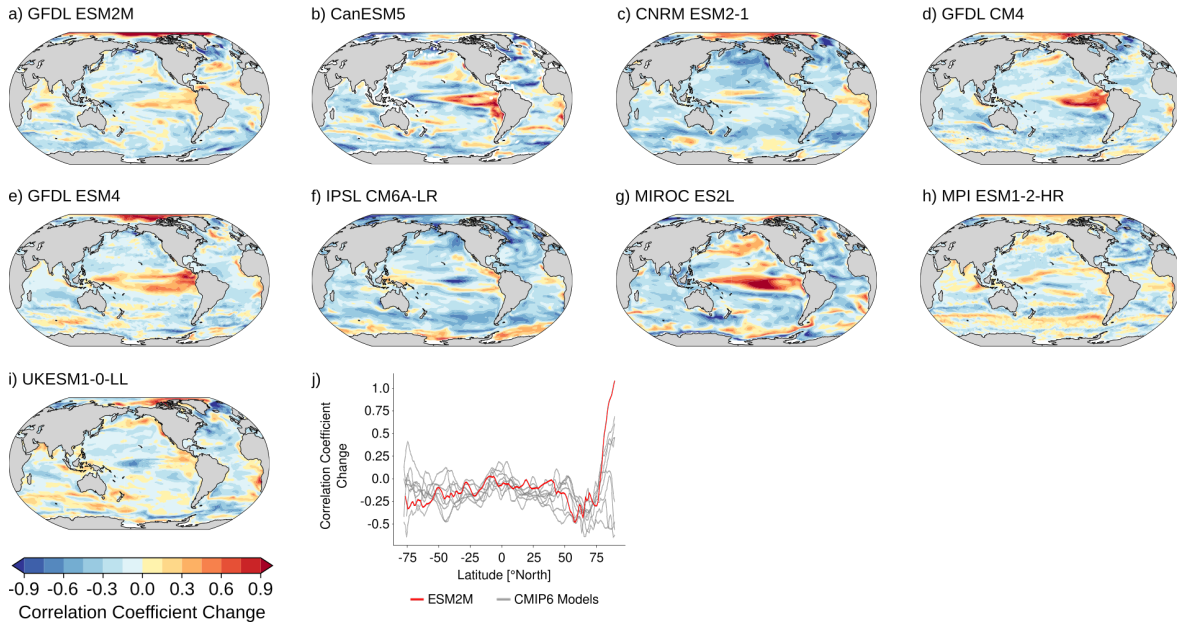
Extended Data Figure 4.8: Ensemble-mean duration of MHW-OAX events simulated by the GFDL ESM2M model over the period 1982-2019. (a) The mean duration of MHW-OAX events, and (b) the globally averaged and ensemble-mean histogram of event durations. The x-axis in (b) was cut for events that last more than 58 days due to the non-visible probability density. The longest MHW-OAX event lasted 433 d.



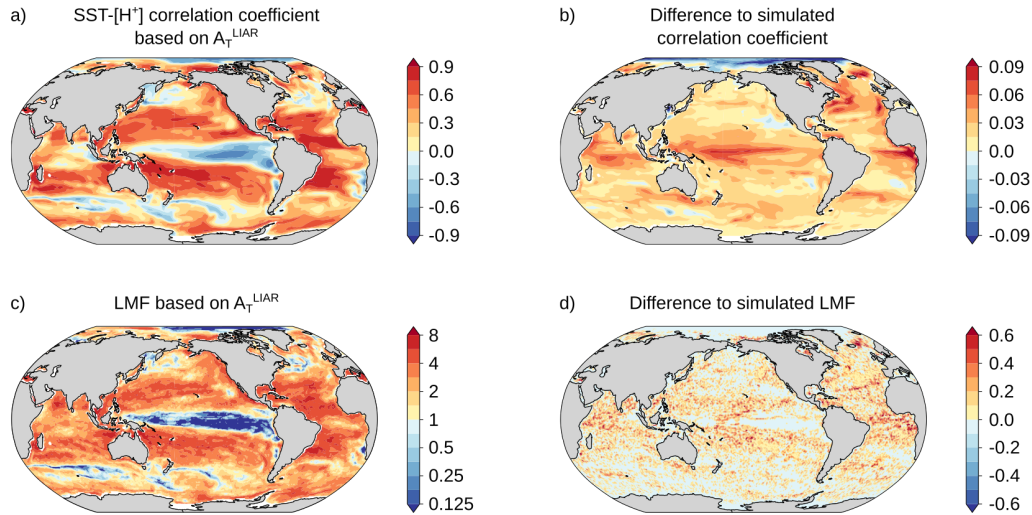
Extended Data Figure 4.9: Change in C_T sensitivity and temperature sensitivity of $[H^+]$ between the preindustrial conditions and 2 °C global warming level in the GFDL ESM2M model. (a) The relative change in C_T sensitivity (global average increase by 114%), (b) the relative change in temperature sensitivity (global average increase by 65%), and (c) the relative change in the ratio of C_T and temperature sensitivities (global average increase by 29%). For the mean sensitivities at 2 °C global warming level, sensitivities were calculated from the RCP8.5 ensemble mean for each day in the period 2045–2064 and then averaged. The sensitivities were calculated with *mocsy 2.0* (Orr & Epitalon, 2015) by numerical differentiation.



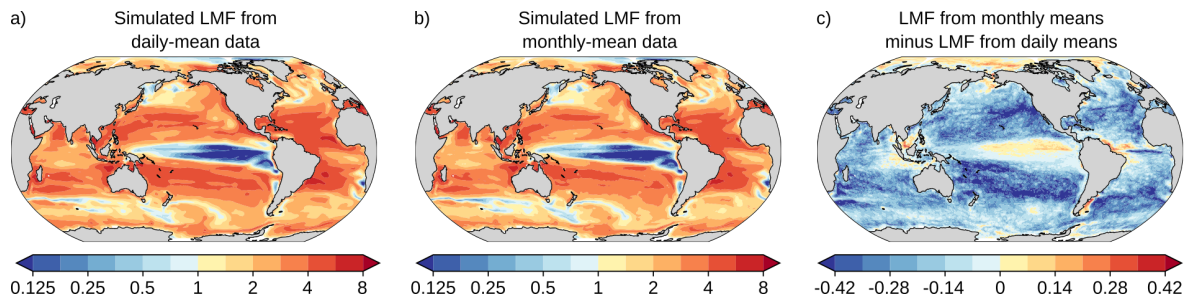
Extended Data Figure 4.10: Correlation coefficient of sea surface temperature and $[H^+]$ anomalies within observation-based data product, GFDL ESM2M model and eight CMIP6 models. (a–j) Spatial patterns of correlation coefficients from gridded observation-based data, GFDL ESM2M and eight CMIP6 models (Ext. Data Table 4.3). (k) The zonal mean correlations from the observation-based product (black), the GFDL ESM2M model (red), and the CMIP6 models (gray). The Taylor diagram (l) displays the correlation with the observation-based pattern and the spatial standard deviation relative to that of the observation-based pattern for the GFDL ESM2M (red), CMIP6 models (gray), and CMIP6 multi-model mean (blue). The correlation coefficient was calculated from monthly-mean data over the 1982–2019 period. The data was linearly detrended prior to analysis.



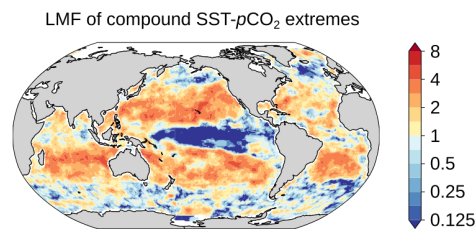
Extended Data Figure 4.11: Projected change in correlation coefficient of temperature and $[H^+]$ anomalies between 1982-2019 and 2071-2100. Spatial patterns of correlation coefficient changes for (a) the GFDL ESM2M model under RCP8.5 and (b-i) eight CMIP6 models under SSP5-8.5 (Ext. Data Table 4.3). (j) The zonal mean correlation coefficient change in the GFDL ESM2M model (red) and the CMIP6 models (grey). In the GFDL ESM2M model, the correlation coefficient decreases globally by -0.11 between the preindustrial period and 2071-2100 under RCP8.5. The CMIP6 models simulate a global decrease of -0.08 to -0.20 between the preindustrial period and 2071-2100 under SSP5-8.5.



Extended Data Figure 4.12: The correlation coefficient of SST and $[H^+]$ within the GFDL ESM2M model when A_T is estimated from temperature and salinity using the *LIARv2* algorithm. (a) The correlation coefficient of SST and $[H^+]$ anomalies obtained by calculating A_T from simulated SST and salinity using *LIARv2* (A_T^{LIAR}) and then calculating $[H^+]$ from simulated SST, salinity, pCO_2 , and *LIARv2* A_T using *CO2SYS*. (b) The difference between the correlation coefficient based on A_T^{LIAR} (panel a) and the simulated correlation coefficient. (c) The LMF with $[H^+]$ calculated from A_T^{LIAR} as in panel a), and (d) the difference between (c) and the simulated LMF. Data is shown for one ensemble member over the period 1982-2019 using monthly mean data.



Extended Data Figure 4.13: Simulated ensemble-mean LMF over the period 1982-2019 from daily-mean and monthly-mean data as simulated by the GFDL ESM2M model. Simulated LMF from daily-mean data (a), from monthly-mean data (b), and the difference between the LMF from monthly-mean and daily-mean data (c).



Extended Data Figure 4.14: The observation-based likelihood multiplication factor of compound MHWs and extremes in $p\text{CO}_2$ over the years 1982 to 2019. Map of the likelihood multiplication factor (LMF) based on the global monthly observation-based SST and surface $p\text{CO}_2$ data (*MPI-SOMFNN* product (Landschützer et al., 2016)). Warm colors indicate $\text{LMF} > 1$ and cold colors indicate $\text{LMF} < 1$. The data was linearly detrended prior to analysis.

References

- Agresti, A., 2012. *Categorical Data Analysis*, Wiley-Blackwell.
- Astor, Y. M., Lorenzoni, L., Thunell, R., Varela, R., Muller-Karger, F., Troccoli, L., Taylor, G. T., Scranton, M. I., Tappa, E., & Rueda, D., 2013. Interannual variability in sea surface temperature and fCO₂ changes in the Cariaco Basin, *Deep Sea Research Part II: Topical Studies in Oceanography*, 93, 33–43.
- Bakker, D. C. E., Pfeil, B., O'Brien, K. M., Currie, K. I., Jones, S. D., Landa, C. S., Lauvset, S. K., Metzl, N., Munro, D. R., Nakaoka, S.-I., Olsen, A., Pierrot, D., Saito, S., Smith, K., Sweeney, C., Takahashi, T., Wada, C., Wanninkhof, R., Alin, S. R., Becker, M., Bellerby, R. G. J., Borges, A. V., Boutin, J., Bozec, Y., Burger, E., Cai, W.-J., Castle, R. D., Cosca, C. E., DeGrandpre, M. D., Donnelly, M., Eiseid, G., Feely, R. A., Gkritzalis, T., González-Dávila, M., Goyet, C., Guillot, A., Hardman-Mountford, N. J., Hauck, J., Hoppema, M., Humphreys, M. P., Hunt, C. W., Ibáñez, J. S. P., Ichikawa, T., Ishii, M., Juranek, L. W., Kitidis, V., Körtzinger, A., Koffi, U. K., Kozyr, A., Kuwata, A., Lefèvre, N., Lo Monaco, C., Manke, A., Marrec, P., Mathis, J. T., Millero, F. J., Monacci, N., Monteiro, P. M. S., Murata, A., Newberger, T., Nojiri, Y., Nonaka, I., Omar, A. M., Ono, T., Padín, X. A., Rehder, G., Rutgersson, A., Sabine, C. L., Salisbury, J., Santana-Casiano, J. M., Sasano, D., Schuster, U., Sieger, R., Skjelvan, I., Steinhoff, T., Sullivan, K., Sutherland, S. C., Sutton, A., Tadokoro, K., Telszewski, M., Thomas, H., Tilbrook, B., van Heuven, S., Vandemark, D., Wallace, D. W., & Woosley, R., 2016. Surface ocean CO₂ atlas (SOCAT) V4.
- Barbieux, M., Uitz, J., Bricaud, A., Organelli, E., Poteau, A., Schmechtig, C., Gentili, B., Obolensky, G., Leymarie, E., Penkerch, C., D'Ortenzio, F., & Claustre, H., 2018. Assessing the variability in the relationship between the particulate backscattering coefficient and the chlorophyll a concentration from a global biogeochemical-argo database, *Journal of Geophysical Research: Oceans*, 123(2), 1229–1250.
- Bates, N. R. & Johnson, R. J., 2020. Acceleration of ocean warming, salinification, deoxygenation and acidification in the surface subtropical North Atlantic Ocean, *Communications Earth & Environment*, 1(1), 33.
- Bednaršek, N., Feely, R. A., Beck, M. W., Glippa, O., Kanerva, M., & Engström-Öst, J., 2018. El Niño-Related Thermal Stress Coupled With Upwelling-Related Ocean Acidification Negatively Impacts Cellular to Population-Level Responses in Pteropods Along the California Current System With Implications for Increased Bioenergetic Costs, *Frontiers in Marine Science*, 5(December), 1–17.
- Bednaršek, N., Feely, R. A., Reum, J. C. P., Peterson, B., Menkel, J., Alin, S. R., & Hales, B., 2014. *Limacina helicina* shell dissolution as an indicator of declining habitat suitability owing to ocean acidification in the california current ecosystem, *Proceedings of the Royal Society B: Biological Sciences*, 281(1785), 20140123.
- Behrenfeld, M. J., O'Malley, R. T., Siegel, D. A., McClain, C. R., Sarmiento, J. L., Feldman, G. C., Milligan, A. J., Falkowski, P. G., Letelier, R. M., & Boss, E. S., 2006. Climate-driven trends in contemporary ocean productivity, *Nature*, 444(7120), 752–755.
- Bopp, L., Resplandy, L., Orr, J. C., Doney, S. C., Dunne, J. P., Gehlen, M., Halloran, P., Heinze, C., Ilyina, T., Séférian, R., Tjiputra, J., & Vichi, M., 2013. Multiple stressors of ocean ecosystems in the 21st century: projections with CMIP5 models, *Biogeosciences*, 10(10).
- Boucher, O., Denvil, S., Levvasseur, G., Cozic, A., Caubel, A., Foujols, M.-A., Meurdesoif, Y., Cadule, P., Devilliers, M., Ghattas, J., Lebas, N., Lurton, T., Mellul, L., Musat, I., Mignot, J., & Cheruy, F., 2018. IPSL IPSL-CM6A-LR model output prepared for CMIP6 CMIP historical.
- Boucher, O., Denvil, S., Levvasseur, G., Cozic, A., Caubel, A., Foujols, M.-A., Meurdesoif, Y., Cadule, P., Devilliers, M., Dupont, E., & Lurton, T., 2019. IPSL IPSL-CM6A-LR model output prepared for CMIP6 ScenarioMIP ssp585.
- Boucher, O., Servonnat, J., Albright, A. L., Aumont, O., Balkanski, Y., Bastrikov, V., Bekki, S., Bonnet, R., Bony, S., Bopp, L., Braconnot, P., Brockmann, P., Cadule, P., Caubel, A., Cheruy, F., Codron, F., Cozic, A., Cugnet, D., D'Andrea, F., Davini, P., de Lavergne, C., Denvil, S., Deshayes, J., Devilliers, M., Ducharne, A., Dufresne, J.-L., Dupont, E., Éthé, C., Fairhead, L., Falletti, L., Flavoni, S., Foujols, M.-A., Gardoll, S., Gastineau, G., Ghattas, J., Grandpeix, J.-Y., Guenet, B., Guez Lionel, E., Guilyardi, E., Guimberteau, M., Hauglustaine, D., Hourdin, F., Idelkadi, A., Joussaume, S., Kageyama, M., Khodri, M., Krinner, G., Lebas, N., Levvasseur, G., Lévy, C., Li, L., Lott, F., Lurton, T., Luyssaert, S., Madec, G., Madeleine, J.-B., Maignan, F., Marchand, M., Marti, O., Mellul, L., Meurdesoif, Y., Mignot, J., Musat, I., Ottlé, C., Peylin, P., Planton, Y., Polcher, J., Rio, C., Rochetin, N., Rousset, C., Sepulchre, P., Sima, A., Swingedouw, D., Thiéblemont, R., Traore, A. K., Vancoppenolle, M., Vial, J., Vialard, J., Viovy, N., & Vuichard, N., 2020. Presentation and Evaluation of the IPSL-CM6A-LR Climate Model, *Journal of Advances in Modeling Earth Systems*, 12(7), e2019MS002010.

- Boyd, P. W. & Brown, C. J., 2015. Modes of interactions between environmental drivers and marine biota, *Frontiers in Marine Science*, 2, 9.
- Boyer, T. P., Antonov, J. I., K., B. O., Coleman, C., Garcia, H. E., Grodsky, A., Johnson, D. R., Locarnini, R. A., Mishonov, V., A., O'Brien, O., T., Paver, C. R., Reagan, J. R., Seidov, D., Smolyar, I. V., & Zwen, M. M., 2016. NCEI standard product: World ocean database (WOD), *NOAA National Centers for Environmental Information. Dataset*.
- Burger, F. A., John, J. G., & Frölicher, T. L., 2020. Increase in ocean acidity variability and extremes under increasing atmospheric CO₂, *Biogeosciences*, 17(18), 4633–4662.
- Carter, B. R., Feely, R. A., Williams, N. L., Dickson, A. G., Fong, M. B., & Takeshita, Y., 2018. Updated methods for global locally interpolated estimation of alkalinity, pH, and nitrate, *Limnology and Oceanography: Methods*, 16(2), 119–131.
- Cavole, L., Demko, A., Diner, R., Giddings, A., Koester, I., Pagniello, C., Paulsen, M.-L., Ramirez-Valdez, A., Schwenck, S., Yen, N., Zill, M., & Franks, P., 2016. Biological Impacts of the 2013–2015 Warm-Water Anomaly in the Northeast Pacific: Winners, Losers, and the Future, *Oceanography*, 29(2), 273–285.
- Cheung, W. W. L., Frölicher, T. L., Lam, V. W. Y., Oyinlola, M. A., Reygondeau, G., Sumaila, U. R., Tai, T. C., Teh, L. C. L., & Wabnitz, C. C. C., 2021. Marine high temperature extremes amplify the impacts of climate change on fish and fisheries, *Science Advances*, 7(40), eabh0895.
- Clopper, C. J. & Pearson, E. S., 1934. The use of confidence or fiducial limits illustrated in the case of the binomial, *Biometrika*, 26(4), 404–413.
- Cochran, W. G., 1954. Some Methods for Strengthening the Common Chi Squared Tests, *Biometrics*, 10(4), 417–451.
- Collins, M., Sutherland, M., Bouwer, L., Cheong, S.-M., Frölicher, T., Des Combes, H., Koll, M., Losada, I., McInnes, K., Ratter, B., Rivera-Arriga, E., Susanto, R., Swingedouw, D., & Tibig, L., 2019. Chapter 6: Extremes, abrupt changes and managing risks, *IPCC Special Report on the Ocean and Cryosphere (SROCC)*.
- Deser, C., Alexander, M. A., Xie, S.-P., & Phillips, A. S., 2010. Sea surface temperature variability: Patterns and mechanisms, *Annual Review of Marine Science*, 2(1), 115–143.
- Deser, C., Lehner, F., Rodgers, K. B., Ault, T., Delworth, T. L., DiNezio, P. N., Fiore, A., Frankignoul, C., Fyfe, J. C., Horton, D. E., Kay, J. E., Knutti, R., Lovenduski, N. S., Marotzke, J., McKinnon, K. A., Minobe, S., Randerson, J., Screen, J. A., Simpson, I. R., & Ting, M., 2020. Insights from Earth system model initial-condition large ensembles and future prospects, *Nature Climate Change*, 10(4), 277–286.
- Doney, S. C., Lima, I., Feely, R. A., Glover, D. M., Lindsay, K., Mahowald, N., Moore, J. K., & Wanninkhof, R., 2009. Mechanisms governing interannual variability in upper-ocean inorganic carbon system and air–sea CO₂ fluxes: Physical climate and atmospheric dust, *Deep Sea Research Part II: Topical Studies in Oceanography*, 56(8), 640–655.
- Doney, S. C., Busch, D. S., Cooley, S. R., & Kroeker, K. J., 2020. The impacts of ocean acidification on marine ecosystems and reliant human communities, *Annual Review of Environment and Resources*, 45(1), 83–112.
- Dore, J. E., Lukas, R., Sadler, D. W., Church, M. J., & Karl, D. M., 2009. Physical and biogeochemical modulation of ocean acidification in the central North Pacific, *Proceedings of the National Academy of Sciences*, 106(30), 12235–12240.
- Dunne, J. P., John, J. G., Adcroft, A. J., Griffies, S. M., Hallberg, R. W., Shevliakova, E., Stouffer, R. J., Cooke, W., Dunne, K. A., Harrison, M. J., Krasting, J. P., Malyshev, S. L., Milly, P. C. D., Philipps, P. J., Sentman, L. T., Samuels, B. L., Spelman, M. J., Winton, M., Wittenberg, A. T., & Zadeh, N., 2012. GFDL's ESM2 global coupled climate–carbon earth system models. Part I: Physical formulation and baseline simulation characteristics, *Journal of Climate*, 25(19), 6646–6665.
- Dunne, J. P., John, J. G., Shevliakova, E., Stouffer, R. J., Krasting, J. P., Malyshev, S. L., Milly, P. C. D., Sentman, L. T., Adcroft, A. J., Cooke, W., Dunne, K. A., Griffies, S. M., Hallberg, R. W., Harrison, M. J., Levy, H., Wittenberg, A. T., Philipps, P. J., & Zadeh, N., 2013. GFDL's ESM2 global coupled climate–carbon earth system models. Part II: Carbon system formulation and baseline simulation characteristics, *Journal of Climate*, 26(7), 2247–2267.

- Dunne, J. P., Horowitz, L. W., Adcroft, A. J., Ginoux, P., Held, I. M., John, J. G., Krasting, J. P., Malyshev, S., Naik, V., Paulot, F., Shevliakova, E., Stock, C. A., Zadeh, N., Balaji, V., Blanton, C., Dunne, K. A., Dupuis, C., Durachta, J., Dussin, R., Gauthier, P. P. G., Griffies, S. M., Guo, H., Hallberg, R. W., Harrison, M., He, J., Hurlin, W., McHugh, C., Menzel, R., Milly, P. C. D., Nikonov, S., Paynter, D. J., Ploshay, J., Radhakrishnan, A., Rand, K., Reichl, B. G., Robinson, T., Schwarzkopf, D. M., Sentman, L. T., Underwood, S., Vahlenkamp, H., Winton, M., Wittenberg, A. T., Wyman, B., Zeng, Y., & Zhao, M., 2020. The GFDL Earth System Model Version 4.1 (GFDL-ESM 4.1): Overall Coupled Model Description and Simulation Characteristics, *Journal of Advances in Modeling Earth Systems*, 12(11), e2019MS002015.
- Engström-Öst, J., Glippa, O., Feely, R. A., Kanerva, M., Keister, J. E., Alin, S. R., Carter, B. R., McLaskey, A. K., Vuori, K. A., & Bednaršek, N., 2019. Eco-physiological responses of copepods and pteropods to ocean warming and acidification, *Scientific Reports*, 9(1), 4748.
- Fassbender, A. J., Rodgers, K. B., Palevsky, H. I., & Sabine, C. L., 2018. Seasonal asymmetry in the evolution of surface ocean $p\text{CO}_2$ and pH thermodynamic drivers and the influence on sea-air CO_2 flux, *Global Biogeochemical Cycles*, 32(10), 1476–1497.
- Feng, M., McPhaden, M. J., Xie, S.-P., & Hafner, J., 2013. La niña forces unprecedented leewind current warming in 2011, *Scientific Reports*, 3(1), 1277.
- Frölicher, T. L., Rodgers, K. B., Stock, C. A., & Cheung, W. W. L., 2016. Sources of uncertainties in 21st century projections of potential ocean ecosystem stressors, *Global Biogeochemical Cycles*, 30(8), 1224–1243.
- Frölicher, T. L., Fischer, E. M., & Gruber, N., 2018. Marine heatwaves under global warming, *Nature*, 560(7718), 360–364.
- Garcia, H. E., Weathers, K. and Paver, C. R., Smolyar, I., Boyer, T. P., Locarnini, R. A., Zweng, M. M., Mishonov, A. V., Baranova, O. K., Seidov, D., & Reagan, J. R., 2019. World Ocean Atlas 2018, volume 4: Dissolved inorganic nutrients (phosphate, nitrate and nitrate+nitrite, silicate).
- Goldenberg, S. U., Nagelkerken, I., Ferreira, C. M., Ullah, H., & Connell, S. D., 2017. Boosted food web productivity through ocean acidification collapses under warming, *Global Change Biology*, 23(10), 4177–4184.
- Good, P., Sellar, A., Tang, Y., Rumbold, S., Ellis, R., Kelley, D., & Kuhlbrodt, T., 2019. MOHC UKESM1.0-LL model output prepared for CMIP6 ScenarioMIP ssp585.
- Good, S. A., Martin, M. J., & Rayner, N. A., 2013. EN4: Quality controlled ocean temperature and salinity profiles and monthly objective analyses with uncertainty estimates, *Journal of Geophysical Research: Oceans*, 118(12), 6704–6716.
- Gray, A. R., Johnson, K. S., Bushinsky, S. M., Riser, S. C., Russell, J. L., Talley, L. D., Wanninkhof, R., Williams, N. L., & Sarmiento, J. L., 2018. Autonomous biogeochemical floats detect significant carbon dioxide outgassing in the high-latitude southern ocean, *Geophysical Research Letters*, 45(17), 9049–9057.
- Gregg, W. & Rousseaux, C., 2017. NASA ocean biogeo-chemical model assimilating satellite chlorophyll data globaldaily VR2017.
- Griffies, S., 2009. Elements of MOM4p1, GFDL ocean group technical report no.6, NOAA/Geophysical Fluid Dynamics Laboratory, Princeton University Forrestal Campus, 201 Forrestal Road, Princeton, NJ 08540-6649.
- Gruber, N., Keeling, C. D., & Bates, N. R., 2002. Interannual Variability in the North Atlantic Ocean Carbon Sink, *Science*, 298(5602), 2374–2378.
- Gruber, N., Boyd, P. W., Frölicher, T. L., & Vogt, M., 2021. Ocean biogeochemical extremes and compound events, *Nature*, in review.
- Guo, H., John, J. G., Blanton, C., McHugh, C., Nikonov, S., Radhakrishnan, A., Rand, K., Zadeh, N. T., Balaji, V., Durachta, J., Dupuis, C., Menzel, R., Robinson, T., Underwood, S., Vahlenkamp, H., Bushuk, M., Dunne, K. A., Dussin, R., Gauthier, P. P. G., Ginoux, P., Griffies, S. M., Hallberg, R., Harrison, M., Hurlin, W., Lin, P., Malyshev, S., Naik, V., Paulot, F., Paynter, D. J., Ploshay, J., Reichl, B. G., Schwarzkopf, D. M., Seman, C. J., Shao, A., Silvers, L., Wyman, B., Yan, X., Zeng, Y., Adcroft, A., Dunne, J. P., Held, I. M., Krasting, J. P., Horowitz, L. W., Milly, P. C. D., Shevliakova, E., Winton, M., Zhao, M., & Zhang, R., 2018a. NOAA-GFDL GFDL-CM4 model output historical.

- Guo, H., John, J. G., Blanton, C., McHugh, C., Nikonov, S., Radhakrishnan, A., Rand, K., Zadeh, N. T., Balaji, V., Durachta, J., Dupuis, C., Menzel, R., Robinson, T., Underwood, S., Vahlenkamp, H., Dunne, K. A., Gauthier, P. P. G., Ginoux, P., Griffies, S. M., Hallberg, R., Harrison, M., Hurlin, W., Lin, P., Malyshev, S., Naik, V., Paulot, F., Paynter, D. J., Ploshay, J., Schwarzkopf, D. M., Seman, C. J., Shao, A., Silvers, L., Wyman, B., Yan, X., Zeng, Y., Adcroft, A., Dunne, J. P., Held, I. M., Krasting, J. P., Horowitz, L. W., Milly, C., Shevliakova, E., Winton, M., Zhao, M., & Zhang, R., 2018b. NOAA-GFDL GFDL-CM4 model output prepared for CMIP6 ScenarioMIP ssp585.
- Hajima, T., Abe, M., Arakawa, O., Suzuki, T., Komuro, Y., Ogura, T., Ogochi, K., Watanabe, M., Yamamoto, A., Tatebe, H., Noguchi, M. A., Ohgaito, R., Ito, A., Yamazaki, D., Ito, A., Takata, K., Watanabe, S., Kawamiya, M., & Tachiiri, K., 2019. MIROC MIROC-ES2L model output prepared for CMIP6 CMIP historical.
- Hajima, T., Watanabe, M., Yamamoto, A., Tatebe, H., Noguchi, M. A., Abe, M., Ohgaito, R., Ito, A., Yamazaki, D., Okajima, H., Ito, A., Takata, K., Ogochi, K., Watanabe, S., & Kawamiya, M., 2020. Development of the MIROC-ES2L Earth system model and the evaluation of biogeochemical processes and feedbacks, *Geoscientific Model Development*, 13(5), 2197–2244.
- Harvey, B. P., Gwynn-Jones, D., & Moore, P. J., 2013. Meta-analysis reveals complex marine biological responses to the interactive effects of ocean acidification and warming, *Ecology and Evolution*, 3(4), 1016–1030.
- Hauri, C., Gruber, N., McDonnell, A. M. P., & Vogt, M., 2013. The intensity, duration, and severity of low aragonite saturation state events on the california continental shelf, *Geophysical Research Letters*, 40(13), 3424–3428.
- Hayashida, H., Matear, R. J., & Strutton, P. G., 2020. Background nutrient concentration determines phytoplankton bloom response to marine heatwaves, *Global Change Biology*, 26(9), 4800–4811.
- Held, I. M., Guo, H., Adcroft, A., Dunne, J. P., Horowitz, L. W., Krasting, J., Shevliakova, E., Winton, M., Zhao, M., Bushuk, M., Wittenberg, A. T., Wyman, B., Xiang, B., Zhang, R., Anderson, W., Balaji, V., Donner, L., Dunne, K., Durachta, J., Gauthier, P. P. G., Ginoux, P., Golaz, J.-C., Griffies, S. M., Hallberg, R., Harris, L., Harrison, M., Hurlin, W., John, J., Lin, P., Lin, S.-J., Malyshev, S., Menzel, R., Milly, P. C. D., Ming, Y., Naik, V., Paynter, D., Paulot, F., Rammasswamy, V., Reichl, B., Robinson, T., Rosati, A., Seman, C., Silvers, L. G., Underwood, S., & Zadeh, N., 2019. Structure and Performance of GFDL's CM4.0 Climate Model, *Journal of Advances in Modeling Earth Systems*, 11(11), 3691–3727.
- Hobday, A. J., Alexander, L. V., Perkins, S. E., Smale, D. A., Straub, S. C., Oliver, E. C., Benthuyssen, J. A., Burrows, M. T., Donat, M. G., Feng, M., Holbrook, N. J., Moore, P. J., Scannell, H. A., Sen Gupta, A., & Wernberg, T., 2016. A hierarchical approach to defining marine heatwaves, *Progress in Oceanography*, 141, 227–238.
- Holbrook, N. J., Scannell, H. A., Sen Gupta, A., Benthuyssen, J. A., Feng, M., Oliver, E. C. J., Alexander, L. V., Burrows, M. T., Donat, M. G., Hobday, A. J., Moore, P. J., Perkins-Kirkpatrick, S. E., Smale, D. A., Straub, S. C., & Wernberg, T., 2019. A global assessment of marine heatwaves and their drivers, *Nature Communications*, 10(1), 2624.
- Hughes, T. P., Kerry, J. T., Álvarez-Noriega, M., Álvarez-Romero, J. G., Anderson, K. D., Baird, A. H., Babcock, R. C., Beger, M., Bellwood, D. R., Berkemans, R., Bridge, T. C., Butler, I. R., Byrne, M., Cantin, N. E., Comeau, S., Connolly, S. R., Cumming, G. S., Dalton, S. J., Diaz-Pulido, G., Eakin, C. M., Figueira, W. F., Gilmour, J. P., Harrison, H. B., Heron, S. F., Hoey, A. S., Hobbs, J.-P. A., Hoogenboom, M. O., Kennedy, E. V., Kuo, C.-y., Lough, J. M., Lowe, R. J., Liu, G., McCulloch, M. T., Malcolm, H. A., McWilliam, M. J., Pandolfi, J. M., Pears, R. J., Pratchett, M. S., Schoepf, V., Simpson, T., Skirving, W. J., Sommer, B., Torda, G., Wachenfeld, D. R., Willis, B. L., & Wilson, S. K., 2017. Global warming and recurrent mass bleaching of corals, *Nature*, 543(7645), 373–377.
- Jacox, M. G., 2019. Marine heatwaves in a changing climate, *Nature*, 571, 485 – 487.
- John, J. G., Blanton, C., McHugh, C., Radhakrishnan, A., Rand, K., Vahlenkamp, H., Wilson, C., Zadeh, N. T., Dunne, J. P., Dussin, R., Horowitz, L. W., Krasting, J. P., Lin, P., Malyshev, S., Naik, V., Ploshay, J., Shevliakova, E., Silvers, L., Stock, C., Winton, M., & Zeng, Y., 2018. NOAA-GFDL GFDL-ESM4 model output prepared for CMIP6 ScenarioMIP ssp585.
- Jungclaus, J., Bittner, M., Wieners, K.-H., Wachsmann, F., Schupfner, M., Legutke, S., Giorgetta, M., Reick, C., Gayler, V., Haak, H., de Vrese, P., Raddatz, T., Esch, M., Mauritsen, T., von Storch, J.-S., Behrens, J., Brovkin, V., Claussen, M., Crueger, T., Fast, I., Fiedler, S., Hagemann, S., Hohenegger, C., Jahns, T., Kloster, S., Kinne, S., Lasslop, G., Kornbluh, L., Marotzke, J., Matei, D., Meraner, K., Mikolajewicz, U., Modali, K., Müller, W.,

- Nabel, J., Notz, D., Peters, K., Pincus, R., Pohlmann, H., Pongratz, J., Rast, S., Schmidt, H., Schnur, R., Schulzweida, U., Six, K., Stevens, B., Voigt, A., & Roeckner, E., 2019. MPI-M MPI-ESM1.2-HR model output prepared for CMIP6 CMIP historical.
- Krasting, J. P., John, J. G., Blanton, C., McHugh, C., Nikonov, S., Radhakrishnan, A., Rand, K., Zadeh, N. T., Balaji, V., Durachta, J., Dupuis, C., Menzel, R., Robinson, T., Underwood, S., Vahlenkamp, H., Dunne, K. A., Gauthier, P. P. G., Ginoux, P., Griffies, S. M., Hallberg, R., Harrison, M., Hurlin, W., Malyshev, S., Naik, V., Paulot, F., Paynter, D. J., Ploshay, J., Reichl, B. G., Schwarzkopf, D. M., Seman, C. J., Silvers, L., Wyman, B., Zeng, Y., Adcroft, A., Dunne, J. P., Dussin, R., Guo, H., He, J., Held, I. M., Horowitz, L. W., Lin, P., Milly, P. C. D., Shevliakova, E., Stock, C., Winton, M., Wittenberg, A. T., Xie, Y., & Zhao, M., 2018. NOAA-GFDL GFDL-ESM4 model output prepared for CMIP6 CMIP historical.
- Kroeker, K. J., Kordas, R. L., Crim, R., Hendriks, I. E., Ramajo, L., Singh, G. S., Duarte, C. M., & Gattuso, J.-P., 2013. Impacts of ocean acidification on marine organisms: quantifying sensitivities and interaction with warming, *Global Change Biology*, 19(6), 1884–1896.
- Kwiatkowski, L. & Orr, J. C., 2018. Diverging seasonal extremes for ocean acidification during the twenty-first century, *Nature Climate Change*, 8(2), 141–145.
- Kwiatkowski, L., Torres, O., Bopp, L., Aumont, O., Chamberlain, M., Christian, J. R., Dunne, J. P., Gehlen, M., Ilyina, T., John, J. G., Lenton, A., Li, H., Lovenduski, N. S., Orr, J. C., Palmieri, J., Santana-Falcón, Y., Schwinger, J., Séférian, R., Stock, C. A., Tagliabue, A., Takano, Y., Tjiputra, J., Toyama, K., Tsujino, H., Watanabe, M., Yamamoto, A., Yool, A., & Ziehn, T., 2020. Twenty-first century ocean warming, acidification, deoxygenation, and upper-ocean nutrient and primary production decline from CMIP6 model projections, *Biogeosciences*, 17(13), 3439–3470.
- Landschützer, P., Gruber, N., & Bakker, D. C. E., 2016. Decadal variations and trends of the global ocean carbon sink, *Global Biogeochemical Cycles*, 30(10), 1396–1417.
- Landschützer, P., Gruber, N., & Bakker, D. C. E., 2020. An observation-based global monthly gridded sea surface $p\text{CO}_2$ product from 1982 onward and its monthly climatology (NCEI Accession 0160558).
- Laufkötter, C., Zscheischler, J., & Frölicher, T. L., 2020. High-impact marine heatwaves attributable to human-induced global warming, *Science*, 369(6511), 1621–1625.
- Le Grix, N., Zscheischler, J., Laufkötter, C., Rousseaux, C. S., & Frölicher, T. L., 2021. Compound high-temperature and low-chlorophyll extremes in the ocean over the satellite period, *Biogeosciences*, 18(6), 2119–2137.
- Leonard, M., Westra, S., Phatak, A., Lambert, M., van den Hurk, B., McInnes, K., Risbey, J., Schuster, S., Jakob, D., & Stafford-Smith, M., 2014. A compound event framework for understanding extreme impacts, *WIREs Climate Change*, 5(1), 113–128.
- Lischka, S. & Riebesell, U., 2012. Synergistic effects of ocean acidification and warming on overwintering pteropods in the Arctic, *Global Change Biology*, 18(12), 3517–3528.
- Meinshausen, M., Smith, S. J., Calvin, K., Daniel, J. S., Kainuma, M. L. T., Lamarque, J.-F., Matsumoto, K., Montzka, S. A., Raper, S. C. B., Riahi, K., Thomson, A., Velders, G. J. M., & van Vuuren, D. P. P., 2011. The rcp greenhouse gas concentrations and their extensions from 1765 to 2300, *Climatic Change*, 109(1), 213.
- Moore, C. M., Mills, M. M., Arrigo, K. R., Berman-Frank, I., Bopp, L., Boyd, P. W., Galbraith, E. D., Geider, R. J., Guieu, C., Jaccard, S. L., Jickells, T. D., La Roche, J., Lenton, T. M., Mahowald, N. M., Maraño, E., Marinov, I., Moore, J. K., Nakatsuka, T., Oschlies, A., Saito, M. A., Thingstad, T. F., Tsuda, A., & Ulloa, O., 2013. Processes and patterns of oceanic nutrient limitation, *Nature Geoscience*, 6(9), 701–710.
- Müller, W. A., Jungclaus, J. H., Mauritsen, T., Baehr, J., Bittner, M., Budich, R., Bunzel, F., Esch, M., Ghosh, R., Haak, H., Ilyina, T., Kleine, T., Kornblueh, L., Li, H., Modali, K., Notz, D., Pohlmann, H., Roeckner, E., Stemmler, I., Tian, F., & Marotzke, J., 2018. A Higher-resolution Version of the Max Planck Institute Earth System Model (MPI-ESM1.2-HR), *Journal of Advances in Modeling Earth Systems*, 10(7), 1383–1413.
- Muñoz, N. J., Farrell, A. P., Heath, J. W., & Neff, B. D., 2015. adaptive potential of a pacific salmon challenged by climate change, *Nature Climate Change*, 5(2), 163–166.
- Nagelkerken, I., Goldenberg, S. U., Ferreira, C. M., Ullah, H., & Connell, S. D., 2020. Trophic pyramids reorganize when food web architecture fails to adjust to ocean change, *Science*, 369(6505), 829–832.
- Najjar, R. & Orr, J., 1998. Design of OCMIP-2 simulations of chlorofluorocarbons, the solubility pump and common biogeochemistry, internal OCMIP report, LSCE/CEA Saclay, Gif-sur-Yvette, France.

- Oliver, E. C., Benthuisen, J. A., Darmaraki, S., Donat, M. G., Hobday, A. J., Holbrook, N. J., Schlegel, R. W., & Sen Gupta, A., 2021. Marine heatwaves, *Annual Review of Marine Science*, 13(1), 313–342.
- Oliver, E. C. J., Donat, M. G., Burrows, M. T., Moore, P. J., Smale, D. A., Alexander, L. V., Benthuisen, J. A., Feng, M., Sen Gupta, A., Hobday, A. J., Holbrook, N. J., Perkins-Kirkpatrick, S. E., Scannell, H. A., Straub, S. C., & Wernberg, T., 2018. Longer and more frequent marine heatwaves over the past century, *Nature Communications*, 9(1), 1324.
- Oliver, E. C. J., Burrows, M. T., Donat, M. G., Sen Gupta, A., Alexander, L. V., Perkins-Kirkpatrick, S. E., Benthuisen, J. A., Hobday, A. J., Holbrook, N. J., Moore, P. J., Thomsen, M. S., Wernberg, T., & Smale, D. A., 2019. Projected marine heatwaves in the 21st century and the potential for ecological impact, *Frontiers in Marine Science*, 6, 734.
- Orr, J. C. & Epitalon, J.-M., 2015. Improved routines to model the ocean carbonate system: mocsy 2.0, *Geoscientific Model Development*, 8(3), 485–499.
- Orr, J. C., Najjar, R. G., Aumont, O., Bopp, L., Bullister, J. L., Danabasoglu, G., Doney, S. C., Dunne, J. P., Dutay, J.-C., Graven, H., Griffies, S. M., John, J. G., Joos, F., Levin, I., Lindsay, K., Matear, R. J., McKinley, G. A., Mouchet, A., Oschlies, A., Romanou, A., Schlitzer, R., Tagliabue, A., Tanhua, T., & Yool, A., 2017. Biogeochemical protocols and diagnostics for the CMIP6 Ocean Model Intercomparison Project (OMIP), *Geoscientific Model Development*, 10(6), 2169–2199.
- Orr, J. C., Epitalon, J.-M., Dickson, A. G., & Gattuso, J.-P., 2018. Routine uncertainty propagation for the marine carbon dioxide system, *Marine Chemistry*, 207, 84 – 107.
- Pinsky, M. L., Worm, B., Fogarty, M. J., Sarmiento, J. L., & Levin, S. A., 2013. Marine taxa track local climate velocities, *Science*, 341(6151), 1239–1242.
- Prada, F., Caroselli, E., Mengoli, S., Brizi, L., Fantazzini, P., Capaccioni, B., Pasquini, L., Fabricius, K. E., Dubinsky, Z., Falini, G., & Goffredo, S., 2017. Ocean warming and acidification synergistically increase coral mortality, *Scientific Reports*, 7(1), 40842.
- Riahi, K., Rao, S., Krey, V., Cho, C., Chirkov, V., Fischer, G., Kindermann, G., Nakicenovic, N., & Rafaj, P., 2011. RCP8.5 — a scenario of comparatively high greenhouse gas emissions, *Climatic Change*, 109(1), 33.
- Ridder, N. N., Pitman, A. J., Westra, S., Ukkola, A., Do, H. X., Bador, M., Hirsch, A. L., Evans, J. P., Di Luca, A., & Zscheischler, J., 2020. Global hotspots for the occurrence of compound events, *Nature Communications*, 11(1), 5956.
- Rodgers, K. B., Lin, J., & Frölicher, T. L., 2015. Emergence of multiple ocean ecosystem drivers in a large ensemble suite with an earth system model, *Biogeosciences*, 12(11), 3301–3320.
- Sarmiento, J. & Gruber, N., 2006. *Ocean Biogeochemical Dynamics*, Princeton University Press.
- Schupfner, M., Wieners, K.-H., Wachsmann, F., Steger, C., Bittner, M., Jungclaus, J., Früh, B., Pankatz, K., Giorgetta, M., Reick, C., Legutke, S., Esch, M., Gayler, V., Haak, H., de Vrese, P., Raddatz, T., Mauritsen, T., von Storch, J.-S., Behrens, J., Brovkin, V., Claussen, M., Crueger, T., Fast, I., Fiedler, S., Hagemann, S., Hohenegger, C., Jahns, T., Kloster, S., Kinne, S., Lasslop, G., Kornblueh, L., Marotzke, J., Matei, D., Meraner, K., Mikolajewicz, U., Modali, K., Müller, W., Nabel, J., Notz, D., Peters, K., Pincus, R., Pohlmann, H., Pongratz, J., Rast, S., Schmidt, H., Schnur, R., Schulzweida, U., Six, K., Stevens, B., Voigt, A., & Roeckner, E., 2019. DKRZ MPI-ESM1.2-HR model output prepared for CMIP6 ScenarioMIP ssp585.
- Séférian, R., 2018. CNRM-CERFACS CNRM-ESM2-1 model output prepared for CMIP6 CMIP historical.
- Séférian, R., Nabat, P., Michou, M., Saint-Martin, D., Voldoire, A., Colin, J., Decharme, B., Delire, C., Berthet, S., Chevallier, M., Sénési, S., Franchisteguy, L., Vial, J., Mallet, M., Joetzjer, E., Geoffroy, O., Guérémy, J.-F., Moine, M.-P., Msadek, R., Ribes, A., Rocher, M., Roehrig, R., Salas-y Mélia, D., Sanchez, E., Terray, L., Valcke, S., Waldman, R., Aumont, O., Bopp, L., Deshayes, J., Éthé, C., & Madec, G., 2019. Evaluation of CNRM Earth System Model, CNRM-ESM2-1: Role of Earth System Processes in Present-Day and Future Climate, *Journal of Advances in Modeling Earth Systems*, 11(12), 4182–4227.
- Sellar, A. A., Jones, C. G., Mulcahy, J. P., Tang, Y., Yool, A., Wiltshire, A., O'Connor, F. M., Stringer, M., Hill, R., Palmieri, J., Woodward, S., de Mora, L., Kuhlbrodt, T., Rumbold, S. T., Kelley, D. I., Ellis, R., Johnson, C. E., Walton, J., Abraham, N. L., Andrews, M. B., Andrews, T., Archibald, A. T., Berthou, S., Burke, E., Blockley, E., Carslaw, K., Dalvi, M., Edwards, J., Folberth, G. A., Gedney, N., Griffiths, P. T., Harper, A. B., Hendry, M. A., Hewitt, A. J., Johnson, B., Jones, A., Jones, C. D., Keeble, J., Liddicoat, S., Morgenstern, O.,

- Parker, R. J., Predoi, V., Robertson, E., Siahahan, A., Smith, R. S., Swaminathan, R., Woodhouse, M. T., Zeng, G., & Zerroukat, M., 2019. UKESM1: Description and Evaluation of the U.K. Earth System Model, *Journal of Advances in Modeling Earth Systems*, 11(12), 4513–4558.
- Sen Gupta, A., Thomsen, M., Benthuisen, J. A., Hobday, A. J., Oliver, E., Alexander, L. V., Burrows, M. T., Donat, M. G., Feng, M., Holbrook, N. J., Perkins-Kirkpatrick, S., Moore, P. J., Rodrigues, R. R., Scannell, H. A., Taschetto, A. S., Ummenhofer, C. C., Wernberg, T., & Smale, D. A., 2020. Drivers and impacts of the most extreme marine heatwave events, *Scientific Reports*, 10(1), 19359.
- Smale, D. A., Wernberg, T., Oliver, E. C. J., Thomsen, M., Harvey, B. P., Straub, S. C., Burrows, M. T., Alexander, L. V., Benthuisen, J. A., Donat, M. G., Feng, M., Hobday, A. J., Holbrook, N. J., Perkins-Kirkpatrick, S. E., Scannell, H. A., Sen Gupta, A., Payne, B. L., & Moore, P. J., 2019. Marine heatwaves threaten global biodiversity and the provision of ecosystem services, *Nature Climate Change*, 9(4), 306–312.
- Sutton, A. J., Feely, R. A., Maenner-Jones, S., Musielwicz, S., Osborne, J., Dietrich, C., Monacci, N., Cross, J., Bott, R., Kozyr, A., Andersson, A. J., Bates, N. R., Cai, W.-J., Cronin, M. F., De Carlo, E. H., Hales, B., Howden, S. D., Lee, C. M., Manzello, D. P., McPhaden, M. J., Meléndez, M., Mickett, J. B., Newton, J. A., Noakes, S. E., Noh, J. H., Olafsdottir, S. R., Salisbury, J. E., Send, U., Trull, T. W., Vandemark, D. C., & Weller, R. A., 2019. Autonomous seawater $p\text{CO}_2$ and pH time series from 40 surface buoys and the emergence of anthropogenic trends, *Earth System Science Data*, 11(1), 421–439.
- Swart, N. C., Cole, J. N. S., Kharin, V. V., Lazare, M., Scinocca, J. F., Gillett, N. P., Anstey, J., Arora, V., Christian, J. R., Hanna, S., Jiao, Y., Lee, W. G., Majaess, F., Saenko, O. A., Seiler, C., Seinen, C., Shao, A., Sigmond, M., Solheim, L., von Salzen, K., Yang, D., & Winter, B., 2019a. The Canadian Earth System Model version 5 (CanESM5.0.3), *Geoscientific Model Development*, 12(11), 4823–4873.
- Swart, N. C., Cole, J. N. S., Kharin, V. V., Lazare, M., Scinocca, J. F., Gillett, N. P., Anstey, J., Arora, V., Christian, J. R., Jiao, Y., Lee, W. G., Majaess, F., Saenko, O. A., Seiler, C., Seinen, C., Shao, A., Solheim, L., von Salzen, K., Yang, D., Winter, B., & Sigmond, M., 2019b. CCCma CanESM5 model output prepared for CMIP6 CMIP historical.
- Swart, N. C., Cole, J. N. S., Kharin, V. V., Lazare, M., Scinocca, J. F., Gillett, N. P., Anstey, J., Arora, V., Christian, J. R., Jiao, Y., Lee, W. G., Majaess, F., Saenko, O. A., Seiler, C., Seinen, C., Shao, A., Solheim, L., von Salzen, K., Yang, D., Winter, B., & Sigmond, M., 2019c. CCCma CanESM5 model output prepared for CMIP6 ScenarioMIP ssp585.
- Tachiiri, K., Abe, M., Hajima, T., Arakawa, O., Suzuki, T., Komuro, Y., Ogochi, K., Watanabe, M., Yamamoto, A., Tatebe, H., Noguchi, M. A., Ohgaito, R., Ito, A., Yamazaki, D., Ito, A., Takata, K., Watanabe, S., & Kawamiya, M., 2019. MIROC MIROC-ES2L model output prepared for CMIP6 ScenarioMIP ssp585.
- Takahashi, T., Sutherland, S. C., Sweeney, C., Poisson, A., Metzl, N., Tilbrook, B., Bates, N., Wanninkhof, R., Feely, R. A., Sabine, C., Olafsson, J., & Nojiri, Y., 2002. Global sea-air CO_2 flux based on climatological surface ocean $p\text{CO}_2$, and seasonal biological and temperature effects, *Deep Sea Research Part II: Topical Studies in Oceanography*, 49(9), 1601–1622.
- Tang, Y., Rumbold, S., Ellis, R., Kelley, D., Mulcahy, J., Sellar, A., Walton, J., & Jones, C., 2019. MOHC UKESM1.0-LL model output prepared for CMIP6 CMIP historical.
- van Heuven, S., Pierrot, D., Rae, J., Lewis, E., & Wallace, D., 2011. MATLAB program developed for CO_2 system calculations, <http://gts.sourceforge.net/>.
- van Vuuren, D. P., Stehfest, E., den Elzen, M. G. J., Kram, T., van Vliet, J., Deetman, S., Isaac, M., Klein Goldewijk, K., Hof, A., Mendoza Beltran, A., Oostenrijk, R., & van Ruijven, B., 2011. RCP2.6: exploring the possibility to keep global mean temperature increase below 2°C , *Climatic Change*, 109(1), 95.
- Vogel, M. M., Zscheischler, J., Fischer, E. M., & Seneviratne, S. I., 2020. Development of future heatwaves for different hazard thresholds, *Journal of Geophysical Research: Atmospheres*, 125(9), e2019JD032070.
- Voldoire, A., 2019. CNRM-CERFACS CNRM-ESM2-1 model output prepared for CMIP6 ScenarioMIP ssp585.
- Wakita, M., Watanabe, S., Murata, A., & Honda, M. C., 2011a. Hydrographic data report at station K2.
- Wakita, M., Watanabe, S., Murata, A., Honda, M. C., & Tsurushima, N., 2011b. Hydrographic data report at station KNOT.
- Weiss, R., 1974. Carbon dioxide in water and seawater: the solubility of a non-ideal gas, *Marine Chemistry*, 2(3), 203 – 215.

- Wilks, D., 2005. *Statistical Methods in the Atmospheric Sciences*, Elsevier, Amsterdam, 2nd edn.
- Xue, L., Cai, W.-J., Jiang, L.-Q., & Wei, Q., 2021. Why are surface ocean pH and CaCO_3 saturation state often out of phase in spatial patterns and seasonal cycles?, *Global Biogeochemical Cycles*, 35(7), e2021GB006949.
- Zeebe, R. E. & Wolf-Gladrow, D., 2001. *CO_2 in seawater: Equilibrium, kinetics, isotopes*, Elsevier, Amsterdam.
- Zscheischler, J. & Seneviratne, S. I., 2017. Dependence of drivers affects risks associated with compound events, *Sci. Adv.*, 3(6).
- Zscheischler, J., Westra, S., van den Hurk, B. J. J. M., Seneviratne, S. I., Ward, P. J., Pitman, A., AghaKouchak, A., Bresch, D. N., Leonard, M., Wahl, T., & Zhang, X., 2018. Future climate risk from compound events, *Nature Climate Change*, 8(6), 469–477.
- Zscheischler, J., Martius, O., Westra, S., Bevacqua, E., Raymond, C., Horton, R. M., van den Hurk, B., AghaKouchak, A., Jézéquel, A., Mahecha, M. D., Maraun, D., Ramos, A. M., Ridder, N. N., Thiery, W., & Vignotto, E., 2020. A typology of compound weather and climate events, *Nature Reviews Earth & Environment*.

Chapter 5

Drivers of ocean acidity extreme events in an Earth system model

Friedrich A. Burger and Thomas L. Frölicher

Manuscript in preparation.

Oceanic uptake of anthropogenic carbon dioxide increases $[\text{H}^+]$ concentrations in seawater and alters the inorganic carbon speciation impacting many ocean species, especially shell-forming organisms such as plankton, mollusks, echinoderms and corals. Of particular concern are extreme ocean acidity events (OAX events), during which the $[\text{H}^+]$ concentrations may be similarly high as those projected for the surface ocean by the middle of this century. However, there is only little knowledge about the driving mechanisms of such OAX events. Here, we use daily mean output from a fully-coupled Earth system model of all processes that influence the surface ocean temperature and carbon budgets and ultimately $[\text{H}^+]$ anomalies to quantify the driving mechanisms of the buildup and decay of OAX events. We show that increases in temperature due to enhanced net ocean heat uptake dominate the buildup of OAX events, especially in the subtropical oceans. These increases in $[\text{H}^+]$ during OAX events are often substantially reduced by co-occurring reductions in surface carbon concentration due to enhanced carbon loss to the atmosphere. In the high latitudes, decreased downward vertical diffusion and mixing of warm temperature are the main drivers of the buildup of OAX events, whereas in the tropical Pacific, increases in vertical advection of carbon drive the buildup of OAX events. Furthermore, we also find a more pronounced role of increases in carbon for preconditioning OAX events than for driving event buildup and decay. Our results provide a first global overview of the driving processes of OAX events and can be used as a first step towards skillful predictions of impactful OAX events.

5.1 Introduction

The ocean has absorbed between 20 and 30% of the anthropogenic carbon dioxide (CO_2) emissions since the beginning of the industrial era (Friedlingstein et al., 2020; Khatiwala et al., 2013). This uptake of anthropogenic CO_2 has led to an observed increase in acidity (hydrogen ion concentration $[\text{H}^+]$) of about 29 %, a decrease in pH of about 0.11 units (Jiang et al., 2019; Rhein et al., 2013), and a decrease in carbonate ion concentration ($[\text{CO}_3^{2-}]$) by more than 10 % (Orr et al., 2005). These changes are generally referred to as ocean acidification (Caldeira & Wickett, 2003; Doney et al., 2009a; Bindoff et al., 2019). By the end of this century, surface ocean pH is projected to decrease by another 0.1–0.4 units and $[\text{CO}_3^{2-}]$ concentration by up to 50 % (Orr et al., 2005; Canadell et al., 2021). Ocean acidification may impact marine organisms in a variety of ways. Over a broad range of organisms, meta-analyses reveal decreases in survival, calcification, growth, development, and abundance in response to the increases in $[\text{H}^+]$ and from co-occurring changes in calcium carbonate saturation state and other carbonate system variables (Kroeker et al., 2013; Doney et al., 2020). Research also suggests that changing ocean chemistry and reduced pH may impact the physiology and population dynamics of many species (Doney et al. 2009; Gattuso et al. 2015).

In addition to the long-term increase in ocean acidity, variations in $[\text{H}^+]$ and in other carbonate system variables also occur on much shorter timescales. The intensity of such extreme events in ocean acidity (herein referred to OAX events) can be of similar magnitude as the changes expected from long-term ocean acidification during the 21st century (Hofmann et al., 2011; Leinweber & Gruber, 2013; Torres et al., 2021). OAX events can amplify the ongoing impacts on marine organisms and ecosystems due to long-term ocean acidification, because such extreme events can push these systems and their constituents beyond the limits of their resilience (e.g., Spisla et al., 2021; Gruber et al., 2021). For example, laboratory and field studies found that calcifying organisms show signs of shell dissolution already after several days in waters that are undersaturated with respect to calcium carbonate (Bednaršek et al., 2012, 2014), highlighting the significance of short-term exposures to acidic waters during OAX events.

Modeling studies suggest that the number of OAX days will strongly increase under climate change. By year 2030 and under a high-emission no-mitigation scenario, climate model simulations suggest that more than 360 days per year are under extreme conditions, when OAX events are defined relative to a preindustrial reference period (Chapter 3; Burger et al., 2020). The long-term ocean acidification will therefore push the global surface ocean towards a near-permanent extreme state for acidity conditions (Chapter 3; Burger et al., 2020). Even when defining OAX events relative to a shifting-mean baseline so that the long-term changes in acidity are neglected, the global number of OAX days will increase by a factor of 14 (Chapter 3; Burger et al., 2020). This is because the variability in $[\text{H}^+]$ increases with ocean acidification and warming (Chapter 3; Burger et al., 2020), a consequence of the nonlinear nature of oceanic carbon chemistry (Orr et al., 2018; Fassbender et al., 2018; Burger et al., 2020).

Most of the available studies on drivers of OAX events focused on the long-term changes in OAX events under climate change (Burger et al., 2020; Hauri et al., 2013) or on drivers of the mean seasonal cycle (Hagens & Middelburg, 2016; Xue et al., 2021). However, the processes leading to individual OAX events and especially to variations in $[\text{H}^+]$ anomalies, i.e. in the departures of $[\text{H}^+]$ from the mean seasonal cycle, are currently unknown. Anomalies in $[\text{H}^+]$ around the seasonal cycle arise due to departures in the driving variables from their seasonal cycles, most importantly in temperature and carbon (Deser et al., 2010; Doney et al., 2009b). Burger et al. (2020) identified the contributions from the driving variables to changes in $[\text{H}^+]$

variability with anthropogenic CO₂ emissions. However, the mean-state contributions from the driving variables to variations in $[\text{H}^+]$ anomaly have not been analyzed. In addition, the role of the different physical and biogeochemical processes, underlying the variations in the drivers in causing extreme variations in $[\text{H}^+]$ anomaly, such as air-sea heat and CO₂ exchange and vertical mixing of heat and carbon, is currently unknown. Insights in the driving processes of extreme variations in $[\text{H}^+]$ would enable more robust predictions of such harmful OAX events at the regional scale.

In this study, the driving mechanisms of extreme events in $[\text{H}^+]$ are analyzed in a preindustrial simulation of the GFDL ESM2M Earth system model. The analysis is based on a suite of model tendency terms for the carbon and temperature budgets (Gnanadesikan et al., 2012; Palter et al., 2014; Griffies et al., 2015) that allow to decompose changes in temperature and carbon into the contributions from the underlying physical and biogeochemical processes. These model tendency terms are here used for the first time to analyze variations in $[\text{H}^+]$. Based on the tendency contributions, the driving mechanisms of $[\text{H}^+]$ evolution during OAX events are identified. The remainder of this article is structured as follows. In Sect. 5.2, the methods used to analyze the drivers of $[\text{H}^+]$ extremes are introduced. Sect. 5.3 presents the results and a discussion of the results is given in Sect. 5.4.

5.2 Methods

5.2.1 Model and experimental design

This study is based on a 500 y preindustrial control simulation conducted with the Earth system model GFDL ESM2M (Dunne et al., 2012, 2013). The GFDL ESM2M is a fully coupled carbon cycle-climate model that was developed at NOAA’s Geophysical Fluid Dynamics Laboratory (GFDL). It consists of an ocean (MOM4p1; Griffies, 2009), atmosphere (AM2; Anderson et al., 2004), land (LM3; Shevliakova et al., 2009) and sea ice (Winton, 2000) module. The Modular Ocean Model version 4p1 (MOM4p1) uses a horizontal grid with a nominal 1° resolution that increases near the equator to 0.3° and a time-varying vertical resolution of about 10 m in the upper ocean. In this study, we analyze data for the uppermost vertical layer that extends from the surface to about 10 m depth. MOM4p1 is coupled to the ocean biogeochemistry model Tracers of Ocean Phytoplankton with Allometric Zooplankton version two (TOPAZv2; Dunne et al., 2013) that simulates the cycling of 30 biogeochemical tracers, three phytoplankton groups, and zooplankton grazing. Carbonate chemistry follows the OCMIP2 recommendations (Najjar & Orr, 1998; Burger et al., 2020).

We used output of a preindustrial control simulation that was run under prescribed atmospheric CO₂ levels of 286 ppm. Aerosol and solar forcing were also set to preindustrial 1860 values, and no anthropogenic land use and volcanic activity was assumed. We analyzed daily-mean output of $[\text{H}^+]$ and its drivers, temperature (T), dissolved inorganic carbon (C_T), total alkalinity (A_T), and salinity (S), as well as all processes that modulate T and C_T (i.e., T and C_T tendency terms).

5.2.2 Extreme event definition and identification of buildup and decay periods

We define OAX events based on seasonally-varying thresholds (Hobday et al., 2016, Chapter 4). At each location and for each day of the year, an extreme event threshold is determined as the 90th percentile of the 500 anomaly values with respect to the climatological seasonal cycle for

that day of the year. As a result, the likelihood that $[\text{H}^+]$ anomaly exceeds the threshold is equal across locations and across the year. At a specific location, extreme events in $[\text{H}^+]$ are then defined as coherent periods over which the $[\text{H}^+]$ anomaly is above the local seasonally varying threshold.

At each location and for each OAX event, we identify its buildup and decay period. The buildup phase is defined as the period between the start of the extreme event, i.e., where the $[\text{H}^+]$ anomaly crosses the threshold, and the peak of the extreme event, where the difference between $[\text{H}^+]$ anomaly and the seasonally varying threshold is at its maximum. Likewise, the decay phase is defined as the period between the peak of the extreme event and the time when $[\text{H}^+]$ anomaly falls below the extreme event threshold again. In this study, we average the change in $[\text{H}^+]$ anomaly and its drivers over these two periods. We assign the day of event peak to the decay period, as the change in $[\text{H}^+]$ anomaly on that day characterizes the reduction in $[\text{H}^+]$ anomaly between the peak day and the following day. Likewise, the last day of the decay period is excluded, as the change in $[\text{H}^+]$ anomaly on that day characterizes the transition from the last day of the event to the first day after the event. Changes in $[\text{H}^+]$ anomalies averaged over the full duration of events, i.e., over the buildup and decay phases of the events, are close to zero ($1 \cdot 10^{-4} \text{ nmol kg}^{-1} \text{ d}^{-1}$ on global average; Table 5.1) indicating that the increase in $[\text{H}^+]$ anomaly during event buildup is similar in magnitude to the decrease in $[\text{H}^+]$ anomaly during the decay of events.

5.2.3 Decomposition of OAX events into drivers

Changes in $[\text{H}^+]$ seasonal anomalies ($\text{H}^{+'}$) in each grid cell are decomposed into contributions from T, S, C_T and A_T (Fig. 5.1). The change in $[\text{H}^+]$ anomaly between day i and day $i + 1$, denoted by $\Delta\text{H}^{+'}(i)$, is approximated by employing a first order Taylor expansion of $[\text{H}^+]$ at day i , and by calculating the seasonal anomalies (denote by primes) of the obtained terms from T, salinity-normalized C_T and A_T (sC_T and sA_T ; defined below), and freshwater variations (last term on right-hand side of Eq. (5.1)):

$$\begin{aligned} \Delta\text{H}^{+'}(i) \simeq & \left(\frac{\partial\text{H}^+}{\partial\text{T}}(i) \Delta\text{T}(i) \right)' + \left(\frac{\partial\text{H}^+}{\partial\text{C}_\text{T}}(i) \frac{\text{S}(i)}{\bar{\text{S}}} \Delta\text{sC}_\text{T}(i) \right)' + \left(\frac{\partial\text{H}^+}{\partial\text{A}_\text{T}}(i) \frac{\text{S}(i)}{\bar{\text{S}}} \Delta\text{sA}_\text{T}(i) \right)' \\ & + \left(\left[\frac{\partial\text{H}^+}{\partial\text{S}}(i) + \frac{\partial\text{H}^+}{\partial\text{C}_\text{T}}(i) \frac{\text{sC}_\text{T}(i)}{\bar{\text{S}}} + \frac{\partial\text{H}^+}{\partial\text{A}_\text{T}}(i) \frac{\text{sA}_\text{T}(i)}{\bar{\text{S}}} \right] \Delta\text{S}(i) \right)'. \end{aligned} \quad (5.1)$$

$\Delta\text{T}(i)$, $\Delta\text{sC}_\text{T}(i)$, $\Delta\text{sA}_\text{T}(i)$, and $\Delta\text{S}(i)$ denote the changes in the respective variables between day i and day $i + 1$. $\bar{\text{S}}$ is a reference salinity (Lovenduski et al., 2007) that is chosen as the temporal-mean salinity at each grid cell. The definition of salinity-normalized C_T and A_T ($\text{sC}_\text{T} = \frac{\bar{\text{S}}}{\text{S}} \text{C}_\text{T}$ and $\text{sA}_\text{T} = \frac{\bar{\text{S}}}{\text{S}} \text{A}_\text{T}$) based on the reference salinity $\bar{\text{S}}$ excludes the effects from variations in salinity on C_T and A_T . However, since the effects from salinity variations on C_T and A_T are similarly large and with opposite effects on $[\text{H}^+]$, they largely cancel each other out and the overall effect on $[\text{H}^+]$ is small. Since the direct effect of salinity variations on $[\text{H}^+]$ is also small, the freshwater term (last term in first row in Eq. (5.1)) can be neglected. Likewise, the contribution from the sA_T term (third term in first row in Eq. (5.1)) can be neglected in most regions, because A_T varies mostly with S, and as a result, variations in sA_T are comparably small. Making these assumptions, we here decompose $\Delta\text{H}^{+'}(i)$ into a T term and a sC_T term. Furthermore, it can be shown that the sC_T term can be represented by the difference between the C_T term and a C_T freshwater term that incorporates variations in C_T that are proportional

to variations in salinity (calculation in Appendix A):

$$\begin{aligned} \Delta H^{+'}(i) &\simeq \underbrace{\left(\frac{\partial H^+}{\partial T}(i) \Delta T(i) \right)'}_{T \text{ term}} + \underbrace{\left(\frac{\partial H^+}{\partial C_T}(i) \frac{S(i)}{\bar{S}} \Delta s C_T(i) \right)'}_{s C_T \text{ term}} \\ &\simeq \underbrace{\left(\frac{\partial H^+}{\partial T}(i) \Delta T(i) \right)'}_{T \text{ term}} + \underbrace{\left(\frac{\partial H^+}{\partial C_T}(i) \Delta C_T(i) \right)'}_{C_T \text{ term}} - \underbrace{\left(\frac{\partial H^+}{\partial C_T}(i) C_T(i) \frac{\Delta S(i)}{S(i)} \right)'}_{C_T \text{ freshwater term}}. \end{aligned} \quad (5.2)$$

The partial derivatives with respect to T and C_T in Eq. (5.2) for each day are calculated from daily-mean T , C_T , A_T , and S , as well as from temporal mean values for total phosphate and total silicate using *mocsy* 2.0 (Orr & Epitalon, 2015). While it is important to take into account the mean contributions to alkalinity from phosphoric and silicic acids, only little error arises when neglecting variations in total phosphate and total silicate (Orr & Epitalon, 2015).

The approximation of the changes in $[H^+]$ seasonal anomalies through the sum of the T and sC_T terms, as described in Eq. (5.2), works well. At the global scale, the average sum of the T and sC_T terms during OAX events differs from the simulated $[H^+]$ anomaly change by $-3.1 \cdot 10^{-4} \text{ nmol kg}^{-1} \text{ d}^{-1}$ (-3.5 % relative error) during the buildup phase and by $6.9 \cdot 10^{-4} \text{ nmol kg}^{-1} \text{ d}^{-1}$ (8.3 %) during the decay phase (Appendix Fig. 5.7). The mismatch is due to the omission of the sA_T and freshwater terms and due to the linear approximation for variations in $[H^+]$. Nevertheless, the small mismatch gives us confidence in using Eq. (5.2) to study the drivers of OAX events.

5.2.4 Decomposition of T and sC_T changes during OAX events into tendency terms

Within the ESM2M model, changes in T and C_T in a grid cell between two time steps are calculated from a number of tendencies that describe the changes in T and C_T due to the individual physical and biogeochemical processes represented by the model. We make use of these tendency terms for T and C_T to further decompose changes in T and C_T into individual physical and biogeochemical drivers. The individual process contributions to the total tendencies allow then to attribute changes in T and C_T to the individual physical and biogeochemical drivers. Finally, changes in $[H^+]$ are then attributed to these physical and biogeochemical drivers based on Eq. (5.2).

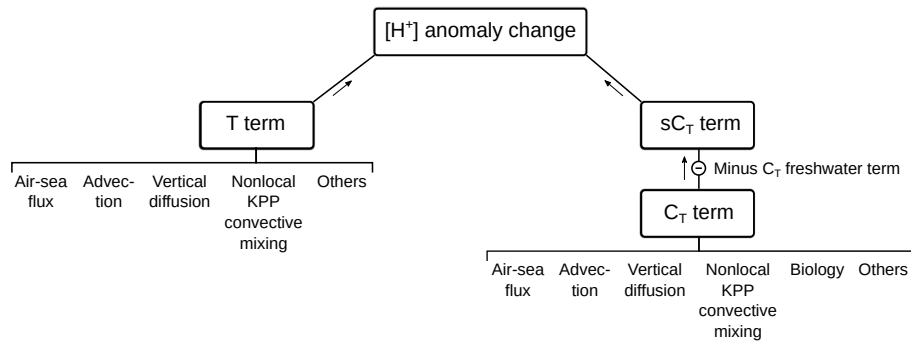


Figure 5.1: A scheme depicting the decomposition of $[H^+]$ anomaly change ($\Delta H^{+'}$) in the T and sC_T terms (Eq. 5.2). The sC_T term is further decomposed into the difference between the C_T term and the C_T freshwater term (Eq. 5.2). Furthermore, the decomposition of the T and C_T terms into tendency contributions (Eqs. (5.6) and (5.4)) is depicted.

The total temperature tendency (ξ_T , in K s^{-1}) at the sea surface is calculated as the sum of the tendency terms that represent air-sea exchange of heat ($\xi_{T,\text{air}}$), resolved and parameterized subgrid-scale advection of heat ($\xi_{T,\text{adv}}$), vertical diffusion and mixing of heat (here referred to as *vertical diffusion* only; $\xi_{T,\text{vdiff}}$), convective vertical mixing of heat in the ocean boundary layer as represented by the nonlocal KPP (K -profile) parameterization ($\xi_{T,\text{kpp}}$), and other smaller terms such as neutral diffusion and river runoff ($\xi_{T,\text{oth}}$; see Appendix B):

$$\xi_T = \xi_{T,\text{air}} + \xi_{T,\text{kpp}} + \xi_{T,\text{vdiff}} + \xi_{T,\text{adv}} + \xi_{T,\text{oth}}. \quad (5.3)$$

Likewise, total C_T tendency at the surface (ξ_{C_T} , in $\text{mol kg}^{-1} \text{s}^{-1}$) is calculated as the sum of the tendency terms that represent air-sea exchange of CO_2 ($\xi_{C_T,\text{air}}$), resolved and parameterized subgrid advection of carbon ($\xi_{C_T,\text{adv}}$), vertical diffusion and mixing of carbon (here referred to as *vertical diffusion* only; $\xi_{C_T,\text{vdiff}}$), nonlocal KPP convective mixing of carbon ($\xi_{C_T,\text{kpp}}$), biological carbon uptake and release ($\xi_{C_T,\text{bio}}$), and various other smaller terms ($\xi_{C_T,\text{oth}}$):

$$\xi_{C_T} = \xi_{C_T,\text{air}} + \xi_{C_T,\text{kpp}} + \xi_{C_T,\text{vdiff}} + \xi_{C_T,\text{adv}} + \xi_{C_T,\text{bio}} + \xi_{C_T,\text{oth}}. \quad (5.4)$$

More details on the individual tendencies and their underlying parametrizations can be found in Appendix B. The tendency contributions from the 'other' processes ($\xi_{T,\text{oth}}$ and $\xi_{C_T,\text{oth}}$) are comparably small (Table 5.1) and thus neglected in the analysis.

The individual tendencies are multiplied by the time span of a day ($1 \text{ d} = 86400 \text{ s}$) to obtain the change in the respective variable due to a tendency over the course of a day. They are also averaged over the day of interest and the subsequent day to approximate the change in the respective variable due to the tendency between the two days. For example, the change in T from day i to day $i + 1$ ($\Delta T(i)$) due to the air-sea heat exchange tendency ($\xi_{T,\text{air}}$) is calculated as

$$\Delta T^{\xi_{\text{air}}}(i) = \frac{1 \text{ d}}{2} (\xi_{T,\text{air}}(i + 1) + \xi_{T,\text{air}}(i)). \quad (5.5)$$

Calculating the change in T and C_T from each tendency, we can decompose the T and C_T terms (defined in Eq. (5.2)) into the individual tendency contributions:

$$\begin{aligned} \left(\frac{\partial H^+}{\partial T}(i) \Delta T(i) \right)' &\simeq \left(\frac{\partial H^+}{\partial T}(i) \Delta T^{\xi_{\text{air}}}(i) \right)' + \left(\frac{\partial H^+}{\partial T}(i) \Delta T^{\xi_{\text{kpp}}}(i) \right)' + \left(\frac{\partial H^+}{\partial T}(i) \Delta T^{\xi_{\text{vdiff}}}(i) \right)' \\ &\quad + \left(\frac{\partial H^+}{\partial T}(i) \Delta T^{\xi_{\text{adv}}}(i) \right)' + \left(\frac{\partial H^+}{\partial T}(i) \Delta T^{\xi_{\text{oth}}}(i) \right)', \\ \left(\frac{\partial H^+}{\partial C_T}(i) \Delta C_T(i) \right)' &\simeq \left(\frac{\partial H^+}{\partial C_T}(i) \Delta C_T^{\xi_{\text{air}}}(i) \right)' + \left(\frac{\partial H^+}{\partial C_T}(i) \Delta C_T^{\xi_{\text{kpp}}}(i) \right)' \\ &\quad + \left(\frac{\partial H^+}{\partial C_T}(i) \Delta C_T^{\xi_{\text{vdiff}}}(i) \right)' + \left(\frac{\partial H^+}{\partial C_T}(i) \Delta C_T^{\xi_{\text{adv}}}(i) \right)' \\ &\quad + \left(\frac{\partial H^+}{\partial C_T}(i) \Delta C_T^{\xi_{\text{bio}}}(i) \right)' + \left(\frac{\partial H^+}{\partial C_T}(i) \Delta C_T^{\xi_{\text{oth}}}(i) \right)'. \end{aligned} \quad (5.6)$$

$\Delta T^{\xi}(i)$ and $\Delta C_T^{\xi}(i)$ (the sums of the changes in T and C_T due to the individual tendency contributions as defined in Eq. (5.5)) slightly differ from the simulated changes in T ($\Delta T(i)$) and C_T ($\Delta C_T(i)$). This is because the changes in T and C_T within the model are calculated on the two-hour model time step, while the tendencies in the model output are only

available on daily-mean resolution. Nevertheless, the differences for the analyses presented here are generally small (Appendix Fig. 5.8c, d and Appendix Fig. 5.9e, f). At the global scale, the average sum of the tendency contributions to the T term differs from the directly simulated T term by $-4 \cdot 10^{-4} \text{ nmol kg}^{-1} \text{ d}^{-1}$ (-6.0 % relative error) during the buildup phase of events and by $-2 \cdot 10^{-5} \text{ nmol kg}^{-1} \text{ d}^{-1}$ (-0.6 %) during the decay phase (Appendix Fig. 5.8c,d). Likewise, the average sum of the tendency contributions to the C_T term, with the C_T freshwater term subtracted (Eq. 5.2), differs from the sC_T term by $1 \cdot 10^{-4} \text{ nmol kg}^{-1} \text{ d}^{-1}$ (10.2 %) during the buildup phase of events and by $2 \cdot 10^{-4} \text{ nmol kg}^{-1} \text{ d}^{-1}$ (4.3 %) during the decay phase (Appendix Fig. 5.9e,f).

5.3 Results

We first analyze the temperature and carbon contribution to the buildup and decay of OAX extremes in Sect. 5.3.1, and then quantify the individual processes that modulate temperature (Sect. 5.3.2) and carbon concentrations (Sect. 5.3.3) at the surface ocean. Sect. 5.3.4 summarizes the contribution of the individual terms to the total changes in $[H^+]$ anomalies.

5.3.1 Contributions of temperature and carbon anomalies to the buildup and decay of OAX events

Fig. 5.2 shows the simulated changes in $[H^+]$ anomalies and their drivers over the buildup (left column) and decay phase (right column) of OAX events. Averaged over the buildup period, the increase in $[H^+]$ anomalies is $0.009 \text{ nmol kg}^{-1} \text{ d}^{-1}$ on global average (Fig. 5.2a, Table 5.1). This increase is mainly due to increases in temperature during the event buildup that contribute $0.007 \text{ nmol kg}^{-1} \text{ d}^{-1}$ on global average (Fig. 5.2c). Increases in sC_T also contribute to the increase in $[H^+]$, but the contribution of $0.001 \text{ nmol kg}^{-1} \text{ d}^{-1}$ is much smaller than the contribution from increases in temperature at the global scale.

At the regional scale, we find that the increase in temperature is the dominant driver of $[H^+]$ anomalies during the buildup phase in 84 % of the global ocean surface area. A particular exception is the eastern tropical Pacific, where temperature decreases during the buildup of OAX events and therefore the contribution from the temperature is negative (Fig. 5.2c). There, increases in $[H^+]$ result from increases in sC_T (Fig. 5.2e). In the subtropics, increases in temperature and associated increases in positive $[H^+]$ anomalies are somewhat damped by decreases in sC_T and associated decreases in $[H^+]$ anomalies, whereas in the Kuroshio and Gulf Stream regions, the Arctic Ocean and near the Antarctic ice shelf, increases in temperature-induced $[H^+]$ anomalies are reinforced by increases in sC_T -induced $[H^+]$ anomalies.

During the decay period of OAX events and at the global scale, simulated decreases in temperature (Fig. 5.2d) and in sC_T (Fig. 5.2f) decrease $[H^+]$ to a similar extent (both by about $-0.004 \text{ nmol kg}^{-1} \text{ d}^{-1}$). This is in contrast to the buildup period, where the temperature term dominates at the global scale. At the regional scale, the sC_T term decreases almost everywhere (in 98 % of the ocean surface area), with the largest decreases simulated in the tropical Pacific and the high latitudes (Fig. 5.2f). Similarly, the temperature term also decreases in most regions (in 87 % of the surface ocean), with the most pronounced decreases in the subtropics (Fig. 5.2d), where the temperature term is the main driver of $[H^+]$ decay. An exception is again the equatorial Pacific, where temperature increases during the decay period of OAX events, thereby counteracting event decay.

in 10^{-3} $\text{nmol kg}^{-1} \text{ d}^{-1}$	Global		Tropical Pacific		Subtropics		Southern Ocean	
	Buildup	Decay	Buildup	Decay	Buildup	Decay	Buildup	Decay
Sum of T contributions	6.9	-3.9	-1.1	2.9	7.8	-6.7	9.4	-3.2
Air-sea flux	12.2	-2.2	11.8	8.4	23.3	-5.4	3.6	-0.6
Advection	-0.6	-0.4	-4.4	-0.0	-1.9	-0.9	0.4	0.3
Vertical diffusion	4.5	-1.5	-5.0	-3.6	2.6	-2.1	11.1	-1.2
Nonlocal KPP convective mixing	-9.1	0.3	-3.6	-2.0	-16.6	1.8	-5.6	-1.5
Others	-0.1	0.0	0.1	0.2	0.5	-0.0	-0.1	-0.1
Sum of C_T contributions minus C_T freshwater term	1.3	-3.7	10.3	-11.5	-0.3	-0.8	-0.4	-4.1
Air-sea flux	-4.7	-5.9	-6.0	-5.9	-2.8	-3.8	-10.4	-12.0
Advection	4.9	-1.5	18.6	-3.2	-1.0	0.3	1.6	-1.5
Vertical diffusion	0.6	2.0	3.4	1.4	-1.3	0.9	5.4	5.8
Nonlocal KPP convective mixing	2.4	2.6	1.8	2.0	4.8	2.2	2.9	3.6
Biology	0.1	-1.0	-4.6	-4.1	0.3	0.1	0.8	-0.1
Others	-1.3	-1.0	-2.2	-1.9	-0.3	-0.3	-0.5	-0.6
C_T freshwater term (subtracted)	0.8	-1.3	0.6	-0.1	-0.1	0.1	0.2	-0.8
Total	8.2	-7.6	9.2	-8.6	7.6	-7.5	9.0	-7.3
$[\text{H}^+]$ change	8.8	-8.4	9.5	-8.8	7.9	-7.9	9.8	-8.3

Table 5.1: The tendency contributions to the buildup and decay of OAX events for the global ocean, the tropical Pacific, the Subtropics, and the Southern Ocean (the definition of regions is shown in Fig. 5.2a). For each period and region, the two largest positive and negative contributions are highlighted in bold font. 'Total' denotes the sum of all tendency contributions and $[\text{H}^+]$ change is the actual simulated $[\text{H}^+]$ change during the buildup and decay phases.

5.3.2 Drivers of temperature variations during OAX events

To understand the processes driving the changes in temperature anomalies during OAX events and hence the temperature contribution to buildup and decay of OAX events (Fig. 5.2c, d), the change in temperature anomaly during event buildup and decay is decomposed (see Eq. (5.6)) into the contributions from air-sea heat exchange (Fig. 5.3b, c), advection (Fig. 5.3e, f), vertical diffusion (Fig. 5.3h, i), and nonlocal KPP convective mixing (Fig. 5.3k, l). For ease of interpretation of the anomaly patterns, we also show the climatological means of the tendency contributions to the T term (Fig. 5.3a,d,g,j). These are determined by calculating the temporal mean values of the tendency contributions to the T term (Eq. 5.2) instead of calculating their seasonal anomalies.

At the global scale, reduced ocean heat loss (i.e., net ocean heat uptake) contributes most to the increases in temperature anomalies during the buildup period of OAX events (Fig. 5.3; Table 5.1). The net ocean heat uptake increases $[H^+]$ anomalies by $0.012 \text{ nmol kg}^{-1} \text{ d}^{-1}$ (138 % of $[H^+]$ anomaly increase, Fig. 5.3b) at the global scale. In addition, reduced vertical diffusion of warm waters to the subsurface and associated increases in the temperature anomalies during the buildup period cause an increase in $[H^+]$ anomalies of $0.005 \text{ nmol kg}^{-1} \text{ d}^{-1}$ (51 % of $[H^+]$ anomaly increase, Fig. 5.3h). These temperature-induced increases in $[H^+]$ anomalies are strongly damped by reduced nonlocal KPP convective mixing of warm subsurface water to the surface, which reduces the surface temperature and therefore $[H^+]$ anomalies during the buildup (Fig. 5.3k; $-0.009 \text{ nmol kg}^{-1} \text{ d}^{-1}$, -103 % of $[H^+]$ anomaly increase). In the climatological mean, convective mixing increases surface temperature by transporting heat to the surface when surface waters lose buoyancy due to heat loss to the atmosphere (Fig. 5.3j). This mechanism is less active during positive anomalies in air-sea heat flux.

At the regional scale (Fig. 5.3), the positive contribution from air-sea heat exchange is largest in the low-to-mid latitudes and in particular in the subtropical oceans (Table 5.1; Fig. 5.3b), while the contribution is much smaller or negative in the high latitudes. In the subtropics, air-sea heat exchange often changes the sign from net loss to the atmosphere to net uptake during OAX event (Fig. 5.3a,b). Vertical diffusion increases temperature anomaly and hence contributes positively to the T term in all ocean regions, except in the tropical Pacific and Indian Ocean, where vertical diffusion of heat to the subsurface is increased during OAX events. The vertical diffusion contribution is most positive in the North Atlantic, North Pacific, and Southern Ocean (Table 5.1) during the buildup. In parts of these regions, vertical diffusion increases surface temperatures in the climatological mean (Fig. 5.3g) and enhanced vertical diffusion during OAX events further increases temperature. Such temperature increases due to enhanced vertical diffusion occur in 43 % of the high latitudes (above 45° latitude). This is in contrast to the remaining ocean, where vertical diffusion usually reduces surface temperatures and a decrease in vertical diffusion increases surface temperatures during the buildup of OAX events. Decreases in nonlocal KPP convective mixing decreases surface temperature and $[H^+]$ almost in the entire global surface ocean, especially in the subtropics (Fig. 5.3k; Table 5.1), where also increases in temperature anomaly due to air-sea heat exchange are largest (Fig. 5.3b). The contribution from advective heat transport is generally small (Fig. 5.3e). However, its contribution is substantial in some regions such as the tropical Pacific (Fig. 5.3e, Table 5.1).

During the decay phase of OAX events, the temperature decrease in the subtropics mainly results from increased heat losses to the atmosphere (Fig. 5.3c). The smaller temperature decreases in the Southern Ocean (Fig. 5.2d) arise from negative anomalies in nonlocal KPP convective mixing and vertical diffusion that are partly compensated by reduced air-sea heat loss and reduced advective heat loss. In the tropical Pacific, the increases in the temperature term

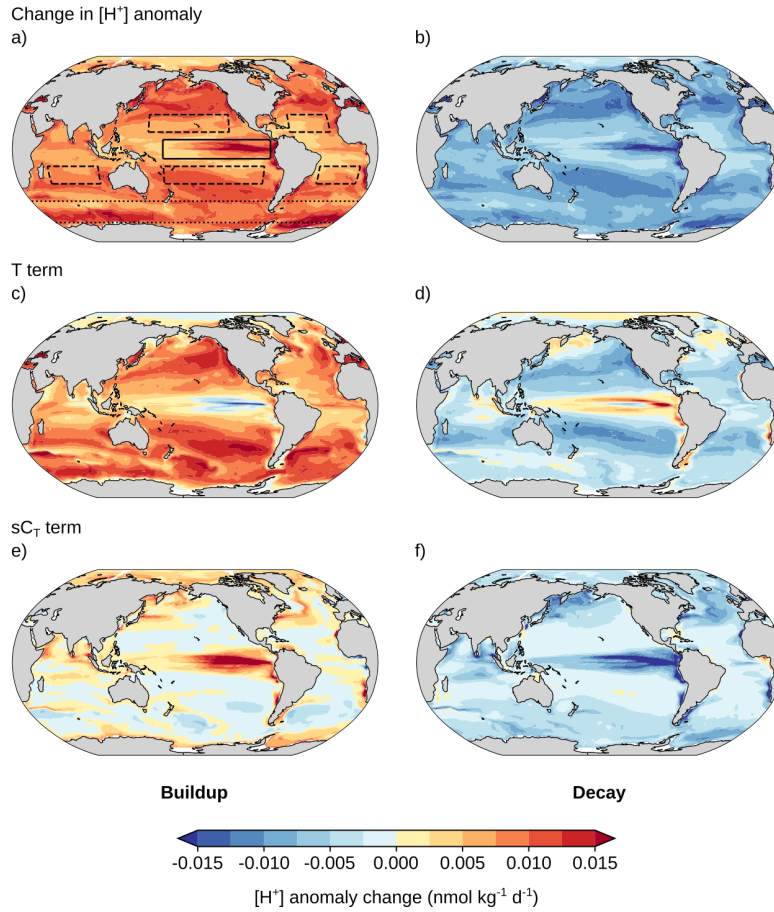


Figure 5.2: The $[H^+]$ anomaly change during buildup and decay of OAX events and the contributions from the T and sC_T terms. (a, b) The simulated change in $[H^+]$ anomalies during the buildup and decay phases of OAX events, (c, d) the contribution from the T term, and (e, f) the contribution of the sC_T term (see Eq. (5.2)). The solid, dashed, and dotted boxes in a) indicate the Tropical Pacific ($8^\circ\text{S} - 8^\circ\text{N}$ and $190^\circ\text{W} - 85^\circ\text{W}$), the Subtropics ($15^\circ\text{N} - 30^\circ\text{N}$ and $205^\circ\text{W} - 125^\circ\text{W}$ in the North Pacific, $30^\circ\text{S} - 15^\circ\text{S}$ and $190^\circ\text{W} - 90^\circ\text{W}$ in the South Pacific, $15^\circ\text{N} - 30^\circ\text{N}$ and $65^\circ\text{W} - 25^\circ\text{W}$ in the North Atlantic, $30^\circ\text{S} - 15^\circ\text{S}$ and $35^\circ\text{W} - 5^\circ\text{E}$ in the South Atlantic, and $30^\circ\text{S} - 15^\circ\text{S}$ and $55^\circ\text{E} - 105^\circ\text{E}$ in the Indian Ocean), and the Southern Ocean ($65^\circ\text{S} - 45^\circ\text{S}$), respectively. These regions are used in Table 5.1.

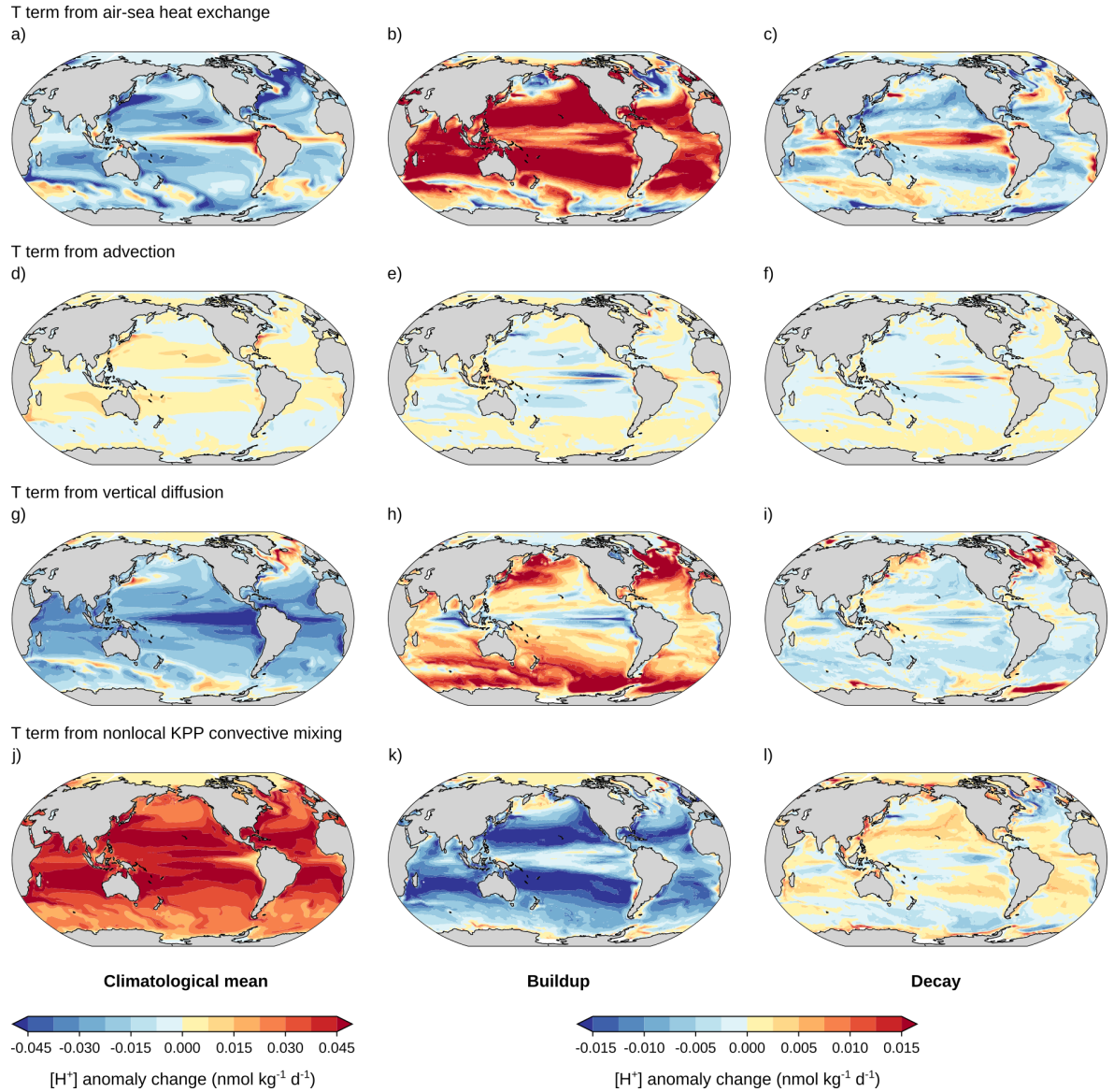


Figure 5.3: The decomposition of the T term into tendency contributions. The climatological means of the tendency contributions to the T term (first column) as well as their contributions to the buildup (second column) and decay (third column) means of the T term (Fig. 5.2 c, d). The remaining processes and the difference between the sum of the contributions and the T term during event buildup and decay are shown in Appendix Fig. 5.8.

(Fig. 5.2d)) that counteract the $[H^+]$ event decay result from enhanced ocean heat uptake during the decay phase.

5.3.3 Drivers of carbon variations during OAX events

To understand the processes driving the changes in sC_T anomaly during OAX events and the sC_T contribution to buildup and decay of OAX events (Fig. 5.2e, f), the sC_T term is decomposed into the C_T term and the C_T freshwater term (see Eq. (5.2)). The C_T freshwater term is comparably small in most regions (Fig. 5.9c d; Table 5.1) and hence neglected here. The C_T term is decomposed into contributions from air-sea CO_2 exchange (Fig. 5.4b, c), advection (Fig. 5.4e, f), vertical diffusion (Fig. 5.4h, i), nonlocal KPP convective mixing (Fig. 5.4k, l), and biological activity (Fig. 5.4n, o) (see Eq. (5.6)).

At the global scale, advection is the most important driver of C_T increase during OAX event buildup, increasing $[H^+]$ anomaly by $0.005 \text{ nmol kg}^{-1} \text{ d}^{-1}$ (56 % of $[H^+]$ anomaly increase). Also reduced nonlocal KPP convective vertical mixing increases $[H^+]$ by $0.002 \text{ nmol kg}^{-1} \text{ d}^{-1}$ (28 % of $[H^+]$ anomaly increase). These increases are balanced by decreases in C_T anomalies from increased carbon loss to the atmosphere during the buildup of OAX events ($-0.005 \text{ nmol kg}^{-1} \text{ d}^{-1}$, -54 % of $[H^+]$ anomaly increase). Negative anomalies in air-sea CO_2 flux, i.e., increased carbon loss to the atmosphere or decreased CO_2 uptake from the atmosphere (Fig. 5.4a), occur when partial pressure of CO_2 (pCO_2) in the surface water is increased. Due to the high correlation between $[H^+]$ and pCO_2 anomalies (Pearson correlation coefficient of 0.99 on global average in the model), negative anomalies in air-sea CO_2 flux during high $[H^+]$ events are expected. The contributions from vertical diffusion and biology are small at the global scale.

At the regional scale (Fig. 5.4), the contribution from advection to OAX event buildup is largest in the tropics (Fig. 5.4e). Smaller positive contributions from advection are also simulated in high-latitude regions (Fig. 5.4e). However, the advection contribution is slightly negative in the subtropics (Table 5.1). Advection of C_T in the GFDL ESM2M model includes changes in surface C_T from the balance between precipitation and evaporation. Here, the advection tendency from precipitation and evaporation alone is isolated using an offline estimate (Appendix C). While the climatological mean of the advection tendency (Fig. 5.4d) is largely due to mean precipitating and evaporation patterns (Appendix Fig. 5.10a), we find that oceanic advection, such as due to upwelling, is the main driver of the increases in C_T anomaly during event buildup in the tropics (Appendix Fig. 5.10e). Notably, the contribution from precipitation and evaporation is large around the maritime continent (Appendix Fig. 5.10b). The negative anomalies in air-sea CO_2 flux are largest in the high latitudes. Similar to temperature, the anomalies in air-sea CO_2 exchange are offset by opposing tendencies from nonlocal KPP convective mixing of carbon in most regions. The convective mixing from the nonlocal KPP parameterization increases C_T and $[H^+]$ everywhere except in the tropical oceans. Vertical diffusion generally increases surface C_T in the climatological mean (Fig. 5.4g). During OAX event buildup, negative anomalies in vertical diffusion counteract increases in $[H^+]$ anomaly in the subtropics, the mid latitudes, and parts of the tropics (Fig. 5.4h). In contrast, vertical diffusion increases $[H^+]$ anomalies in the high-latitude regions of the the North Pacific, North Atlantic, and Southern Ocean. Its contribution is often opposite to that of temperature vertical diffusion due to opposite vertical gradients in temperature and C_T . This is not the case in the high-latitude regions where temperature and C_T gradients are often both positive (Figs. 5.3h and 5.4h). The reductions in vertical diffusion of temperature and C_T (increasing temperature and decreasing C_T) in the low-to-mid latitudes coincide with negative anomalies in wind stress during

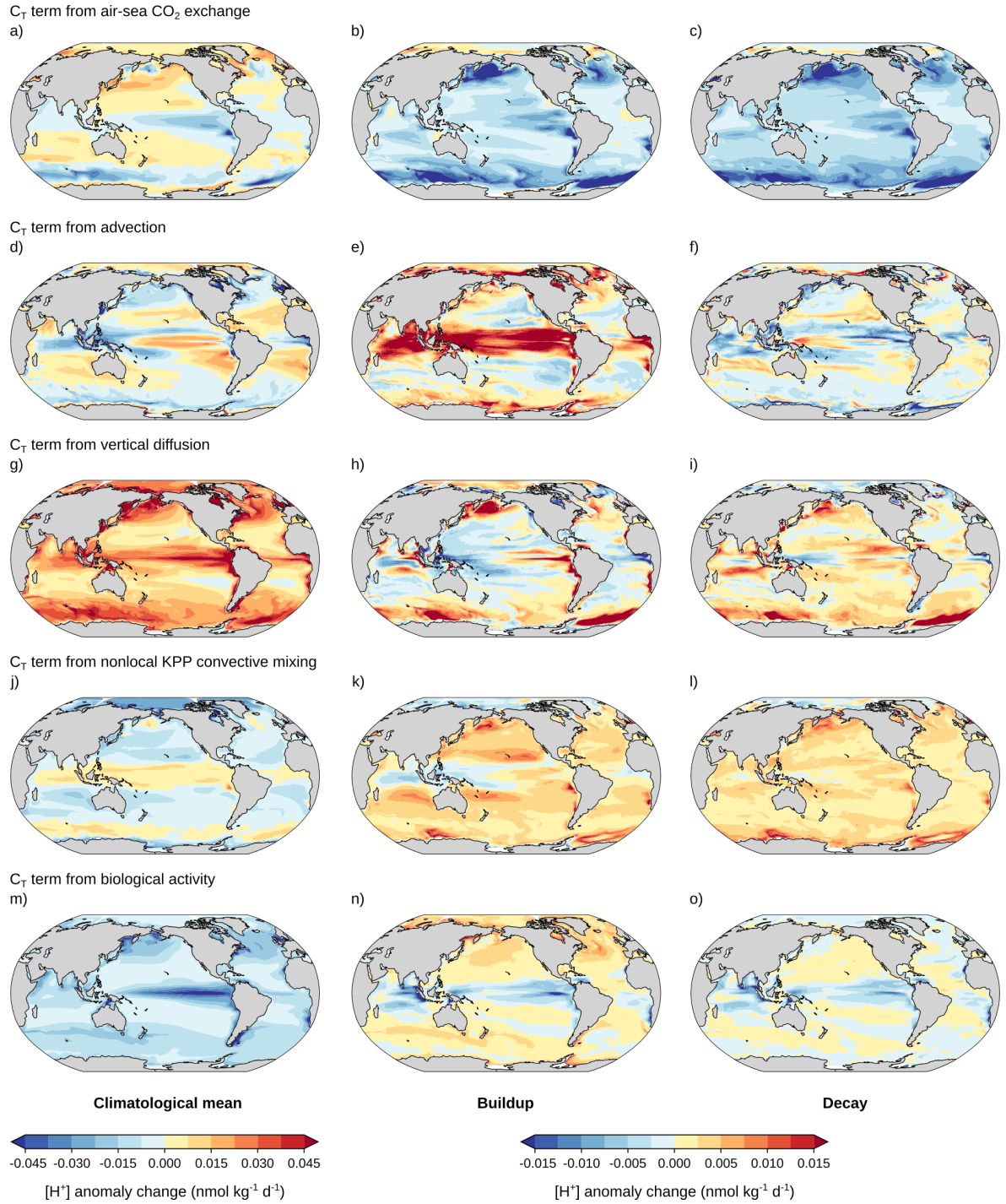


Figure 5.4: The decomposition of the C_T term into tendency contributions. The climatological means of the tendency contributions to the C_T term (first column) as well as their contributions to the buildup (second column) and decay (third column) means of the C_T term (Fig. 5.2 e, f). The remaining processes, the C_T freshwater term that is subtracted to obtain the sC_T term from the C_T term (Eq. 5.2), as well as the difference between the sum of the contributions to the sC_T term and the sC_T term during event buildup and decay are shown in Appendix Fig. 5.9.

event buildup (not shown). In the high-latitude regions where positive anomalies in vertical diffusion of temperature and C_T are simulated (Figs. 5.3h and 5.4h), also wind stress is increased during event buildup. The increased wind stress may be the reason for enhanced vertical mixing during event buildup in these regions. Biological activity generally reduces C_T everywhere, because biological production outweighs decomposition at the surface (Fig. 5.4m). During OAX event buildup, increases in biological production significantly decrease $[H^+]$ anomaly in the tropics (Table 5.1), while reductions in biological production increase $[H^+]$ anomaly in the mid-to-high latitudes (Fig. 5.4n). In the tropical regions, increased nutrient concentrations are simulated during OAX events (not shown), which may cause increased phytoplankton growth there.

During the decay phase of $[H^+]$ extremes, sC_T anomaly decreases almost in the entire ocean (Fig. 5.2f). This decrease is mainly due to loss of carbon to the atmosphere (Fig. 5.4c), which remains as strong during the decay phase as during the buildup phase. In the tropical ocean, biological production continues to decrease C_T anomaly during event decay, and also advection reduces C_T anomaly during event decay. The convective mixing term counteracts $[H^+]$ event decay everywhere in the ocean (Fig. 5.4l), and also vertical diffusion increases $[H^+]$ anomaly during event decay in many regions (Fig. 5.4i).

5.3.4 Summary of global drivers during $[H^+]$ extremes events

In the previous two sections the drivers of temperature and carbon variations during OAX events were discussed separately. Here, we provide a short overview of the combined importance of the individual processes. Fig. 5.5 summarizes them at the global scale.

We find enhanced net ocean heat uptake to be the dominant driver of OAX event buildup at the global scale. Also positive anomalies in advection of carbon, such as due to increased upwelling of carbon-rich subsurface waters, and positive anomalies in vertical diffusion of temperature, due to reduced vertical mixing with colder subsurface waters and also due to increased vertical mixing with warmer subsurface waters, contribute substantially to OAX event buildup. The increases in temperature anomaly due to enhanced net ocean heat uptake are balanced by reduced warming from nonlocal KPP convective mixing. Positive anomalies in nonlocal KPP convective mixing also partly balance the decreases in surface C_T following from decreased net air-sea CO_2 flux. These decreases in net air-sea CO_2 flux substantially counteract OAX event buildup.

We find decreased net air-sea CO_2 flux to be the dominant driver of OAX event decay, offset by positive anomalies in convective mixing. Also decreased net ocean heat uptake and negative anomalies in advection of carbon contribute substantially to event decay. Increased vertical diffusion and mixing drives event decay by reducing surface temperatures, but counteracts event decay by increasing surface carbon concentrations.

5.4 Discussion and conclusions

Our analysis shows that the buildup of OAX events is mainly driven by enhanced sea surface temperature and somewhat damped locally by reduced sea surface carbon content, while variations in alkalinity and freshwater are negligible. Furthermore, we show that increases in temperature dominate the $[H^+]$ buildup in all regions, except in the tropical Pacific. By analyzing the physical and biogeochemical drivers of temperature and carbon variations during the buildup and decay of OAX events, enhanced net ocean heat uptake was identified

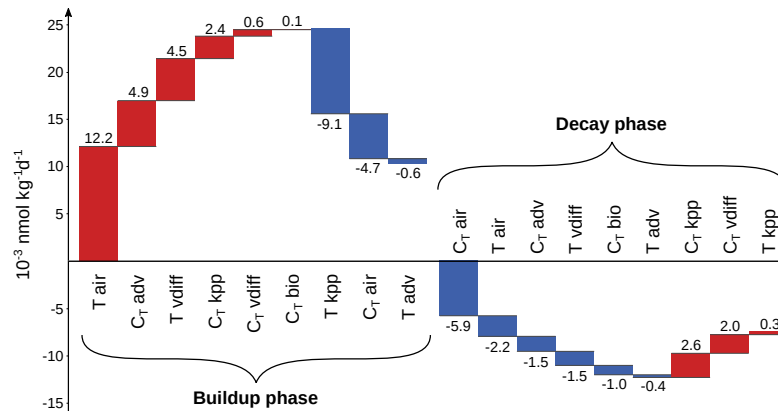


Figure 5.5: The global mean contributions to $[\text{H}^+]$ anomaly change from T air-sea flux, T advection, T vertical diffusion, and T nonlocal KPP convective mixing, as well as from C_T air-sea flux, C_T advection, C_T vertical diffusion, C_T nonlocal KPP convective mixing, and C_T biology in the buildup and decay phases of $[\text{H}^+]$ extremes.

as the main driver of the increase in temperature during OAX events, in particular in the subtropical oceans. Reduction in temperature due to reduced nonlocal KPP convective mixing of heat to the surface partly offset the temperature increase due to ocean heat uptake (Fig. 5.3; Table 5.1). In the mid-to-high-latitude regions, reduced vertical diffusion of heat to the subsurface or increased vertical diffusion of heat to the surface are the main cause of the temperature increases during OAX events. In the tropical regions and in particular in the tropical Pacific, advection of C_T was identified as the main driver of $[\text{H}^+]$ extremes (Fig. 5.4).

Our main focus in this study was on attributing changes in $[\text{H}^+]$ anomaly to the driving processes during the buildup and decay phases of OAX events. However, the processes responsible for increasing $[\text{H}^+]$ anomaly before event onset were not investigated so far. We therefore investigate the contributions from anomalies in T and sC_T to the anomaly in $[\text{H}^+]$ during the events, which also include the increases in $[\text{H}^+]$ anomaly before event onset. This is done by approximating $[\text{H}^+]$ anomaly during the events by a first-order Taylor expansion in the drivers about their seasonal cycles. In most of the ocean, the $[\text{H}^+]$ anomaly during the events results from both positive anomalies in sC_T (91 % of the ocean surface area) and in T (86 %; Fig. 5.6). Over 46 % of the ocean, the positive anomalies in sC_T contribute more to the $[\text{H}^+]$ anomaly during the extreme events than temperature anomalies, including large parts of the tropics and mid-to-high latitude regions in the North Pacific, North Atlantic, Southern Ocean, and Arctic Ocean (Fig. 5.6c, d). In these regions, $[\text{H}^+]$ anomalies during the events tend to be also larger. As a result, $[\text{H}^+]$ anomaly during the events ($0.26 \text{ nmol kg}^{-1}$) is globally more strongly driven by positive anomalies in sC_T (60 %; Fig. 5.6b, d) than by positive temperature anomalies (37 %; Fig. 5.6a, c). The remaining 3 % arise due to the missing sA_T and freshwater terms as well as the linear approximation.

These results show that sC_T is a more important driver for the overall $[\text{H}^+]$ anomaly during the events than it is for the evolution of $[\text{H}^+]$ between event onset and peak (Sect. 5.3). This suggests that OAX events often arise mainly due to positive anomalies in sC_T , while the increases in $[\text{H}^+]$ after crossing the threshold are mainly driven by increases in temperature. In Sect. 5.3.3, it has been shown that sC_T anomaly during the events is reduced by negative anomalies in air-sea gas exchange that result from positive anomalies in $p\text{CO}_2$ during the events. Before event onset, when $[\text{H}^+]$ and $p\text{CO}_2$ are lower, sC_T is likely less reduced by negative anomalies in air-sea gas exchange. This may partly explain the more pronounced role of sC_T in driving the overall $[\text{H}^+]$ anomaly than in driving increases in $[\text{H}^+]$ after event onset.

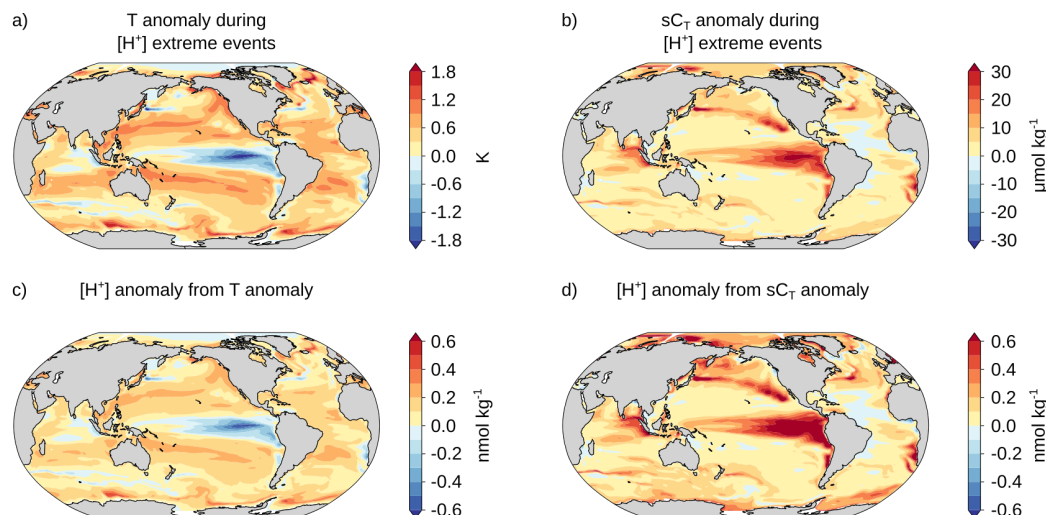


Figure 5.6: Decomposition of $[H^+]$ anomaly during OAX events into contributions from T and sC_T . a) Mean T anomaly during OAX events, b) mean sC_T anomaly during OAX events, c) $[H^+]$ anomaly resulting from the T anomaly during OAX events, and d) $[H^+]$ anomaly resulting from the sC_T anomaly during OAX events.

In regions where temperature is unusually high during OAX events, such as in the subtropical oceans (Fig. 5.6a), the physical drivers of temperature evolution during these events may be similar to the physical drivers of temperature evolution during marine heatwaves. In addition, if temperature is the main driver of $[H^+]$ during the events, as it is the case in the subtropical oceans (Fig. 5.2c, d), then the drivers of $[H^+]$ extreme event buildup and decay are likely similar to those of marine heatwave buildup and decay. In fact, Vogt et al. (in preparation) showed that surface heat fluxes are the main driver of temperature increases during the buildup of marine heatwaves, counteracted by temperature decreases from nonlocal KPP convective mixing (Fig. 1 in Vogt et al. (in preparation)). Likewise they identify surface heat flux to be the main driver of marine heatwave decay, again offset by convective mixing. This is similar to the results in this study for the subtropical oceans. Here, surface heat flux was identified as the main driver of $[H^+]$ increase during the buildup period of OAX events and also the main driver of $[H^+]$ decrease during event decay (Fig. 5.3b, c; Table 5.1). Likewise, vertical mixing from the nonlocal KPP parameterization was found to be the main inhibiting factor during the buildup period, and, to a lesser extent, also an important inhibiting factor for event decay (Fig. 5.3k, l; Table 5.1).

In regions such as the subtropical oceans, where temperature is strongly elevated during the OAX events (Fig. 5.6a), also temperature may frequently exceed extreme event thresholds during $[H^+]$ extremes. As a result, compound extreme events in temperature and $[H^+]$ are more likely to occur in these regions. This is consistent with the findings in Chapter 4, where it has been shown in observation-based data that compound extreme events in these two variables are most likely to occur in the subtropical oceans (Fig. 4.1 in Chapter 4). Recalling from the present analysis and from Vogt et al. (in preparation) that the simulated drivers of extreme event buildup and decay are similar for $[H^+]$ extremes and marine heatwaves in those regions, one can expect that also the evolution of temperature and $[H^+]$ during the compound events is governed by air-sea heat fluxes with compensating tendencies from convective vertical mixing.

The present study focused on the analysis of the mean driving processes over the buildup and decay periods of OAX events. The mean process contributions to $[H^+]$ extreme event buildup and decay therefore characterize an average $[H^+]$ extreme event in a region. However, individual extreme events may be governed by different processes, and the processes may vary during the

buildup and decay periods of individual events. Different processes may arise for example from seasonal differences or different types of extremes, as has been shown for marine heatwaves by Vogt et al. (in preparation). However, t-tests reveal that the mean contributions during event buildup and decay, as shown in Figs. 5.2-5.6, generally differ significantly from zero, indicating that the mean process contributions are statistically robust despite variations within individual events and between events (not shown).

A number of caveats remain. First, the drivers of OAX events were analyzed using data from an Earth system model only as many processes cannot be validated independently with observational-based estimates, since the necessary observational data is generally not available. The robustness of our results depends therefore on the skill of the Earth system model in simulating the physical and biogeochemical processes leading to $[\text{H}^+]$ variations and extremes. More insights into the robustness of our results could be obtained by comparing the identified drivers to those from other Earth system models that could provide the necessary diagnostic output. Second, the spatial resolution of the MOM4p1 model is relatively coarse and the model cannot explicitly simulate small-scale circulation features, such as meso- and submesoscale dynamics (Griffies et al., 2015). Our analysis may therefore underestimate the impact of these small-scale circulation features on the buildup and decay of OAX events. The relatively coarse resolution ocean model also limits our analysis to the open ocean, as a high resolution ocean model including improved biogeochemistry is needed to accurately represent the bathymetry and the exchange fluxes within the ocean-land continuum (Turi et al., 2018; Terhaar et al., 2019). Third, in Chapter 4 it has been shown that the GFDL ESM2M model, similar to other CMIP5 and CMIP6 Earth system models, overestimates the contribution from variations in temperature on $[\text{H}^+]$ dynamics, in particular in the high latitudes, while underestimating the effect from variations in sC_T on $[\text{H}^+]$. As a result, the contributions from the temperature term to the buildup and decay of OAX events may be also slightly overestimated in this study. Finally, this study analyzes the drivers under a preindustrial stationary climate. However, the ongoing warming and acidification of the upper ocean may modulate the main drivers of $[\text{H}^+]$ extremes, as the background ocean carbon and temperature fields on which the drivers act on as well as the drivers themselves may change with climate change. Our analysis should therefore be extended to simulations that include the climate change signal.

In summary, the analysis reveals that temperature is an important driver of the buildup and decay of OAX events, with large contributions from air-sea heat flux that are most pronounced in the subtropical oceans. Reductions in surface ocean carbon due to loss of carbon to the atmosphere substantially dampen the $[\text{H}^+]$ anomalies during the extreme events. An exception is the tropical Pacific, where enhanced advection of carbon is the main driver of OAX events. The identification of the main processes leading to OAX events may be a first step towards skillful predictions of these extremes with potentially detrimental effects on marine ecosystems.

5.5 Appendix of Chapter 5

Appendix A Decomposition of the sC_T term into the C_T term and the C_T freshwater term

The C_T term minus the C_T freshwater term is equivalent to the sC_T term:

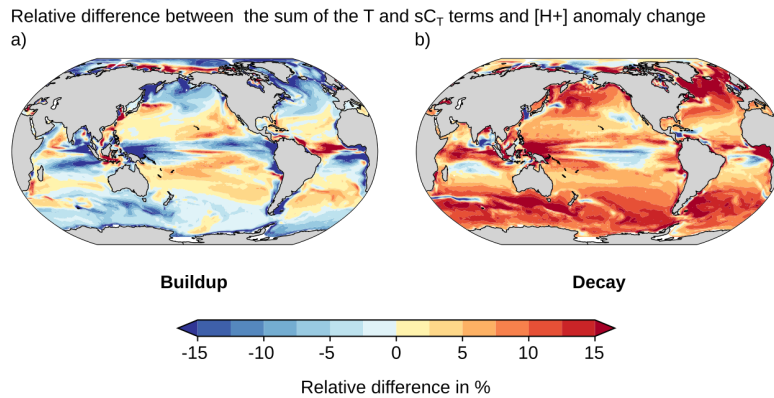
$$\begin{aligned}
 & \frac{\partial H^+}{\partial C_T}(i) \Delta C_T(i) - \frac{\partial H^+}{\partial C_T}(i) C_T(i) \frac{\Delta S(i)}{S(i)} \\
 &= \frac{\partial H^+}{\partial C_T}(i) \Delta \left(\frac{S(i)}{\bar{S}} sC_T(i) \right) - \frac{\partial H^+}{\partial C_T}(i) \left(\frac{S(i)}{\bar{S}} sC_T(i) \right) \frac{\Delta S(i)}{S(i)} \\
 &\simeq \frac{\partial H^+}{\partial C_T}(i) \frac{S(i)}{\bar{S}} \Delta sC_T(i) + \frac{\partial H^+}{\partial C_T}(i) \frac{sC_T(i)}{\bar{S}} \Delta S(i) - \frac{\partial H^+}{\partial C_T}(i) \frac{sC_T(i)}{\bar{S}} \Delta S(i) \\
 &= \frac{\partial H^+}{\partial C_T}(i) \frac{S(i)}{\bar{S}} \Delta sC_T(i)
 \end{aligned} \tag{5.7}$$

Appendix B Detailed description of tendency terms for T and C_T

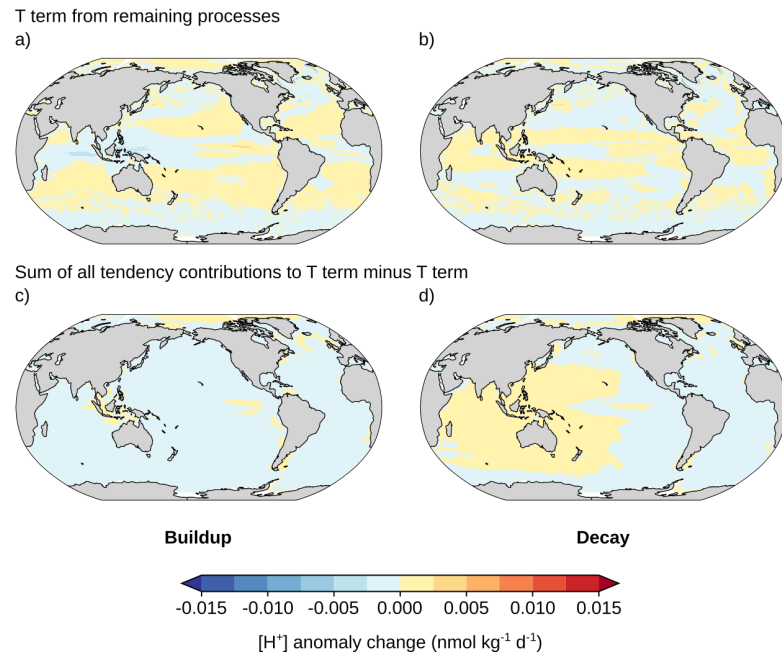
In the following, key characteristics of the individual tendency terms of the ocean temperature and C_T budgets are described. Further information on the temperature tendency terms can be found in Palter et al. (2014), Griffies (2009), and Vogt et al. (in preparation).

Surface heat flux ($\xi_{T,air}$). Surface heat flux contains contributions from net shortwave and net longwave radiation fluxes as well as sensible and latent heat fluxes across the ocean-atmosphere interface. A fraction of the shortwave radiation entering the surface ocean is transmitted to the levels below the surface to mimic the penetration of shortwave radiation into the water column (Manizza et al., 2005). The absorption of shortwave radiation from organic matter is taken into account based on the chlorophyll concentrations that are simulated by the ocean biogeochemistry component TOPAZv2 (Manizza et al., 2005).

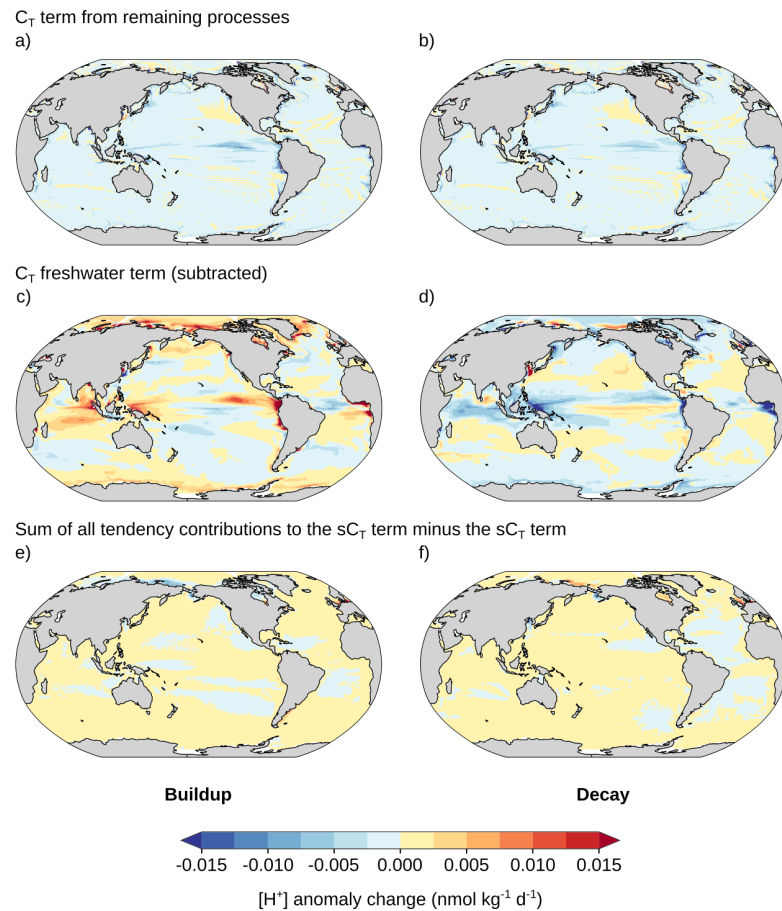
Surface CO_2 exchange ($\xi_{C_T,air}$). The C_T change from CO_2 exchange with the atmosphere follows the OCMIP-2 recommendations (Najjar & Orr, 1998). Gas exchange occurs when surface ocean CO_2 concentration deviates from the saturation concentration where ocean and



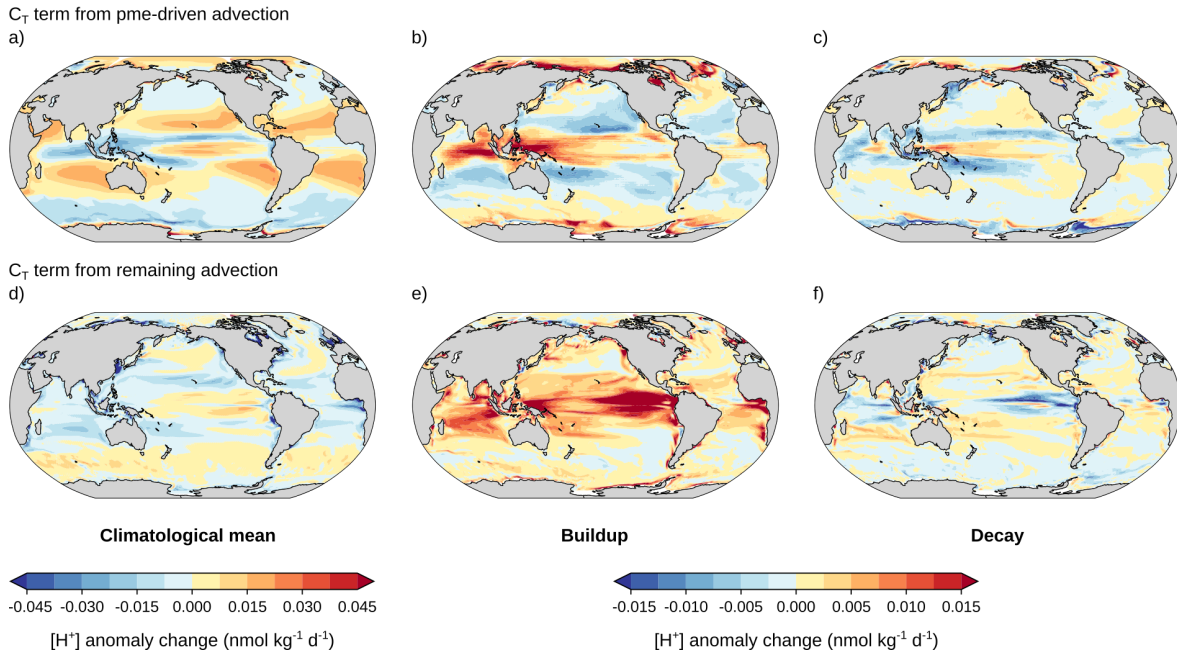
Appendix Figure 5.7: The relative difference between the sum of the T and sC_T terms and the change in $[H^+]$ anomaly during event buildup (a) and decay (b) of OAX events. Differences arise due to the neglected contributions from the sA_T and freshwater terms as well as due to the linear approximation for variations in $[H^+]$ (Eq. 5.2).



Appendix Figure 5.8: (a, b) The tendency contribution from the remaining ('other') processes to the buildup and decay means of the T term (Fig. 5.2 c, d), and (c, d) the difference between the sum of the contributions (together with the tendency contributions in Fig. 5.3) and the T term.



Appendix Figure 5.9: (a, b) The tendency contribution from the remaining ('other') processes to the buildup and decay means of the C_T term (Fig. 5.2 e, f), (c, d) the C_T freshwater term that is proportional to salinity change and subtracted to obtain the sC_T term from the C_T term (Eq. 5.2), and (e, f) the difference between the sum of the contributions to the sC_T term (together with the tendency contributions in Fig. 5.4) and the sC_T term.



Appendix Figure 5.10: (a, b, c) The climatological mean of the contribution from precipitation minus evaporation to the C_T term from advection and its contribution to event buildup and decay, and (d, e, f) the same for the residual part of the C_T term from advection that is not due to precipitation minus evaporation.

atmosphere are in equilibrium. The saturation concentration depends on the solubility of oceanic CO_2 (Weiss, 1974) and the fugacity of atmospheric CO_2 . Gas transfer velocity is calculated from wind speed at 10 m and Schmidt number (Wanninkhof, 1992).

Advection ($\xi_{T,\text{adv}}$, $\xi_{C_T,\text{adv}}$). Ocean advection of temperature and C_T from the resolved velocity field is implemented using the minimally diffusive MDPPM numerical scheme from Marshall et al. (1997) that is based on the piecewise parabolic method by Colella & Woodward (1984). Parametrizations for mesoscale advection (Griffies, 2009) and submesoscale advection are also included (Fox-Kemper et al., 2008).

Vertical diffusion ($\xi_{T,\text{vdiff}}$, $\xi_{C_T,\text{vdiff}}$). Vertical mixing in the ocean boundary layer is parameterized by the K profile parameterization (Large et al., 1994). It is increased when shear forces overcome water column stratification, resulting in a deep boundary layer. Tidal mixing is implemented following the schemes by Simmons et al. (2004) and Lee et al. (2006). In addition, a constant background vertical diffusivity of $1 \cdot 10^{-5} \text{ m}^2 \text{ s}^{-1}$ below 35° latitude and $1.5 \cdot 10^{-5} \text{ m}^2 \text{ s}^{-1}$ above 35° latitude is assumed.

Nonlocal K-profile (KPP) parameterization for vertical mixing ($\xi_{T,\text{kpp}}$, $\xi_{C_T,\text{kpp}}$). The nonlocal part of the K-profile parameterization by Large et al. (1994) represents convective vertical mixing in the ocean boundary layer, redistributing heat to the surface under negative surface buoyancy forcing, and hence mainly during heat loss to the atmosphere (see also Palter et al. (2014)).

Biological carbon uptake simulated by TOPAZv2 ($\xi_{C_T,\text{bio}}$). Biological uptake of inorganic carbon by phytoplankton and release of inorganic carbon by remineralization of organic matter is simulated by TOPAZv2 (Dunne et al., 2013). In the surface layers, uptake dominates over release. Phytoplankton production and hence phytoplankton carbon uptake in TOPAZv2 is proportional to the phytoplankton biomass and to the growth rate (Frölicher et al., 2020) that is

limited by temperature (Eppley, 1972), light, and the nutrient availability of nitrate, ammonium, phosphate, silicate, and iron.

Other terms ($\xi_{T,oth}$, $\xi_{C_T,oth}$). The *other* terms include tendencies for neutral diffusion, river runoff and ice calving, parametrizations for exchange between closed-off marginal seas and the open ocean, and a tendency that compensates for a numerical artifact in the model formulation (Chapter 8.3 in Griffies, 2009). River runoff from the land model is assumed to transport heat relative to 0°C and C_T in a fixed ratio to A_T of 0.5. For temperature, the *other* group also contains tendencies for frazil ice formation and the advective heat transport from precipitation and evaporation.

Appendix C Changes in dissolved inorganic carbon concentration from precipitation and evaporation

Within the ESM2M model, precipitation does not carry carbon. As a result, precipitation and evaporation do not transport carbon between atmosphere and ocean. This is in contrast to heat that is transported across the ocean-atmosphere boundary by precipitation and evaporation. However, while precipitation and evaporation do not change the ocean's carbon content, they dilute or concentrate the surface water such that the concentration of tracers like C_T decreases or increases. In the ESM2M model, this is treated as an advective carbon flux within the ocean model and hence part of the advection tendency. The contribution from precipitation and evaporation to the C_T advection tendency is here estimated from model output for the mass flux from precipitation and evaporation that causes variations in ocean surface height.

The MOM4p1 ocean model uses a z^* vertical coordinate (Griffies, 2009), where the vertical boundaries of the grid cells throughout the water column shift with variations in ocean surface height. In the open ocean, where the ocean component has up to 50 vertical levels, variations in height of the surface grid cell are much smaller than the variations in ocean surface height due to precipitation and evaporation. The mean change in surface grid cell height between two days is on global average only 7% of the change in ocean surface height from precipitation and evaporation, with values smaller than 7% in the open ocean. Due to the comparably small variations, the surface grid cell height h_1 is assumed to be constant in the following. When the ocean surface height increases by Δh due to net precipitation ($\Delta h > 0$), the bottom face of the surface grid cell is shifted upwards approximately by Δh . Carbon is removed from the surface grid cell, because it is now contained in the grid cell below. The carbon concentration in the surface grid cell is reduced by the ratio between the change in ocean surface height and grid cell height, $\Delta C_T = -\Delta h/h_1 \cdot C_T$. When the ocean surface decreases by Δh due to net evaporation ($\Delta h < 0$), the bottom face of the surface grid cell is shifted downwards by Δh , transporting carbon from the grid cell below to the surface grid cell. Assuming C_T to be similar between the surface grid cell and that below, C_T increases by $-\Delta h/h_1 \cdot C_T$. In summary, the change in C_T due to precipitation and evaporation is approximated by

$$\Delta C_{T,pme} \simeq -\frac{\Delta h}{h_1} C_T, \quad (5.8)$$

with $\Delta h > 0$ if precipitation minus evaporation (pme) is positive and $\Delta h < 0$ if precipitation minus evaporation is negative. The mean contributions to $[H^+]$ extreme event buildup and decay from pme-driven changes in C_T anomaly are shown in Appendix Fig. 5.10b, c.

References

- Anderson, J. L., Balaji, V., Broccoli, A. J., Cooke, W. F., Delworth, T. L., Dixon, K. W., Donner, L. J., Dunne, K. A., Freidenreich, S. M., Garner, S. T., Gudgel, R. G., Gordon, C. T., Held, I. M., Hemler, R. S., Horowitz, L. W., Klein, S. A., Knutson, T. R., Kushner, P. J., Langenhost, A. R., Cheung, L. N., Liang, Z., Malyshev, S. L., Milly, P. C. D., Nath, M. J., Ploshay, J. J., Ramaswamy, V., Schwarzkopf, M. D., Shevliakova, E., Sirutis, J. J., Soden, B. J., Stern, W. F., Thompson, L. A., Wilson, R. J., Wittenberg, A. T., & Wyman, B. L., 2004. The new GFDL global atmosphere and land model AM2-LM2: Evaluation with prescribed SST simulations, *Journal of Climate*, 17(24), 4641–4673.
- Bednaršek, N., Tarling, G. A., Bakker, D. C. E., Fielding, S., Jones, E. M., Venables, H. J., Ward, P., Kuzirian, A., Lézé, B., Feely, R. A., & Murphy, E. J., 2012. Extensive dissolution of live pteropods in the southern ocean, *Nature Geoscience*, 5, 881–885.
- Bednaršek, N., Feely, R. A., Reum, J. C. P., Peterson, B., Menkel, J., Alin, S. R., & Hales, B., 2014. *Limacina helicina* shell dissolution as an indicator of declining habitat suitability owing to ocean acidification in the california current ecosystem, *Proceedings of the Royal Society B: Biological Sciences*, 281(1785), 20140123.
- Bindoff, N., Cheung, W., Kairo, J., Aristegui, J., Guinder, V., Hallberg, R., Hilmi, N., Jiao, N., Karim, M., Levin, L., O'Donoghue, S., Purca Cuicapusa, S., Rinkevich, B., Suga, T., Tagliabue, A., & Williamson, P., 2019. Chapter 5: Changing ocean, marine ecosystems, and dependent communities, *IPCC Special Report on the Ocean and Cryosphere (SROCC)*.
- Burger, F. A., John, J. G., & Frölicher, T. L., 2020. Increase in ocean acidity variability and extremes under increasing atmospheric CO₂, *Biogeosciences*, 17(18), 4633–4662.
- Caldeira, K. & Wickett, M. E., 2003. Anthropogenic carbon and ocean pH, *Nature*, 425(6956), 365–365.
- Canadell, J. G., Monteiro, P. M. S., Costa, M. H., Cotrim da Cunha, L., Cox, P. M., Eliseev, A. V., Henson, S., Ishii, M., Jaccard, S., Koven, C., Lohila, A., Patra, P. K., Piao, S., Rogelj, J., Syampungani, S., Zaehle, S., & Zickfeld, K., 2021. Global carbon and other biogeochemical cycles and feedbacks, *Climate Change 2021: The Physical Science Basis. Contribution of Working Group I to the Sixth Assessment Report of the Intergovernmental Panel on Climate Change [Masson-Delmotte, V., P. Zhai, A. Pirani, S. L. Connors, C. Péan, S. Berger, N. Caud, Y. Chen, L. Goldfarb, M. I. Gomis, M. Huang, K. Leitzell, E. Lonnoy, J.B.R. Matthews, T. K. Maycock, T. Waterfield, O. Yelekçi, R. Yu and B. Zhou (eds.)]*. Cambridge University Press. In Press.
- Colella, P. & Woodward, P. R., 1984. The piecewise parabolic method (PPM) for gas-dynamical simulations, *Journal of Computational Physics*, 54(1), 174–201.
- Deser, C., Alexander, M. A., Xie, S.-P., & Phillips, A. S., 2010. Sea surface temperature variability: Patterns and mechanisms, *Annual Review of Marine Science*, 2(1), 115–143.
- Doney, S. C., Fabry, V. J., Feely, R. A., & Kleypas, J. A., 2009a. Ocean acidification: The other CO₂ problem, *Annual Review of Marine Science*, 1(1), 169–192.
- Doney, S. C., Lima, I., Feely, R. A., Glover, D. M., Lindsay, K., Mahowald, N., Moore, J. K., & Wanninkhof, R., 2009b. Mechanisms governing interannual variability in upper-ocean inorganic carbon system and air–sea CO₂ fluxes: Physical climate and atmospheric dust, *Deep Sea Research Part II: Topical Studies in Oceanography*, 56(8), 640–655.
- Doney, S. C., Busch, D. S., Cooley, S. R., & Kroeker, K. J., 2020. The impacts of ocean acidification on marine ecosystems and reliant human communities, *Annual Review of Environment and Resources*, 45(1), 83–112.
- Dunne, J. P., John, J. G., Adcroft, A. J., Griffies, S. M., Hallberg, R. W., Shevliakova, E., Stouffer, R. J., Cooke, W., Dunne, K. A., Harrison, M. J., Krasting, J. P., Malyshev, S. L., Milly, P. C. D., Philipps, P. J., Sentman, L. T., Samuels, B. L., Spelman, M. J., Winton, M., Wittenberg, A. T., & Zadeh, N., 2012. GFDL's ESM2 global coupled climate–carbon earth system models. Part I: Physical formulation and baseline simulation characteristics, *Journal of Climate*, 25(19), 6646–6665.
- Dunne, J. P., John, J. G., Shevliakova, E., Stouffer, R. J., Krasting, J. P., Malyshev, S. L., Milly, P. C. D., Sentman, L. T., Adcroft, A. J., Cooke, W., Dunne, K. A., Griffies, S. M., Hallberg, R. W., Harrison, M. J., Levy, H., Wittenberg, A. T., Phillips, P. J., & Zadeh, N., 2013. GFDL's ESM2 global coupled climate–carbon earth system models. Part II: Carbon system formulation and baseline simulation characteristics, *Journal of Climate*, 26(7), 2247–2267.
- Eppley, R. W., 1972. Temperature and phytoplankton growth in the sea, *Fish. Bull.*, 70, 41063–41085.

- Fassbender, A. J., Rodgers, K. B., Palevsky, H. I., & Sabine, C. L., 2018. Seasonal asymmetry in the evolution of surface ocean $p\text{CO}_2$ and pH thermodynamic drivers and the influence on sea-air CO_2 flux, *Global Biogeochemical Cycles*, 32(10), 1476–1497.
- Fox-Kemper, B., Ferrari, R., & Hallberg, R., 2008. Parameterization of Mixed Layer Eddies. Part I: Theory and Diagnosis, *Journal of Physical Oceanography*, 38(6), 1145–1165.
- Friedlingstein, P., O'Sullivan, M., Jones, M. W., Andrew, R. M., Hauck, J., Olsen, A., Peters, G. P., Peters, W., Pongratz, J., Sitch, S., Le Quéré, C., Canadell, J. G., Ciais, P., Jackson, R. B., Alin, S., Aragão, L. E. O. C., Arneeth, A., Arora, V., Bates, N. R., Becker, M., Benoit-Cattin, A., Bittig, H. C., Bopp, L., Bultan, S., Chandra, N., Chevallier, F., Chini, L. P., Evans, W., Florentie, L., Forster, P. M., Gasser, T., Gehlen, M., Gilfillan, D., Gkritzalis, T., Gregor, L., Gruber, N., Harris, I., Hartung, K., Haverd, V., Houghton, R. A., Ilyina, T., Jain, A. K., Joetzjer, E., Kadono, K., Kato, E., Kitidis, V., Korsbakken, J. I., Landschützer, P., Lefèvre, N., Lenton, A., Lienert, S., Liu, Z., Lombardozzi, D., Marland, G., Metzl, N., Munro, D. R., Nabel, J. E. M. S., Nakaoka, S.-I., Niwa, Y., O'Brien, K., Ono, T., Palmer, P. I., Pierrot, D., Poulter, B., Resplandy, L., Robertson, E., Rödenbeck, C., Schwinger, J., Séférian, R., Skjelvan, I., Smith, A. J. P., Sutton, A. J., Tanhua, T., Tans, P. P., Tian, H., Tilbrook, B., van der Werf, G., Vuichard, N., Walker, A. P., Wanninkhof, R., Watson, A. J., Willis, D., Wiltshire, A. J., Yuan, W., Yue, X., & Zaehle, S., 2020. Global carbon budget 2020, *Earth System Science Data*, 12(4), 3269–3340.
- Frölicher, T. L., Ramseyer, L., Raible, C. C., Rodgers, K. B., & Dunne, J., 2020. Potential predictability of marine ecosystem drivers, *Biogeosciences*, 17(7), 2061–2083.
- Gnanadesikan, A., Dunne, J. P., & John, J., 2012. Understanding why the volume of suboxic waters does not increase over centuries of global warming in an earth system model, *Biogeosciences*, 9(3), 1159–1172.
- Griffies, S., 2009. Elements of MOM4p1, GFDL ocean group technical report no.6, NOAA/Geophysical Fluid Dynamics Laboratory, Princeton University Forrestal Campus, 201 Forrestal Road, Princeton, NJ 08540-6649.
- Griffies, S. M., Winton, M., Anderson, W. G., Benson, R., Delworth, T. L., Dufour, C. O., Dunne, J. P., Goddard, P., Morrison, A. K., Rosati, A., Wittenberg, A. T., Yin, J., & Zhang, R., 2015. Impacts on ocean heat from transient mesoscale eddies in a hierarchy of climate models, *Journal of Climate*, 28(3).
- Gruber, N., Boyd, P. W., Frölicher, T. L., & Vogt, M., 2021. Ocean biogeochemical extremes and compound events, *Nature*, in review.
- Hagens, M. & Middelburg, J. J., 2016. Attributing seasonal pH variability in surface ocean waters to governing factors, *Geophysical Research Letters*, 43(24), 12,528–12,537.
- Hauri, C., Gruber, N., McDonnell, A. M. P., & Vogt, M., 2013. The intensity, duration, and severity of low aragonite saturation state events on the california continental shelf, *Geophysical Research Letters*, 40(13), 3424–3428.
- Hobday, A. J., Alexander, L. V., Perkins, S. E., Smale, D. A., Straub, S. C., Oliver, E. C., Benthuyssen, J. A., Burrows, M. T., Donat, M. G., Feng, M., Holbrook, N. J., Moore, P. J., Scannell, H. A., Sen Gupta, A., & Wernberg, T., 2016. A hierarchical approach to defining marine heatwaves, *Progress in Oceanography*, 141, 227–238.
- Hofmann, G. E., Smith, J. E., Johnson, K. S., Send, U., Levin, L. A., Micheli, F., Paytan, A., Price, N. N., Peterson, B., Takeshita, Y., Matson, P. G., Crook, E. D., Kroeker, K. J., Gambi, M. C., Rivest, E. B., Frieder, C. A., Yu, P. C., & Martz, T. R., 2011. High-frequency dynamics of ocean pH: A multi-ecosystem comparison, *PloS One*, 6(12), 1–11.
- Jiang, L.-Q., Carter, B. R., Feely, R. A., Lauvset, S. K., & Olsen, A., 2019. Surface ocean pH and buffer capacity: past, present and future, *Scientific Reports*, 9(1), 18624.
- Khatiwal, S., Tanhua, T., Mikaloff Fletcher, S., Gerber, M., Doney, S. C., Graven, H. D., Gruber, N., McKinley, G. A., Murata, A., Ríos, A. F., & Sabine, C. L., 2013. Global ocean storage of anthropogenic carbon, *Biogeosciences*, 10(4), 2169–2191.
- Kroeker, K. J., Kordas, R. L., Crim, R., Hendriks, I. E., Ramajo, L., Singh, G. S., Duarte, C. M., & Gattuso, J.-P., 2013. Impacts of ocean acidification on marine organisms: quantifying sensitivities and interaction with warming, *Global Change Biology*, 19(6), 1884–1896.
- Large, W. G., McWilliams, J. C., & Doney, S. C., 1994. Oceanic vertical mixing: A review and a model with a nonlocal boundary layer parameterization, *Reviews of Geophysics*, 32(4), 363–403.

- Lee, H.-C., Rosati, A., & Spelman, M. J., 2006. Barotropic tidal mixing effects in a coupled climate model: Oceanic conditions in the northern atlantic, *Ocean Modelling*, 11(3), 464–477.
- Leinweber, A. & Gruber, N., 2013. Variability and trends of ocean acidification in the southern california current system: A time series from santa monica bay, *Journal of Geophysical Research: Oceans*, 118(7), 3622–3633.
- Lovenduski, N. S., Gruber, N., Doney, S. C., & Lima, I. D., 2007. Enhanced CO₂ outgassing in the southern ocean from a positive phase of the southern annular mode, *Global Biogeochemical Cycles*, 21(2).
- Manizza, M., Le Quéré, C., Watson, A. J., & Buitenhuis, E. T., 2005. Bio-optical feedbacks among phytoplankton, upper ocean physics and sea-ice in a global model, *Geophysical Research Letters*, 32(5).
- Marshall, J., Hill, C., Perelman, L., & Adcroft, A., 1997. Hydrostatic, quasi-hydrostatic, and nonhydrostatic ocean modeling, *Journal of Geophysical Research: Oceans*, 102(C3), 5733–5752.
- Najjar, R. & Orr, J., 1998. Design of OCMIP-2 simulations of chlorofluorocarbons, the solubility pump and common biogeochemistry, internal OCMIP report, LSCE/CEA Saclay, Gif-sur-Yvette, France.
- Orr, J. C. & Epitalon, J.-M., 2015. Improved routines to model the ocean carbonate system: mocsy 2.0, *Geoscientific Model Development*, 8(3), 485–499.
- Orr, J. C., Fabry, V. J., Aumont, O., Bopp, L., Doney, S. C., Feely, R. A., Gnanadesikan, A., Gruber, N., Ishida, A., Joos, F., Key, R. M., Lindsay, K., Maier-Reimer, E., Matear, R., Monfray, P., Mouchet, A., Najjar, R. G., Plattner, G.-K., Rodgers, K. B., Sabine, C. L., Sarmiento, J. L., Schlitzer, R., Slater, R. D., Totterdell, I. J., Weirig, M.-F., Yamanaka, Y., & Yool, A., 2005. Anthropogenic ocean acidification over the twenty-first century and its impact on calcifying organisms, *Nature*, 437(7059), 681–686.
- Orr, J. C., Epitalon, J.-M., Dickson, A. G., & Gattuso, J.-P., 2018. Routine uncertainty propagation for the marine carbon dioxide system, *Marine Chemistry*, 207, 84 – 107.
- Palter, J. B., Griffies, S. M., Samuels, B. L., Galbraith, E. D., Gnanadesikan, A., & Klocker, A., 2014. The deep ocean buoyancy budget and its temporal variability, *Journal of Climate*, 27(2), 551 – 573.
- Rhein, M., Rintoul, S., Aoki, S., Campos, E., Chambers, D., Feely, R., Gulev, S., Johnson, G., Josey, S., Kostianoy, A., Mauritzen, C., Roemmich, D., Talley, L., & Wang, F., 2013. Observations: Ocean, *Climate Change 2013: The Physical Science Basis. Contribution of Working Group I to the Fifth Assessment Report of the Intergovernmental Panel on Climate Change [Stocker, T.F., D. Qin, G.-K. Plattner, M. Tignor, S.K. Allen, J. Boschung, A. Nauels, Y. Xia, V. Bex and P.M. Midgley (eds.)]. Cambridge University Press, Cambridge, United Kingdom and New York, NY, USA.*
- Shevliakova, E., Pacala, S. W., Malyshev, S., Hurtt, G. C., Milly, P. C. D., Caspersen, J. P., Sentman, L. T., Fisk, J. P., Wirth, C., & Crevoisier, C., 2009. Carbon cycling under 300 years of land use change: Importance of the secondary vegetation sink, *Global Biogeochemical Cycles*, 23(2), 1–16.
- Simmons, H. L., Jayne, S. R., Laurent, L. C., & Weaver, A. J., 2004. Tidally driven mixing in a numerical model of the ocean general circulation, *Ocean Modelling*, 6(3), 245–263.
- Spisla, C., Taucher, J., Bach, L. T., Haunost, M., Boxhammer, T., King, A. L., Jenkins, B. D., Wallace, J. R., Ludwig, A., Meyer, J., Stange, P., Minutolo, F., Lohbeck, K. T., Nauendorf, A., Kalter, V., Lischka, S., Sswat, M., Dörner, I., Ismar-Rebitz, S. M. H., Aberle, N., Yong, J. C., Bouquet, J.-M., Lechtenböcker, A. K., Kohnert, P., Krudewig, M., & Riebesell, U., 2021. Extreme levels of ocean acidification restructure the plankton community and biogeochemistry of a temperate coastal ecosystem: A mesocosm study, *Frontiers in Marine Science*, 7, 1240.
- Terhaar, J., Orr, J. C., Ethé, C., Regnier, P., & Bopp, L., 2019. Simulated arctic ocean response to doubling of riverine carbon and nutrient delivery, *Global Biogeochemical Cycles*, 33(8), 1048–1070.
- Torres, O., Kwiatkowski, L., Sutton, A. J., Dorey, N., & Orr, J. C., 2021. Characterizing mean and extreme diurnal variability of ocean CO₂ system variables across marine environments, *Geophysical Research Letters*, 48(5), e2020GL090228.
- Turi, G., Alexander, M., Lovenduski, N. S., Capotondi, A., Scott, J., Stock, C., Dunne, J., John, J., & Jacox, M., 2018. Response of O₂ and pH to ENSO in the california current system in a high-resolution global climate model, *Ocean Science*, 14(1), 69–86.
- Vogt, L., Burger, F. A., & Frölicher, T. L., in preperation. Marine heatwave drivers in an earth system model, *Geophysical Research Letters*.

-
- Wanninkhof, R., 1992. Relationship between wind speed and gas exchange over the ocean, *Journal of Geophysical Research: Oceans*, 97(C5), 7373–7382.
- Weiss, R., 1974. Carbon dioxide in water and seawater: the solubility of a non-ideal gas, *Marine Chemistry*, 2(3), 203 – 215.
- Winton, M., 2000. A reformulated three-layer sea ice model, *Journal of Atmospheric and Oceanic Technology*, 17(4), 525–531.
- Xue, L., Cai, W.-J., Jiang, L.-Q., & Wei, Q., 2021. Why are surface ocean pH and CaCO_3 saturation state often out of phase in spatial patterns and seasonal cycles?, *Global Biogeochemical Cycles*, 35(7), e2021GB006949.

Chapter 6

Discussion and outlook

6.1 Summary and discussion of the main results

In the previous chapters, extreme events in hydrogen ion concentration ($[\text{H}^+]$; Chapters 3 to 5) and in aragonite saturation state (Ω_{A} ; Chapter 3) have been analyzed for the first time at the global scale. These variables are known to be important stressors for marine organisms, especially for shell-forming organisms such as plankton, mollusks, echinoderms and corals (Orr et al., 2005; Doney et al., 2009; Kroeker et al., 2013). The analyses focused on preindustrial characteristics of $[\text{H}^+]$ and Ω_{A} extremes at surface and subsurface (Chapter 3), their physical and biogeochemical drivers (Chapter 5), as well as changes in extreme event occurrence and characteristics due to climate change (Chapter 3). The occurrence likelihood for compound extreme events in temperature and $[\text{H}^+]$ was also analyzed and changes in such compound extreme events under climate change were simulated and quantified (Chapter 4). The main results of Chapters 3 to 5 are summarized and discussed in the following.

Simulated characteristics of extreme events in $[\text{H}^+]$ and Ω_{A}

Based on simulations by the GFDL ESM2M model, the preindustrial characteristics of high $[\text{H}^+]$ and low Ω_{A} extremes were described in Chapter 3. Globally, simulated preindustrial extremes in surface $[\text{H}^+]$ based on fixed local 99th percentiles lasted on average 11 d with an average maximal intensity of $0.08 \text{ nmol kg}^{-1}$ (Table 2 in Chapter 3). Many of these events lasted only a few days. For example, 43 % of events lasted less than five days. Longer events tend to be also more intense. Excluding events with duration of less than five days, the average mean intensity increases by 41 % and the average maximal intensity increases by 46 %. Regionally, high $[\text{H}^+]$ events were found to be particularly long-lasting and intense in the tropical Pacific and in the Southern Ocean and the North Pacific (Chapter 3 Fig. A3). Long-lasting events were also simulated in the sea ice regions of the Arctic Ocean. Preindustrial extremes in aragonite saturation state lasted on average 20 d, with an average maximal intensity of 0.003 units (Table A1 in Chapter 3). The larger duration of aragonite saturation state extremes relative to $[\text{H}^+]$ extremes is connected to the more pronounced dependence of Ω_{A} on C_{T} and A_{T} compared to $[\text{H}^+]$ that is especially sensitive to temperature variations. This is because simulated variability in C_{T} and A_{T} has larger contributions from variations on long timescales compared to temperature. For example, the global simulated preindustrial fraction of interannual-to-decadal variance to total variance is 36 % for C_{T} and 56 % for A_{T} , while it is only 12 % for temperature.

Simulated preindustrial extreme events have also been analyzed at subsurface. The 200 m depth layer was chosen to exemplify extreme events in the seasonal thermocline. Events in $[\text{H}^+]$

and also in Ω_A were found to be more intense and in particular also more long-lasting at 200 m depth compared to the surface. At depth, events in both variables last almost 40 d on average. Intensity only slightly increases for Ω_A (globally +14 % at 200 m compared to the surface), while it increases sharply for $[H^+]$ (+113 %). This is because larger decreases in variance between the surface and 200 m depth are simulated for temperature (-86 %) than for C_T (-68 %). Due to the larger decrease in temperature variability, variations in $[H^+]$ from variations in C_T are less attenuated by opposing variations in temperature, resulting in larger variability for $[H^+]$ and larger event intensity. Also variations in A_T and salinity become less important at depth (90 % decrease in variance in both cases). The more pronounced role of C_T for $[H^+]$ at depth compared to at the surface implies that the drivers of $[H^+]$ and Ω_A extremes become more similar at depth compared to the surface. As a result, spatial patterns of intensity and duration of $[H^+]$ and Ω_A extremes become more similar at depth. Pattern correlation for mean intensity of $[H^+]$ and Ω_A extremes increases from 0.27 at the surface to 0.66 at 200 m depth, and pattern correlation for duration of $[H^+]$ and Ω_A extremes increases from 0.60 to 0.89. The similarity of the drivers is also reflected in the similar average event duration for both variables at depth. Regional differences in variability and event intensity are much more pronounced at depth compared to at the surface. Simulated event intensity for $[H^+]$ and Ω_A at 200 m depth is largest in tropical and subtropical regions.

Driving processes of extreme events in $[H^+]$

In Chapter 5, the driving processes of surface $[H^+]$ extreme events (also called *OAX events*) were analyzed. $[H^+]$ anomalies were decomposed into a temperature and a carbon term, which were then further decomposed into several temperature and carbon tendency terms. In this chapter, extremes were defined with respect to seasonally varying thresholds (Chapter 2.3.1) to separate the processes driving the seasonal cycles in temperature, C_T , and $[H^+]$ from those driving the anomalies that result in the occurrence of unusually high $[H^+]$. Under this definition, extremes arise when $[H^+]$ anomalies, driven by anomalies in temperature and C_T , cross a seasonally varying threshold.

During $[H^+]$ extreme event buildup (i.e., the period between the onset and peak of an extreme event), increases in $[H^+]$ anomaly result mainly from increases in temperature anomaly. Regionally, temperature is the most important driver of event buildup in most open-ocean regions aside from the tropical Pacific and the western boundary current regions of the North Pacific and North Atlantic. In the low-to-mid latitudes and particularly in the subtropics, these temperature increases are mainly due to positive anomalies in air-sea heat fluxes (Fig. 5.3b in Chapter 5). In the subtropics, surface waters usually lose heat to the atmosphere. However, during the $[H^+]$ extremes, surface heat fluxes are close to zero or slightly positive. The reduced heat loss to the atmosphere may be connected to reduced turbulent heat loss from sensible and latent heat fluxes or to changes in shortwave and longwave radiative fluxes (Bond et al., 2015). Co-occurring decreases in wind stress during event buildup in these regions indicate that reductions in turbulent heat loss play an important role in driving the positive anomalies in air-sea heat fluxes (Bond et al., 2015). Yet, a co-occurring increase in shortwave radiation may be important, too. In the high latitudes, increases in temperature anomaly during $[H^+]$ event buildup mainly result from positive anomalies in vertical diffusion and mixing of temperature (Fig. 5.3h in Chapter 5). In 43 % of the high latitude regions ($> 45^\circ$ latitude) of the North Atlantic, North Pacific, and Southern Ocean, vertical diffusion and mixing transport heat to the surface during event buildup¹. There, enhanced wind stress is likely the cause of the increases in vertical mixing and

¹Due to the seasonal variations in vertical temperature gradients and hence the sign of vertical diffusion of temperature, one can expect seasonal differences in the role of vertical diffusion. Increases in surface temperature

surface temperature. Reductions in convective vertical mixing limit the increase in temperature during $[H^+]$ event buildup (Fig. 5.3k in Chapter 5), in particular in the subtropical regions where large positive anomalies in surface heat flux are simulated. Convective vertical mixing normally balances heat loss to the atmosphere by upwards heat transport. It is thus strongly reduced when surface heat loss is close to zero, such as during $[H^+]$ event buildup in the subtropics.

Variations in C_T were found to be less important for event buildup than temperature variations in 84 % of the ocean. However, C_T variations were identified as the main driver in the tropical Pacific. There, large positive anomalies in the advective flux of C_T are simulated (Fig. 5.4e in Chapter 5). These are likely due to increased upwelling of carbon-rich subsurface waters, such as during La Niña phases of the El Niño Southern Oscillation (ENSO). In the subtropics, a decrease in vertical diffusion of C_T often reduces surface C_T , thereby opposing the effect of the temperature increases from reduced vertical diffusion of heat. The decrease in vertical diffusion and mixing may be again connected to the reductions in wind stress during the event built-up in subtropical regions. In contrast, increases in upward transport of C_T by vertical diffusion and mixing in high-latitude regions increase C_T and may be driven by enhanced wind stress. These C_T increases are compensated by large negative anomalies in air-sea gas exchange that are caused by the positive anomalies in pCO_2 during the $[H^+]$ extreme events. Negative anomalies in air-sea gas exchange are simulated almost everywhere in the ocean, with the largest negative anomalies in high-latitude regions. There, extremes in $[H^+]$ are especially intense and the associated pCO_2 anomalies particularly large. Furthermore, simulated mean wind stress is larger in these high latitude regions compared to the low and mid latitudes. As a result, also gas transfer velocity, which is proportional to squared wind speed in the model (Wanninkhof, 1992), is larger in these regions. Biological activity generally decreases surface C_T and $[H^+]$, because biological production outweighs microbial decomposition at the surface. During the buildup of $[H^+]$ events, biological activity decreases surface C_T in the tropical regions. There, coinciding increases in surface nitrate indicate a higher primary productivity from increased nutrient availability. Convective mixing of C_T , which normally reduces surface C_T in the extratropics, is less active during $[H^+]$ event buildup and thus increasing C_T anomaly.

That C_T is overall less important for event buildup than temperature is likely connected to the net loss of carbon by air-sea flux, either by intensified outgassing where oceanic pCO_2 is usually higher than atmospheric pCO_2 or by decreased uptake where oceanic pCO_2 is usually lower. This loss of carbon is particularly important in the high latitudes. In the Southern Ocean for example, it causes a decrease in $[H^+]$ that is as large as the overall increase in $[H^+]$ during the event buildup. Air-sea gas exchange is likely to be less important before the onset of $[H^+]$ extreme events, because also pCO_2 is lower before event onset. This implies that C_T may be more important for increasing $[H^+]$ to the extreme event threshold than it is for increasing $[H^+]$ from the threshold to the peak of the event. In fact, the overall $[H^+]$ anomaly during the extremes that also includes $[H^+]$ increases before event onset was found to be globally more driven by increased C_T (60 % globally) than by increased temperature (37 %; Fig. 5.6 in Chapter 5). A future study could extend the framework from Chapter 5 to look at the driving processes of $[H^+]$ increases before event onset.

During $[H^+]$ extreme event decay (the period between event peak and the end of the event), decreases in $[H^+]$ anomaly result to a similar extent from decreases in temperature anomaly and in C_T anomaly. Reductions in temperature anomaly tend to be more important in subtropical regions, while decreases in C_T anomaly tend to be more important in the mid-to-high latitudes and the tropical regions. The decreases in temperature anomaly in the subtropics are mainly caused by a revitalization of heat losses to the atmosphere. Furthermore, heat losses due to

from vertical diffusion are most likely to occur in winter when positive temperature gradients are prevalent.

vertical diffusion increase again, which is likely connected to a return of wind stress to the normal level. Decreases in C_T again follow in all oceans from negative anomalies in air-sea gas exchange due to still elevated $p\text{CO}_2$, in particular in the mid-to-high latitudes.

Changes in extreme event characteristics under climate change

The simulated changes in extreme event characteristics for $[\text{H}^+]$ and Ω_A between 1861 and 2100 under two different greenhouse gas emissions scenarios have been analyzed in Chapter 3. Increases in mean concentrations and changes in variability have been identified as the main causes for changes in extremes. To analyze the contributions from these two causes, extreme events in the historical ensemble simulation and the RCP8.5/RCP2.6 ensemble simulations were defined relative to two baselines: a fixed preindustrial baseline, and a shifting-mean baseline. The fixed baseline is expected to be most useful for organisms with low capability to adapt to ocean acidification and that can not migrate to regions with reduced stress from ocean acidification. The shifting-mean baseline, on the other hand, is expected to be more useful for mobile organisms and for those that can adapt to the ocean acidification trends.

Under the fixed preindustrial baseline (Chapter 2.3.1), changes in extreme event characteristics arise mainly due to the secular ocean acidification trends, increasing $[\text{H}^+]$ and decreasing Ω_A . These trends are mainly due to an increase in upper ocean C_T from the oceanic uptake of anthropogenic carbon. The trends in $[\text{H}^+]$ and Ω_A are large compared to natural variability in the variables. This has been shown in earlier studies using the time of emergence framework (Keller et al., 2014; Frölicher et al., 2016; Henson et al., 2016; Schlunegger et al., 2019; Bindoff et al., 2019). Keller et al. (2014), for example, analyzed the time of emergence for surface pH, defining it as the point in time when a trend exceeds two times the standard deviation of natural variability. They found that the trend in pH emerges from the natural variability already after 12 years over most of the ocean in historical simulations. Likewise, Schlunegger et al. (2019) found that 50 % of ocean grid cells emerged after 16 years for Ω_A compared to 8 years for pH. Hence, time of emergence for Ω_A is slightly delayed compared to that for pH. Nonetheless, it is shorter than that of other biogeochemical or physical ocean variables despite $p\text{CO}_2$ (Schlunegger et al., 2019). The short time of emergence for $[\text{H}^+]$ and Ω_A manifests in rapid increases in extreme event occurrence over the historical period when extremes are referenced to fixed preindustrial 99th percentile thresholds. By year 2030 and under the RCP8.5 scenario, the ESM2M model projects a global near-permanent extreme state for surface $[\text{H}^+]$ where globally more than 360 d per year are under extreme conditions. Similarly but with a slight delay, such a near-permanent extreme state is projected for surface Ω_A by year 2062. Near-permanent extreme states are also projected at 200 m depth in years 2049 and 2074 for $[\text{H}^+]$ and Ω_A , respectively.

Pronounced, although smaller changes in extreme event occurrence were also found when defining extremes relative to a shifting-mean baseline (Chapter 2.3.1). The shifting-mean baseline adjusts the thresholds for the acidification trends, so that the latter do not alter extreme event characteristics. Instead, changes in variability are the main cause for changes in extreme events. Variability in $[\text{H}^+]$ and Ω_A is expected to change with ocean acidification and warming, because $[\text{H}^+]$ and Ω_A depend non-linearly on the driving variables (e.g., approximated $[\text{H}^+]$ in Eq. (1.10)). The sensitivities of $[\text{H}^+]$ and Ω_A to variations in the drivers thus depend on the mean states of the drivers (e.g., Eq. (6.1)). For $[\text{H}^+]$, large increases in variability and therefore in the numbers of extreme event days are simulated by the ESM2M model under climate change at the global scale. At the surface, the number of extreme event days per year increases from 3.65 d during the

preindustrial period to about 50 d during the period 2081-2100 under the RCP8.5 scenario, due to a quadrupling of $[\text{H}^+]$ variance between the two periods. Most of the variance increase is due to increases in $[\text{H}^+]$ seasonality (87 % of the total variance change). The rise in variance is mainly driven by increases in mean surface C_T that make $[\text{H}^+]$ more sensitive to variations in its drivers. The sensitivity is further increased by reductions in mean A_T due to surface freshening in the high latitudes (Chapter 3 Fig. 9) and slightly reduced by increases in A_T in the low-to-mid latitudes, in particular in the Atlantic Ocean (Chapter 3 Fig. A5). In particular in the high latitudes, the increase in $[\text{H}^+]$ variance is dampened by simulated reductions in variability of C_T (Chapter 3 Fig. A6). Similar, although smaller changes in extremes relative to a shifting-mean baseline were found at 200 m depth. The number of extreme event days per year is projected to increase globally from 3.65 d to 32 d by the end of the 21st century under RCP8.5. This increase is connected to a 36 % rise in $[\text{H}^+]$ variance that is mostly caused by increases in interannual and seasonal variability (42 % and 37 % of total variance increase, respectively). The increase in event duration of 61 d is larger than at the surface (+21 d), likely reflecting the more pronounced role of increases in interannual variability at depth. The increases in $[\text{H}^+]$ variability at depth result from the balance between the amplifying effect from increases in mean C_T and the attenuating effect from co-occurring decreases in C_T variability.

Unlike for $[\text{H}^+]$, a decrease in extreme event occurrence is simulated for Ω_A when extremes are defined relative to a shifting-mean baseline. This decrease in extremes results from a decrease in Ω_A variability. Variability in Ω_A decreases for two reasons. First, the sensitivity of Ω_A to variations in temperature, C_T , A_T , and salinity decreases as Ω_A itself decreases with the rise in anthropogenic carbon in the ocean (Chapter 3 Fig. 11). Second, also the simulated decreases in C_T variability in the mid to high latitudes at the surface and in particular at 200 m depth strongly reduce Ω_A variability. These reductions in C_T variability are the major driver of reductions in Ω_A variability at depth (Chapter 3 Fig. 11b). The simulated decreases in variability of C_T are linked to changes in the underlying physical and biogeochemical processes that cause C_T variability (Chapter 5). For example, it has been shown in Chapter 5 that advective C_T fluxes, such as due to upwelling, are the dominating driver of C_T increases during $[\text{H}^+]$ extremes in the equatorial Pacific. More general, variance in the C_T advection tendency in the ESM2M model is larger than the variances in the other C_T tendency terms in this region at preindustrial times. It is thus expected that the simulated decreases in C_T variability in the equatorial Pacific are connected to decreases in advective C_T variability, possibly connected to a decrease in upwelling.

Present day patterns and trends in the occurrence of compound T- $[\text{H}^+]$ extremes

In Chapter 4, compound extreme events in sea surface temperature (SST) and sea surface $[\text{H}^+]$ were analyzed (referred to as marine heatwave ocean acidity extreme events, in short MHW-OAX events). Defining high temperature and $[\text{H}^+]$ extremes relative to seasonally-varying thresholds (Chapter 2.3.1), MHW-OAX events were identified to occur more frequently than expected from chance in the subtropical oceans. In contrast, MHW-OAX events were found to occur less often than expected from chance in the tropical Pacific and in the mid-to-high latitudes. Although the extremes occur independently from the seasonal cycles in SST and $[\text{H}^+]$, this pattern is remarkably similar to the correlation of seasonal variability in SST and $[\text{H}^+]$. In the subtropics, where MHW-OAX events occur frequently, also the seasonal cycles of SST and $[\text{H}^+]$ are strongly correlated². In contrast, the seasonal cycles are negatively correlated in the tropical Pacific and

²As a result, compound MHW-OAX events would also occur most frequently in the subtropics regions when the extremes were defined with respect to fixed percentile thresholds.

the mid-to-high latitudes, where also MHW-OAX events occur seldomly. This indicates that the drivers of seasonal variability in SST and $[\text{H}^+]$ may also be similar to the drivers of variability in the seasonal anomalies of SST and $[\text{H}^+]$. In the subtropics, where the seasonal cycle of $[\text{H}^+]$ mostly follows that of temperature, $[\text{H}^+]$ anomalies co-vary with temperature anomalies as well. As a result, large positive departures in temperature and $[\text{H}^+]$ often fall together and MHW-OAX events occur frequently. In the equatorial Pacific and the mid-to-high latitudes in contrast, where the seasonal cycle of $[\text{H}^+]$ tends to follow that of C_T , also $[\text{H}^+]$ anomalies tend to co-vary with C_T anomalies. Since C_T anomalies most often oppose SST anomalies, positive departures in $[\text{H}^+]$ and SST only seldomly fall together, resulting in a low likelihood for MHW-OAX events.

Changes in MHW-OAX event occurrence were projected with large-ensemble historical and RCP simulations conducted with the ESM2M model (Table A.2). These changes were analyzed with respect to fixed preindustrial baselines, shifting-mean baselines (Chapter 2.3.1), and fully adapting baselines. The large ensemble simulations with 30 ensemble members allowed to identify the forced changes in temperature and $[\text{H}^+]$ to define the shifting-mean baselines. The ensemble distribution for each day allowed to define percentile thresholds for each day under the fully adapting baseline. When defining extremes in SST and $[\text{H}^+]$ relative to fixed preindustrial baselines, MHW-OAX event occurrence is projected to strongly increase. This is because marine heatwaves are projected to become more frequent in the future (Frölicher et al., 2018) and because of the strong increase in $[\text{H}^+]$ extremes with ocean acidification (Chapter 3). With more frequent MHWs and OAX events, also the frequency of events where the two fall together increases. The change in bivariate compound events is generally sensitive to the dependence between the univariate variables. However, already at about 0.3°C global warming, $[\text{H}^+]$ extremes globally occur more than 360 d per year due to the large signal-to-noise ratio for $[\text{H}^+]$ ³. After that, almost every MHW is also an $[\text{H}^+]$ extreme event and hence a MHW-OAX event. Changes in MHW-OAX occurrence are thus independent of the dependence between SST and $[\text{H}^+]$ anomalies after 0.3°C global warming.

Relative to a shifting-mean baseline, MHW-OAX occurrence is also projected to increase. The projected changes are relatively small compared to those with respect to fixed preindustrial baselines. The increases occur mainly due to the increases in $[\text{H}^+]$ variability that result in more frequent $[\text{H}^+]$ extreme events (Chapter 3). Also changes in temperature variability change the frequency of MHWs. For example, an increase in MHWs is simulated in the North Atlantic, the Southern Ocean, and the Arctic Ocean. These are also regions where the seasonality of SST is projected to increase (Alexander et al., 2018). However, the increase in $[\text{H}^+]$ extremes is much larger than that in MHWs (globally 58 days per year and 7 days per year at 2°C global warming, respectively). The increase in MHW-OAX events that results from the increase in $[\text{H}^+]$ extremes varies with the dependence between temperature and $[\text{H}^+]$ anomalies. For example, if temperature and $[\text{H}^+]$ anomalies were independent (likelihood multiplication factor (LMF) of one, defined in Chapter 4), a doubling in $[\text{H}^+]$ extremes would result in a doubling of MHW-OAX events, from 3.65 MHW-OAX days per year to 7.3 MHW-OAX days per year. The relative increase is smaller when SST and $[\text{H}^+]$ anomalies are positively correlated. For example, when assuming SST and $[\text{H}^+]$ anomalies to be described by a bi-variate normal distribution with correlation coefficient of 0.5 (resulting in an LMF of 3.2; Eqs. (4.2) and (4.3)), MHW-OAX event frequency increases by 59 % due to a doubling in $[\text{H}^+]$ extremes, from 11.8 to 18.8 MHW-OAX days per year.

Furthermore, changes in MHW-OAX events relative to a shifting-mean baseline are also influenced by changes in the statistical dependence between SST and $[\text{H}^+]$. When, for example,

³The earlier onset of near-permanent $[\text{H}^+]$ extremes is earlier than reported in Chapter 3, because the signal-to-noise ratio is larger when using seasonally-varying thresholds. Seasonal variability is here included in the threshold definition and does not contribute to extreme event occurrence.

the correlation coefficient of SST and $[\text{H}^+]$ anomalies (again assuming a bivariate normal distribution) decreases from 0.5 to 0.25 while $[\text{H}^+]$ extremes double (and MHWs stay constant), MHW-OAX frequency increases only slightly, from 11.8 to 12.4 MHW-OAX days per year. On the other hand, an increase in correlation coefficient by 0.25 units co-occurring with a doubling in $[\text{H}^+]$ extremes would result in an increase in MHW-OAX frequency from 11.8 to 27.0 MHW-OAX days per year. The influence of dependence changes on MHW-OAX occurrence was isolated by analyzing changes in compound events relative to fully adapting baselines. Under this definition, the frequency of univariate extremes in temperature and $[\text{H}^+]$ does not change. The analysis showed decreases in MHW-OAX occurrence due to the dependence changes in most regions (Fig. 4.4f). These reductions in dependence between SST and $[\text{H}^+]$ anomalies, here quantified by the Pearson correlation coefficient, may be due to the simulated over-proportionally larger increase in the sensitivity of $[\text{H}^+]$ to variations in C_T compared to the sensitivity to variations in temperature (Ext. Data Fig. 4.9; see also Fassbender et al. (2018)). The larger increase in C_T sensitivity arises due to the increases in background C_T from ocean acidification. The effect can be understood based on the simple analytical approximation of $[\text{H}^+]$ given in Eq. (1.10). Calculating the partial derivative of the so approximated $[\text{H}^+]$ with respect to C_T and T , one obtains

$$\frac{\partial[\text{H}^+]}{\partial C_T} = \frac{K_2(\text{S},\text{T})}{A_T} \cdot \frac{1}{(1 - C_T/A_T)^2}; \quad \frac{\partial[\text{H}^+]}{\partial T} = \frac{\partial K_2(\text{S},\text{T})}{\partial T} \cdot \frac{2 \cdot C_T/A_T - 1}{1 - C_T/A_T}. \quad (6.1)$$

Ocean acidification, which increases C_T and the ratio of C_T to A_T , has a larger impact on $\partial[\text{H}^+]/C_T$, which is proportional to $(1 - C_T/A_T)^{-2}$, than on $\partial[\text{H}^+]/T$. Between the preindustrial period and today, surface C_T has globally increased by about $70 \mu\text{mol kg}^{-1}$, corresponding to an increase in C_T to A_T ratio from about 0.86 to 0.89 globally (Gattuso & Hansson, 2011). Based on the approximation from Eq. (6.1), the partial derivatives of $[\text{H}^+]$ with respect to C_T and T increase by 62 % and 38 %, respectively⁴. The stronger increase in sensitivity of $[\text{H}^+]$ to C_T may strengthen the negative C_T contribution to the correlation coefficient of SST and $[\text{H}^+]$ (Fig. 4.2c in Chapter 4) and thereby reduce SST- $[\text{H}^+]$ correlation. Recalling the aforementioned sensitivity of the results under the shifting-mean baseline to changes in dependence, it is apparent that increases in MHW-OAX events relative to shifting-mean baselines would be overall considerably larger without the co-occurring decreases in correlation. However, there are also regions where the correlation of SST and $[\text{H}^+]$ anomalies and MHW-OAX occurrence is projected to increase, such as the equatorial Pacific (Ext. Data Fig. 4.11a and Fig. 4.4f in Chapter 4). There, the increase in correlation may be connected to simulated decreases in variability of C_T (Fig. A6a in Chapter 3) that attenuate the negative C_T contribution to SST- $[\text{H}^+]$ correlation.

The pattern of compound event occurrence in SST and $p\text{CO}_2$ is very similar to that for SST and $p\text{CO}_2$ (Fig. 4.1 and Ext. Data Fig 4.14). The reason is that $[\text{H}^+]$ and $p\text{CO}_2$ are highly positively correlated. This can be understood from the equilibrium relations of carbonate chemistry. Combining Eqs. (1.4) and (1.6), one obtains

$$p\text{CO}_2 = \frac{[\text{HCO}_3^-]}{K_0 K_1} \cdot [\text{H}^+]. \quad (6.2)$$

Partial pressure of CO_2 is almost proportional to $[\text{H}^+]$ at the surface, because the prefactor of $[\text{H}^+]$ in Eq. (6.2) often varies only little (see also Omta et al., 2010; Orr, 2011). This is because relative changes in $[\text{HCO}_3^-]$ are often small in the pH regime of the ocean (Fig. 1.3)⁵,

⁴Using *mocsy 2.0* to calculate the partial derivatives and taking also into account the ocean warming (Gattuso & Hansson, 2011), one obtains smaller but qualitatively similar relative changes of 54 % and 33 %, respectively.

⁵In Fig. 1.3, changes in $[\text{HCO}_3^-]$ due to variations in C_T and A_T are shown. Also relative changes in $[\text{HCO}_3^-]$ due to temperature and salinity variations are small. For example, an increase in temperature from 0°C to 35°C

and because the solubility of CO_2 , K_0 , decreases with temperature and salinity, while the first dissociation constant, K_1 , increases with temperature and salinity (Fig. 1.2). The product $K_0 K_1$ is thus less sensitive to variations in temperature and salinity than K_0 and K_1 themselves.

6.2 Caveats and limitations

A number of caveats and limitations need to be discussed. These are connected to biases in the ESM2M model simulations, the relatively coarse spatial resolution of the ESM2M model, the omission of temporal variability on diurnal timescales, and the choice of carbonate system variables to assess impacts on marine ecosystems.

The robustness of the results in this thesis depends on the skill of the model in representing variations in $[\text{H}^+]$ and Ω_A . Little directly measured data exist to constrain the model results for $[\text{H}^+]$ and Ω_A in this thesis. This is in contrast to sea surface temperature, where satellite measurements of the ocean skin temperature are available on high temporal resolution and with near-global coverage (Reynolds et al., 2007). Available surface ocean CO_2 measurements from ships, drifters, and moorings are, for example, collected in the *Surface Ocean CO_2 Atlas (SOCAT)* (Bakker et al., 2016). However, compared to SST, data coverage is comparably sparse. As a result, more data interpolation is required when mapping the data to global gridded and time-varying fields (Landschützer et al., 2016; Landschützer et al., 2020; Gregor & Gruber, 2021), resulting in comparably high uncertainties, in particular in the Southern Ocean (Gray et al., 2018), and allowing only for monthly-mean temporal resolution.

These data products and additional gridded climatologies, such as from the *Global Ocean Data Analysis Project, Version 2 (GLODAPv2)* (Lauvset et al., 2016; Key et al., 2015) or by Takahashi et al. (2014), were used to constrain simulated characteristics of $[\text{H}^+]$ and Ω_A . Simulated mean pH and $[\text{CO}_3^{2-}]$ (similar to Ω_A) were compared to such observational data (Bopp et al., 2013), finding that pattern correlation between simulated pH (ESM2M model) and observation-based pH is below 0.4, while pattern correlation for $[\text{CO}_3^{2-}]$ is above 0.95. However, the spatial correlation between simulated pH for the ESM2M model and the observational data used in this thesis is larger than that found by Bopp et al. (2013). Simulated mean pH and $[\text{H}^+]$ from a historical and RCP8.5 simulation over the period 1982-2019 (Appendix Table A.2) showed a pattern correlation of 0.76 when compared to the observation-based data set that builds on *MPI-SOMFNN* (Chapter 4; Landschützer et al., 2020). Furthermore, the phasing and amplitude of the seasonal cycles in $[\text{H}^+]$ and Ω_A were compared to observation-based data (Kwiatkowski & Orr, 2018). Seasonal amplitudes of $[\text{H}^+]$ and Ω_A agree with observational climatologies within 20 % at the global scale, but larger biases are simulated regionally. Correlation with the observational climatologies reveals again larger deviations in the phasing of the seasonal cycles for $[\text{H}^+]$ (globally $r = 0.6$) compared to Ω_A ($r = 0.8$), with strong deviations for $[\text{H}^+]$ in the Southern Ocean. In Chapter 3, long-term changes in seasonal amplitude were assessed. While showing a good agreement in the low-to-mid latitudes, the ESM2M model was found to show a negative bias in the trends for $[\text{H}^+]$ and Ω_A in the high latitudes.

Simulated variability on timescales of days to weeks can at most places not be constrained with observational data, because no global observation-based datasets for $[\text{H}^+]$ or Ω_A exist with higher than monthly temporal resolution. Likewise, the roles of the individual physical and biogeochemical processes in driving $[\text{H}^+]$ extremes (Chapter 5) can not be validated with observation-based data, because observational data is not available for ocean interior processes such as mixing and advection. In Chapter 4, it has also been shown that the spatial patterns in

under average present-day conditions for the other drivers results in a 1 % decrease in $[\text{HCO}_3^-]$.

correlation of $[H^+]$ and temperature are similar to observations in the low-to-mid latitudes, but with a simulated positive bias in correlation.

In summary, the comparison to observational data, where available, shows that some biases in Ω_A and in particular $[H^+]$ are simulated, in particular in high-latitude regions. Nonetheless, the ESM2M model overall captures large-scale patterns in the mean states, simulates seasonal cycles in $[H^+]$ and Ω_A that are roughly similar to observed seasonal variations, and captures trends in seasonal variability in most regions. It is thus suitable for the global analyses in this thesis.

Biases in $[H^+]$ and Ω_A are connected to the limitations of the TOPAZv2 model in representing ocean ecology (Dunne et al., 2013), because biological production and remineralization drive variations in dissolved inorganic carbon and alkalinity (Sarmiento & Gruber, 2006) and hence $[H^+]$ and Ω_A . ESM2M coupled to TOPAZv2 globally simulates a positive bias in net primary productivity (NPP) (Sect. 2.1.4). In contrast, the regional differences in NPP are relatively well simulated by ESM2M compared to other CMIP5-era Earth system models (Laufkötter et al., 2015). The global positive bias in NPP may be connected to positively biased surface ocean nitrate and silicate concentrations (globally 21 % and 44 % overestimation of observational estimates, respectively; Laufkötter et al., 2015) that may allow for a too high phytoplankton production. Inaccuracies in simulated production and remineralization may also arise due to the relatively simple oceanic food web representation. TOPAZv2 does not explicitly simulate zooplankton or bacteria, but instead handles zooplankton grazing and bacterial remineralization implicitly. Finally, also the representation of riverine fluxes of biogeochemical tracers is idealized. For example, the ratio between dissolved inorganic carbon and alkalinity in river runoff is assumed to be constant across the globe.

Another potential caveat is the relatively coarse horizontal and vertical resolution of the ocean model incorporated in GFDL ESM2M. The ocean model of ESM2M has a horizontal grid resolution of about 1° . As a result, it does not resolve circulation structures on smaller scales. To represent tracer advection from mesoscale eddies (on horizontal scales of 10 to 100 km), the ocean model MOM4p1 relies on the Gent-McWilliams parameterization (Griffies, 1998). Furthermore, ESM2M uses the parameterization by Fox-Kemper et al. (2008) to represent the tracer advection from eddies on the sub-mesoscale. While global simulations with models that resolve sub-mesoscale features are not feasible, mesoscale circulation is explicitly represented by global models such as the GFDL CM2.6 model with a 0.1° horizontal (about 10 km) resolution for the ocean component. Griffies et al. (2015) found that the mesoscale-eddy-resolving CM2.6 model better matches the satellite-observed sea-level variability that is connected to mesoscale eddy variability and shows lower biases in sea surface and ocean interior temperature compared to model version with lower horizontal ocean resolution. Explicit representation of mesoscale eddies also impacts the transport of biogeochemical tracers (Dufour et al., 2015; Yamamoto et al., 2018) and thus carbonate system variables such as $[H^+]$. Higher model resolution also allows to study variations in biogeochemical variables in coastal oceans (Turi et al., 2018), where an accurate representation of the bathymetry is required. Unfortunately, high-resolution models like CM2.6 are computationally very expensive and do not allow for long spin-up or ensemble simulations. In addition to model resolution, biogeochemical processes in coastal oceans are also highly dependent on riverine fluxes of C_T , A_T , and nutrients (Terhaar et al., 2019) that are not sufficiently well represented by the ESM2M model. As a result, the analyses in this thesis are constrained to the open oceans.

Based on the two-hour time step for the ocean component, the ESM2M model includes the diurnal cycle in solar insolation and simulates, to some extent, diurnal variations in physical and biogeochemical ocean variables such as temperature and net primary productivity. However, it misses important processes such as the diel vertical migration of zooplankton (Longhurst & Glen

Harrison, 1988). Furthermore, also the relatively low spatial resolution of the model may limit its capability in representing variations on diurnal timescales. Due to these caveats, diurnal variations in $[\text{H}^+]$ and Ω_{A} were not analyzed in this thesis. Diurnal variability is an important contributor to total variability in carbonate system variables like $[\text{H}^+]$, in particular in coastal oceans (Hofmann et al., 2011; Torres et al., 2021). However, diurnal variability is generally lower in the open ocean (Torres et al., 2021). Across the seven open ocean autonomous stations with 3-hourly measurement frequency analyzed in Chapter 4 (Ext. Data Table 4.2), the contribution from diurnal $[\text{H}^+]$ variance to total $[\text{H}^+]$ variance is between 2 % and 12 %.

In Chapters 3 to 5, simulated extreme events in $[\text{H}^+]$ and Ω_{A} were analyzed. However, the stress on organisms from ocean acidification, that has been reported extensively, implies shifts in all carbonate system variables (Hurd et al., 2020). Partial pressure of CO_2 ($p\text{CO}_2$), $[\text{H}^+]$ (or pH), and calcium carbonate saturation state, very often for aragonite minerals, Ω_{A} , are best understood to impact marine organisms. Too high $p\text{CO}_2$ is associated with detrimental physiological, neurological, and behavioral effects for organisms, referred to as *hypercapnia* (McNeil & Sasse, 2016). Similarly, too high $[\text{H}^+]$ is connected to physiological impacts such as metabolic depression and a reduction in protein synthesis (Pörtner, 2008), and energetic costs (Pörtner et al., 2011; Bednaršek et al., 2018), as well as neurotransmitter functionality (Chivers et al., 2014). Reductions in Ω_{A} are mainly associated with stress for calcifying organisms due to decreased calcification or shell dissolution (Bednaršek et al., 2012). However, other carbonate system parameters, such as the ratio between $[\text{HCO}_3^-]$ and $[\text{H}^+]$, may also determine calcification (Fassbender et al., 2016). Often, co-variations among these variables lead to elevated $p\text{CO}_2$ and $[\text{H}^+]$ but reduced Ω_{A} at the same time. This is the case when these changes are caused by either an increase in C_{T} or salinity, or by a decrease in A_{T} . In contrast, an increase in temperature will increase $p\text{CO}_2$ and $[\text{H}^+]$, but it will also increase Ω_{A} . As a result, it is important to know which of the variables is most relevant to ecosystems, in particular in situations where temperature significantly contributes to changes in these variables. As discussed in Sect. 6.1, variations in $p\text{CO}_2$ and $[\text{H}^+]$ are strongly linked. Hence, when $p\text{CO}_2$ is strongly elevated, the same is likely true for $[\text{H}^+]$. However, it has been shown in Chapter 4 and 5 that extremes in $[\text{H}^+]$ are often significantly driven by elevated temperatures and that they often co-occur with high-temperature extremes, in particular in the subtropical oceans. Due to this pronounced role of temperature for $[\text{H}^+]$ extremes, these events are not necessarily connected to extremely low Ω_{A} . Within the observation-based dataset that was analyzed in Chapter 4, only 27 % of months during which $[\text{H}^+]$ is extremely high (based on seasonally-varying thresholds) also show extremely low Ω_{A} on global average. Notably, the effects from increases in C_{T} due to ocean acidification on extremes in $p\text{CO}_2$, $[\text{H}^+]$, and Ω_{A} are similar when the extremes are defined with respect to fixed baselines (Chapter 3).

The impacts of the extreme events discussed in this thesis depend, among other factors, on the amplitudes of the perturbations in $[\text{H}^+]$ or Ω_{A} . Variations in $[\text{H}^+]$ and Ω_{A} in the open ocean are often relatively small (Torres et al., 2021). For example, the average difference between the peak of simulated $[\text{H}^+]$ extremes based on fixed 99th percentiles and the annual mean is globally 0.8 nmol kg^{-1} under preindustrial conditions (Chapter 3). In contrast, laboratory experiments often use comparably large perturbations to assess impacts on organisms. For example, Kroeker et al. (2013) included studies with pH perturbations up to 0.5 ($\simeq 18 \text{ nmol kg}^{-1}$)⁶ for their meta-analysis. As a result, the impacts identified in laboratory experiments may not always be applicable to extreme events in the open-ocean. Finally, impacts also depend on the duration of the exposure. As a result, impacts that were identified in long-exposure laboratory experiments may not be similar during relatively short extreme events. Impacts could potentially be larger due to higher rates of changes during extremes compared to the long-term changes and due to

⁶An initial pH of 8.07 was assumed to calculate a corresponding perturbation in $[\text{H}^+]$. The change in $[\text{H}^+]$ for a given pH change depends on initial pH (Fassbender et al., 2021).

acclimation or adaption during long exposures (Form & Riebesell, 2012).

6.3 Outlook

There are many possibilities to extend or improve the work that was presented in this thesis. Possible future analyses could extend the analysis on the drivers of $[\text{H}^+]$ extremes, could move from bivariate to trivariate extremes including additional marine ecosystem stressors such as oxygen or net primary productivity, could use climate models of different complexity and resolution, or could build bridges to ecosystem impact models.

The analyses on the driving processes of $[\text{H}^+]$ extremes in the ESM2M model (Chapter 5) can be extended in various ways. First, one could investigate the driving mechanisms of the $[\text{H}^+]$ increases before extreme event onset to understand which processes cause the generally high anomalies in $[\text{H}^+]$ during the extremes. Second the analysis could be extended to $[\text{H}^+]$ extremes at subsurface, where variations in C_T generally become more important (Sect. 6.1) and where the driving mechanisms of extremes likely differ much due to the absence of air-sea heat and carbon fluxes and because of changes in the contributions from vertical mixing and advection (Vogt et al., in preparation). Furthermore, also the role of biological activity at subsurface could be investigated in more detail, because at subsurface increases in carbon due to remineralization of organic matter become more important. Third, the analysis could be repeated for Ω_A to resolve the differences in the driving mechanisms of $[\text{H}^+]$ and Ω_A extreme events. For Ω_A , variations in C_T are likely the main driver of extremes, because Ω_A is considerably less influenced by temperature variations than $[\text{H}^+]$. Finally, changes in the driving processes of $[\text{H}^+]$ extremes as a result of ocean acidification and warming could be analyzed. Such changes could, for example, arise because of changes in vertical mixing, which may be driven by changes in stratification and winds, and because of changes in air-sea fluxes of heat and carbon. Furthermore, the contributions from temperature and C_T variations to $[\text{H}^+]$ extremes could change due to the disparate changes in $[\text{H}^+]$ sensitivity to temperature and C_T variations (discussed in Sect. 6.1). To project changes in the drivers of $[\text{H}^+]$ extremes, it is necessary to assess the robustness of the simulated changes in the processes that drive variations in temperature and C_T . Such changes in the processes also manifest in temperature and C_T variability. ESM2M simulates decreases in C_T variability, in particular in the equatorial Pacific and high-latitude regions (Fig. A6 in Chapter 3). Hence, a potential first step would be to analyze how robust projected C_T variability changes are in the CMIP6 model ensemble.

The analyses on bivariate extremes in temperature and $[\text{H}^+]$ in Chapter 4 could be extended by including coinciding stress from other marine ecosystem stressors such as net primary productivity (NPP) at the ocean surface or oxygen content at subsurface. Compound stress from warming and acidification is expected to increase energetic demand of organisms (Bednaršek et al., 2018). As a result, impacts of these compound events could be worsened under co-occurring low extremes in net primary productivity (Bednaršek et al., 2018). Simply by chance, such trivariate extremes are relatively unlikely to occur. For example, when defining extremes based on 90th percentile thresholds, one in one thousand days (around one day in 3 years) would be expected to be under trivariate extreme conditions. However, the frequency of such trivariate compound events could be much higher in regions where high temperature, low $[\text{H}^+]$, and low NPP tend to occur together. This could be particularly the case in the subtropical regions, where high-temperature-low- $[\text{H}^+]$ extremes are frequent (Fig. 4.1) and where also compound high-temperature-low-chlorophyll extremes often occur (Le Grix et al., 2021). Also trivariate extreme events in temperature, $[\text{H}^+]$, and oxygen at subsurface likely impact organisms. Increased temperature elevates organismal oxygen demand. As a result, thermal tolerance windows are narrowed under low-oxygen

conditions (Pörtner, 2010). Co-occurring low-pH conditions may further narrow thermal tolerance windows, for example due to impairment of oxygen uptake in blood with lowered pH (Pörtner et al., 2011; Gobler & Baumann, 2016), and organismal acid-base regulation may also be hampered under high-temperature-low-oxygen conditions (Pörtner, 2010; Gobler & Baumann, 2016). Furthermore, high $[H^+]$ and low oxygen conditions at the subsurface are likely to occur at the same time, because the respiration of organic matter decreases oxygen and increases CO_2 and $[H^+]$.

The analyses in this thesis did not include coastal regions and did not take into account variability in acidity on the mesoscale and submesoscale due to oceanic eddies. Both is not feasible with the ESM2M model due to the relatively coarse model resolution and missing processes. This could be achieved by using a global high-resolution model that resolves ocean eddies and has higher skill in coastal regions. One option would be the aforementioned GFDL CM2.6, when coupled to a complete biogeochemistry component such as COBALT that was used in Turi et al. (2018). However, the computational burden increases drastically when running a simulation with such a high-resolution model, since the ocean component has about one hundred times more grid cells than that of ESM2M. To analyze acidity extremes and compound events in coastal regions, also a regional ocean model such as the Regional Oceanic Model System (ROMS; Shchepetkin & McWilliams, 2005) would be a good choice (Hauri et al., 2020). Biases in the simulations could be reduced by switching from the GFDL ESM2M model to its successor, the GFDL ESM4.1 model (Dunne et al., 2020). Among other aspects, improvements of ESM4.1 compared to its predecessor concern the Southern Ocean, with a reduction of biases in sea surface temperature, mixed layer depth, and ventilation. Furthermore, the ocean biogeochemical component of ESM4.1, COBALTv2, improved the representation of ocean food webs, carbon sequestration, and nutrient exchanges with the atmosphere and land components relative to ESM2M (Stock et al., 2020). ESM4.1 was also shown here to have lower biases in the correlation coefficient of temperature and $[H^+]$ in the Southern Ocean and the subpolar North Pacific when compared to the ESM2M model (Ext. Data Fig. 4.10), indicating a higher skill in simulating compound temperature- $[H^+]$ extremes there. However, the positive bias in simulated correlation coefficient is larger than that of the ESM2M model in tropical and subtropical regions.

In this thesis, acidity extreme events were based on local percentile thresholds. Under this approach, there is no direct link between the hazard during an extreme event and the impacts on vulnerable and exposed species. This gap could be bridged by analyzing the potential stress on organisms during the extremes based on ecosystem impact models, such as for marine invertebrates (Tai et al., 2021) or for pteropods (Bednaršek et al., 2021). In principle, another approach to link hazards and impacts is to define a biology-informed environmental index that connects environmental stressors to ecological impacts. An example is the aerobic growth index (Clarke et al., 2021), which connects stress from ocean warming and deoxygenation to species-dependent impacts on organisms. The 10th percentile of aerobic growth index values in the global distribution for a species is proposed as an impact-driven extreme-event threshold (Clarke et al., 2021). $\Omega_A = 1$ is a well established threshold for biogenic calcification and more specific Ω_A thresholds have been defined for pteropods (Bednaršek et al., 2019). However, a generally applicable index for stress from ocean acidification is currently not available.

References

- Alexander, M. A., Scott, J. D., Friedland, K. D., Mills, K. E., Nye, J. A., Pershing, A. J., & Thomas, A. C., 2018. Projected sea surface temperatures over the 21st century: Changes in the mean, variability and extremes for large marine ecosystem regions of Northern Oceans, *Elementa: Science of the Anthropocene*, 6.
- Bakker, D. C. E., Pfeil, B., O'Brien, K. M., Currie, K. I., Jones, S. D., Landa, C. S., Lauvset, S. K., Metzl, N., Munro, D. R., Nakaoka, S.-I., Olsen, A., Pierrot, D., Saito, S., Smith, K., Sweeney, C., Takahashi, T., Wada, C., Wanninkhof, R., Alin, S. R., Becker, M., Bellerby, R. G. J., Borges, A. V., Boutin, J., Bozec, Y., Burger, E., Cai, W.-J., Castle, R. D., Cosca, C. E., DeGrandpre, M. D., Donnelly, M., Eiseid, G., Feely, R. A., Gkritzalis, T., González-Dávila, M., Goyet, C., Guillot, A., Hardman-Mountford, N. J., Hauck, J., Hoppema, M., Humphreys, M. P., Hunt, C. W., Ibáñez, J. S. P., Ichikawa, T., Ishii, M., Juranek, L. W., Kitidis, V., Körtzinger, A., Koffi, U. K., Kozyr, A., Kuwata, A., Lefèvre, N., Lo Monaco, C., Manke, A., Marrec, P., Mathis, J. T., Millero, F. J., Monacci, N., Monteiro, P. M. S., Murata, A., Newberger, T., Nojiri, Y., Nonaka, I., Omar, A. M., Ono, T., Padín, X. A., Rehder, G., Rutgersson, A., Sabine, C. L., Salisbury, J., Santana-Casiano, J. M., Sasano, D., Schuster, U., Sieger, R., Skjelvan, I., Steinhoff, T., Sullivan, K., Sutherland, S. C., Sutton, A., Tadokoro, K., Telszewski, M., Thomas, H., Tilbrook, B., van Heuven, S., Vandemark, D., Wallace, D. W., & Woosley, R., 2016. Surface ocean CO₂ atlas (SOCAT) V4.
- Bednaršek, N., Feely, R. A., Beck, M. W., Glippa, O., Kanerva, M., & Engström-Öst, J., 2018. El Niño-Related Thermal Stress Coupled With Upwelling-Related Ocean Acidification Negatively Impacts Cellular to Population-Level Responses in Pteropods Along the California Current System With Implications for Increased Bioenergetic Costs, *Frontiers in Marine Science*, 5(December), 1–17.
- Bednaršek, N., Tarling, G. A., Bakker, D. C. E., Fielding, S., Jones, E. M., Venables, H. J., Ward, P., Kuzirian, A., Lézé, B., Feely, R. A., & Murphy, E. J., 2012. Extensive dissolution of live pteropods in the southern ocean, *Nature Geoscience*, 5, 881–885.
- Bednaršek, N., Feely, R. A., Howes, E. L., Hunt, B. P. V., Kessouri, F., León, P., Lischka, S., Maas, A. E., McLaughlin, K., Nezhlin, N. P., Sutula, M., & Weisberg, S. B., 2019. Systematic review and meta-analysis toward synthesis of thresholds of ocean acidification impacts on calcifying pteropods and interactions with warming, *Frontiers in Marine Science*, 6, 227.
- Bednaršek, N., Naish, K.-A., Feely, R. A., Hauri, C., Kimoto, K., Hermann, A. J., Michel, C., Niemi, A., & Pilcher, D., 2021. Integrated assessment of ocean acidification risks to pteropods in the northern high latitudes: Regional comparison of exposure, sensitivity and adaptive capacity, *Frontiers in Marine Science*, 8, 1282.
- Bindoff, N., Cheung, W., Kairo, J., Aristegui, J., Guinder, V., Hallberg, R., Hilmi, N., Jiao, N., Karim, M., Levin, L., O'Donoghue, S., Purca Cuicapusa, S., Rinkevich, B., Suga, T., Tagliabue, A., & Williamson, P., 2019. Chapter 5: Changing ocean, marine ecosystems, and dependent communities, *IPCC Special Report on the Ocean and Cryosphere (SROCC)*.
- Bond, N. A., Cronin, M. F., Freeland, H., & Mantua, N., 2015. Causes and impacts of the 2014 warm anomaly in the ne pacific, *Geophysical Research Letters*, 42(9), 3414–3420.
- Bopp, L., Resplandy, L., Orr, J. C., Doney, S. C., Dunne, J. P., Gehlen, M., Halloran, P., Heinze, C., Ilyina, T., Séférián, R., Tjiputra, J., & Vichi, M., 2013. Multiple stressors of ocean ecosystems in the 21st century: projections with CMIP5 models, *Biogeosciences*, 10(10).
- Chivers, D. P., McCormick, M. I., Nilsson, G. E., Munday, P. L., Watson, S.-A., Meekan, M. G., Mitchell, M. D., Corkill, K. C., & Ferrari, M. C. O., 2014. Impaired learning of predators and lower prey survival under elevated CO₂: a consequence of neurotransmitter interference, *Global Change Biology*, 20(2), 515–522.
- Clarke, T. M., Wabnitz, C. C., Striegel, S., Frölicher, T. L., Reygondeau, G., & Cheung, W. W., 2021. Aerobic growth index (AGI): An index to understand the impacts of ocean warming and deoxygenation on global marine fisheries resources, *Progress in Oceanography*, 195, 102588.
- Doney, S. C., Fabry, V. J., Feely, R. A., & Kleypas, J. A., 2009. Ocean acidification: The other CO₂ problem, *Annual Review of Marine Science*, 1(1), 169–192.
- Dufour, C. O., Griffies, S. M., de Souza, G. F., Frenger, I., Morrison, A. K., Palter, J. B., Sarmiento, J. L., Galbraith, E. D., Dunne, J. P., Anderson, W. G., & Slater, R. D., 2015. Role of mesoscale eddies in cross-frontal transport of heat and biogeochemical tracers in the southern ocean, *Journal of Physical Oceanography*, 45(12), 3057 – 3081.

- Dunne, J. P., John, J. G., Shevliakova, E., Stouffer, R. J., Krasting, J. P., Malyshev, S. L., Milly, P. C. D., Sentman, L. T., Adcroft, A. J., Cooke, W., Dunne, K. A., Griffies, S. M., Hallberg, R. W., Harrison, M. J., Levy, H., Wittenberg, A. T., Phillips, P. J., & Zadeh, N., 2013. GFDL's ESM2 global coupled climate-carbon earth system models. Part II: Carbon system formulation and baseline simulation characteristics, *Journal of Climate*, 26(7), 2247–2267.
- Dunne, J. P., Horowitz, L. W., Adcroft, A. J., Ginoux, P., Held, I. M., John, J. G., Krasting, J. P., Malyshev, S., Naik, V., Paulot, F., Shevliakova, E., Stock, C. A., Zadeh, N., Balaji, V., Blanton, C., Dunne, K. A., Dupuis, C., Durachta, J., Dussin, R., Gauthier, P. P. G., Griffies, S. M., Guo, H., Hallberg, R. W., Harrison, M., He, J., Hurlin, W., McHugh, C., Menzel, R., Milly, P. C. D., Nikonov, S., Paynter, D. J., Ploshay, J., Radhakrishnan, A., Rand, K., Reichl, B. G., Robinson, T., Schwarzkopf, D. M., Sentman, L. T., Underwood, S., Vahlenkamp, H., Winton, M., Wittenberg, A. T., Wyman, B., Zeng, Y., & Zhao, M., 2020. The GFDL Earth System Model Version 4.1 (GFDL-ESM 4.1): Overall Coupled Model Description and Simulation Characteristics, *Journal of Advances in Modeling Earth Systems*, 12(11), e2019MS002015.
- Fassbender, A. J., Sabine, C. L., & Feifel, K. M., 2016. Consideration of coastal carbonate chemistry in understanding biological calcification, *Geophysical Research Letters*, 43(9), 4467–4476.
- Fassbender, A. J., Rodgers, K. B., Palevsky, H. I., & Sabine, C. L., 2018. Seasonal asymmetry in the evolution of surface ocean $p\text{CO}_2$ and pH thermodynamic drivers and the influence on sea-air CO_2 flux, *Global Biogeochemical Cycles*, 32(10), 1476–1497.
- Fassbender, A. J., Orr, J. C., & Dickson, A. G., 2021. Technical note: Interpreting pH changes, *Biogeosciences*, 18(4), 1407–1415.
- Form, A. U. & Riebesell, U., 2012. Acclimation to ocean acidification during long-term CO_2 exposure in the cold-water coral lophelia pertusa, *Global Change Biology*, 18(3), 843–853.
- Fox-Kemper, B., Ferrari, R., & Hallberg, R., 2008. Parameterization of Mixed Layer Eddies. Part I: Theory and Diagnosis, *Journal of Physical Oceanography*, 38(6), 1145–1165.
- Frölicher, T. L., Rodgers, K. B., Stock, C. A., & Cheung, W. W. L., 2016. Sources of uncertainties in 21st century projections of potential ocean ecosystem stressors, *Global Biogeochemical Cycles*, 30(8), 1224–1243.
- Frölicher, T. L., Fischer, E. M., & Gruber, N., 2018. Marine heatwaves under global warming, *Nature*, 560(7718), 360–364.
- eds Gattuso, J.-P. & Hansson, L., 2011. *Ocean Acidification*, Oxford University Press.
- Gobler, C. J. & Baumann, H., 2016. Hypoxia and acidification in ocean ecosystems: coupled dynamics and effects on marine life, *Biology letters*, 12(5), 20150976.
- Gray, A. R., Johnson, K. S., Bushinsky, S. M., Riser, S. C., Russell, J. L., Talley, L. D., Wanninkhof, R., Williams, N. L., & Sarmiento, J. L., 2018. Autonomous biogeochemical floats detect significant carbon dioxide outgassing in the high-latitude southern ocean, *Geophysical Research Letters*, 45(17), 9049–9057.
- Gregor, L. & Gruber, N., 2021. OceanSODA-ETHZ: a global gridded data set of the surface ocean carbonate system for seasonal to decadal studies of ocean acidification, *Earth System Science Data*, 13(2), 777–808.
- Griffies, S. M., 1998. The Gent–McWilliams Skew Flux, *Journal of Physical Oceanography*, 28(6), 831–841.
- Griffies, S. M., Winton, M., Anderson, W. G., Benson, R., Delworth, T. L., Dufour, C. O., Dunne, J. P., Goddard, P., Morrison, A. K., Rosati, A., Wittenberg, A. T., Yin, J., & Zhang, R., 2015. Impacts on ocean heat from transient mesoscale eddies in a hierarchy of climate models, *Journal of Climate*, 28(3).
- Hauri, C., Schultz, C., Hedstrom, K., Danielson, S., Irving, B., Doney, S. C., Dussin, R., Curchitser, E. N., Hill, D. F., & Stock, C. A., 2020. A regional hindcast model simulating ecosystem dynamics, inorganic carbon chemistry, and ocean acidification in the gulf of alaska, *Biogeosciences*, 17(14), 3837–3857.
- Henson, S. A., Beaulieu, C., & Lampitt, R., 2016. Observing climate change trends in ocean biogeochemistry: when and where, *Global Change Biology*, 22(4), 1561–1571.
- Hofmann, G. E., Smith, J. E., Johnson, K. S., Send, U., Levin, L. A., Micheli, F., Paytan, A., Price, N. N., Peterson, B., Takeshita, Y., Matson, P. G., Crook, E. D., Kroeker, K. J., Gambi, M. C., Rivest, E. B., Frieder, C. A., Yu, P. C., & Martz, T. R., 2011. High-frequency dynamics of ocean pH: A multi-ecosystem comparison, *PloS One*, 6(12), 1–11.

- Hurd, C. L., Beardall, J., Comeau, S., Cornwall, C. E., Havenhand, J. N., Munday, P. L., Parker, L. M., Raven, J. A., & McGraw, C. M., 2020. Ocean acidification as a multiple driver: how interactions between changing seawater carbonate parameters affect marine life, *Marine and Freshwater Research*, 71(3), 263–274.
- Keller, K. M., Joos, F., & Raible, C. C., 2014. Time of emergence of trends in ocean biogeochemistry, *Biogeosciences*, 11(13), 3647–3659.
- Key, R. M., Olsen, A., van Heuven, S., Lauvset, S. K., Velo, A., Lin, X., Schirnick, C., Kozyr, A., Tanhua, T., Hoppema, M., Jutterström, S., Steinfeldt, R., Jeansson, E., Ishii, M., Perez, F. F., & Suzuki, T., 2015. Global ocean data analysis project, version 2 (GLODAPv2), NDP document, Carbon Dioxide Information Analysis Center, OAK RIDGE NATIONAL LABORATORY Oak Ridge, Tennessee 37831-6335.
- Kroeker, K. J., Kordas, R. L., Crim, R., Hendriks, I. E., Ramajo, L., Singh, G. S., Duarte, C. M., & Gattuso, J.-P., 2013. Impacts of ocean acidification on marine organisms: quantifying sensitivities and interaction with warming, *Global Change Biology*, 19(6), 1884–1896.
- Kwiatkowski, L. & Orr, J. C., 2018. Diverging seasonal extremes for ocean acidification during the twenty-first century, *Nature Climate Change*, 8(2), 141–145.
- Landschützer, P., Gruber, N., & Bakker, D. C. E., 2016. Decadal variations and trends of the global ocean carbon sink, *Global Biogeochemical Cycles*, 30(10), 1396–1417.
- Landschützer, P., Gruber, N., & Bakker, D. C. E., 2020. An observation-based global monthly gridded sea surface $p\text{CO}_2$ product from 1982 onward and its monthly climatology (NCEI Accession 0160558).
- Laufkötter, C., Vogt, M., Gruber, N., Aita-Noguchi, M., Aumont, O., Bopp, L., Buitenhuis, E., Doney, S. C., Dunne, J., Hashioka, T., Hauck, J., Hirata, T., John, J., Le Quéré, C., Lima, I. D., Nakano, H., Seferian, R., Totterdell, I., Vichi, M., & Völker, C., 2015. Drivers and uncertainties of future global marine primary production in marine ecosystem models, *Biogeosciences*, 12(23), 6955–6984.
- Lauvset, S. K., Key, R. M., Olsen, A., van Heuven, S., Velo, A., Lin, X., Schirnick, C., Kozyr, A., Tanhua, T., Hoppema, M., Jutterström, S., Steinfeldt, R., Jeansson, E., Ishii, M., Perez, F. F., Suzuki, T., & Watelet, S., 2016. A new global interior ocean mapped climatology: the $1^\circ \times 1^\circ$ GLODAP version 2, *Earth System Science Data*, 8(2), 325–340.
- Le Grix, N., Zscheischler, J., Laufkötter, C., Rousseaux, C. S., & Frölicher, T. L., 2021. Compound high-temperature and low-chlorophyll extremes in the ocean over the satellite period, *Biogeosciences*, 18(6), 2119–2137.
- Longhurst, A. R. & Glen Harrison, W., 1988. Vertical nitrogen flux from the oceanic photic zone by diel migrant zooplankton and nekton, *Deep Sea Research Part A. Oceanographic Research Papers*, 35(6), 881–889.
- McNeil, B. I. & Sasse, T. P., 2016. Future ocean hypercapnia driven by anthropogenic amplification of the natural CO_2 cycle, *Nature*, 529, 383–386.
- Omta, A. W., Goodwin, P., & Follows, M. J., 2010. Multiple regimes of air-sea carbon partitioning identified from constant-alkalinity buffer factors, *Global Biogeochemical Cycles*, 24(3).
- Orr, J., 2011. Recent and future changes in ocean carbonate chemistry, *Ocean Acidification*, pp. 41–66.
- Orr, J. C., Fabry, V. J., Aumont, O., Bopp, L., Doney, S. C., Feely, R. A., Gnanadesikan, A., Gruber, N., Ishida, A., Joos, F., Key, R. M., Lindsay, K., Maier-Reimer, E., Matear, R., Monfray, P., Mouchet, A., Najjar, R. G., Plattner, G.-K., Rodgers, K. B., Sabine, C. L., Sarmiento, J. L., Schlitzer, R., Slater, R. D., Totterdell, I. J., Weirig, M.-F., Yamanaka, Y., & Yool, A., 2005. Anthropogenic ocean acidification over the twenty-first century and its impact on calcifying organisms, *Nature*, 437(7059), 681–686.
- Pörtner, H., 2008. Ecosystem effects of ocean acidification in times of ocean warming: a physiologist's view, *Marine Ecology Progress Series*, 373, 203–217.
- Pörtner, H.-O., 2010. Oxygen- and capacity-limitation of thermal tolerance: a matrix for integrating climate-related stressor effects in marine ecosystems, *Journal of Experimental Biology*, 213(6), 881–893.
- Pörtner, H.-O., Gutowska, M., Ishimatsu, A., Lucassen, M., Melzner, F., & Seibel, B., 2011. Effects of ocean acidification on nektonic organisms, *Ocean Acidification*, pp. 154–175.
- Reynolds, R. W., Smith, T. M., Liu, C., Chelton, D. B., Casey, K. S., & Schlax, M. G., 2007. Daily high-resolution-blended analyses for sea surface temperature, *Journal of Climate*, 20(22), 5473 – 5496.

- Sarmiento, J. & Gruber, N., 2006. *Ocean Biogeochemical Dynamics*, Princeton University Press.
- Schlunegger, S., Rodgers, K. B., Sarmiento, J. L., Frölicher, T. L., Dunne, J. P., Ishii, M., & Slater, R., 2019. Emergence of anthropogenic signals in the ocean carbon cycle, *Nature Climate Change*, 9(9), 719–725.
- Shchepetkin, A. F. & McWilliams, J. C., 2005. The regional oceanic modeling system (ROMS): a split-explicit, free-surface, topography-following-coordinate oceanic model, *Ocean Modelling*, 9(4), 347–404.
- Stock, C. A., Dunne, J. P., Fan, S., Ginoux, P., John, J., Krasting, J. P., Laufkötter, C., Paulot, F., & Zadeh, N., 2020. Ocean Biogeochemistry in GFDL’s Earth System Model 4.1 and Its Response to Increasing Atmospheric CO₂, *Journal of Advances in Modeling Earth Systems*, 12(10), e2019MS002043.
- Tai, T. C., Sumaila, U. R., & Cheung, W. W. L., 2021. Ocean acidification amplifies multi-stressor impacts on global marine invertebrate fisheries, *Frontiers in Marine Science*, 8, 839.
- Takahashi, T., Sutherland, S., Chipman, D., Goddard, J., Ho, C., Newberger, T., Sweeney, C., & Munro, D., 2014. Climatological distributions of pH, pCO₂, total CO₂, alkalinity, and CaCO₃ saturation in the global surface ocean, and temporal changes at selected locations, *Marine Chemistry*, 164, 95–125.
- Terhaar, J., Orr, J. C., Ethé, C., Regnier, P., & Bopp, L., 2019. Simulated arctic ocean response to doubling of riverine carbon and nutrient delivery, *Global Biogeochemical Cycles*, 33(8), 1048–1070.
- Torres, O., Kwiatkowski, L., Sutton, A. J., Dorey, N., & Orr, J. C., 2021. Characterizing mean and extreme diurnal variability of ocean CO₂ system variables across marine environments, *Geophysical Research Letters*, 48(5), e2020GL090228.
- Turi, G., Alexander, M., Lovenduski, N. S., Capotondi, A., Scott, J., Stock, C., Dunne, J., John, J., & Jacox, M., 2018. Response of O₂ and pH to ENSO in the california current system in a high-resolution global climate model, *Ocean Science*, 14(1), 69–86.
- Vogt, L., Burger, F. A., & Frölicher, T. L., in preperation. Marine heatwave drivers in an earth system model, *Geophysical Research Letters*.
- Wanninkhof, R., 1992. Relationship between wind speed and gas exchange over the ocean, *Journal of Geophysical Research: Oceans*, 97(C5), 7373–7382.
- Yamamoto, A., Palter, J. B., Dufour, C. O., Griffies, S. M., Bianchi, D., Claret, M., Dunne, J. P., Frenger, I., & Galbraith, E. D., 2018. Roles of the ocean mesoscale in the horizontal supply of mass, heat, carbon, and nutrients to the northern hemisphere subtropical gyres, *Journal of Geophysical Research: Oceans*, 123(10), 7016–7036.

Appendix

Modeling activities with the GFDL ESM2M model at CSCS

During the PhD project, a number of simulations with the GFDL ESM2M Earth system model, version Siena from August 2013, were performed at the Swiss National Supercomputing Centre (CSCS). The model code was ported to CSCS by Richard Slater from Princeton University and Thomas Frölicher. The model was compiled using the Intel Fortran compiler version 17.0.4. Intel Fortran Compiler version 18, the currently installed compiler version at CSCS, was found not to be compatible with GFDL ESM2M, because the necessary compiler flag `override-limits` is no longer supported under that version. While it is possible to compile the model with Intel Fortran Compiler version 18 when replacing the `override-limits` flag by the `qoverride-limits` flag, the model crashes at runtime due to a segmentation fault.

The remainder of this chapter is going to introduce in detail how the GFDL ESM2M simulations were run at CSCS. First, the setup scripts used to prepare the simulations are introduced (Sect. A.1), which copy necessary model files (Sect. A.2), configuration files (Sect. A.3), restart files from previous simulations, and the compiled model executable to the working directory. Sect. A.4 details how the model was run. Finally, Sect. A.5 discusses the data transfer to Bern and the compression of the data.

A.1 Model setup

Each model simulation was prepared by running a setup script written in bash that copied the necessary data to run the model to the `$SCRATCH` directory. Within each script, a working directory `WRKDIR=$SCRATCH/$JOBNAME` is created, with the according simulation name `JOBNAME=...` specified before, and the necessary data is copied to that directory.

```
mkdir $WRKDIR/INPUT
cp $FORCINGDIR/* $WRKDIR/INPUT/
cp $FILEDIR/* $WRKDIR/INPUT/
cp $RESTARTDIR/* $WRKDIR/INPUT/
cp $CONFIGDIR/{data_table,field_table,input.nml} $WRKDIR/
cp $EXECDIR/executable.x $WRKDIR/
```

The model forcing files (`FORCINGDIR`) and other model files (`FILEDIR`) are listed in Sect A.2. The model configuration files (`CONFIGDIR`) are listed in Sect A.3. The setup scripts used for the simulations performed during this thesis (Table A.2) are available on gitlab (https://gitlab.climate.unibe.ch/burger/ESM2M_setup_run_scripts).

A.2 Model files

The model forcing files, which were provided by Jasmin John from NOAA/GFDL, include aerosol forcing in the form of 3D decadal aerosol climatologies for the historical period and under the RC2.6 and RCP8.5 scenarios (provided by J.-F. Lamarque, adapted by V. Naik)

```
aerosol.climatology_1855-2015.nc
aerosol.climatology_rcp26_2005-2105.nc
aerosol.climatology_rcp85_2005-2105.nc,
```

zonally and vertically resolved volcanic aerosol forcing on monthly resolution for the historical period based on Stenchikov et al. (1998)

```
asmsw_data.nc
omgsw_data.nc
extlw_data.nc
extsw_data.nc,
```

3D ozone forcing on monthly resolution for the historical period and under the RCP2.6 and RCP8.5 scenarios (based on Cionni et al. (2011))

```
CM3_CMIP5_ACC_SPARC_1850-2009_T3M_03.nc
CM3_CMIP5_ACC_SPARC_2005-2101_RCP2.6_T3M_03.nc
CM3_CMIP5_ACC_SPARC_2005-2101_RCP8.5_T3M_03.nc,
```

gridded land use forcing files on annual resolution for the historical period and under the RCP2.6 (RCP3.0) and RCP8.5 scenarios (Hurtt et al., 2006)

```
landuse_1700-2005.nc
lu.1999-2100.image.v1.1_rc3_RCP3.nc
lu.1999-2100.message_RCP85.nc,
```

solar forcing (Lean, 2009)

```
CMIP5_1610-2300_monthly_data_b18
esf_sw_input_data_n38b18_2000_version_ckd2.1.lean.nov89.ref.with.ch4.and.n2o,
```

ocean CFC forcing for the historical period on the ocean model grid on annual resolution

```
cfc11_cfc12_cfc113_cc14_atm_om3_bc-1-9999.nc,
```

and annual global atmospheric greenhouse gas concentrations for the historical period either extended by RCP8.5 or by RCP2.6 (RCP3.0) from Meinshausen et al. (2011)

```
CO2_rcp3_gblannualdata_1800-2500
CO2_rcp85_gblannualdata_1800-2500
```

```
CH4_rcp3_gblannualdata_1800-2500
CH4_rcp85_gblannualdata_1800-2500
```

```
N2O_rcp3_gblannualdata_1800-2500
N2O_rcp85_gblannualdata_1800-2500
```

```
f11_rcp3_gblannualdata_1800-2500
f11_rcp85_gblannualdata_1800-2500
```

```
f12_rcp3_gblannualdata_1800-2500
f12_rcp85_gblannualdata_1800-2500
```

```
f22_rcp3_gblannualdata_1800-2500
f22_rcp85_gblannualdata_1800-2500
```

```
f113_rcp3_gblannualdata_1800-2500
f113_rcp85_gblannualdata_1800-2500.
```

These forcing files are also available for the RCP4.5 and RCP6.0 scenarios. Gridded CO₂ emission files on monthly resolution for the historical period and the RCP8.5 scenario are available to force the model with CO₂ emissions instead of prescribed concentrations

```
gridcar_Andres_AR5_1751-2006_monthly.nc
FFwShipsCO2_RCP85_2006-2500_monthly_05_rev2.nc.
```

Furthermore, non-forcing model files required to run the model (e.g., grid specification data, topography, bathymetry, geothermal heating, climatologies for oceanic nutrient input from aerosol deposition and from runoff) were provided by Jasmin John and Richard Slater from NOAA/GFDL.

A.3 Configuration files

The ESM2M model can be configured after compilation using a set of configuration files, namely `input.nml`, `data_table`, `field_table`, and `diag_table`. The configuration files used for the simulation in Table A.2 were adapted from initial configuration files that were provided by Richard Slater from NOAA/GFDL.

The input namelist (`input.nml`) configures the individual modules within MOM4p1, TOPAZv2, the sea ice model, LM3, and AM2 - allowing to chose between parametrizations and to chose parameter values. Furthermore, it configures the coupler that couples these model components (`coupler.nml`). There, also the current date at the beginning of the simulation needs to be set (e.g., 2006,1,1 for a simulation under a RCP scenario), and the parallelization layout is set (see Sect. A.4). The input namelist needs to be configured for the individual model simulations. For example, between a historical and a preindustrial, one needs to switch between time-varying and constant aerosol, ozone, and solar forcing and greenhouse gas concentrations. Furthermore, one needs to switch between activated or deactivated volcanic aerosol forcing and land use changes. As another example, CO₂ emission forcing needs to be activated in the `input.nml` for emission-driven simulations.

The data table (`data_table`) mainly specifies the name of the CO₂ forcing file (either prescribed concentrations or emissions) or if instead a constant prescribed CO₂ concentration should be used for the simulation. This section was adapted when switching between preindustrial, historical, and RCP simulations and between concentration-driven and emission-driven simulations. The field table (`field_table`) defines a number of model properties such as the used advection schemes and parameter values for the parametrizations for volume and tracer exchange between the open oceans and marginal seas. The field table was only adapted for the historical and RCP2.6/RCP8.5 simulations that include CFCs to set an ocean advection scheme for the CFCs

(the MDPPM scheme that is also used for the other tracers).

The diagnostic table (`diag_table`) specifies which data should be saved as output. Within the diagnostic table, output files and the temporal resolution on which fields in that output file are saved are specified similar to

```
"atmos_scalar", 1, "months", 1, "days", "time",
```

with `atmos_scalar` being the file name and 1, "months" specifying monthly output resolution. Then, the output fields are assigned to these files. For example, assigning the CO₂ mixing ratio `rrvco2` to the file `atmos_scalar` reads

```
"radiation", "rrvco2", "rrvco2", "atmos_scalar", "all", .true., "none", 2.
```

The first column states the module name, the second column gives the variable identifier within the model, the third row gives the name used in the output file, and the fourth column assigns the variable to a output file. The sixth row refers to whether temporal mean values (`.true.`) or point values should be saved (`.false.`). The seventh row allows to specify a vertical range over which the data should be saved (not specified here), and the eighth column gives the number precision (2 for float, 1 for double).

A particular focus of the PhD project was on simulations with high temporal resolution output. Hence, a variety of output fields were saved on daily-mean resolution. For most of the simulations, either of two diagnostic tables were used. One is that of the `control` simulation (some of the simulations with this diagnostic table include tendency terms for potential temperature, DIC, and O₂ on monthly-mean resolution, but they are all identical in terms of the output on daily-mean resolution), and the other one is that of the `control_ext` simulation. The output fields with daily-mean resolution for these two diagnostic tables are listed in Table A.1.

File name	Vertical level(s)	control	control_ext
ocean_daily_200	0–200 m	temp	
ocean_daily_600	600 m	salt	
ocean_daily_1000	1000 m	pot_rho_0	
		dht	
ocean_daily_100	0–100 m		
ocean_daily_200	200 m		pot_rho_0
ocean_daily_1000	1000 m		
ocean_daily_2000	0–2000 m		temp
			salt
			dht
			temp_tendency
			temp_advection
			neutral_gm_temp
			neutral_diffusion_temp
			temp_submeso
			temp_runoffmix
			temp_calvingmix
			temp_vdiffuse_impl
			temp_nonlocal_KPP
			temp_sigma_diff
			sw_heat
			mixdownslope_temp
ocean_tendency_daily_100	0–100 m		temp_xland
ocean_tendency_daily_200	200 m		temp_xlandinsert
ocean_tendency_daily_1000	1000 m		temp_vdiffuse_sbc

			sfc_hflux_pme frazil_2d temp_eta_smooth dic_tendency dic_advection neutral_gm_dic neurtal_diffusion_dic dic_submeso dic_runoffmix dic_calvingmix dic_vdiffuse_impl dic_nonlocal_KPP dic_sigma_diff mixdownslope_dic dic_xland dic_xlandinsert dic_eta_smooth dic_stf dic_btf jdic jalk
ocean_topaz_daily	2D data	jprod_ntot_100 pco2surf dic_stf o2_stf sfc_chl fndet_100	jprod_ntot_100 pco2surf dic_stf o2_stf sfc_chl fndet_100
ocean_topaz_daily_200	0–200 m	no3	
ocean_topaz_daily_600	600 m	o2	
ocean_topaz_daily_1000	1000 m	dic	
		co3_ion	
		co3_sol_arag	
		co3_sol_calc	
		htotal	
		alk	
ocean_topaz_daily_100	0–100 m	no3	
ocean_topaz_daily_200	200 m	dic	
ocean_topaz_daily_1000	1000 m	alk	
		o2	
		co3_ion	
ocean_topaz_daily_2000	0–2000 m	co3_sol_arag	
		co3_sol_calc	
		htotal	
		irr_inst	
		irr_mem	
		mu_Sm	
		mu_Lg	
		irrlim_Sm	
		irrlim_Lg	
		liebig_lim_Sm	
		liebig_lim_Lg	
		nh4lim_Sm	
		nh4lim_Lg	
		no3lim_Sm	
		no3lim_Lg	
		po4lim_Sm	
		po4lim_Lg	
ocean_topaz_rates _daily_100	0–100 m	felim_Sm	

			felim_Lg
			nLg
			nsm
			ndi
			jprod_nLg
			jprod_nsm
			jprod_ndi
			jgraz_n_Sm
			jgraz_n_Lg
			jgraz_n_Di
			chl_Sm
			chl_Lg
			chl_Di
			def_fe_Sm
			def_fe_Lg
			q_p_2_n_Lg
			q_p_2_n_Sm
		t_ref	t_ref
		t_surf	t_surf
atmos_daily	2D data	tau_x	tau_x
		tau_y	tau_y

Table A.1: List of daily-mean output fields that are saved in the diagnostic tables of all simulations that share their diagnostic table with the `control` simulation and in the simulations that share their diagnostic table with the `control_ext` simulation (see Table A.2).

A.4 Running the model

Each model simulation was run by submitting a run script with `sbatch` to Slurm. The first part of the run script defines the Slurm settings for the simulation. For the performed simulations, the configuration was chosen as

```
#SBATCH --job-name=...
#SBATCH --mail-type=FAIL
#SBATCH --mail-user=...
#SBATCH --time=10:00:00
#SBATCH --ntasks-per-core=1
#SBATCH --ntasks=180
#SBATCH --cpus-per-task=1
#SBATCH --partition=normal
#SBATCH --constraint=mc
#SBATCH --account=...
```

`ntasks-per-core` is set to 1 to not use hyper-threading. `ntasks` is set to 180 to run the model with 180 tasks (hence with 180 CPU cores, since `cpus-per-task=1`). Since each node of the multicore cluster at CSCS (chosen with the option `constraint=mc`) has 36 cores, this means that the job allocates 5 nodes. Within the `input.nml` configuration file under `coupler.nml`, these 180 CPU cores are distributed over the ocean and atmosphere grids,

```
atmos_npes = 0,
ocean_npes = 150,
```

which sets the number of cores assigned to the ocean grid to 150 and the number of cores assigned to the atmosphere grid to 30 (`atmos_npes = 0` assigns the remaining CPU cores, here

180 – 150 = 30, to the atmosphere grid). These numbers need to be compatible with the grid resolutions of the ocean and atmosphere grids since the assigned numbers of cores need to be distributed over equally-sized fractions of the horizontal grids. The atmospheric grid is divided zonally into 30 sections extending over 3 latitude slices each (`layout = 1,30` in the input namelist), and the ocean grid is separated into 150 boxes that each extend over 24 longitude slices and 20 latitude slices (`layout = 15,10`). Other choices for the number of allocated CPU cores (and hence also nodes) and layouts that assign these cores to the ocean and atmosphere grids were tested, but the choice reported above was found to be optimal in terms of the runtime per model year and the node hours needed to simulate a model year. With the chosen layout, it takes roughly 1.5 hours and 7.5 node hours to simulate one model year. However, the runtime fluctuates somewhat. Due to that, the allocated time was chosen much longer (`time=10:00:00`) to avoid cancellation of jobs.

The model is then run by calling `srun $WRKDIR/executable.x`. It writes the restart files needed to run the next model year into the subfolder `RESTART`. It is necessary to concatenate the `iceberg.res.nc*` restart files using `ncrcat` and to create the `ocmip_cfc.res.nc` restart file with numbers set to zero if it is not already existing (e.g., at the beginning of a historical simulation). The restart files are then copied into `INPUT` for the next model year, and they are also saved in a new folder `restart.$YEAR`, where `YEAR` is the simulated model year, to be able to restart the simulation at this stage also at a later point in time.

The diagnostic output is saved in the working directory. The diagnostic output for the atmosphere is saved as individual files for each latitude slice defined in the parallelization layout and needs to be combined using `mppnccombine`. In some simulations, the output files were also compressed using the `nczip` script at this stage (Sect. A.5). Finally, the diagnostic output is moved to a new folder `$YEAR` and the run script calls itself to simulate the next model year if no errors have occurred. The run scripts used for the simulations performed during this thesis (Table A.2) are available on gitlab (https://gitlab.climate.unibe.ch/burger/ESM2M_setup_run_scripts).

A.5 File transfer to Bern and file compression

After the simulations were finished, the diagnostic output had to be copied timely to Bern since data is deleted on scratch at CSCS after 30 days. This was done using a wrapper around `gridftp` (<https://gitlab.climate.unibe.ch/burger/gridftp-wrapper>), that copies the data and checks the copied files for corruption by comparing the checksums of the files before and after copying.

To save space, the diagnostic output was then also compressed without loss in number precision to save storage space. This was done using a wrapper around `nczip` (<https://git.iac.ethz.ch/heimc/package/-/blob/master/nczip>) that itself compresses the data using NCO. The wrapper is available under <https://gitlab.climate.unibe.ch/burger/nczip-wrapper>.

Simulation name	Description	Used in
<code>spin_up_final</code>	preindustrial conditions, 220 y duration, started from 1000 y preindustrial simulation conducted at GFDL	
<code>landuse_spin_up</code>	preindustrial conditions but with anthropogenic landuse changes over 1700-1860, started from <code>spin_up_final</code>	

<code>control</code>	preindustrial conditions, 500 y duration, started from <code>spin_up_final</code>	Chap. 3
<code>control_ext</code>	preindustrial conditions, 500 y duration, extends <code>control</code> with extended diag table	Chap. 4, Chap. 5, Vogt et al., in prep., Legrix et al., in prep.
<code>historical</code> , <code>historical_ENS2-5</code> , <code>historical_ENS16-20</code> , <code>historical_ENS26-30</code>	historical forcing, period 1861-2005, diag table of <code>control</code> , started from <code>landuse_spin_up</code> with perturbed initial conditions	Chap. 3, Chap. 4, Gruber et al. (2021), Cheung & Frölicher (2020), Cheung et al. (2021)
<code>historical_ENS6-15</code> , <code>historical_ENS21-25</code>	historical forcing, period 1861-2005, diag table of <code>control_ext</code> , started from <code>landuse_spin_up</code> with perturbed initial conditions	Chap. 4, Cheung & Frölicher (2020), Cheung et al. (2021)
<code>RCP85</code> , <code>RCP85_ENS2-5</code> , <code>RCP85_ENS16-20</code> , <code>RCP85_ENS26-30</code>	RCP8.5 forcing, period 2006-2100, diag table of <code>control</code> , extend ensemble members of <code>historical</code> ensemble	Chap. 3, Chap. 4, Gruber et al. (2021), Cheung & Frölicher (2020), Cheung et al. (2021)
<code>RCP85_ENS6-15</code> , <code>RCP85_ENS21-25</code>	RCP8.5 forcing, period 2006-2100, diag table of <code>control_ext</code> , extend ensemble members of <code>historical</code> ensemble	Chap. 4, Cheung & Frölicher (2020), Cheung et al. (2021)
<code>RCP26</code> , <code>RCP26_ENS2-5</code> , <code>RCP26_ENS11-30</code>	RCP2.6 forcing, period 2006-2100, diag table of <code>control</code> , extend ensemble members of <code>historical</code> ensemble	Chap. 3, Chap. 4
<code>RCP26_ENS6-10</code>	RCP2.6 forcing, period 2006-2100, diag table of <code>control_ext</code> , extend ensemble members of <code>historical</code> ensemble	Chap. 4
<code>ZEC-MIP_Bell_750</code> , <code>ZEC-MIP_Bell_1000</code> , <code>ZEC-MIP_Bell_2000</code>	750, 1000, and 2000 PgC CO ₂ cumulative emissions over 100 y, then zero emissions, otherwise preindustrial conditions, 500 y duration, started from <code>spin_up_final</code>	Jones et al. (2019), MacDougall et al. (2020)
<code>ZEC-MIP_Zero_750</code> , <code>ZEC-MIP_Zero_1000</code> , <code>ZEC-MIP_Zero_2000</code>	branched off <code>CDRMIP_1pctCO2_pv</code> after 750, 1000, and 2000 PgC CO ₂ cumulative emissions reached, then zero emissions, otherwise preindustrial conditions, 500 y duration	Jones et al. (2019), MacDougall et al. (2020)
<code>CDRMIP_1pctCO2_pv</code> , <code>CDRMIP_1pctCO2-cdr_pv</code>	1 % yearly increase in atm. CO ₂ over 140 y, 1 % decrease over 140 y, then constant, otherwise preindustrial conditions, 500 y duration, started from <code>spin_up_final</code>	Keller et al., in prep.
<code>CDRMIP_esm-piControl</code>	preindustrial conditions, but with freely evolving instead of prescribed CO ₂ , 600 y duration, started from <code>control</code> after 250 y	
<code>CDRMIP_esm-pi-CO2pulse</code> , <code>CDRMIP_esm-pi-cdr-pulse</code>	initial 100 PgC emission and removal pulse, then zero emissions, otherwise preindustrial conditions, 500 y duration, started from <code>CDRMIP_esm-piControl</code> after 100 y	

EmissionHist, EmissionHist_ENS2-5	historical forcing with CO ₂ emissions instead of prescribed CO ₂ , period 1861-2005, diag table of control , started from landuse_spin_up with perturbed initial conditions
EmissionRCP85, EmissionRCP85_ENS2-5	RCP8.5 forcing with CO ₂ emissions, period 2006-2100, diag table of control , extend ensemble members of EmissionHist ensemble
NatHistPOT, NatHistPOT_ENS2-5	natural historical forcing (volcanic, solar), zero CO ₂ emissions, no land use, period 1861-2005, diag table of control , started from landuse_spin_up with perturbed initial conditions
historical_rad, historical_res, historical_res_no_nonco2	historical forcing with CO ₂ radiatively coupled only (rad), biogeochemically coupled CO ₂ only (res), with non-CO ₂ forcing at preindustrial conditions (res_no_nonco2), period 1861-2005, diag table of control , started from landuse_spin_up
RCP85_rad, RCP85_res, RCP85_res_no_nonco2	RCP8.5 forcing with CO ₂ radiatively coupled only (rad), CO ₂ biogeochemically coupled only (res), with non-CO ₂ forcing at preindustrial conditions (res_no_nonco2), period 2006-2100, diag table of control , extend respective historical simulations
control_diurnal, historical_diurnal, RCP85_diurnal	with 2-hourly output for ocean physics and biogeochemistry, 20 y duration, historical period 1986-2005, RCP8.5 period 2081-2100
70yrs_1pct_decrease	1 % yearly decrease in atm. CO ₂ over 70 y, then constant, otherwise preindustrial conditions, 186 y duration, started from spin_up_final

Table A.2: List of simulations performed during the PhD project. The **EmissionHist**, **EmissionRCP85**, and **70yrs_1pct_decrease** simulations have been performed together with Mathias Aschwanden. The **historical_ENS11-30** and **RCP85_ENS11-30** simulations have been performed together with Natacha Le Grix. **landuse_spin_up** was branched from **spin_up_final** in such a way that all **historical** and **RCP** simulations are synchronous to **control** (the model years in **control** correspond to those in **historical** and **RCP**). The ZEC-MIP simulations were performed to participate in the Zero Emissions Commitment Model Intercomparison Project (Jones et al., 2019). The CDRMIP simulations were submitted to the Carbon Dioxide Model Intercomparison Project (Keller et al., 2018).

References

- Cheung, W. W. L. & Frölicher, T. L., 2020. Marine heatwaves exacerbate climate change impacts for fisheries in the northeast pacific, *Scientific Reports*, 10(1), 6678.
- Cheung, W. W. L., Frölicher, T. L., Lam, V. W. Y., Oyinlola, M. A., Reygondeau, G., Sumaila, U. R., Tai, T. C., Teh, L. C. L., & Wabnitz, C. C. C., 2021. Marine high temperature extremes amplify the impacts of climate change on fish and fisheries, *Science Advances*, 7(40), eabh0895.
- Cionni, I., Eyring, V., Lamarque, J. F., Randel, W. J., Stevenson, D. S., Wu, F., Bodeker, G. E., Shepherd, T. G., Shindell, D. T., & Waugh, D. W., 2011. Ozone database in support of CMIP5 simulations: results and corresponding radiative forcing, *Atmospheric Chemistry and Physics*, 11(21), 11267–11292.
- Gruber, N., Boyd, P. W., Frölicher, T. L., & Vogt, M., 2021. Ocean biogeochemical extremes and compound events, *Nature*, *in review*.
- Hurtt, G. C., Frohling, S., Fearon, M. G., Moore, B., Shevliakova, E., Malyshev, S., Pacala, S. W., & Houghton, R. A., 2006. The underpinnings of land-use history: three centuries of global gridded land-use transitions, wood-harvest activity, and resulting secondary lands, *Global Change Biology*, 12(7), 1208–1229.
- Jones, C. D., Frölicher, T. L., Koven, C., MacDougall, A. H., Matthews, H. D., Zickfeld, K., Rogelj, J., Tokarska, K. B., Gillett, N. P., Ilyina, T., Meinshausen, M., Mengis, N., Séférian, R., Eby, M., & Burger, F. A., 2019. The zero emissions commitment model intercomparison project (ZECMIP) contribution to C4MIP: quantifying committed climate changes following zero carbon emissions, *Geoscientific Model Development*, 12(10), 4375–4385.
- Keller, D. P., Lenton, A., Scott, V., Vaughan, N. E., Bauer, N., Ji, D., Jones, C. D., Kravitz, B., Muri, H., & Zickfeld, K., 2018. The carbon dioxide removal model intercomparison project (CDRMIP): rationale and experimental protocol for CMIP6, *Geoscientific Model Development*, 11(3), 1133–1160.
- Lean, J. L., 2009. Calculations of solar irradiance: Monthly means from 1882 to 2008, annual means from 1610 to 2008, https://solarisheppa.geomar.de/solarisheppa/sites/default/files/data/Calculations_of_Solar_Irradiance.pdf.
- MacDougall, A. H., Frölicher, T. L., Jones, C. D., Rogelj, J., Matthews, H. D., Zickfeld, K., Arora, V. K., Barrett, N. J., Brovkin, V., Burger, F. A., Eby, M., Eliseev, A. V., Hajima, T., Holden, P. B., Jeltsch-Thömmes, A., Koven, C., Mengis, N., Menviel, L., Michou, M., Mokhov, I. I., Oka, A., Schwinger, J., Séférian, R., Shaffer, G., Sokolov, A., Tachiiri, K., Tjiputra, J., Wiltshire, A., & Ziehn, T., 2020. Is there warming in the pipeline? a multi-model analysis of the zero emissions commitment from CO₂, *Biogeosciences*, 17(11), 2987–3016.
- Meinshausen, M., Smith, S. J., Calvin, K., Daniel, J. S., Kainuma, M. L. T., Lamarque, J.-F., Matsumoto, K., Montzka, S. A., Raper, S. C. B., Riahi, K., Thomson, A., Velders, G. J. M., & van Vuuren, D. P. P., 2011. The rcp greenhouse gas concentrations and their extensions from 1765 to 2300, *Climatic Change*, 109(1), 213.
- Stenchikov, G. L., Kirchner, I., Robock, A., Graf, H.-F., Antuña, J. C., Grainger, R. G., Lambert, A., & Thomason, L., 1998. Radiative forcing from the 1991 mount pinatubo volcanic eruption, *Journal of geophysical research. Atmospheres*, 103(D12), 13837–13857.

Acknowledgements

First of all, I want to thank Thomas Frölicher for his invaluable help over the last four years, for introducing me to the numerous intricacies of the climate system, for always being kind, generous, and available if I needed help, and for providing so much valuable feedback on my writing attempts.

I also want to thank Fortunat Joos for his willingness to be my co-supervisor and for the valuable input on my manuscripts. Likewise, I want to thank Nicolas Gruber for being my external referee and for the valuable discussions, Jens Terhaar for his large contribution to Chapter 4, and Jasmin John for her input on Chapter 3. I also want to acknowledge Hubertus Fischer for chairing my PhD defense, Claudia Maschke, Doris Rätz, and Bettina Schüpbach for their support on administrative matters, and Gunnar Jansen for his help on technical problems and the enjoyable discussions about computers.

I owe special thanks to Sandra for her valuable feedback, in particular on the biological aspects of the thesis, to Kristian for his advice on chemistry, and to Simone for proof-reading my drafts.

I am grateful to Simone for her support, care, and patience over the last years and in particular during the final phase of my PhD, to my parents and my sisters, Hannah and Klara, for always being there for me, and to Yannick, Nadine, Joshua, and Kristian for their support.

Finally, I want to thank everyone at KUP for the welcoming atmosphere, which allowed me to feel at home at KUP so quickly, and for all the good times during FAB beers, morning coffees (greetings to Aurich and Lars), coffee break discussions, hikes, Apéros, barbecues,...

Publications

Published:

Burger, F. A., John, J. G., and Frölicher, T. L., 2020. Increase in ocean acidity variability and extremes under increasing atmospheric CO₂, *Biogeosciences*, 17, 4633–4662, <https://doi.org/10.5194/bg-17-4633-2020>.

Jones, C. D., Frölicher, T. L., Koven, C., MacDougall, A. H., Matthews, H. D., Zickfeld, K., Rogelj, J., Tokarska, K. B., Gillett, N. P., Ilyina, T., Meinshausen, M., Mengis, N., Séférian, R., Eby, M., and Burger, F. A., 2019. The Zero Emissions Commitment Model Intercomparison Project (ZECMIP) contribution to C4MIP: quantifying committed climate changes following zero carbon emissions, *Geosci. Model Dev.*, 12, 4375–4385, <https://doi.org/10.5194/gmd-12-4375-2019>.

MacDougall, A. H., Frölicher, T. L., Jones, C. D., Rogelj, J., Matthews, H. D., Zickfeld, K., Arora, V. K., Barrett, N. J., Brovkin, V., Burger, F. A., Eby, M., Eliseev, A. V., Hajima, T., Holden, P. B., Jeltsch-Thömmes, A., Koven, C., Mengis, N., Menviel, L., Michou, M., Mokhov, I. I., Oka, A., Schwinger, J., Séférian, R., Shaffer, G., Sokolov, A., Tachiiri, K., Tjiputra, J., Wiltshire, A., and Ziehn, T., 2020. Is there warming in the pipeline? A multi-model analysis of the Zero Emissions Commitment from CO₂, *Biogeosciences*, 17, 2987–3016, <https://doi.org/10.5194/bg-17-2987-2020>.

Schlunegger, S., Eddebar, Y., Brady, R. X., Burger, F. A., 2020. Applications of Large Ensembles to Marine Biogeochemistry. *US Clivar Variations* 18 (2), 18-25.

Under review:

Burger, F. A., Terhaar, J., and Frölicher, T. L.: Compound marine heatwaves and ocean acidity extremes, *Nature Communications*, under review.

In preparation:

Burger, F. A. and Frölicher, T. L.: Drivers of ocean acidity extreme events in an Earth system model, *in preparation*.

Vogt, L., Burger, F. A., and Frölicher, T. L.: Local drivers of marine heatwaves: A global analysis with an Earth system model, *in preparation*.

Keller D.P., Lenton, A., Scott V., Vaughan, N.E., Ji, D., Jones, C., Kravitz, B., Muri, H., Zickfeld, K., Séférian, R., Köhler, P., John, J., Eliseev, A.V., Quilcaille, Y., Gasser, T., Shaffer, G., Pedersen, J.O.P., Ziehn, T., Yamamoto, A., Kawamiya, M., Fröb, F., Lawrence, D., Jeltsch-Thömmes, A., Christian J., Tjiputra, J., Burger F.A., Joos, F., Frölicher, T.L., and Wiltshire, A.: Is Anthropogenic Climate Change Reversible? The Earth system response to a massive CO₂ increase then decrease (emissions followed by negative emissions), *in preparation*.

Erklärung

gemäss Art. 18 PromR Phil.-nat. 2019

Name/Vorname: Burger, Friedrich Anton

Matrikelnummer: 17-126-475

Studiengang: Physik

Bachelor ☐

Master ☐

Dissertation ☒

Titel der Arbeit: Modeling extreme events in ocean acidity and compound extreme events using a comprehensive Earth system model

LeiterIn der Arbeit: Prof. Dr. Thomas Frölicher

Ich erkläre hiermit, dass ich diese Arbeit selbständig verfasst und keine anderen als die angegebenen Quellen benutzt habe. Alle Stellen, die wörtlich oder sinn-gemäss aus Quellen entnommen wurden, habe ich als solche gekennzeichnet. Mir ist bekannt, dass andern-falls der Senat gemäss Artikel 36 Absatz 1 Buchstabe r des Gesetzes über die Universität vom 5. September 1996 und Artikel 69 des Universitätssta-tuts vom 7. Juni 2011 zum Entzug des Dokortitels be-rechtigt ist.

Für die Zwecke der Begutachtung und der Überprüfung der Einhaltung der Selbständigkeitserklärung bzw. der Reglemente betreffend Plagiate erteile ich der Univer-sität Bern das Recht, die dazu erforderlichen Perso-nendaten zu bearbeiten und Nutzungshandlungen vor-zunehmen, insbesondere die Doktorarbeit zu vervielfäl-tigen und dauerhaft in einer Datenbank zu speichern sowie diese zur Überprüfung von Arbeiten Dritter zu verwenden oder hierzu zur Verfügung zu stellen.

Bern, 26.10.2021

Ort/Datum



Unterschrift